ANALYSIS OF MEASUREMENTS AND IMPROVEMENTS UPON THE ACTIVE TISSUE EQUIVALENT DOSIMETER

By

BRYAN MICHAEL HAYES

Bachelor of Science in Physics
University of La Verne
La Verne, California
2016

Submitted to the Faculty of the
Graduate College of the
Oklahoma State University
in partial fulfillment of
the requirements for
the Degree of
DOCTOR OF PHILOSOPHY
July, 2020

ANALYSIS OF MEASUREMENTS AND

IMPROVEMENTS UPON THE

ACTIVE TISSUE EQUIVALENT DOSIMETER

Dissertation Approved:

Dr. Eric Benton

Dissertation Adviser

Dr. Al Rosenberger

Dr. Mario Borunda

Dr. Ranji Vaidyanathan

ACKNOWLEDGEMENTS

There are many people who deserve to be acknowledged for helping me get to this point in my scientific career. I first would like to thank my advisor Eric Benton for being a mentor that taught me how to critically think and inspired me through his devotion and passion for science. My time at Oklahoma State University has been overwhelmingly rewarding because of his dedication to being an excellent teacher. I cherish the mentor-mentee relationship we have formed. I would also like to thank my committee members Al Rosenberger, Mario Borunda, and Ranji Vaidyanathan for their generous help in the pursuit of this degree.

Bradford "Buddy" Gersey deserves great acknowledgement in teaching me the intricacies of working with tissue equivalent proportional counters and their data. He was always eager to talk about my research and guide me through problems I was facing. Many more thanks for allowing the use his TEPC data in this dissertation and providing his wisdom in all aspects in life.

I would like to thank Ryan Rios, formerly of the Space Radiation Analysis Group (SRAG), for providing orbital position data for the Active Tissue Equivalent Dosimeter (ATED) International Space Station experiment. Ryan offered advice that was vital in the characterization of ATED in the space radiation environment.

Thank you to Jack Miller of NASA GeneLab and Lawrence Berkeley National Laboratory for guidance during our HIMAC experiments. Thank you especially for the wisdom in regards to choosing a career path and using personal connections to open doors for me.

I would also like to thank the current and former members of the Oklahoma State University Radiation Physics Laboratory. Huge thanks to Oliver Causey, who gave me a head start by teaching me instrumentation and developing much of the ATED that flew on the International Space Station. Thank you to Paul Inman, for providing the simulation of ATED used in this dissertation and for supporting our experimental efforts at Los Alamos. Thank you to Art and Barbara Lucas for their plethora of stories that were full of invaluable information. Rajesh Panthi for allowing me the opportunity to join one of his experiments and learn from his example. I also would like to thank Conner Heffernan, Tristin Lee, and Martin Yang.

Our experiments at HIMAC would not have been possible without the support and help from the scientists and staff of NIRS. Special thanks to Satoshi Kodaira for including me as a part of his research efforts and supporting ATED calibration and characterization. I would also like to thank: Yukio Uchihori, Hisashi Kitamura, Tamon Kusumoto, Nama Biiru, Masayuki Naito, and Ryo Ogawara. I would like to thank Mitsubishi Heavy Industries for providing the materials tested at HIMAC.

Many thanks to the scientists and support staff at Los Alamos National Lab (LANL). A special thank you to Steve Wender for the beam time at LANSCE and answering our questions. Thank you to Valerie Salazar for the quick return of our instruments and being our reliable point of contact. Also, thank you to Carl Johnson for setting up the special opportunity to give presentations to LANL staff.

I would like to thank the scientists and engineers at NASA Langley Research Center for getting my career in space radiation dosimetry started. Very Special thanks to Chris Mertens who was my

mentor, and taught me to always “stay in the yolk”. Thank you to Francis Badavi, who bullied me to pursue a PhD in Physics. Special thanks to Ryan Norman, James Rosenthal, and John Wilson. I also would like to thank the entire RaD-X team including: Kevin Daugherty and Amanda Cutright.

My parents were fundamental in getting me to where I am today. They always allowed me to be curious and gave me the freedom to explore my interests. My father who taught me the importance of working hard, and keeping in balance with the rest of life. My mother who ingrained the “work hard, play hard” mentality into me at a young age. I can never repay the constant love and support they have provided over the years.

Most importantly, I would like to thank my wife Andrea. I thank her for the unending support in my pursuit of being an accomplished scientist. She has always challenged me in ways that have kept me honest and made me a better person. Her love inspires me to be the best at everything I do. She has invested as much time and effort into this PhD as I have. This accomplishment is as much hers and it is mine. I would not have gotten to this point in my life without her love and support. Andrea, I love you very much.

Name: BRYAN MICHAEL HAYES

Date of Degree: JULY, 2020

Title of Study: ANALYSIS OF MEASUREMENTS AND IMPROVEMENTS UPON THE ACTIVE TISSUE DOSIMETER

Major Field: PHYSICS

Abstract: The Oklahoma State University Radiation Physics Lab is nearing completion in the development of a tissue equivalent proportional counter (TEPC), the Active Tissue Equivalent Dosimeter (ATED), to monitor cosmic radiation exposure of astronauts and aircrew. This dissertation is a detailed analysis of ATED measurements in the space and atmospheric radiation environments, and a comprehensive description of improvements made on the ATED instrument. The ATED was sent to the International Space Station (ISS) on May 21, 2018. ATED measurements were analyzed in terms of time, latitude, longitude, and altitude of the ISS in order to correlate with features that exist in the ISS orbit. Comparisons with computer simulations and previous measurements on the ISS strongly indicate that the ATED functioned as designed. The ATED was exposed to a similar neutron energy spectrum to that found at aviation altitudes at the Los Alamos Neutron Science Center (LANSCE). Comparisons of ATED measurements at LANSCE with the same measurement by a NASA TEPC and simulations in MCNP_6.2 demonstrate that ATED has the appropriate response to these neutrons. ATED has also been shown to be useful at charged particle accelerators, including the development of a new method to assess the suitability of materials for use as radiation shielding in spacecraft, concentrating on their propensity to produce secondary neutrons. Areas of improvement have been identified and implemented into recent ATED models. This includes the validation or refutation of previously made assumptions and the implementation of new hardware/designs. Cost was significantly reduced by programming a Red Pitaya to function as a dual-input spectrometer, saving $8000 per ATED instrument. For the first time, the individual contributions by positive ions and electrons to pulse amplitude inside a proportional counter have been measured. This demonstrated that positive ions contribute anywhere from 4-12 times more to pulse amplitude than electrons, refuting previous assumptions that only electrons contribute to pulse amplitude. It was demonstrated for the first time that ATED collects 100% of the separated charge inside its active volume.

TABLE OF CONTENTS

Chapter Page

I. INTRODUCTION 1

II. THE SPACE RADIATION ENVIRONMENT 11

2.1 Galactic Cosmic Rays 11
2.2 Van Allen Radiation Belts and the South Atlantic Anomaly 15
2.3 Solar Particle Events 18
2.4 Secondary Particles 19
2.5 The Radiation Environment in the Atmosphere 22
2.6 Terrestrial Gamma Flashes 23

III. DESCRIPTION OF THE ACTIVE TISSUE EQUIVALENT DOSIMETER 25

3.1 Description of Gas Filled Detectors 25
3.2 Formation of Signals Inside Proportional Counters 27
3.3 Supporting Electronics & Hardware 31
3.4 Charge Collection in the ATED Active Volumes 35
3.5 The Electric Fields Inside ATED Active Volumes 40
3.6 Mean Chord Length 47
3.7 Lineal Energy Spectra 52
3.8 Tissue Equivalence and Simulated Volumes 54
3.9 Measurement of Indirectly Ionizing Radiation 55
3.10 The Representation of Lineal Energy Spectra 57
3.11 Calculation of Absorbed Dose and Dose Equivalent 62
3.12 Utility of a Red Pitaya Field Programmable Gate Array as a MCA 64

IV. CALIBRATION METHODS FOR THE ACTIVE TISSUE EQUIVALENT DOSIMETER 71

4.1 Calibration with Charged Particle Beams at HIMAC 72
4.2 Calibration Using Neutrons 74
4.3 Calibration Using Gamma Rays 78
4.4 Combining Spectra Measured at Different Gain Settings 82

Chapter Page

V. CONVERSION OF LINEAL ENERGY MEASURMENTS INTO LINEAR ENERGY TRANSFER....86

5.1 Motivation to Convert to LET Spectra....86
5.2 Geometric Conversion to LET....88
5.3 The Kellerer LET Conversion Method....92
5.4 The Conversion of Measurements into LET....95

VI. ANALYSIS OF THE CONTRIBUTIONS TO PULSE AMPLITUDES IN PROPORTIONAL COUNTERS....98

6.1 Motivation....98
6.2 The Function Form of Pulses Inside a Proportional Counter and Experimental Methods....100
6.3 Results....103

VII. NEUTRON MEASURMENTS AT THE LOS ALAMOS NEUTRON SCIENCE CENTER....107

7.1 Description of the Beamline....108
7.2 Nominal Beam Measurement....111
7.3 Shielding Experiments....114
7.4 Comparison of Nominal Beam Measurement with Shuttle TEPC....118
7.4 Comparison with Simulation....120

VIII. OFF-AXIS MEASUREMENTS AT HIMAC....122

8.1 Introduction and Motivation....122
8.2 Description of the experimental Setup....123
8.3 Shadow Bar Subtraction....125
8.4 Comparison of Different Materials....127
8.5 Comparison Between Beams....130
8.5 Depths of Aluminum....132

IX. MEASUREMENTS TAKEN ON THE INTERNATIONAL SPACE STATION WITH THE ACTIVE TISSUE EQUIVALENT DOSIMETER....135

9.1 Description of the Experiment and Hardware....136
9.2 Results from ATED Measurements....141
9.3 Comparison to Model Calculations....150
9.4 Separation into Orbital Regions....156
9.5 Conversion of ATED Measurements into LET....165

Chapter Page

X. CONCLUSIONS....169

10.1 Accomplishments....170
10.2 Future Work....172
10.3 Final Words....174

REFERENCES....176

APPENDICES....184

Appendix 1 Uncertainties in ATED Measurements....184
A.1.1 Negligible Sources of Error in ATED Absorbed Dose Calculations...184
A.1.2 Description of Uncertainty Associated with the Mass of Tissue Equivalent Gas....185
A.1.2 Description of Uncertainty in Chord Length of the Simulated Volume....187
A.1.3 Uncertainty in Absorbed Dose....188
Appendix 2: Dosimetric Quantities in Microdosimetry....189
A.2.1 Particle Fluence and Flux....190
A.2.2 Stopping Power and Linear Energy Transfer....190
A.2.3 Lineal Energy....192
A.2.4 Absorbed Dose and Dose Equivalent....193
Appendix 3: Preliminary Cylindrical ATED Measurements at HIMAC....195
A.3.1 Dose-Depth Experiment with Cylindrical ATED....195

LIST OF TABLES

Table Page

Table 4.1: The bin values of the electron edge location for the PuBe and Gamma measurement shown in Figure 4.5 and the percent difference between the two. 82

Table 6.1: The ratio of fitted values for the spherical ATED geometry1 106

Table 6.2: The ratio of fitted values for the cylindrical ATED geometry 106

Table 7.1: Normalized absorbed dose for each material and the nominal beam at the ICE House 118

Table 8.1: Reduction of Dose due to use of the iron shadow bar 126

Table 9.1: Absorbed dose for each day ATED was on ISS. (*) Data was lost after 12:10:17 on July 20th.....144

Table 9.2: Absorbed dose as calculated by ATED measurements and the OLTARIS computer code for each day ATED was on ISS. (*) Data was lost after 12:10:17 on July 20th. 154

Table 9.3: Percentage of absorbed dose for each region and percentage of ISS orbit each region occupies as calculated by ATED measurements 161

Table A.1.1: Internal diameters of the ATED spherical active volumes and the height of the cylindrical ATED volume with their associated uncertainties.....186

Table A.1.2: The functions of pressure as a function of temperature as a function of temperature for each ATED active volume 187

Table A.1.3: The relative uncertainty in mass for ATED active volumes.....187

Table Page

Table A.1.4: Relative uncertainty in mean chord length for ATED simulated volumes 188

Table A.1.5: The relative uncertainty in absorbed dose measurements for different ATED active volumes 188

LIST OF FIGURES

Figure Page

Figure 2.1: 10 day GCR differential flux as a function of kinetic energy effected by the solar cycle for hydrogen, helium, oxygen, and iron. The plotted data is from the 2010 solar minimum and the 2001 solar maximum. Solid lines represent solar maximum and dashed solar minimum. Significant attenuation during solar maxima occurs at GCR energies below 1 GeV/n. [adapted from: Badwhar, 1997] 12

Figure 2.2: The complex Sun-Earth magnetic interaction. Solar wind from the left distorts the magnetic field of Earth into a tear-drop shape as seen above. Labels are placed at the various features seen in this interaction, but are not described in the text.....13

Figure 2.3: The geomagnetic cutoff rigidity for particles normal to the surface of Earth. Each contour is labeled with its value in GV and increase as they get closer to the geomagnetic equator. Not shown is the zero value for the magnetic poles [Smart et al., 2009]. 15

Figure 2.4: A cross-section of the two Van Allen radiation belts associated with the geomagnetic field. Note the close approach of the South Atlantic Anomaly, penetrating the ISS orbit [SRAG 2016]. 17

Figure 2.5: The GCR, SAA and Electron Cusp regions as a function of latitude and longitude for July 2018. These region boundaries are described in the text. The SAA region is shown in red and the GCR in blue. 18

Figure 2.6: Target fragmentation of a target nucleus from an incident proton or neutron. The reactions are separated by color for the type of particles that are produced [adapted from Dewitt 2011].....20

Figure 2.7: Projectile fragmentation of a heavy ion particle that interacts with a target nucleus like that in a spacecraft. The result of this interaction is a nuclear fireball that emits protons and neutrons until a more stable heavy fragment is produced. [adapted from Dewitt 2011]. 21

Figure Page

Figure 2.8: Air shower illustration showing an example of the secondary particles involved. Also shown is the typical altitude that a commercial flight takes place, where a high altitude plane would fly, and a region known as the Pfotzer Maximum 22

Figure 3.1: Ion pairs being separated by traversing ionizing radiation in a gas filled volume. The resulting ions will drift according to the electric field inside and are collected by the electrodes. 26

Figure 3.2: The number of collected ions per unit time as function of applied bias, showing the various regions for gas filled detectors. Each region is separated by a voltage value and a corresponding vertical line. [adapted from Tsoulfanidis, 1995].....27

Figure 3.3: Illustration of a Townsend avalanche from a single electron. The secondary ionization process occurs roughly a distance equal to the diameter of the wire collecting charge. 28

Figure 3.4: A Flow chart of signals for a proportional counter system. Details are described in the text. Signal and pulse are used interchangeably. 30

Figure 3.5: A picture of a 2-inch diameter ATED spherical active volume 32

Figure 3.6: A schematic of the ATED detector head. Both a cylindrical and spherical active volume are shown. The detector head holds the active volume, supporting structures, a preamplifier and the tissue equivalent gas.....33

Figure 3.7: The electronics used in the ATED system. They include a high voltage supply, +/-12VDC supply, +5VDC supply, a CR-110 preamplifier, one or two CR-160 evaluation boards, and one or two CR-200 Gaussian shaping amplifiers. Not shown is the linear regulator circuit placed as the input voltage for the high voltage supply. 34

Figure 3.8 A re-sealable can with BNC and SHV feedthroughs. The large brass component is the valve which gas can be evacuated and refilled into the can. This older model of ATED detector head was fabricated by [Collums, 2012].....36

Figure 3.9: The experimental set up for finding collected charge as a function of applied bias. The re-sealable can was outfitted with an ATED active volume, a CR-110 preamplifier, an Am-241 alpha source, and filled to an appropriate pressure of tissue equivalent gas. Signals were passed through a preamplifer and Gaussian shaping amplifier. The resulting pulse height was measured in an oscilloscope 37

Figure 3.10: Collected charge as a function of applied bias for the 2-inch sphere. Each region of operation is labeled. Error is quantified as the standard deviation of the ten measurements taken at each applied bias.....39

Figure Page

Figure 3.11: The electric field lines for a spherical ATED of 2" diameter. The field lines are evenly spaced on the inside of the outer shell and converge at the center wire. Calculations for the above electric field were done in MATLAB. 42

Figure 3.12: The relative electric field strength for a Spherical ATED. A power law fit is put over the data. The fit and coefficient of determination are also displayed. 43

Figure 3.13: The electric field lines for the first cylindrical ATED. Significant end effects occur close to where the central wire is supported by the wall of the detector. 44

Figure 3.14: The relative electric field strength for cylindrical ATED. The shaded region is the region inside the active volume where there are significant end effects. 45

Figure 3.15: The electric field inside the cylindrical ATED with field tubes. The cylinder has been elongated in order to keep the active volume inside to have equal diameter and height.....46

Figure 3.16: A Spherical ATED active volume during an ionization event. Freed electrons will accelerate towards the center wire and produce a Townsend avalanche near the wire. The total number of freed electrons will be directly proportional to the energy deposited in the tissue equivalent gas 47

Figure 3.1: The simplified case of considering particles approaching from a single direction. Supporting labels are explained in the text.....48

Figure 3.18: A right cylinder and incident ionizing radiation passing though its height cylinder. This kind of measurement will have a uniform chord length distribution....51

Figure 3.19: Number of counts (N, arbitrary) as a function of lineal energy bins, y. An ideal measurement of particles of a single LET and the corresponding lineal energy spectrum in a spherical TEPC [Rossi, 1996] 53

Figure 3.2: Indirectly ionizing radiation (gammas and neutrons) producing example secondary particles in the dense wall surrounding the active volume of a spherical ATED. TE stands for tissue equivalent. An identical process will happen for cylindrical geometries. 57

Figure 3.21: The probability density normalized by bin width, p(y), as a function of lineal energy, y, of a four-week measurement of a PuBe neutron source plotted on log-log axes. Because the number of counts measured spans several orders of magnitude p(y) is typically shown on a log-log fashion. 59

Figure Page

Figure 3.22: The relative dose distribution for the 4-week measurement with a spherical ATED measuring neutrons from a PuBe source. We can visually see that most of the dose came from a range of lineal energies between 101 102 keV/µm.....61

Figure 3.23: Measurement of counts as a function of channel number for 400 MeV/n Oxygen at HIMAC as measured by a Red Pitaya MCA. Red is the high gain amplification channel, and blue is the low gain amplification channel.....66

Figure 3.24: Percent dead time as a function of frequency for the Red Pitaya MCA. Dead time was calculated by the Red Pitaya MCA software by taking the time to digest pulses divided by the total acquisition time. Multiple measurements were made and uncertainty is quantified as the standard deviation. 67

Figure 3.25: A Poisson Distribution around the frequency of particles measured at HIMAC (2026.8 Hz). The calculated standard deviation around this point yields the uncertainty in this value. 69

Figure 4.3:The nominal beam measurement of 400 MeV/n Oxygen by a spherical ATED, counts as a function of bin number normalized to peak height. The high gain channel is shown in red and the low gain channel shown in blue 73

Figure 4.2: Calibration functions for the high and log gain channels from three separate measurements taken at HIMAC. The dots represent the centroids of Gaussian fits for nominal beam measurements by 500 MeV/n iron, 400 MeV/n oxygen, and 400 MeV/n carbon.....74

Figure 4.3: The low-gain channel of a measurement of neutrons from a PuBe source. The measurement was taken over four weeks to ensure the maximum amount of resolution of the proton edge. The vertical black dotted line is the bin value of the proton edge. This is then used for calibrating the low gain channel. 77

Figure 4.4: A conceptual count spectrum of the measurement of a mixed gamma-neutron radiation field by a TEPC. The vertical blue lines represent the perceived and actual electron edges.....79

Figure 4.4: The high gain channel count spectra for a PuBe (red line) and gamma (black line) measurement. The dotted lines show the location of the electron edges for their associated measurement.....81

Figure 4.6: Both the high-gain and low-gain channel count spectra from the previous PuBe measurement, normalized by bin-width. The intersection of the two spectra is the point where they are combined. 83

Figure Page

Figure 4.7: The probability distribution, normalized by bin-width, for a PuBe neutron measurement. Both amplification gains have been combined. 84

Figure 4.8: The relative dose distribution as measured at LANSCE. Linearly spaced bins (black) and logarithmically spaced bins (red) are shown. 85

Figure 5.1: Number of counts (N, arbitrary) as a function of lineal energy, y. This is an ideal measurement of particles of a single LET and the corresponding lineal energy spectrum in a spherical TEPC [Rossi, 1996] 88

Figure 5.2: The superposition of four different triangles representing an ideal measurement of four different lineal energies [Adapted from Collums, 2012]. 90

Figure 5.3: The shaded region represents the total number of particles contributing to the two smallest LET values [Adapted from Collums, 2012]. 90

Figure 5.3: 400MeV/n Oxygen lineal energy measurement in black and its corresponding LET conversions in red and blue. 96

Figure 6.5: An illustration of how electrons and positive ions produce a pulse across the ATED coupling capacitor. For details, see accompanying text 99

Figure 6.2: Pulse amplitude from an ionization event in a proportional counter as a function of time. This is the functional form of equation 6.2 and shows the contributions from electrons and positive ions. Relative values were chosen to illustrate the fast nature of electrons vs the slower positive ions. 102

Figure 6.3: The experimental setup for the collection of pulses across a 1nF coupling capacitor. No preamplifier was used. The can was at the appropriate pressure and the active volume was biased at the appropriate voltage with a high voltage supply. Pulses were saved onto a USB drive. 103

Figure 6.4: A saved pulse from an ATED capacitor discharge as a function of time, shown as black dots. The resulting fit is shown as a red line. The equation of the fit and the coefficient of determination are also displayed. 104

Figure 6.5: The fit of a pulse separated into its different parts. Fast electrons contribute to overall pulse height very briefly before RC decay dominates. Slower positive ions will contribute to pulse amplitude over a longer amount of time and thus contribute more to pulse amplitude. 105

Figure Page

Figure 7.1: The process of how neutrons are created at LANSCE, Target 4. Pulsed protons are incident onto a tungsten target. Secondary particles are produced via spallation in all directions. Secondary particles leave at specific angles, where charged particles are deflected away from the beamline with sweeping magnets. 108

Figure 7.2: The Differential Neutron Flux as a function of energy at LANSCE ICE House facility and neutron flux found in the atmosphere at an altitude of 12km [Adapted from Gersey, et al., 2003]. 109

Figure 7.3: ATED on the ICE House Beamline. The neutron beam came from the far wall, through the fission chamber, and passed through ATED. The electronics were placed off-axis to the beamline. 110

Figure 7.4: The probability distribution normalized by bin-width for the nominal beam at the LANSCE ICE House 112

Figure 7.5: The relative dose distribution measured by ATED at the LASNCE ICE House (nominal beam). 114

Figure 7.6: The Relative dose distribution of the nominal beam measurement and each shielding material. Each distribution has been normalized to the number of incident neutrons.....117

Figure 7.7: Relative dose distributions for the nominal beam at the LANSCE ICE House for the ATED and the Shuttle TEPC. Both distributions have been normalized by peak height in order to highlight differences between the two spectra. 119

Figure 7.8: The relative dose distribution for ATED and a simulation of ATED at the LANSCE ICE House beamline. The simulation was performed in MCNP_6.2. 121

Figure 8.1: Geometry of the off-axis experimental setup. ATED and the CR-39 PNTD are located 45 degrees off the beamline from the target material.....123

Figure 8.2: The relative dose distribution of 5g/cm2 aluminum with and without a shadow bar for an 800 MeV/n Si beam. 125

Figure 8.3: Relative dose distribution for all shadow bar and no target measurements.....127

Figure 8.4: The relative dose distribution of 5g/cm2 of different materials. Incident particles were 800 MeV/n Si.....128

Figure Page

Figure 8.5: Relative dose distribution for 5g/cm2 of different materials for 650 MeV/n Fe.....129

Figure 8.6: The relative dose distribution for 5g/cm2 of aluminum across three different beams. Carbon and silicon beams are set on a different scale in the top-right. Also, the dose per fluence for each beam is shown.....130

Figure 8.7: The relative dose distribution for 5g/cm2 of HDPE for the three different beams. The dose per fluence for each beam is shown. 131

Figure 8.8: The relative dose distribution for 5g/cm2 of copper. All three beams are shown along with their corresponding dose per fluence.....132

Figure 8.9: Absorbed dose per fluence as a function of depth of aluminum. As more material is placed in the beam, the more propensity of creating secondary neutrons133

Figure 9.7: Top left is the ATED outer box and AC power line. 137

Figure 9.2: Top right is the ATED active volume showing the acrylic shell and the central wire holders.....137

Figure 9.3: Bottom is the inside of the ATED box, showing the various faraday cages for each electrical component.....137

Figure 9.4: The ATED on ISS. ATED was located in Node-3. Additional instruments were to be placed next to ATED for comparison of measurements. 139

Figure 9.5 Detailed look inside Node-3 of the ISS. The location of ATED (labeled “Active Tissue” in this diagram) and the radiation instruments are next to the Waste Housing Compartment (WHC). 140

Figure 9.6: The location of Node-3 on the ISS. The shielding distribution around Node 3 is highly eccentric and not well known.....141

Figure 9.7 Absorbed Dose Rate as a function of time for ATED on the ISS. The fluctuation below 1 μGy/minute is due to the ISS traversing the equator and moving towards the poles. Intermittent large spikes are from the ISS passing through the SAA. Total absorbed dose was 3.1815 ± 0.2672 mGy for this period. 144

Figure Page

Figure 9.8: A linearly interpolated LOWESS fit of absorbed dose rate as a function of latitude and longitude. An exponential increase in absorbed dose rate is seen over the South Atlantic Ocean and South America. Also, elevated absorbed dose rates are seen close to the poles.....145

Figure 9.9: The probability distribution as a function of lineal energy (P(y)) for the ISS ATED for 16-20 July, 2018. The proton edge is seen around 150 keV/µm. HZE particles contribute to counts up to 1000 keV/µm. Uncertainty is quantified as the standard deviation of counts per unit time. 148

Figure 9.10: The relative dose distribution of the ISS ATED. The area under the curve is equal to the relative amount of contribution to absorbed dose in a range of lineal energies 150

Figure 9.11: The differential LET and lineal energy flux from OLTARIS and the ISS ATED. Different uniform depths of aluminum were simulated in spherical distributions in the OLTARIS code to find the best agreement with ATED measurements. This will serve as an approximate depth of shielding for ATED simulation comparisons.....153

Figure 9.12: ATED differential flux as a function of lineal energy and the differential flux behind 10 g/cm2 of aluminum as a function of LET calculated by OLTARIS.....155

Figure 9.13: The location of each ATED data point used as a function of latitude and longitude. Each data point has been color-coded to show which region the data points belong to.....157

Figure 9.14: The frequency of counts per second as a function of lineal energy for the SAA, Electron Cusp, and GCR regions. Data is separated based on the regions described in the text.....158

Figure 9.15: Dose Distribution of the ATED ISS data separated into different regions. the area under the curve corresponds to the amount of dose absorbed. Uncertainty is quantified as the 8.40% of ATED calculated absorbed dose values.....159

Figure 9.16: The Comparison of ATED measurements taken inside the SAA and the calculated differential flux of trapped protons as calculated by OLTARIS. Uncertainty is quantified as the standard deviation of SAA files. 162

Figure 9.17: Absorbed dose rate as a function of magnetic flux density for region-separated ATED measurements aboard the ISS. Each region is color-coded to its corresponding region. 163

Figure Page

Figure 9.18: Absorbed dose rate as a function of L-Shell parameter in Earth radii. The dashed lines represent the general trend for the upper and lower bounds of data and encompass 95% of all data in the GCR and electron cusp regions. The lower bound is a linear trend with increasing L-Shell. 165

Figure 9.19: Differential Flux of the LET found in Low Earth Orbit, the measured lineal energy spectrum measured by ATED, and the two LET conversions of ATED measurement. 166

Figure A.2.1: Quality factor as a function of LET. These values are derived from the definition in ICRP 60. 194

Figure A.3.1: Absorbed dose normalized by fluence as a function of depth (left) and thickness (right) for aluminum, polyethylene and PPSiC20 as measured by a spherical ATED. 197

Figure A.3.2: Absorbed dose from 500 MeV/n Fe, normalized by fluence, as a function of depth (left) and thickness (right) as measured by a spherical 2-inch ATED. The materials are aluminum, polyethylene and PPSiC20. 198

CHAPTER I

INTRODUCTION

Cosmic radiation is a potentially serious health hazard to astronauts in space and aircrew in the atmosphere [Badhwar, 2002, Thomas, et al., 2016, Mertens, 2016]. There is a moral and scientific need to monitor the cosmic radiation exposure for these occupations to help mitigate the health issues associated with exposure to ionizing radiation. There is currently a lack of ionizing radiation dosimeters that can measure aircrew exposure during flight. The radiation environment inside spacecraft can significantly vary throughout, requiring ionizing radiation dosimeters in multiple locations inside a single space vehicle [Badhwar, 1997]. The best means to measure aircrew and astronaut ionizing radiation exposure is with a small instrument that has a similar response to ionizing radiation that human tissue does, is low-cost, easy to use, and records time resolved data. The Radiation Physics Laboratory at Oklahoma State University is developing the Active Tissue Equivalent Dosimeter (ATED) to meet this need. The ATED development program is an ongoing project with the goal of producing tissue equivalent proportional counters (TEPCs) that can be widely used in aviation and in multiple locations onboard spacecraft through being low-cost, easy to use, and having a small resource demand [Collums, 2012; Causey, 2018].

Recent improvements, refinements, and demonstration measurements indicate that the ATED development program is nearing completion. This work has demonstrated the validity of key assumptions about how ATED operates, has significantly reduced cost of production, and demonstrated that ATED can successfully measure absorbed dose in tissue both in the atmosphere and in space.

NASA produced a number of groundbreaking portable TEPCs for use on the NASA Space Shuttle missions and the Russian Mir Space Station. The major innovations of these instruments was the technology that made them self-contained and portable. Although these instruments made significant contributions to our understanding of the radiation environment aboard spacecraft, their age has made them obsolete. Far West Technology, Inc. produces the only commercially available TEPC based on the original NASA design, called the HAWK TEPC. There are two major shortcomings with the HAWK TEPC: 1) the instrument costs upwards of $30,000, making its widespread use aboard commercial and business aircraft cost prohibitive and 2) the data produced by the instrument is subject to internal processing, none of it transparent, that makes analysis and interpretation of measurements extremely difficult and problematic.

The OSU Radiation Physics Laboratory is developing ATED as a low-cost and easy-to-use alternative to the NASA and HAWK TEPCs. The ATED can be used on a variety of types of aircraft, including commercial jetliners, business jets, and military transports, as well as in multiple locations in spacecraft because of its low-cost and portability. Data produced by ATED instruments are fundamental, unprocessed pulse-height spectra that are easily accessible. The process of using these spectra and calculating absorbed dose in tissue is explicitly explained in this dissertation to eliminate ambiguity.

The space radiation environment is the most challenging environment to quantify the human health risk associated with ionizing radiation due to the wide range of energies that particles possess [Benton

et al, 2001]. Many dosimeters used in space are silicon based, which is a suitable detecting medium for dosimetry when only the ionization of charged particles is important to absorbed dose. Using silicon-based dosimeters is problematic with the high-energy particles found in space. Incoming particles with sufficient energy create secondary particles in the hull of the spacecraft and inside the bodies of astronauts through nuclear interactions with nuclei. Some of these secondary particles will be short-range, high LET particles that have the potential of inflicting massive amounts of damage to nearby human tissue. The nuclear reactions that produce secondary particles inside the bodies of astronauts depend on the nuclear cross sections of the nuclei of the constituent atoms that make up human tissue. The nuclear cross sections for silicon are utterly different than that of human tissue. This difference means silicon will not measure the same secondary nuclear products that are produced inside the bodies of astronauts. In addition, secondary neutrons are produced in these nuclear interactions. Neutrons can only interact with matter via nuclear means and have been found to be highly damaging to human tissue [Cucinotta, et al., 2012]. Silicon will not properly measure the human health impact from secondary neutrons because its nuclear cross sections are not similar to that of tissue.

The non-trivial differences in the nuclear response of different materials necessitates a tissue equivalent detecting medium to fully quantify the human exposure to ionizing radiation in space. The ATED instrument is tissue equivalent, which allows for the direct measurement of absorbed dose in human tissue, i.e. the same quantity that a human would receive. This includes the measurement of neutrons and the short range, high LET secondary particles produced in human tissue. Using the ATED is a cost-effective and appropriate way to help quantify the human health risk associated with ionizing radiation in space. Tissue equivalence is especially important in the atmosphere, where neutrons are the main component of the radiation field that cause biological damage [Benton, 2004].

The sub-orbital aviation industry (i.e. Virgin Galactic, Blue Origin) is growing rapidly, making it necessary to fully understand the human health risks of cosmic radiation in the atmosphere. Computer

models are tailored to estimate absorbed dose for aircrew, but a lack of measurements at various altitudes, latitudes, and longitudes keeps these models from being rigorously validated [Mertens, et. al., 2016; Meier, et. al., 2018]. There is also a significant lack of measurements in the atmosphere during a solar storm event. It is estimated by the International Commission on Radiological Protection (ICRP) that annual exposure limits can be exceeded in a single intercontinental, high latitude flight during a solar storm [AMS, 2007]. There is a major need for widespread, continuous measurements in the atmosphere during the next solar cycle to maximize the chance of measuring one of these events.

New flight plans and the upcoming solar maximum will provide unique opportunities for the widespread use of the ATED to collect much needed data in the atmosphere. The ATED instrument is affordable enough to be deployed across many commercial, military, and civil aircraft to maximize the chance of measuring the effect that a solar storm has on the atmosphere. Widespread measurements by ATED on aircraft, especially during a solar storm, would be a significant step forward in our understanding of the radiation environment in the atmosphere. ATED measurements will monitor the exposure received by aircrew on a flight to flight basis, and rigorously validate aircrew exposure computer models.

The ATED instrument has been characterized in space and at aviation altitudes as a part of recent major achievements. An ATED was sent to the International Space Station (ISS) on May 21, 2018 [Causey, 2018]. The goal of this experiment was to demonstrate that ATED can perform as a dosimeter in the low Earth orbit (LEO) radiation environment. The most challenging aspect of designing the ISS ATED was making it portable and autonomous. Previous ATED models were dependent on NIM-style electronics and had a separate ionization chamber, similar to those that are commercially available [FWT, 2003]. The final piece of work, and my most significant responsibility, was the analysis of the data taken on the ISS. Proper interpretation of the data and rigorous characterization of ATED in LEO was non-trivial due to damage incurred by the ATED while on the

ISS. Measurements were analyzed in terms of time, latitude, longitude, and altitude of the ISS in order to correlate with features that exist in the ISS orbit. Comparisons were made with computer simulations and previous measurements on the ISS. Lessons learned from this experiment were identified in order to improve future ATED models. For characterization at aviation altitudes, ATED was repurposed again and exposed to a similar neutron energy spectrum found at aviation altitudes in the atmosphere at the Los Alamos Neutron Science Center (LANSCE). This was the first time that ATED successfully measured this high-energy neutron spectrum. Novel data analysis techniques were implemented in order to thoroughly interrogate data and fully characterize ATED measurements in the atmosphere. Comparisons were made with measurements made by a NASA TEPC and a Monte Carlo simulation of the experiment. Again, the lessons learned from this experiment have been implemented to improve future ATED models. Despite the complicated nature of the ISS and LANSCE experiments, the ATED demonstrated that it functioned as designed in the radiation environments of LEO and in the atmosphere.

Cost was significantly reduced by programming a Red Pitaya field programmable gate array (FPGA) board to function as a dual-input spectrometer. This became an inexpensive alternative to using two separate spectrometers and saves nearly $8000 in the fabrication of a single ATED instrument. TEPC measurements originate in femto-Coulomb to pico-Coulomb amounts of separated charged. This miniscule amount of charge must be amplified in order to obtain a useful signal. These signals are very susceptible to electronic and mechanical noise. Proper grounding in the amplification circuitry is imperative to keep noise at an absolute minimum. An electronics suite was specifically designed to use a shielded, common ground to significantly reduce noise compared to that of previous designs and to optimize data collection for ATED experiments at particle accelerators. A new ATED geometry in the shape of a cylinder was designed to significantly reduce uncertainties in measurements of mono-directional radiation. It was demonstrated that this cylindrical geometry outperforms previous ATED models when used in charged particle beams.

When operating correctly, a TEPC depends on 100% collection of separated charge inside its active volume. It was previously assumed, but never demonstrated, that ATED did this. A major accomplishment during this research project was the demonstration, through empirical measurements and investigation of different electrode configurations, that the current ATED design collects all the separated charge inside its active volume. A similar assumption was made about signals, i.e. that only electrons contribute to pulse amplitude. Another major accomplishment was demonstrating, though an iterative fitting process, that positive ions are actually the most significant contributor to pulse amplitude.

The radiation environments in space and in the atmosphere are discussed first to highlight the many variables that make understanding the human health risk in these environments complex. Galactic Cosmic Rays (GCR) and their interaction with Earth's magnetic field, the trapped radiation belts around Earth, and the influence of the Sun make the study of cosmic radiation a multifaceted issue. Regions in the ISS orbit and solar particle events are described according the particles that dominate. Energetic particles produce secondary particles when they interact with matter. These secondary particles can be produced in the hull of spacecraft, in the human body, or in the atmosphere. Secondary particles are the main component of the radiation environment in the atmosphere.

The construction and operation of ATED are outlined in detail. This includes: how gas-filled detectors work, the formation of signals created inside proportional counters, supporting electronics and hardware, how ATED measures photon and neutron radiation, the electric fields inside different ATED volumes, and the representation of measurements by ATED. Also included is the method of calculating absorbed dose in tissue and dose equivalent from ATED measurements.

Two different methods to convert ATED lineal energy measurements into LET are derived. Lineal energy measurements closely relate to the deposition of energy in cells, but LET is the standard quantity for dosimetric calculations [ICRP, 1991]. The first method is a geometric derivation of an

ideally measured lineal energy spectrum in a spherical TEPC [Rossi et. al., 1996]. The second method involves folding counts into a chord length distribution via a Fourier transform, provided by [Kellerer, 1972]. The goal of converting lineal energy into LET is to compare ATED measurements with instruments that directly measured the LET of the space radiation environment.

Empirical measurements of collected charge as a function of applied bias were done with each ATED geometry. This process shows the range of voltage values that each ATED geometry can operate at and which are optimal. It was also confirmed though this process that ATED collects all of the separated charge inside its volume.

A detailed look into how pulses are formed in ATED revealed the individual contributions to pulse amplitude by electrons and positive ions. It was previously assumed that collected electrons were the only contributor to pulse amplitude. The positive ion contribution was thought to be negligible. An iterative fitting process is used on measured pulses (voltage as a function of time) from a DC coupling capacitor to quantify the contribution of each. The resulting fit identifies the positive ion and electron contributions to pulse amplitude. This process showed that the majority of pulse amplitude comes from positive ions, as indicated by their slow rise time.

A Red Pitaya FPGA board was programmed to work as a dual-input MCA [RedPitaya, 2017]. Many other MCAs only have a single input, but ATED has two amplification channels. By using the Red Pitaya FPGA board as an MCA, the cost of building a single ATED instrument is reduced by about $8000, allowing more ATED instruments to be built. One disadvantage of the Red Pitaya MCA is that it has low processing power and thus is only suitable for measurements in the atmosphere.

Direct charged particle beam measurements at the Heavy Ion Medical Accelerator in Chiba (HIMAC) are used to calibrate ATED and test the effectiveness of materials to shield space radiation. Calibration at charged particle beams serve as the highest quality calibration for ATED. This is because the beam energy, and therefore LET, is known to high precision. Previously, a spherical

ATED was used to test candidate space radiation shielding materials, but this geometry has large uncertainties in measured absorbed dose. A cylindrical ATED has been developed to replace spherical ATED instruments for space radiation shielding experiments. A cylindrical ATED geometry inherently has a smaller uncertainty for mono-directional particles in measured absorbed dose compared to that of a spherical geometry.

A calibration method using measurements of neutrons and gamma rays from radio-isotopes are discussed in detail. The measurement of radio-isotopes is a cost-effective alternative to calibrating with a charged particle beam. Measurements take about 48 hours in total, but the ATED does not need to be disassembled and does not require the expense of travelling to and operating a particle accelerator. The process of splicing together two amplification channels is also discussed. Finally, how to use logarithmically-space bins for relative dose distribution plots is shown.

Measurements taken at the Los Alamos Neutron Science Center (LANSCE) calibrated the response of ATED to a similar neutron energy spectrum that is found in the atmosphere at aviation altitudes. The lineal energy spectrum and relative dose distribution of the nominal beam measurement showed the expected trends of a neutron measurement by ATED. Different materials used in aircraft were placed in the beamline to measure how they affect absorbed dose and the relative dose distribution. These materials were: 5.34 g/cm² of aluminum, 5.38 g/cm² of high-density polyethylene (HDPE), and a simulated aircraft wall composed of 5.3 g/cm² of aluminum and 3.2 g/cm² of HDPE [Tobiska, et al., 2018]. Aluminum had the smallest effect on the incident neutrons, as expected for its low neutron cross section. HDPE performed best in reducing absorbed dose by 47 ± 3%. A measurement of the nominal beam at LANSCE by a NASA TEPC showed good agreement to that of ATED. The small differences in the relative dose distribution between the NASA TEPC and ATED are explained by differences in geometry of the two instruments. A MCNP simulation of ATED and the nominal beam at LANSCE showed good agreement to the nominal beam measurement by ATED. The agreement of

ATED measurements with that of the NASA TEPC and the MCNP simulation indicate that ATED had the appropriate response to the neutron energy spectrum found at aviation altitudes.

A new method of testing the propensity of space radiation shielding materials to produce secondary neutrons from energetic charged particles, as measured by ATED, was developed at HIMAC. Aluminum, HDPE, copper, and polypropylene doped with silicon carbide, 20% by weight, (PPSiC20) were tested by placing various thicknesses of each into the beamline while ATED measured off-axis to the beam. The charged particle beams were 400 MeV/n carbon, 800 MeV/n silicon, and 650 MeV/n iron. HDPE is used as an ideal standard, and copper is considered a "worst-case" material for producing secondary neutrons. The production of secondary neutrons increased with the atomic number of the target material and the thickness of the material tested for each beam. Secondary neutrons were produced significantly more in the 650 MeV/n iron beam compared to the other two beams for every material tested. These trends were expected and demonstrate the validity of this method to test the propensity of materials to produce secondary neutrons.

Finally, there is a detailed analysis of measurements taken by ATED onboard the ISS. This ATED was co-developed specifically for the ISS with a previous student as part of their PhD project [Causey, 2018]. ATED continuously measured the lineal energy spectrum and absorbed dose as functions of time with 30s resolution [Benton, et. al., 2019]. Absorbed dose rate measurements were correlated with time, orbital position, and altitude. Absorbed dose quantities from the entire ISS orbit, trapped protons in the South Atlantic Anomaly (SAA), trapped electrons at high latitudes, and the GCR region were found with this data set. In each case, the trends seen in absorbed dose and absorbed dose rate meet the expectations of the understanding of the LEO radiation environment. This was a strong indication that ATED had the appropriate response to the space radiation environment inside the ISS. Absorbed dose rates agree well with calculations done with the On-Line Tool for the Assessment of Radiation in Space (OLTARIS). The ATED lineal energy spectra were

converted into corresponding LET spectra in two different ways, but the assumptions of each method are not valid for the large range of LET in space radiation environment.

Recent advancements in the ATED development program indicate that ATED is nearing completion. The ATED instrument has achieved development to the point that it is on the cusp of flying routinely on aircraft, and being easily adapted for space and balloon payloads. Already the ATED instrument has been demonstrated to be useful at accelerators, in neutron radiation fields, in the atmosphere, and in space to give insights to the human health impact by ionizing radiation. Areas where improvement can be made have been identified, and will be part of the final development of the ATED instrument.

CHAPTER II

THE SPACE RADIATION ENVIRONMENT

The space radiation environment is highly complex and non-uniform in both space and in time. The properties of ionizing radiation in low Earth orbit (LEO) and aviation altitudes are the result of complex interactions between the Earth's magnetic field, galactic cosmic rays (GCR), and solar particle events (SPE) [Dachev, et al., 2017]. Particles trapped in Earth's magnetic field are a major contributor to the LEO radiation environment [Schwadron, et al., 2017]. The following sections describe the space radiation environments in the radiation environment in the atmosphere.

2.1 Galactic Cosmic Rays

Galactic Cosmic Rays (GCR) originate from outside the solar system and are thought to come from sources inside the Milky Way [Fry, 1989; Schwadron, et al., 2017]. GCR are fully ionized atomic nuclei that are believed to be accelerated to high energies via shockwaves created during supernova explosions, neutron star collisions, and black hole interactions [Cronin, 1997;

Bustamante, et al., 2015; Galiautdinov, et al., 2018]. The composition of GCR consists of approximately 85% protons, 12% helium ions, 2% electrons and positrons, and 1% heavier ions [Benton et al., 2001]. GCR can possess energies up to 10^{21} eV, but particles with such high energies are extremely rare [Cronin, 1997]. In near-Earth space, the distribution of this field is considered to be isotropic. The energy-flux spectrum of GCR shows a broad peak around 100 MeV/n in proximity to Earth [NCRP, 1989].

As GCRs propagate through the solar system, they are attenuated by solar wind [Schwadron, et al., 2017; Badhwar, 2002]. The solar cycle is an important influence on the GCR spectrum, as is seen in **Figure 2.1**. The higher flux of solar wind during solar maxima decreases the flux of low energy GCR more than at solar minima [Zhao, 2014]. This is attenuation is predominately seen in particles with energy less than 1GeV/amu.

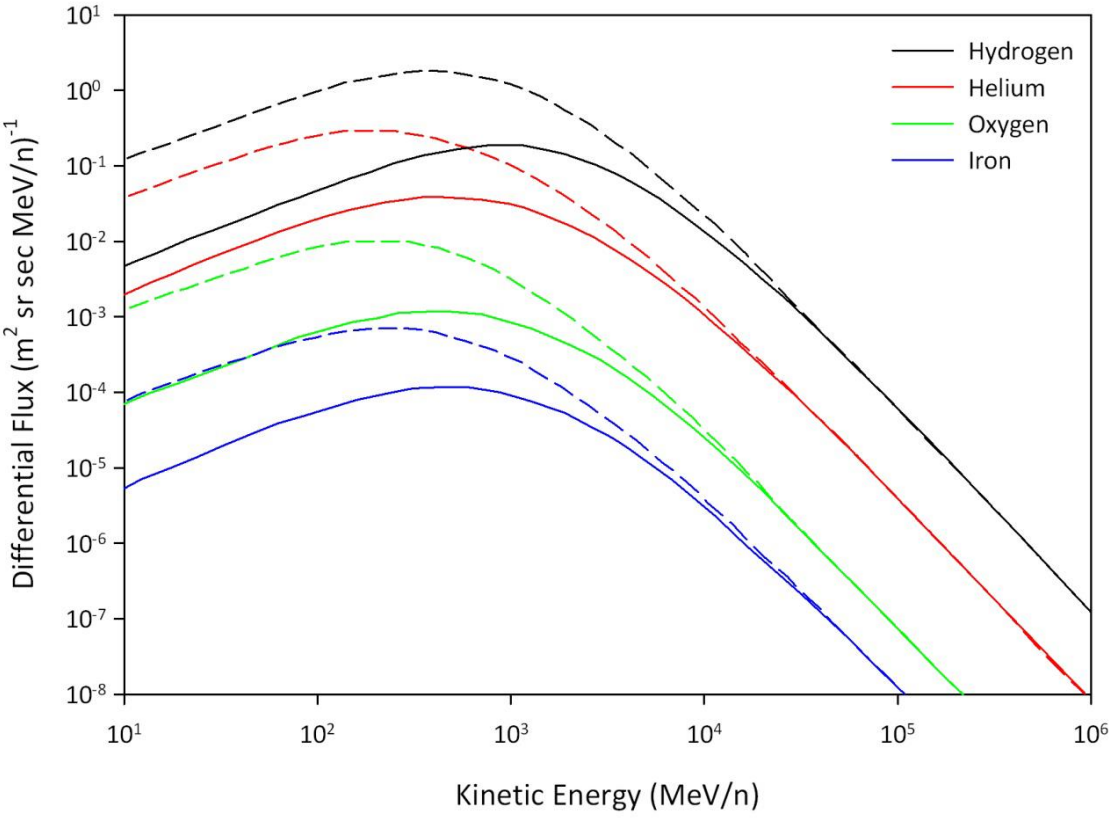

Figure 2.1: 10 day GCR differential flux as a function of kinetic energy effected by the solar cycle for hydrogen, helium, oxygen, and iron. The plotted data is from the 2010 solar minimum and the 2001 solar maximum. Solid lines represent solar maximum and dashed solar minimum. Significant attenuation during solar maxima occurs at GCR energies below 1 GeV/n. [adapted from: Badwhar, 1997]

GCR are subjected to and sometimes deflected by Earth's magnetic field [Badhwar, et al., 2001]. A simplified illustration of Earth's magnetic field is shown in **Figure 2.2**. The Earth's geomagnetic field can be approximated as a dipole in its simplest form, but contains higher order moments as well [Shcherbakov et al., 2015]. The Sun's magnetic field and the solar wind distorts the Earth's magnetic field into a tear-drop shape Since the geomagnetic field lines are parallel to the Earth's surface near the equator, all but the most energetic charged particles are deflected away. The Sun interacts with and alters the geomagnetic field over time, which changes how and how much GCR are deflected away from Earth over time [Smart, et al., 2009].

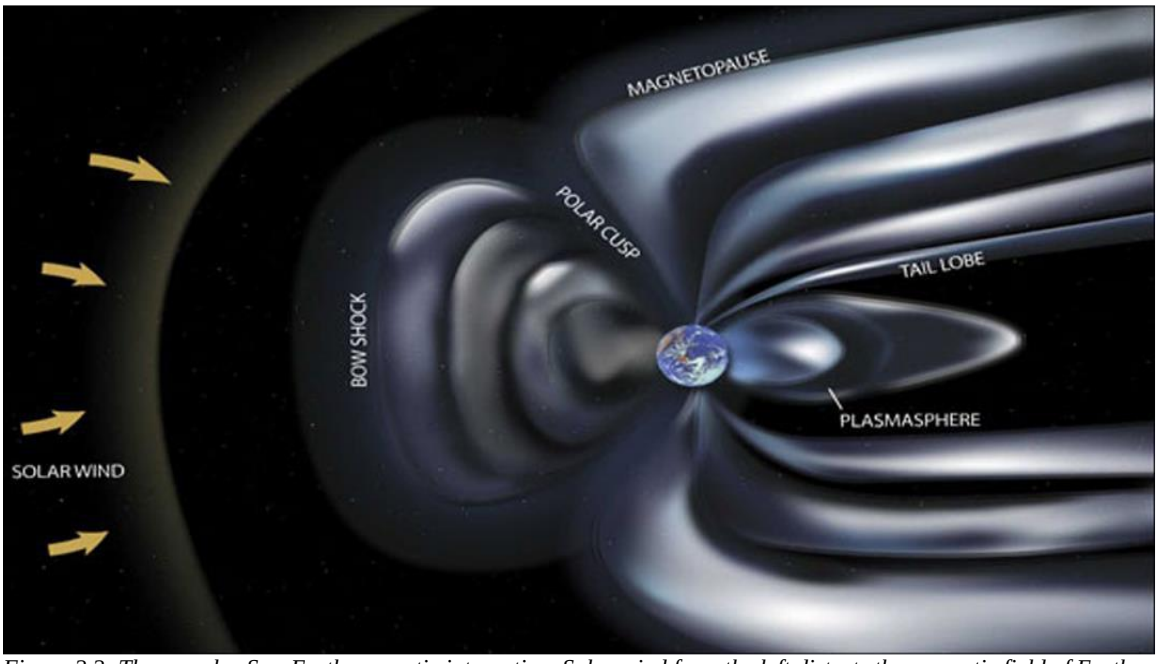

Figure 2.2: The complex Sun-Earth magnetic interaction. Solar wind from the left distorts the magnetic field of Earth into a tear-drop shape as seen above. Labels are placed at the various features seen in this interaction, but are not described in the text. [NASA, 2006]

In LEO, low energy GCR are deflected away from the geomagnetic equator, significantly reducing the amount of ionizing radiation that would otherwise be present and thereby protecting astronauts in LEO [Benton, 2004]. The resistance of a charged particle to being deflected from interacting with Earth's Magnetic field is called geomagnetic rigidity [Smart et al., 2009]. The definition of rigidity is,

$$R = p/q, \tag{2.1}$$

where p is the momentum and q is the charge of a particle. The units of geomagnetic cutoff rigidity are typically gigavolts (GV).

Figure 2.3 shows an example of vertical cutoff rigidity for the 1980 epoch as a function of latitude and longitude. The cutoff rigidity corresponds to the minimum amount of energy a particle must possess in order to reach a location in the magnetic field [Mertens et al., 2016]. Cutoff rigidity changes with the orientation and strength of the magnetic field. Cutoff rigidity values are nearly zero at the magnetic poles, and highest at the geomagnetic equator. As a result, only the most energetic particles will penetrate through the geomagnetic field at lower latitudes and those that do not possess enough kinetic energy are deflected. Cutoff values also change with time due to the Earth's magnetic field being dynamic in both strength and orientation [Smart et al., 2009].

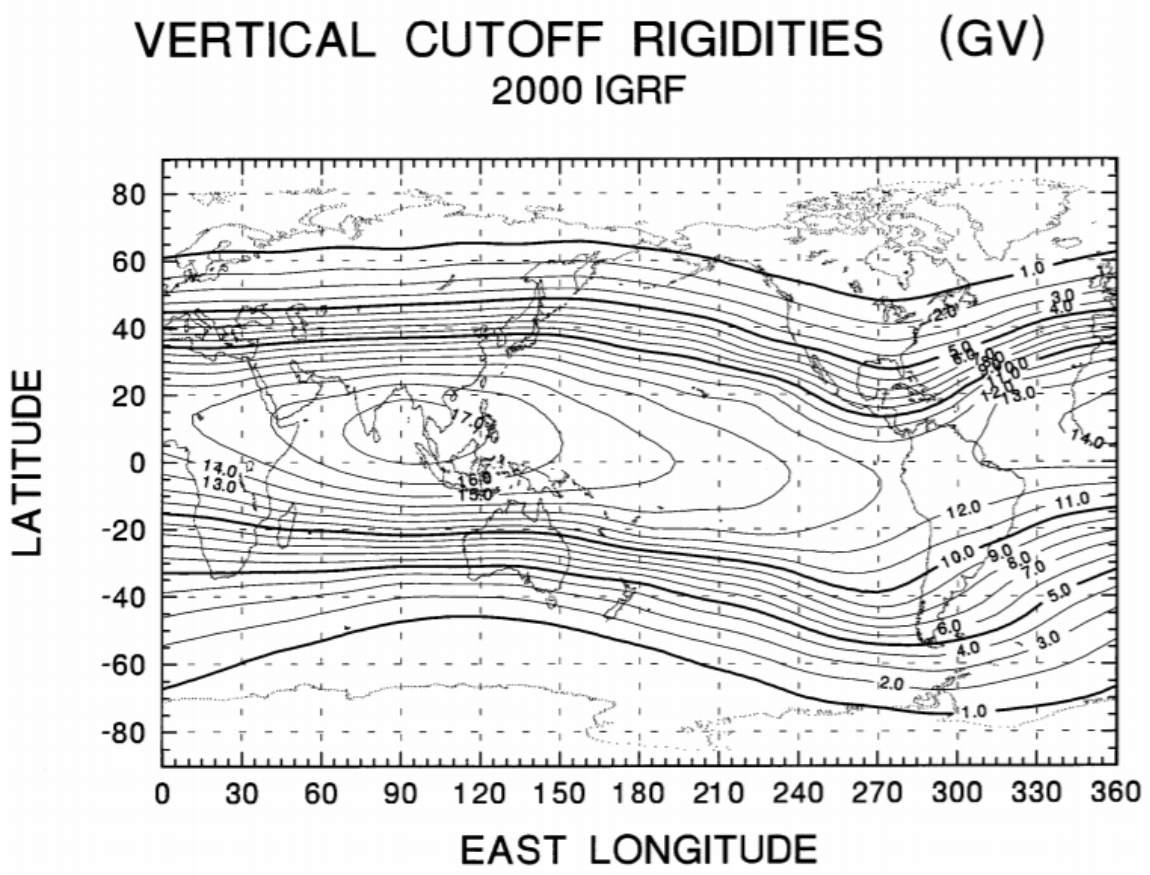

Figure 2.3: The geomagnetic cutoff rigidity for particles normal to the surface of Earth. Each contour is labeled with its value in GV and increase as they get closer to the geomagnetic equator. Not shown is the zero value for the magnetic poles [Smart et al., 2009].

2.2 Van Allen Radiation Belts and the South Atlantic Anomaly

The geomagnetic field traps charged particles in regions of space surrounding Earth known as the Van Allen radiation belts [Van Allen, 1959]. **Figure 2.4** illustrates the shape and orientation of the radiation belts around Earth. There is an outer and inner belt. The outer belt is composed of mainly electrons of energies ranging from 0.1 MeV to 10 MeV [Lugaz, et al., 2016]. The inner belt consists of electrons of energies up to ~6 MeV and protons of energies up to ~250 MeV [Benton et al., 2001]. Protons of this energy are able to penetrate the hull of spacecraft and directly contribute towards absorbed dose. Electrons in the belts do not possess enough energy to fully penetrate the hull of spacecraft and directly contribute towards absorbed dose. Instead,

electrons of this energy will rapidly deaccelerate when interacting with the spacecraft materials and produce Bremsstrahlung. The resulting Bremsstrahlung photons can then indirectly contribute towards absorbed dose.

There is a part of the inner radiation belt that approaches closest to the surface of Earth, known as the South Atlantic Anomaly (SAA). The inner radiation belt comes as close as 200 km to Earth as pointed out in **Figure 2.4**. Earth's magnetic field is considered eccentric because it does not pass through the center of the Earth. It instead is tilted at 11° and displaced about 500 km from the center of Earth. This results in a displacement relative to Earth's surface of the magnetic field over the South Atlantic Ocean that allows for trapped particles to come close to the surface of Earth [Stassinopoulos, et al., 2015]. The density of trapped protons inside the SAA increases exponentially with altitude and has the shape of an inverted cone [Benton, 2004]. Also, as the magnetic field changes over time, the shape and orientation of the SAA will also change.

The International Space Station orbits at an altitude of about 400 km and at an inclination of 51.6°. The ISS is directly exposed to the trapped protons in the SAA. It has been reported that the SAA accounts for roughly 50% of the total absorbed dose in the ISS orbit [Badhwar, 2002]. The electrons of outer radiation belt will contribute to absorbed dose closer to the poles (high latitudes) [Badhwar 1997]. The cusp of the outer radiation belt also contributes to absorbed dose in the ISS orbit.

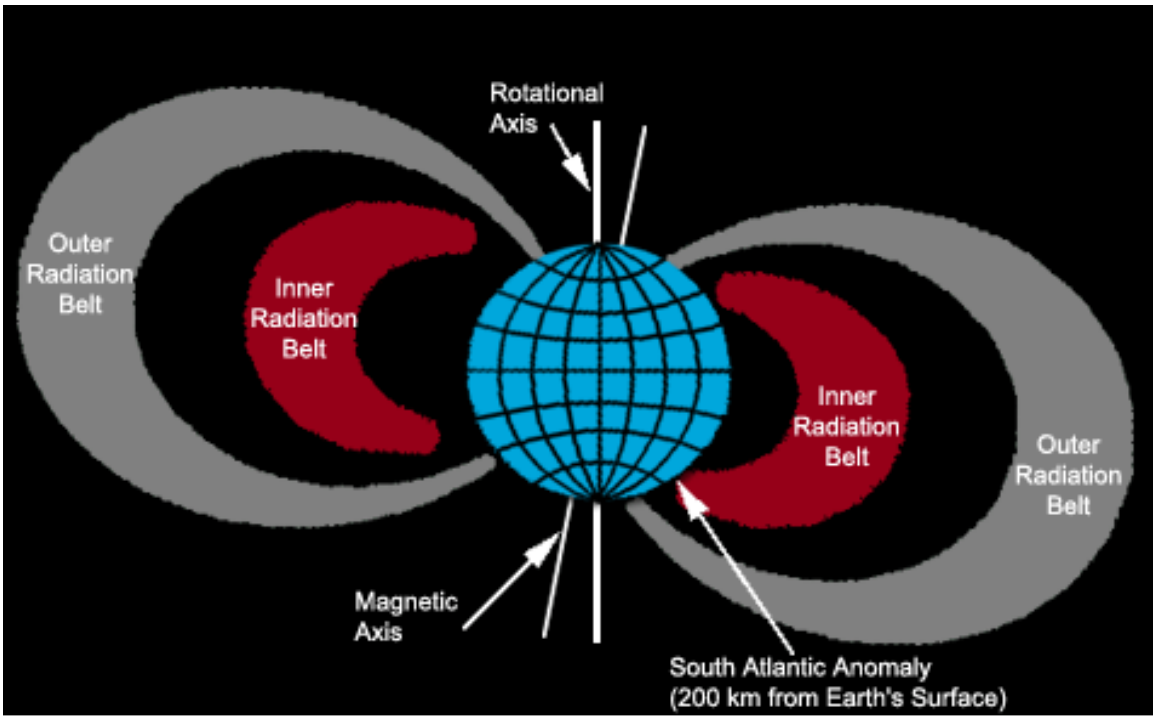

Figure 2.4: A cross-section of the two Van Allen radiation belts associated with the geomagnetic field. Note the close approach of the South Atlantic Anomaly, penetrating the ISS orbit [SRAG 2016].

In **Figure 2.5** approximate regions of the ISS orbit for July 2018 are displayed over a map of Earths coastlines. The portion of the ISS orbit that passes through the SAA which is dominated by trapped radiation of the inner radiation belt is called the SAA region. At the highest latitudes is the Electron Cusp region, dominated by trapped radiation of the outer radiation belt. The remainder of the ISS orbit is the GCR region, where the radiation environment is dominated by galactic cosmic rays. The definition of the SAA region is: $|B| < 23\mu T$ & $L < 3$ where $|B|$ is the magnetic field density and L is the McIlwain L-Shell parameter [Rios, 2017]. The Electron Cusp region is defined as L > 2.8 [Stassinopoulos, 1988].

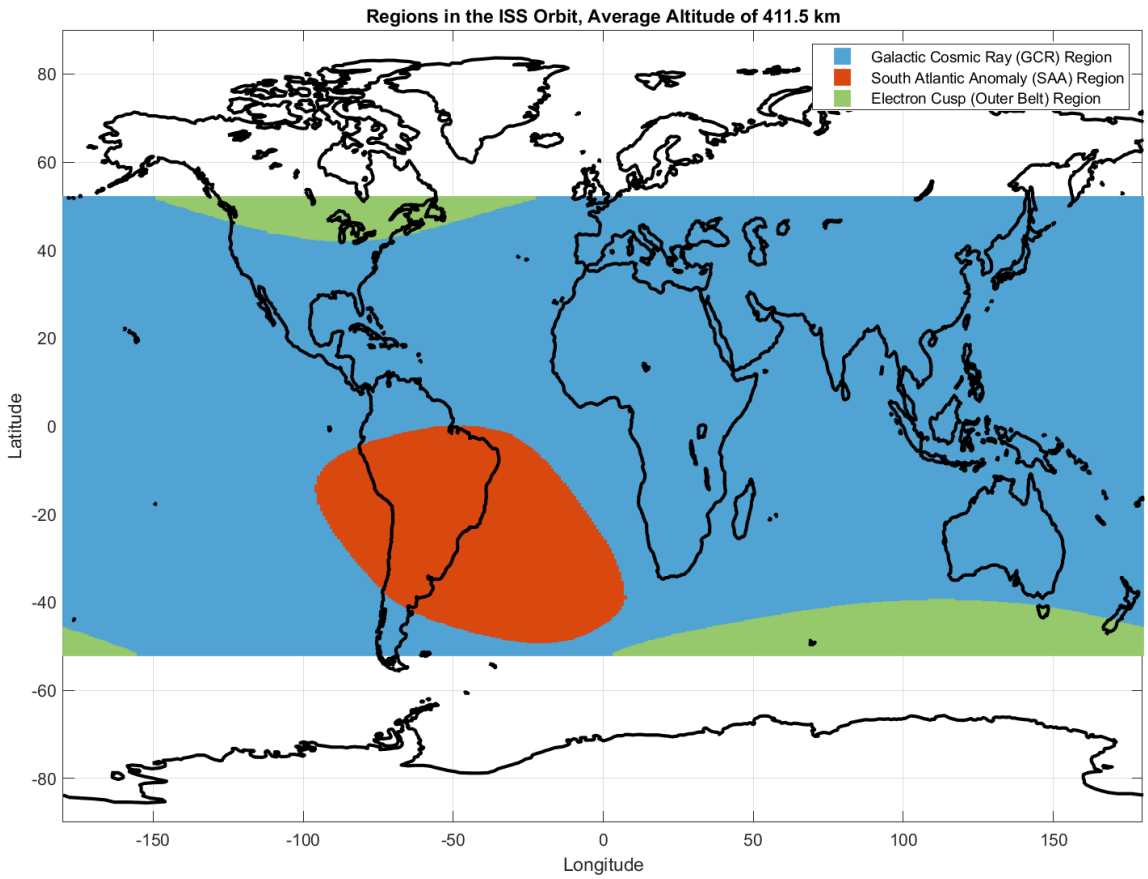

Figure 2.5: The GCR, SAA and Electron Cusp regions as a function of latitude and longitude for July 2018. These region boundaries are described in the text. The SAA region is shown in red and the GCR in blue.

2.3 Solar Particle Events

Another source of ionizing radiation in space is the Sun. Particles are ejected from the Sun in what are called Solar Particle Events (SPEs). There are two kinds of SPE: those caused by coronal mass ejections (CME) and those associated with solar flares [Benton, 2004]. CME and solar flares occur most frequently at the solar maximum of the eleven-year solar cycle [Reedy, 1996]. The frequency of these events is varied and about 50 are expected over a single solar cycle [Reames, 2017]. No solar particle events occurred during the time ATED was on the International Space Station.

Solar flare events are short-lived events that are dominated by large fluxes of 2-100 keV electrons and characterized by enhanced abundancies of ^{3}He and heavy elements like Fe, Mg and Si [Benton, 2004]. Because of their short duration, solar flare events are minor in comparison to their long-lived counterparts, CME. CME are significant releases of solar material that produce long lived increases of proton flux that last on the order of days [Benton, 2004]. Large SPE can result in significant increases in absorbed dose by astronauts in LEO. In the atmosphere, very few measurements have been taken during a SPE.

2.4 Secondary Particles

The main way cosmic rays lose their energy is via atomic interactions in the form of excitation or ionization. On occasion, with sufficiently energetic particles, nuclear interactions produce secondary particles. These nuclear interactions are characterized in two ways: target fragmentation and projectile fragmentation [Benton, 2004]. Production of secondary particles can happen in the hull of a vehicle, in the atmosphere, or even inside the human body. Each secondary particle produced has the potential to cause biological damage and can be more damaging than the primary particle itself.

Target fragmentation is the interaction between an energetic nucleon and a stationary nucleus as illustrated in **Figure 2.6**. The resulting secondary particles are dependent on the primary particles energy, the cross section of the reaction, and the constituents of the incident and target nuclei [ICRU, 1978]. With high energy incident particles, a large array of secondary particles can be produced like neutrons, protons, α-particles, and sometimes heavier nuclei in a process known as an intra-nuclear cascade [Benton 2004]. All of the mentioned secondary particles can themselves undergo more nuclear interactions in what is known as an extra-nuclear cascade. The leftover target nucleus is often left in an excited state and undergoes nuclear decay until it becomes stable.

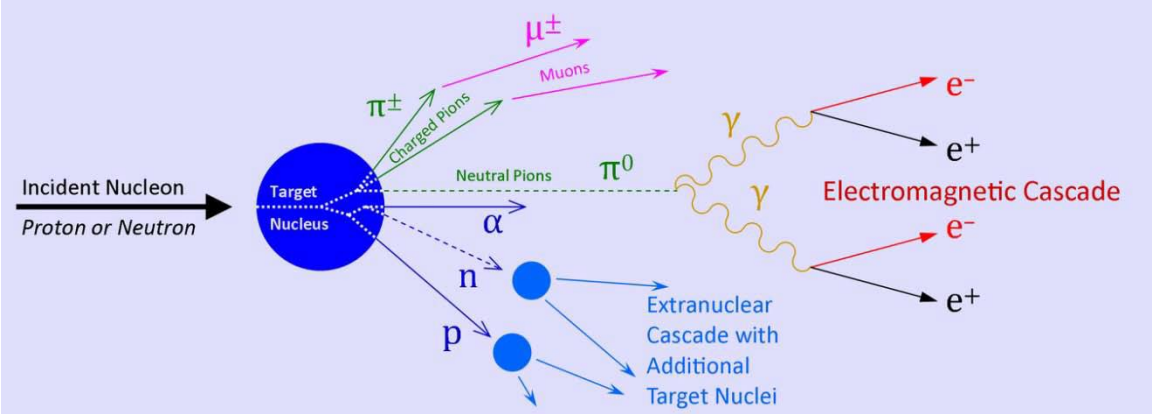

Figure 2.6: Target fragmentation of a target nucleus from an incident proton or neutron. The reactions are separated by color for the type of particles that are produced [adapted from Dewitt 2011].

Projectile fragmentation is similar to target fragmentation and is illustrated in **Figure 2.7**. In projectile fragmentation, a heavy ion is incident on a stationary nucleus and is broken into fragments of lower atomic number (Z) [Heilbronn, et al., 2019]. Again, the reaction is dependent on the energy, cross section of the reaction, and the constituents of the incident and target nuclei. In addition to producing high energy neutrons and protons, these reactions can produce heavy projectile fragments that retain the kinetic energy of the primary heavy particle [Benton 2004]. These secondary particles can themselves undergo more nuclear reactions. This is true especially for high energy neutrons created by projectile fragments.

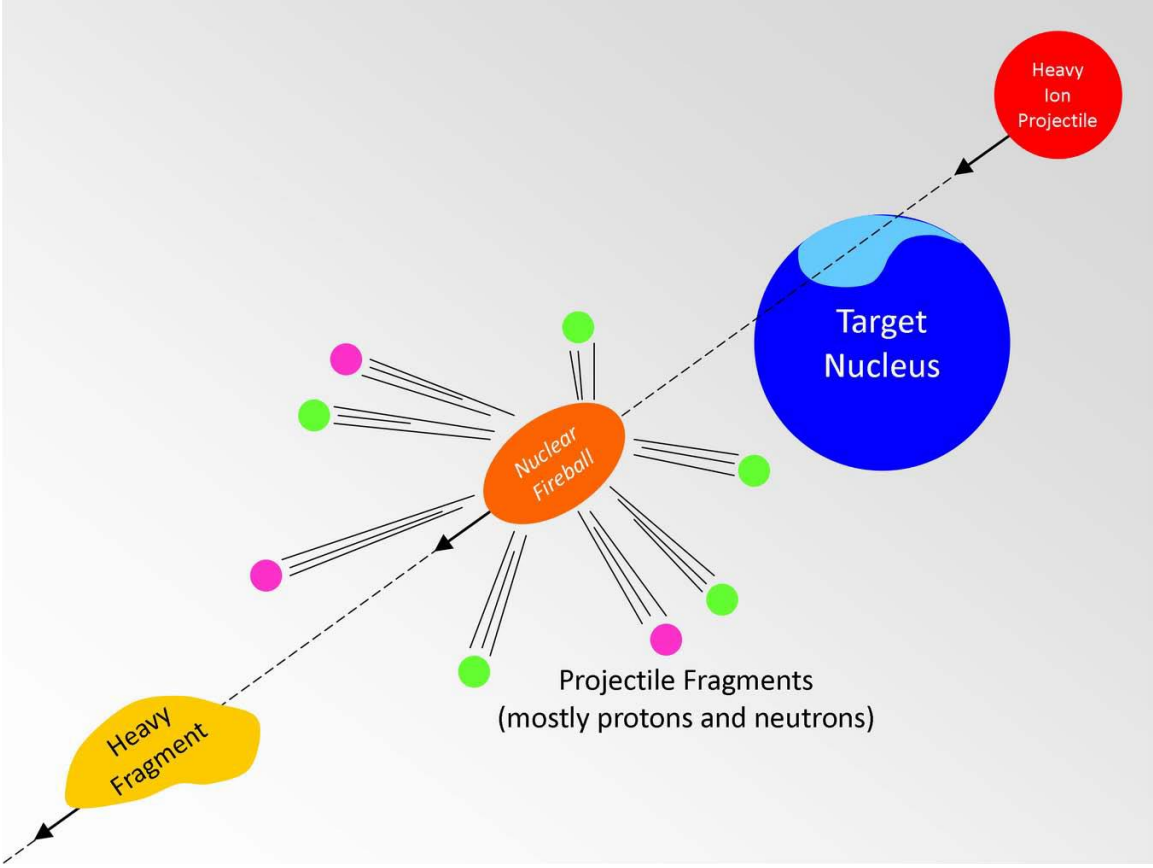

Figure 2.7: Projectile fragmentation of a heavy ion particle that interacts with a target nucleus like that in a spacecraft. The result of this interaction is a nuclear fireball that emits protons and neutrons until a more stable heavy fragment is produced. [adapted from Dewitt 2011].

Each secondary particle from these kinds of nuclear reactions can have the potential to cause damage. Of major concern is the production of secondary neutrons. Neutrons are 4 to 5 times more damaging to human tissue than charged particles [Cucinotta, 1998]. Because neutrons have no charge, they are highly penetrating compared to charged particles. In general, as shielding material thickness is increased the absorbed dose from secondary neutrons increases [Heilbronn, et al., 2004]. In LEO, the main source of an astronaut's neutron dose is from secondary neutrons produced in nearby matter like the hull of the spacecraft. It is estimated that 30-60% of an astronaut's total dose equivalent comes from secondary neutrons [Badhwar, et al., 2001]. The measurement of secondary neutron fluence and their contribution to dose equivalent remains one of the most important challenges in space radiation dosimetry [Benton, 2004].

2.5 The Radiation Environment in the Atmosphere

At aviation altitudes the radiation environment is composed almost entirely of secondary particles. An air shower is a cascade of several secondary particles originating from a primary cosmic ray that underwent one or more nuclear interactions with a nuclei near the top of the atmosphere [Kampert, et al., 2012]. **Figure 2.8** is an illustration of an air shower in Earth's atmosphere. These particles can then undergo more nuclear interactions themselves and produce more particles if they posess enough energy. The flux of these particles reaches a maximum around an altitude of 20 km, a region known as the Pfotzer Maximum [Mertens, 2016].

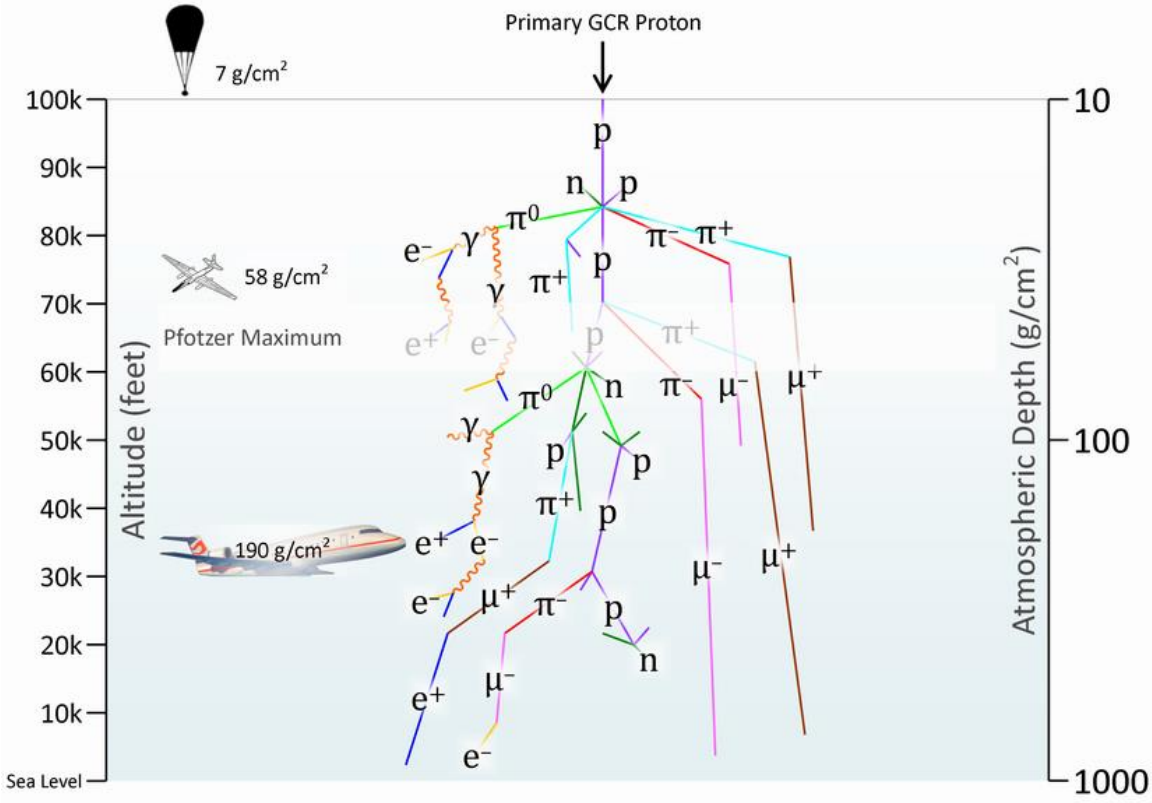

Figure 2.8: Air shower illustration showing an example of the secondary particles involved. Also shown is the typical altitude that a commercial flight takes place, where a high altitude plane would fly, and a region known as the Pfotzer Maximum [OSU RPL]

The influence of Earth's magnetic field is significant to the radiation levels found at aviation altitudes. One of the largest influences on charged particles before they reach atmosphere is geomagnetic latitude. Geomagnetic latitude is similar to geographic latitude but is defined to the

axis of the dipole of Earth's magnetic field. Particles at lower latitudes will be deflected more than those at higher latitudes, resulting in an overall higher flux of particles near the magnetic poles at aviation altitudes. This translates into a basic momentum-per-unit-charge requirement (see equation 2.1) for primary cosmic rays to enter the atmosphere and initiate an air shower.

Solar particle events are another potentially significant source of radiation exposure at aviation altitudes. There have been few dosimetric measurements during large SPEs at these altitudes and thus the details are unclear. One SPE in April 2001 was measured and found the flux of particles to increase by 70% and dose to increase by a factor of two [Spurney, et al., 2003]. It is often seen that little to no change in dose rate at aviation altitudes during SPE, and in some cases to even decrease [Benton, 2004]. The decrease in the intensity of cosmic rays in the atmosphere due to solar activity is called the Forbush Effect [Friedlander, 2011].

2.6 Terrestrial Gamma Flashes

Terrestrial gamma-ray flashes (TGF) are high-energy bursts of gamma-rays that occur during lighting storms [Gjestelant, 2010]. They were first discovered in 1994 by the Burst and Transient Source Experiment (BASTSE) as a part of the Compton Gamma Ray Observatory satellite [Grefenstette, et al., 2008]. It is estimated that 50 TGF occur per day and that they are most likely triggered by lightning [NASA 2005]. The actual mechanism that produces TGF is unknown. It is preliminary theories show that a relativistic runaway electron avalanche may occur in or near cumulonibus storm clouds and emit high-energy photons. Such an event would require a very strong electric field like ones found in cumulonibus clouds. Research on how TGF are produced and their mechamisms is ongoing.

Simulations show that dose equivalents near TGF can reach as high as 0.1 sieverts, or 5 times the recommended annual limit for the general public [Dwyer, 2010]. These claims are contovertial and come with no data to substantiate them. Widespread, systematic measurements on aircraft is a possible avenue to address these claims.

CHAPTER III

DESCRIPTION OF THE ACTIVE TISSUE EQUIVALENT DOSIMETER

The Active Tissue Equivalent Dosimeter (ATED) is a tissue equivalent proportional counter (TEPC) based on the Benjamin or Hurst designs [Benjamin, et al., 1968; Hurst, et al., 1954]. The following sections describe the mechanisms of gas filled detectors, how ionizing radiation produces a signal in a proportional counter, a brief overview of the supporting electronics used with ATED, considerations of the chord lengths involved with different geometries, tissue equivalence, the electric field inside ATED active volumes, representation of data, and the calculation of absorbed dose and dose equivalent.

3.1 Description of Gas Filled Detectors

Radiation detectors whose detecting medium is composed of a gas are called gas-filled detectors [Wilkinson, 1950]. **Figure 3.1** illustrates the separation of ions in a gas medium due to ionizing radiation and their motion due to an external electric field. Ionizing radiation passes through the gas and separates electrons from their molecules, creating ion pairs. These separated

electrons and positive ions drift apart from each other due to the electric field. The electric field is created by two electrodes that also serve to collect the separated electrons and ions. When the electrodes collect these ions, a signal is produced that can then be measured. The portion of the detector that holds gas and collects separated ions is often called the ionization cavity or active volume.

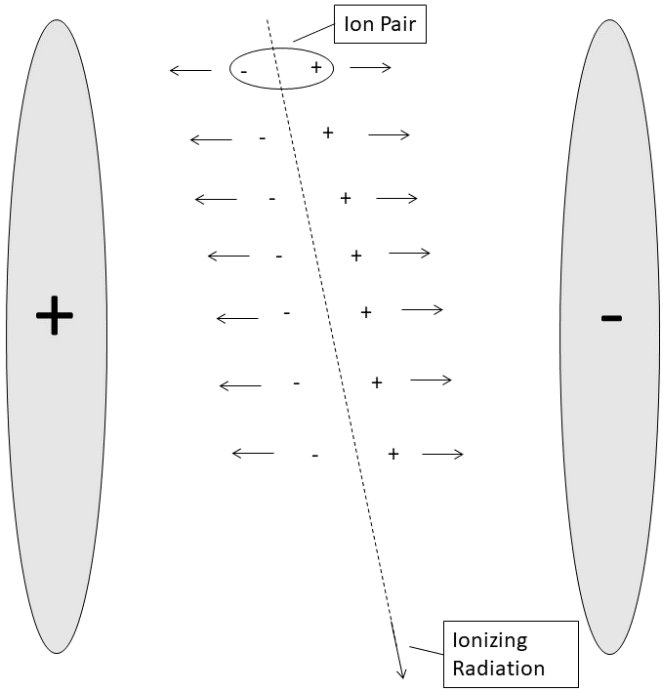

Figure 3.1: Ion pairs being separated by traversing ionizing radiation in a gas filled volume. The resulting ions will drift according to the electric field inside and are collected by the electrodes.

There are many factors that affect the operation of a gas-filled detector. These factors include: voltage between the electrodes, geometry of the active volume, gas pressure, and gas composition [Rossi, et al., 1949]. The relationship between applied voltage and charge collected per unit time in a gas-filled detector is shown in **Figure 3.2**. The labeled regions determine the behavior of collected charge and thus the function of the detector. Region I is where the electric field inside the detector is not strong enough to prevent ion pairs from recombining before being collected. Region II is where all ion pairs in the gas will be collected because the electric field completely overcomes recombination. Detectors that operate in Region II are called ionization chambers.

Region III is where electrons are accelerated to the point where they produce secondary ionizations in the gas via collisions with gas molecules. The number of secondary ionizations, referred to as the multiplication factor, is directly proportional to the number of initially created ion pairs. Detectors in Region III are called proportional counters. In Region IV electrons produce secondary ionizations in numbers that are no longer proportional to the number of initially created ions. Geiger-Muller tubes work in Region IV. In Region V, a single ionization event will result in a steady current of secondary ionizations and the detector ceases to function properly.

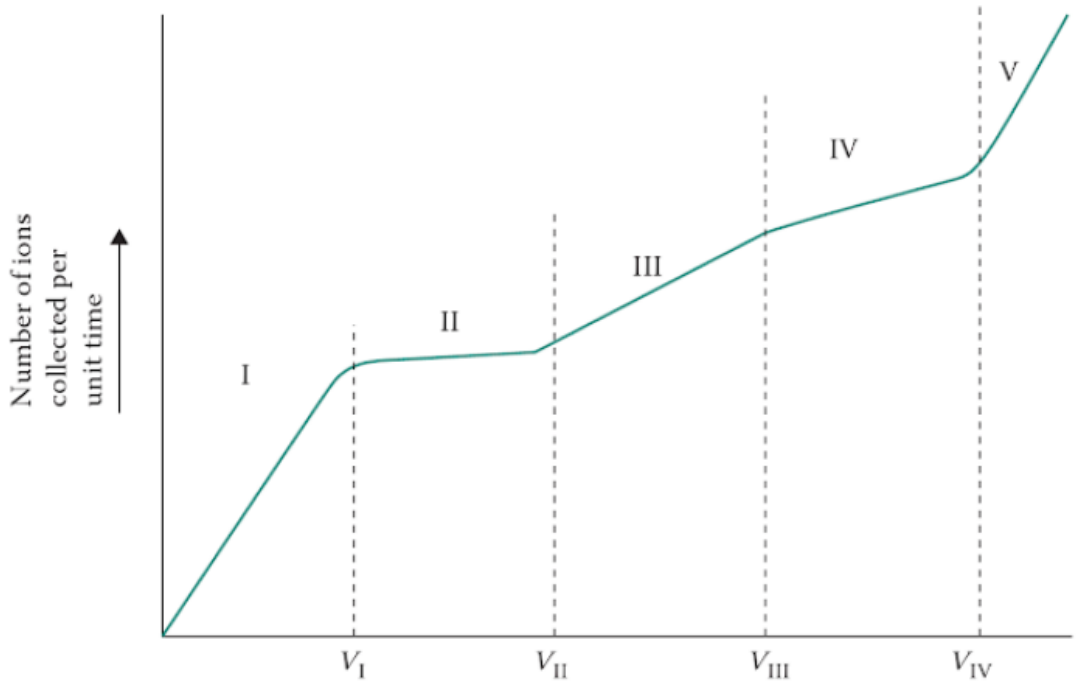

Figure 3.2: The number of collected ions per unit time as function of applied bias, showing the various regions for gas filled detectors. Each region is separated by a voltage value and a corresponding vertical line. [adapted from Tsoulfanidis, 1995].

3.2 Formation of Signals Inside Proportional Counters

Signals produced inside proportional counters are directly proportional in amplitude to the number of ion pairs produced by incident ionizing radiation [Segre, et al., 1953]. Due to the strong electric field imposed across the active volume of a proportional counter, the free electrons

in the gas accelerate and collide with other gas molecules, further ionizing the gas. One electron can cause 10^2-10^3 secondary ionization events in a proportional counter. This secondary ionization process is known as a Townsend avalanche, and requires a strong electric field gradient [Little, 1956].

Figure 3.3 illustrates a single Townsend avalanche. Townsend avalanches occur in close proximity to a central collecting wire, roughly the same distance away as the diameter of the collecting wire itself [Segre, et al., 1953]. Because Townsend Avalanches multiply the number of collected ions, they also amplify the magnitude of signals. This amplification is proportional to the number of initial ion pairs and thus energy deposited in the gas by an ionizing particle [Attix, et al., 1966]. About 10% of the signal amplitude comes from electrons being collected. The remainder comes from more massive positive ions in close proximity to the collecting wire [Wilkinson, 1950]. The amount of amplification from the Townsend avalanche process is called the gas gain or multiplication factor [Segre, et al., 1953].

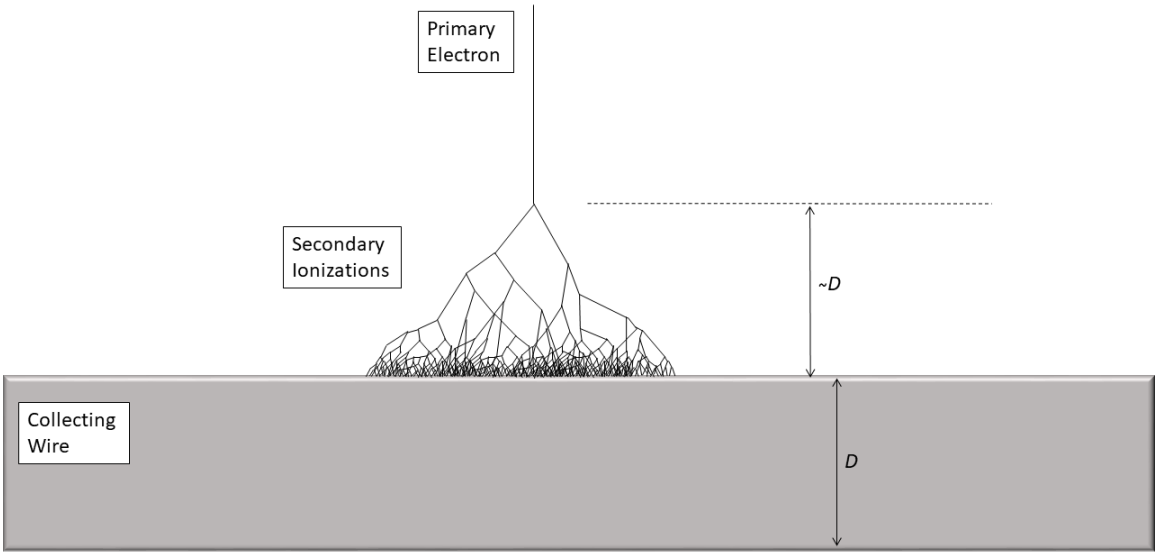

Figure 3.3: Illustration of a Townsend avalanche from a single electron. The secondary ionization process occurs roughly a distance equal to the diameter of the wire collecting charge.

Consider the number of initial ion pairs in a proportional counter from incident ionizing radiation, n, and the total number of ion pairs from a Townsend avalanche, M. Gas gain, G, is then defined as,

$$G = \frac{M}{n} \tag{3.1}$$

[Rossi, et al., 1949]. When the total number of collected ions is equal to the number of initially created ions ($M = n$), the gas gain is one and no avalanche process occurs. This happens in Region II of **Figure 3.3**, where ionization chambers operate. In an optimally configured proportional counter, G is on the order of 10^2-10^3. Equation (3.1) cannot be used directly in a laboratory setting to find gas gain because the number of initial ion pairs is unknown. Empirically, we can collect charge as a function of voltage, define each operational region, and calculate gas gain using,

$$G = \frac{Q_V}{Q_{RII}} \tag{3.2}$$

where Q_V is the charge collected per unit time at voltage V and Q_{RII} is the collected charge per unit time found in Region II. The process of how to implement Equation 3.2 to calculate gas gain, as well as finding the optimal operational voltage for a proportional counter, is discussed in detail in Chapter 6.

The geometry of the detector active volume is designed in order produce a large electric field gradient near a central wire. A thin, central wire inside a larger volume shapes the electric field gradient to sharply increase near the wire. When the wire and surrounding volume are at opposite biases of sufficient magnitude, gas multiplication can occur. The central wire needs to be placed at a high positive voltage in order to attract electrons. The geometry used in ATED designs are discussed in the next section.

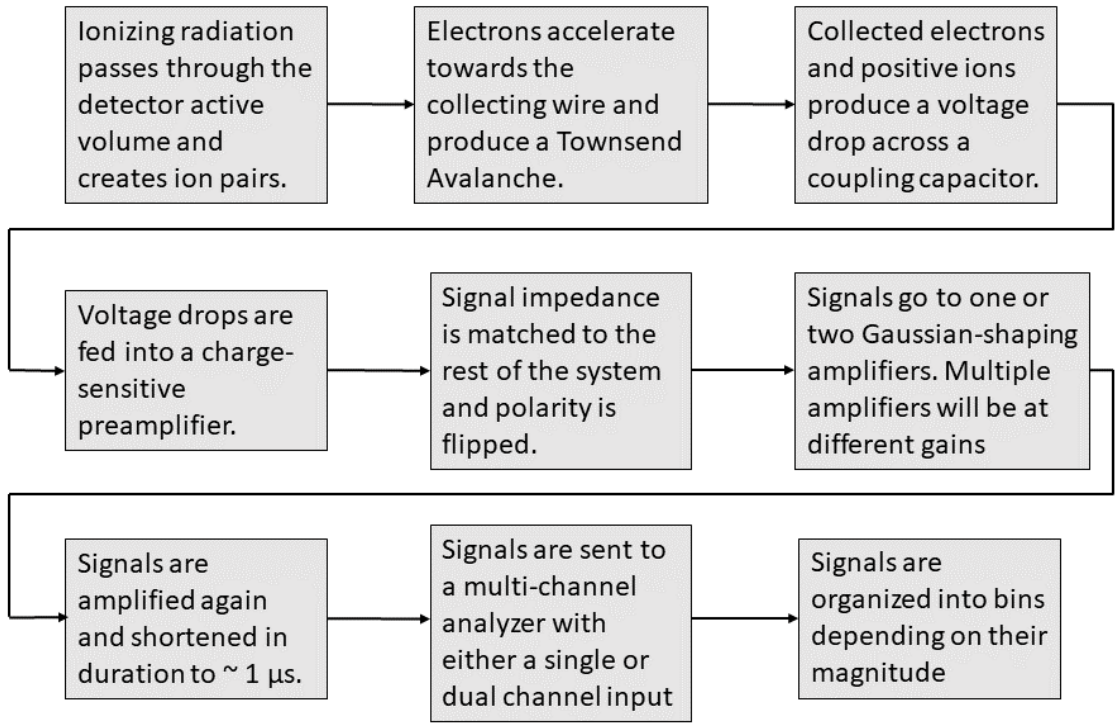

Figure 3.4: A Flow chart of signals for a proportional counter system. Details are described in the text. Signal and pulse are used interchangeably.

Figure 3.4 shows a flow chart of signals from inception to their final measurement. A capacitor is placed between the central wire and the input of a charge-sensitive preamplifier. This capacitor is referred to as the coupling capacitor and it separates the preamplifier from the high voltage on the central wire. When electrons from a Townsend Avalanche are collected by the central wire, there is a voltage drop across the coupling capacitor that is input into the charge-sensitive preamplifier. This voltage drop is transformed into a more readable signal, or pulse. Its impedance is matched to the rest of the system (usually 50 Ω), and the polarity of the signal is made positive. The signal from the preamplifier is on the order of 300 μs in duration, and needs to be shortened to avoid overlap of sequential pulses. Without further shaping, signals will last so long that they overlap and counts will ultimately be lost or spurious [Tsoulfanidis, 1995].

Signals are then fed into a Gaussian-shaping amplifier. This amplifier shortens the duration of pulses to ~1 μs, forms them into a Gaussian-like shape, and amplifies their magnitude. Depending

on the instrument used, either one or two Gaussian-shaping amplifiers will be used. If two amplifiers are used, they are set to two different gain settings (amount of amplification). The resulting signals will then correspond to a “high gain” and “low gain” channel. The use of two gain channels allows for proper resolution of small pulses while covering the entire range of pulse magnitudes. The gain channels will overlap and will need to be joined together during analysis. In general, the high gain channel has a resolution of about 0.1 keV/μm and the low gain channel has a resolution of about 1 keV/μm (see Chapter 10.3).

So far, pulses have been analog. They are sent to a multi-channel analyzer (MCA) where they are converted into a digital signal by an analog-to-digital converter (ADC). The MCA organizes pulses read in by the ADC into bins depending on their magnitude, i.e. their pulse height. The MCA identifies which bin a measured pulse corresponds to and adds a count to that bin. Bins increase in number linearly with the magnitude of the pulse. Each bin corresponds to a range of pulse heights, called the bin width. Typically, 1024-8192 bins are used in a single gain channel. Because signals in each gain channel are amplified differently, their bin widths will differ. This can cause issues when putting the two gains together for data visualization. This is discussed in detail in section 3.8.

3.3 Supporting Electronics & Hardware

All of the supporting electronics for ATED are commercial products or simple circuits fabricated at the Oklahoma State University Radiation Physics Laboratory. The Oklahoma State Physics and Chemistry Instrument Shop is responsible for any custom machined parts.

The active volume is constructed from pre-formed, cast acrylic shapes of ~3mm thickness. A picture of an ATED spherical active volume is shown in **Figure 3.5**. The spherical geometry is

composed of two separate hollow acrylic hemispheres, held together with Torr Seal. The cylindrical geometry is composed of two circles and a cylindrical tube of acrylic, held together with acrylic screws. In both cases, holes are drilled for grounding screws, wire holders, calibrating sources, and to allow gas inside the volume. Screws are self-tapping and are held securely on the inside of the cavity. The inside of the volume is sprayed with Bonderite Aerodag colloidal graphite spray to make it conductive. The screws are then held to ground potential with the green wires shown in **Figure 3.5**. A 0.002-inch-wide wire is held across the diameter by two pinched copper tubes. Pinching the copper securely holds the thin wire in place. The wire is insulated by PTFE tubes on either end. Torr Seal is used to hold the PTFE insulators and copper tubes in place. The active volume is secured to the aluminum lid by an acrylic cylindrical stand with Torr Seal. Holes are drilled in this stand to allow the flow of gas.

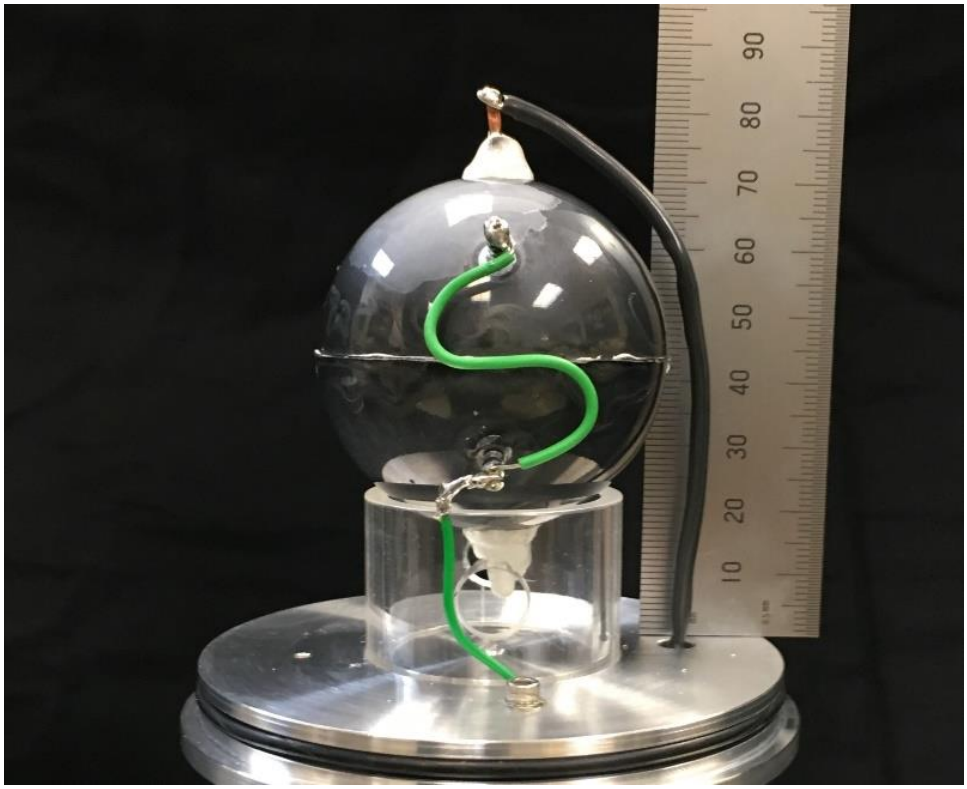

Figure 3.5: A picture of a 2-inch diameter ATED spherical active volume. Scale is in mm.

The detector head is an air-tight, aluminum housing that holds the active volume, a preamplifier, and the tissue equivalent gas. A schematic of the ATED detector heads is shown in **Figure 3.6**.

The entire detector head is held to ground via a wire held in place with a screw. The lid of the detector head is sealed with Torr Seal to prevent tissue equivalent gas from escaping. Air inside the volume is evacuated and then filled to the correct pressure with tissue equivalent gas through a copper tube. The detector head must be held at high vacuum for 48 hours prior to being filled with tissue equivalent gas to prevent outgassing [Collums, 2012]. This tube is then pinched closed when at the correct pressure. Pinching the copper tubes prevents leaking of air into the detector head.

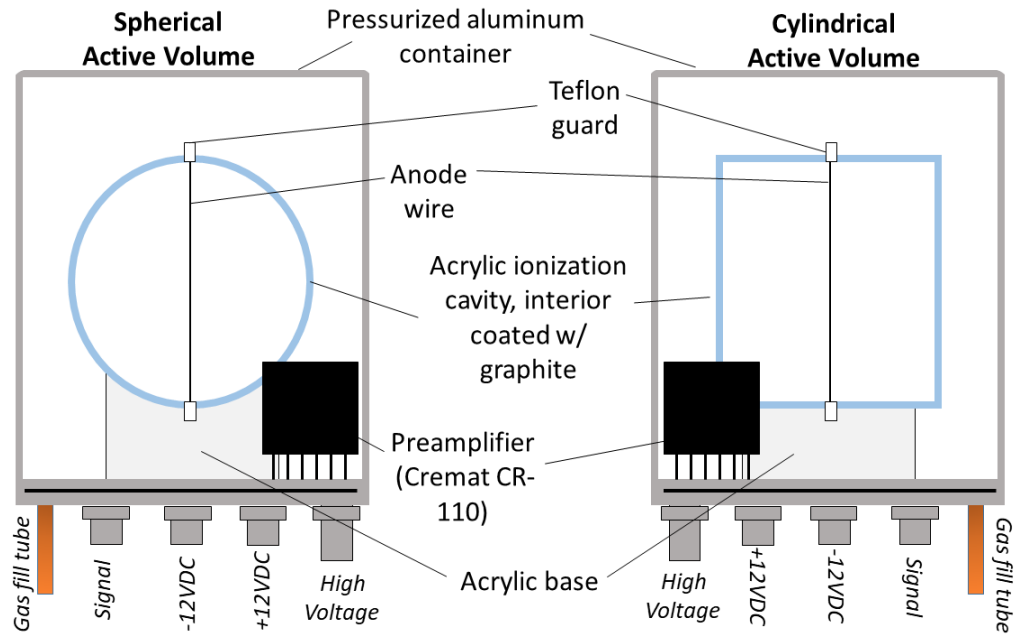

Figure 3.14: A schematic of the ATED detector head. Both a cylindrical and spherical active volume are shown. The detector head holds the active volume, supporting structures, a preamplifier and the tissue equivalent gas.

Inside the detector head is a Cremat CR-110 rev.2 preamplifier coupled though a 1nF capacitor to the center collecting wire. The CR-110 takes the signals from the active volume, matches their impedance to the rest of the electronic system, and flips their polarity. Being close to the active volume is important in order to reduce electrical noise. To reduce noise further, the CR-110 is inside the detector head which acts as a faraday cage [Causey 2018].

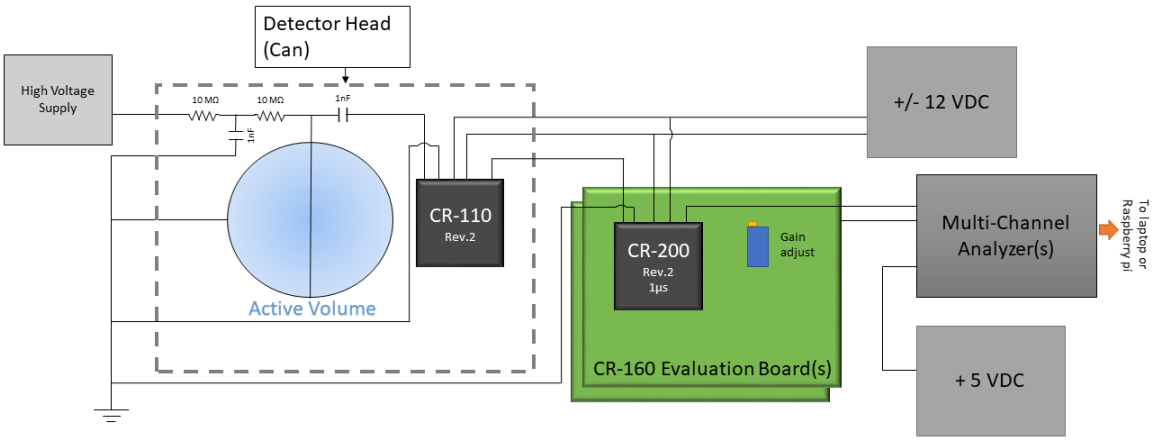

Figure 3.7: The electronics used in the ATED system. They include a high voltage supply, +/-12VDC supply, +5VDC supply, a CR-110 preamplifier, one or two CR-160 evaluation boards, and one or two CR-200 Gaussian shaping amplifiers. Not shown is the linear regulator circuit placed as the input voltage for the high voltage supply.

A Schematic of the supporting electronics is shown in **Figure 3.7**. Depending on the ATED model, one or two CR-200-1µs rev.2 non-inverting Gaussian shaping amplifiers are used. These amplifiers will amplify and shape signals coming from the preamplifier. This allows for control of the total amplification that signals receive. Two amplification channels will ensure proper resolution will be achieved at low lineal energies with one channel while the other covers the entire range of relevant lineal energies [Rossi, et al., 1996]. A CR160 Evaluation board is used as the supporting electronics for CR-200-1µs rev.2 non-inverting Gaussian shaping amplifiers. Both the CR-110 and CR-200 require +/-12 VDC to operate, supplied by a XP Power ECL15UT02-T AC-DC power supply.

An EMCO Q10 supplies high voltage to the center wire inside the active volume. Input voltage has a linear relationship with output voltage (roughly 175x). A linear regulator circuit is placed before the input to adjust the output of the EMCO Q10. Positive 12 VDC is input to the linear regulator and creates a more stable DC voltage. A variable resistor on the circuit (trim pot) is adjusted until the output of the linear regulator sits at roughly +5.83 VDC. This results in a steady output of +900 VDC from the EMCO Q10.

One of two different MCAs are used, depending on the design of the experiment. For experiments in the atmosphere, a Red Pitaya FPGA board is used (Section 3.12). For all other applications, an Amptek MCA-8000D is used. The MCA-8000D can analyze signals up to frequencies of 100MHz at 16-bit resolution, and a conversion time of 10ns. One disadvantage of the MCA-8000D is a single input channel. For ATED systems that have two gain channels, two separate MCA-8000Ds must be used. The output of either MCA is read in by either a laptop computer via Ethernet or a Raspberry Pi single board computer via serial connection.

3.4 Charge Collection in the ATED Active Volumes

During the development of ATED (and indeed previous other TEPCs) it was assumed, but never demonstrated, that ATED collects 100% of separated charge inside its active volume. A TEPC depends on the 100% collection of this charge in order to function properly. In this section, the method for finding collected charge as a function of applied bias is described. This is used to find the range voltages that ATED operates in the proportional region. The collected charge per pulse as a function of applied bias for three different ATED active volumes were found. This was done by measuring the height of pulses from a mono-energetic alpha source. In the process of measuring the collected charge as a function of applied bias, it is demonstrated that all three ATED active volumes collect all separated charge due to ionizing radiation.

The operation of a gas-filled detector depends the type of gas used, the pressure of gas, the geometry of the gas cavity and the electrodes, and the bias applied to these electrodes. The ATED has three different geometries, all of which have a fixed pressure of tissue equivalent gas. It was previously assumed, but not demonstrated, that all of the collected charge inside the ATED active volume is being collected.

Collected charge per unit time as a function of applied bias for the different ATED geometries is found through empirical measurements of pulse amplitude. In this process, a re-sealable detector head, like that shown in **Figure 3.8**, is used. The lid has four electrical feedthroughs: one SHV and three BNC. The SHV connector supplies high voltage to the center wire of the ATED active volume. The three BNC feedthroughs supply +/-12VDC for the CR110 preamplifier and a signal cable. The aluminum housing has a valve where tissue equivalent gas can be filled to the proper pressure. The pressure inside the detector head varies from ~10 mmHg to ~30 mmHg, depending on the active volume used. For the following tests, ATED simulated a 2µm diameter spherical or right circular cylindrical tissue phantom.

Figure 3.8 A re-sealable can with BNC and SHV feedthroughs. The large brass component is the valve which gas can be evacuated and refilled into the can. This older model of ATED detector head was fabricated by [Collums, 2012].

An Americium-241 source was centered over a small hole in the active volume wall. The Am-241 emits mono-energetic alpha particles that will ionize the tissue equivalent gas inside and traverse the active volume with similar chord lengths. In this way, each measured pulse will have a similar magnitude at a given bias.

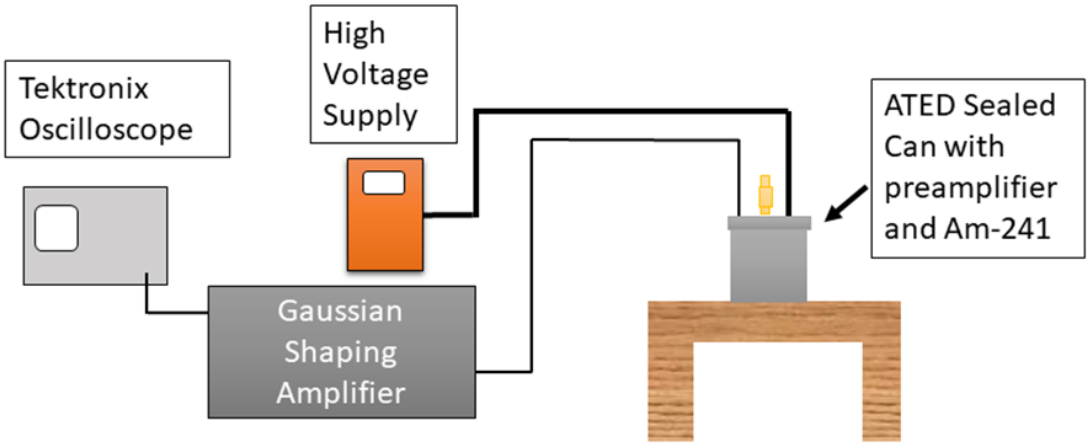

Figure 3.9: The experimental set up for finding collected charge as a function of applied bias. The re-sealable can was outfitted with an ATED active volume, a CR-110 preamplifier, an Am-241 alpha source, and filled to an appropriate pressure of tissue equivalent gas. Signals were passed through a preamplifer and Gaussian shaping amplifier. The resulting pulse height was measured in an oscilloscope.

The magnitude of each signal is measured with a Tektronix TDS 2024B oscilloscope. This set up is shown in **Figure 3.9.** At least ten measurements are made at each bias and averaged. Error is quantified as the standard deviation of these measurements. Pulse height was converted into collected charge per pulse with the conversion value of $1.109 * 10^{-16}$ C/V. This conversion value was found empirically by sending pulses of known voltage across a capacitor of 1 nF. The regions of operation for gas filled detectors are identified and labeled. Gas gain is calculated using,

$$G = \frac{Q_V}{Q_{RII}}, \tag{3.3}$$

where Q_V is the charge collected per unit time at voltage V and Q_{RII} is the average collected charge per pulse found in Region II. The quantity Q can be replaced by pulse height, as it is directly proportional to amount of collected charge per unit time [Rossi, et al., 1949].

The nominal operating voltage of each geometry and pressure was established by looking at these regions. The optimum operational voltage has a gas gain of around 10^3. As stated before, this operational voltage will change with the pressure inside the can, the geometry of the active

volume, and type of gas used. Any small change in these variables can significantly affect how the detector collects charge and thus this empirical measurement should be done again.

It is possible to run ATED at any of the voltage values inside the proportional region. The reported optimized voltages serve only as a benchmark for future experiments, but any voltage values inside the proportional region is sufficient. Previous calibrations will longer be valid if the applied bias changes, and thus the instrument will need to be recalibrated. Using a bias value outside of the proportional region will result in the instrument no longer working as a proportional counter.

Collected charge per pulse as a function of applied bias was found for a 2-inch diameter spherical shell simulating a 2μm diameter sphere of tissue. In **Figure 3.10** the different regions of operation for this curve are labeled. Below 25 volts, no pulses were seen, possibly due to recombination of separated charge inside the active volume. From 50 to 500 V pulses are constant in magnitude. This is the ionization region, or the one-to-one region, where all the collected charge inside the volume is collected, but there is no amplification of the signal. Between 650 and 925 V is the proportional region, where Townsend avalanches amplify the signals inside. At 925 V is the start of the region of limited proportionality, the transition into the G-M region. This is where the non-uniformity of the electric field along the center wire causes a portion of the active volume to enter the G-M region while the rest of the volume is still operating in the proportional region. This point is characterized when the second derivative of this curve becomes negative (inflection point) [Segre, et al., 1953]. After this transitional region, the G-M region starts at 975 V.

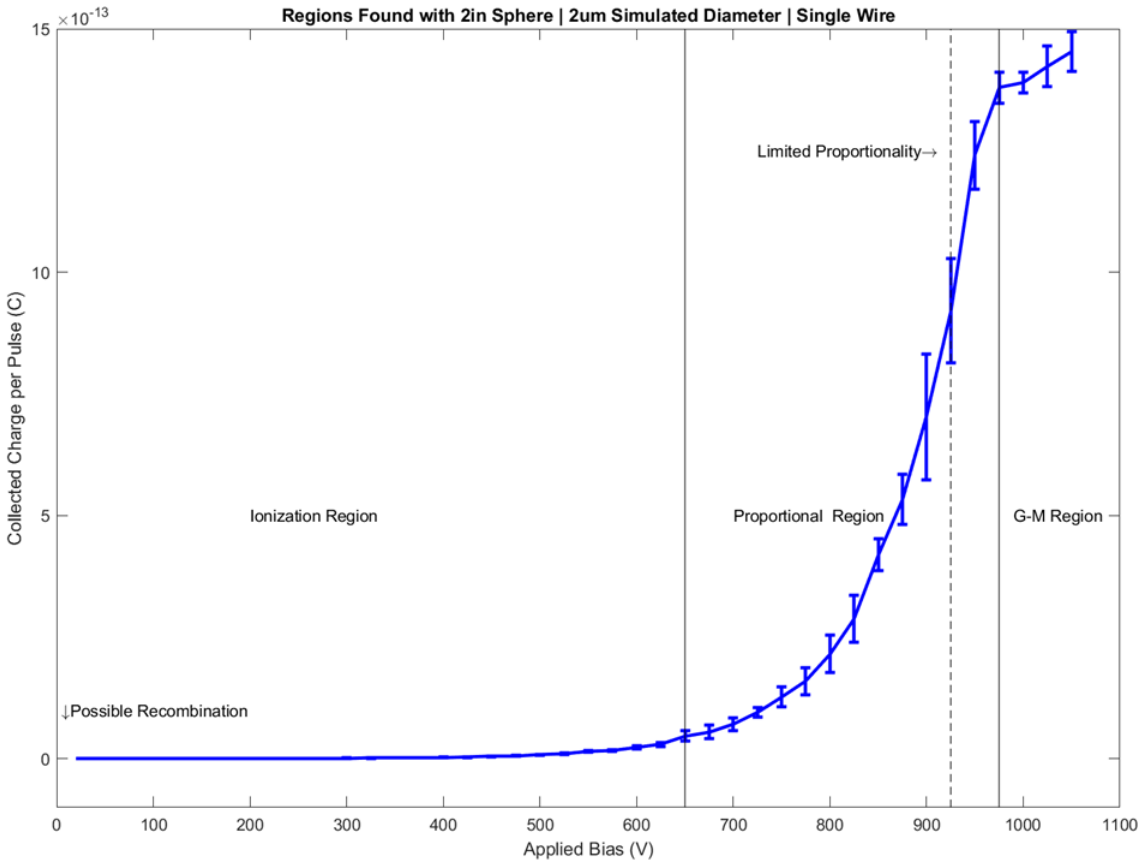

Figure 3.10: Collected charge as a function of applied bias for the 2-inch sphere simulating a 2um diameter sphere of tissue. Each region of operation is labeled. Error is quantified as the standard deviation of the ten measurements taken at each applied bias.

For a simulated 2µm diameter spherical tissue phantom inside a 2-inch sphere, the optimum voltage was found to be 900 V, just before the region of limited proportionality. At this voltage, the 2-inch spherical ATED active volume has a gas gain on the order of 10^3. At lower voltages, the gas gain fell below 10^3, making these voltages not optimal for ATED operations.

The same measurement was performed on a 3-inch diameter spherical shell simulating a 2 µm diameter sphere of tissue. An identical volume was used on the flight model of ATED that went to the ISS. The enlarged diameter maximized the cross-sectional area of interaction with rare high-energy GCR in LEO [Causey, 2018]. The optimal operational voltage was found to be 1050 V. Once again, the gas gain at this voltage was on the order of 10^3, and was outside the region of limited proportionality. The ISS ATED used 900 V as its applied voltage. This does not

affect the results as the calibration for the ISS experiment was done at 900 V, and is still inside the proportional region. The gas gain at 900 V is about 250.

The same measurement was again performed on the 2-inch cylindrical ATED simulating a 2 µm right circular cylinder of tissue of equal height and diameter. It should be noted that the Am-241 source was oriented such that alpha particles would traverse the height of the cylinder, just as charged particle beams would in experiment. The optimal operational voltage for the cylindrical volume was found to be 725 V, where gas gain is on the order of 10^3, and is outside of the region of limited proportionality.

The more important implication of these tests is the demonstration that ATED, in these configurations, collects all of the charge separated inside its active volume. This is seen in the voltage range of 50 to 500 V in **Figure 3.10**, where the collected charge per unit time is constant. In the Ionization Region, measured pulses reach a point of saturation, which indicates that recombination has been completely overcome and all charge is being measured [Knoll, 1999]. In this range of voltages, the charge collected stays constant despite a change in voltage, which is indicative of the recombination rate to be zero and no new charge being created [Tsoulfanidis, 1995].

3.5 The Electric Fields Inside ATED Active Volumes

Ideally, the electric field strength inside any proportional counter will be uniform along the central collecting wire. For both ATED active volumes, spherical and cylindrical, this is not the case. Where the wire is supported by the wall of the cavity, the electric field is strongest. These distortions are called end effects, and have been a long-standing problem in radiation detector

development [Cockroft, et al., 1951]. In some cases, the active volume of a detector cannot be considered be the same as the length of the central collecting wire [Rossi, et al., 1949].

A cross section of the calculated electric field of the spherical ATED geometry is shown in **Figure 3.11**. The calculation of the electric field was done in MATLAB. The geometry was defined with an associated bias voltage, and the magnitude of the electric field was found for a grid of points inside the active volume. The gradient of these calculated magnitudes were then found and linearly interpolated. Field lines are evenly spaced around the inside of the outer wall and converge at the center wire. The spacing of the electric field lines is directly related to the strength of the electric field. The grey cylinders are insulators that hold the central wire, and thus have zero contribution to the electric field. The geometry of a sphere does not have an obvious distortion of the electric field near where the wire is supported by the wall. The outer wall curves to such a degree that the end effects are minimal. Also, the probability of an ionization event happening where end effects are significant is relatively small. This is because the portion of the active volume where end effects exist is small compared to the rest of the volume.

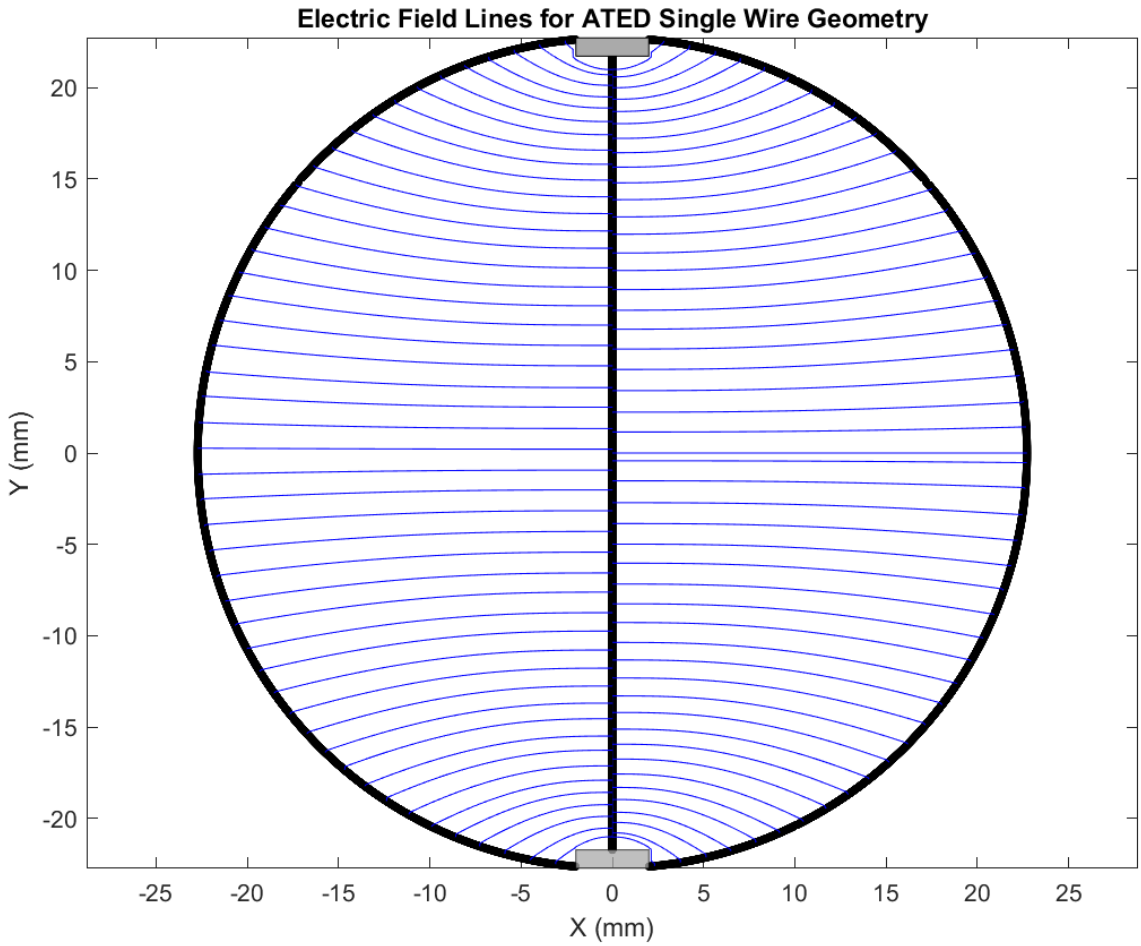

Figure 3.11: The electric field lines for a spherical ATED of 2" diameter. The field lines are evenly spaced on the inside of the outer shell and converge at the center wire. Calculations for the above electric field were done in MATLAB.

In **Figure 3.12**, the relative electric field strength at the wire as a function of the distance away from the end of the wire is shown. Calculated field strength was taken directly from the above figure. Only the middle of the wire inside the active volume to one end was considered. The electric field is somewhat constant from the center to ~6 mm from the end of the wire. These last 6 mm or so show a rapid increase in electric field strength. This is a direct representation of the end effects of a spherical counter. No efforts have been made to alter the electric field to get rid of these end effects. It is generally assumed that these effects are negligible and will not affect measured data significantly.

The data in **Figure 3.12** fits to a power law. The equation of fit for this particular set of data is $1.311 * x^{-0.2655}$ with a coefficient of determination of $R^2 = 0.9722$. At larger values of x, there is a small change in the electric field strength. This change is so small that there will be no measureable change in the gas gain along the central parts of the wire. This is why the majority of the electric field along the wire can be considered uniform. Only at the extreme ends of the wire will the electric field significantly change to the point where a measureable change in gas gain will occur. As stated before, the occurrence of these counts is small compared to the rest of the volume. Further tests with a controlled, charged particle beam of small diameter across different parts of the ATED spherical active volume is needed to justify, and explore these claims.

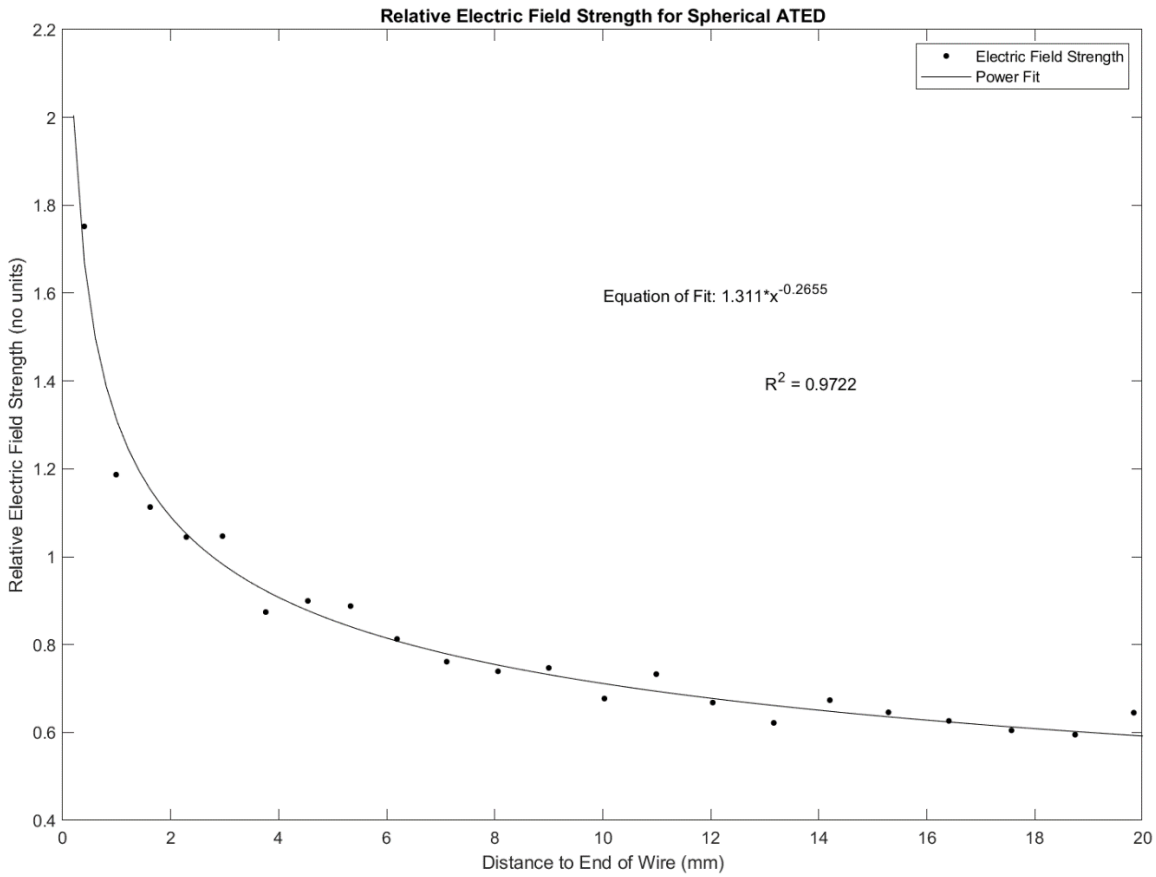

Figure 3.12: The relative electric field strength for a Spherical ATED. A power law fit is put over the data. The fit and coefficient of determination are also displayed.

Figure 3.13 shows the electric field for a cross section inside the cylindrical ATED active volume. Significant end effects can be seen at the ends of the central wire, where electric field

lines originate from the wall perpendicular to the wire. This creates a region inside the cavity where ionization events will have measureable difference in gas gain than the rest of the cavity. This was an oversight in the design of the first cylindrical ATED. In this case, the geometry of the active volume worked against having a suitably uniform electric field along the wire. The electric field lines from the sides of the cylinder parallel to the wire have compressed the field lines from the ends to the point where significant changes in the relative electric field strength occurred.

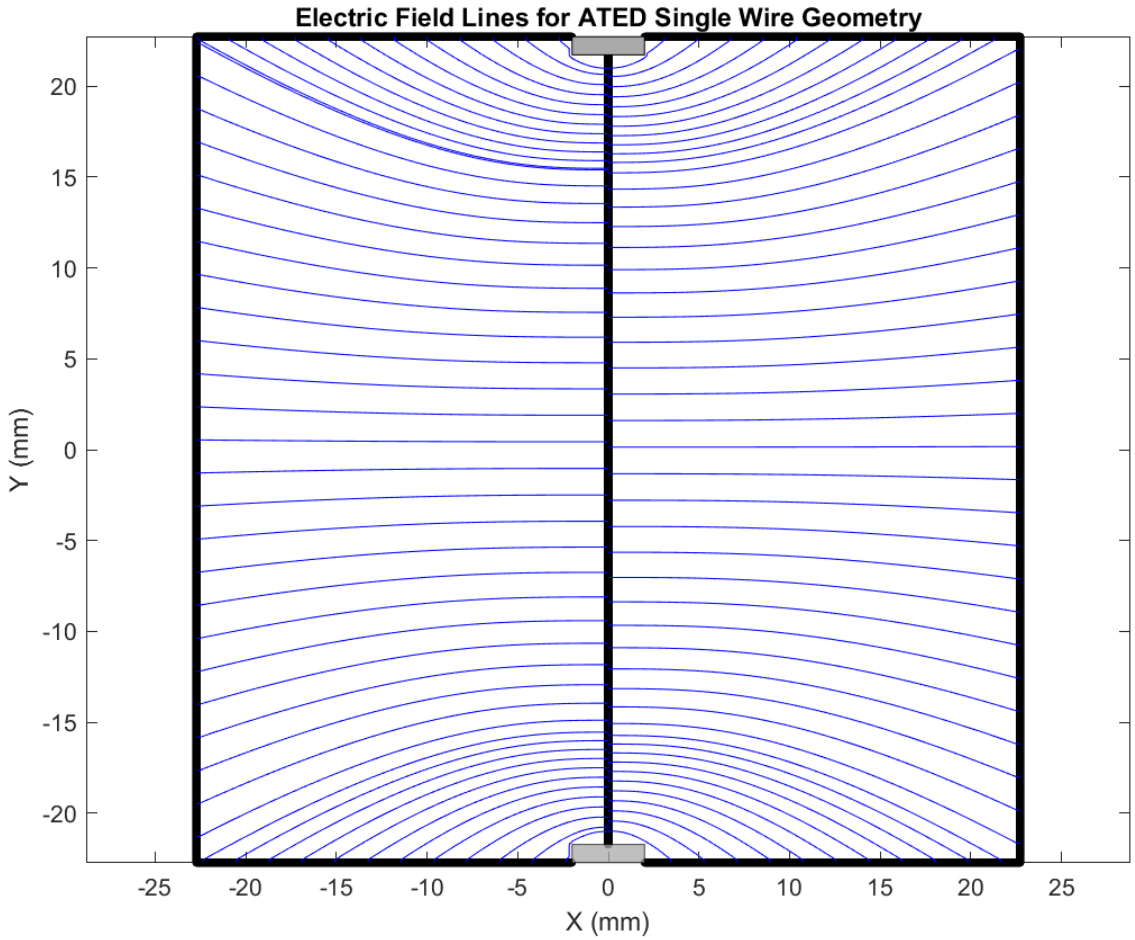

Figure 3.13: The electric field lines for the first cylindrical ATED. Significant end effects occur close to where the central wire is supported by the wall of the detector.

Figure 3.14 shows the relative electric field strength along the center wire as a function of distance away from the end of the wire for the cylindrical ATED volume. In the middle of the wire the electric field is mostly uniform and exhibits the same behavior as a spherical volume. At

~8 mm we see an increase in relative electric field strength as was also seen with the spherical ATED. A clear discontinuity is seen at ~5.5 mm, where end effects create region of large electric field strength. This is the shaded region in the plot, and where electric field lines from the ends of the cylinder have converged. The cause of the severe end effects is the geometry of the volume. The gas gain inside the shaded region will be measurably different than the rest of the chamber. Measurements taken with this geometry exhibited strange behavior, and it is thought that having such strong end effects inside the active volume was the reason for erroneous measurements.

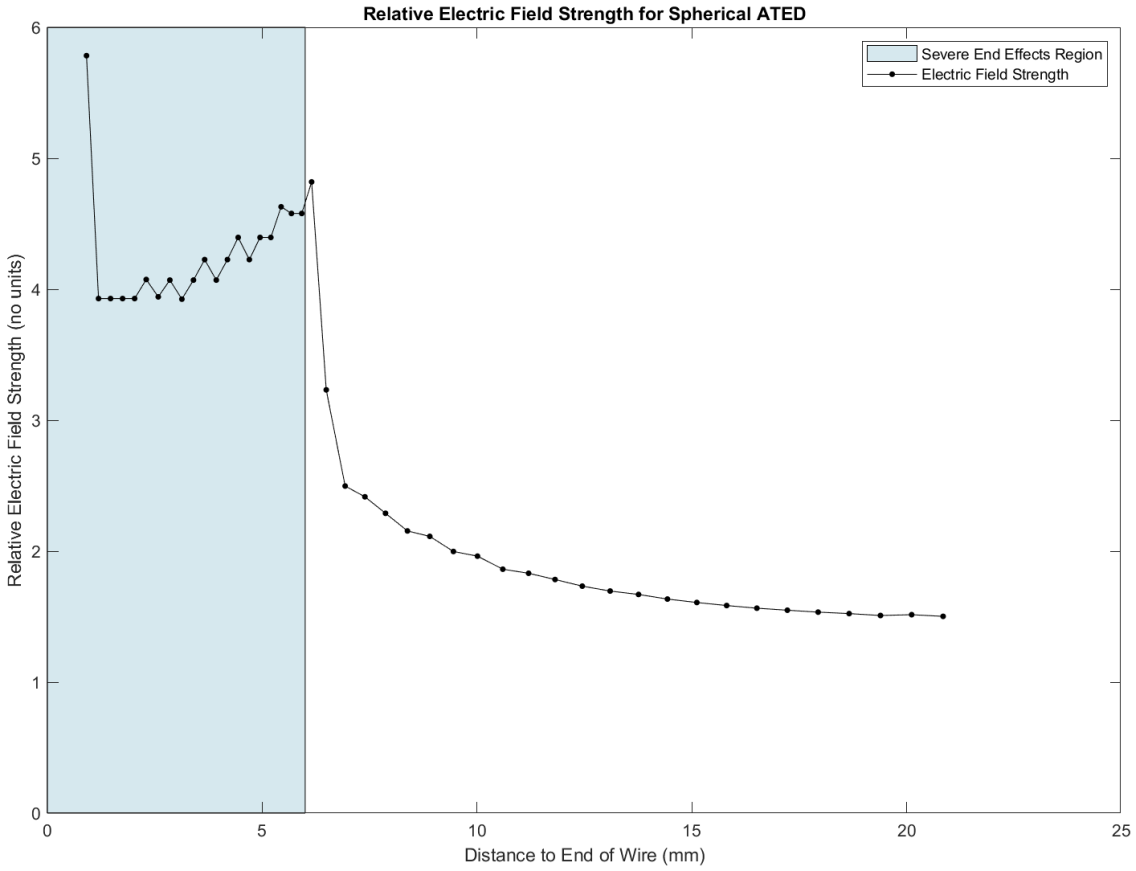

Figure 3.14: The relative electric field strength for cylindrical ATED. The shaded region is the region inside the active volume where there are significant end effects.

There are ways to mitigate end effects. Shielding the central wire with field tubes is the most widely used method. Field tubes encompass the ends of the wire where end effects are large. These field tubes are at such a potential that they do not alter the electric field of the original geometry (i.e. if they were not present) [Cockroft, et al., 1951]. Field tubes will shield the central

wire from these end effects, but also shrink the active volume to include only the volume where charge will be collected by the central wire. This eliminates the discontinuity of electric field strength along the center wire and minimalizes end effects.

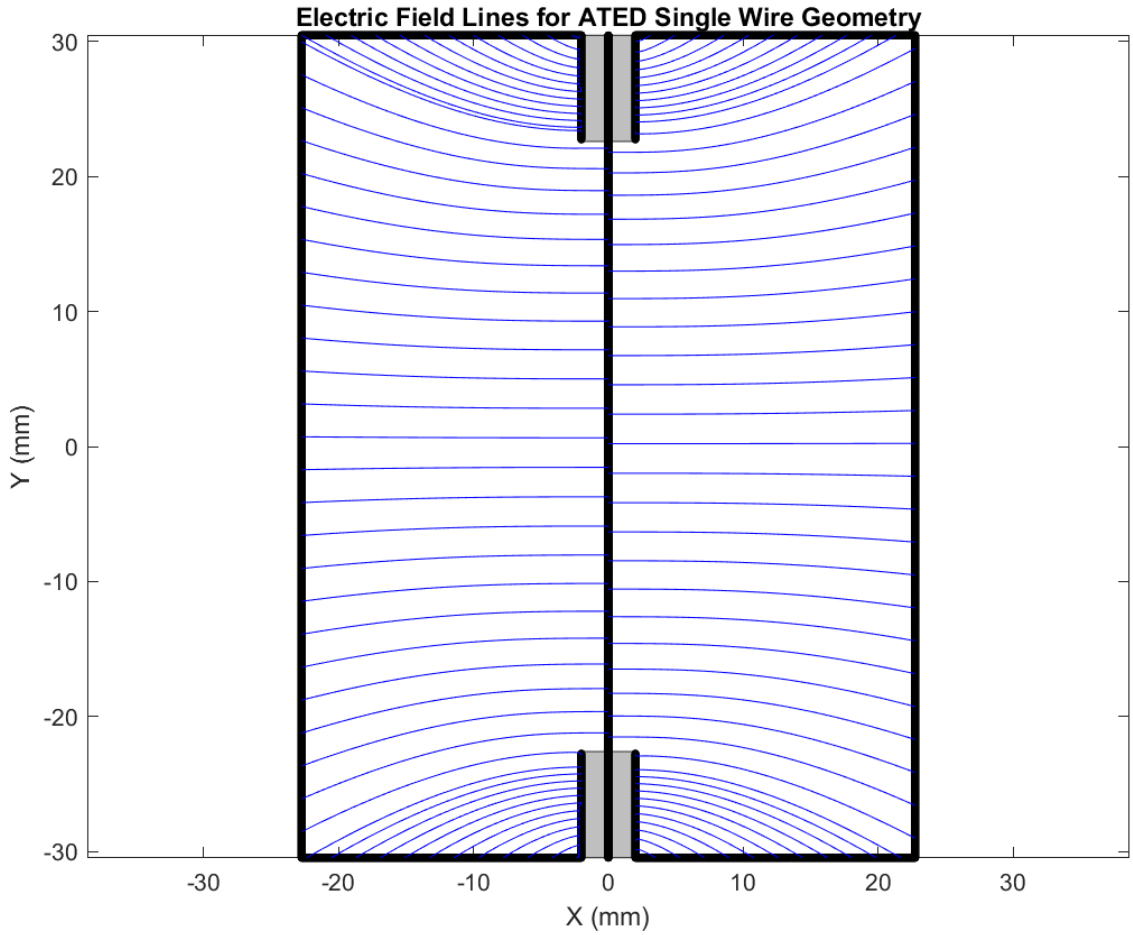

Figure 3.15: The electric field inside the cylindrical ATED with field tubes. The cylinder has been elongated in order to keep the active volume inside to have equal diameter and height.

Figure 3.15 shows the schematic of a cylindrical ATED with field tubes. Note that the cylinder has been elongated in order to make the active volume equal in diameter and height. The electric field along the exposed parts of the center wire, and therefore gas gain, can be considered uniform over the major part of the active volume. The use of field tubes keeps the original electric field, but blocks all ionization events near the ends of the wire from being measured. This geometry has now been adopted for the new ATED cylindrical detectors.

3.6 Mean Chord Length

The path that ionizing radiation takes through the active volume is called a chord. The length of a chord through the detecting medium by ionizing radiation will directly relate to the number of initially created ion pairs. The distribution of chord lengths though a detector will depend on the direction of incident ionizing radiation and the geometry of the active volume.

Figure 3.16 shows an illustration of a spherical ATED active volume during an ionization event. Spherical counters are designed for use in isotropic fields of ionizing radiation like that found in LEO. The spherical geometry yields a chord length distribution that is the same regardless of the direction of incident ionizing radiation.

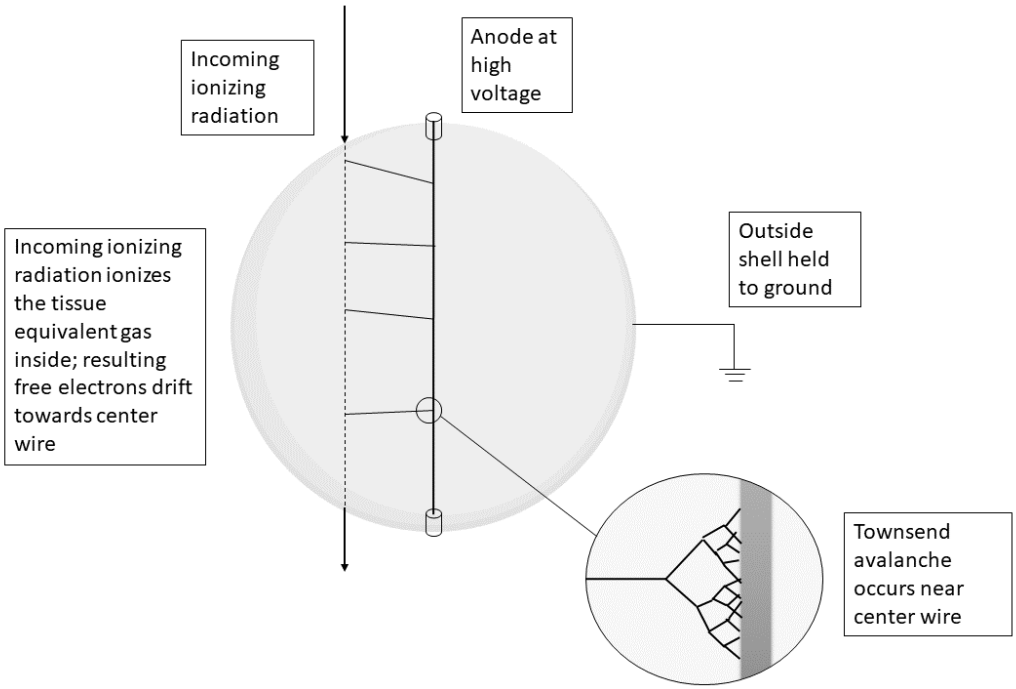

Figure 3.16: A Spherical ATED active volume during an ionization event. Freed electrons will accelerate towards the center wire and produce a Townsend avalanche near the wire. The total number of freed electrons will be directly proportional to the energy deposited in the tissue equivalent gas.

Ionizing radiation passes through the active volume of ATED with an unknown chord length, x. The chord length of an individual passing particle is directly related to the amount of energy

deposited into the detecting medium. Mean chord length of the entire volume is used for dosimetric calculations because we do not know the chord length for each passing particle.

A spherical volume cannot directly measure an LET spectrum because the chord length traversed by each particle is unknown [Collums, 2012]. The distribution of chord lengths for a sphere in an isotropic radiation field can be used to construct an LET spectrum from a lineal energy spectrum [Rossi, et al., 1996; Kellerer, 1972]. We proceed to determine the chord length distribution for a spherical volume in an isotropic field.

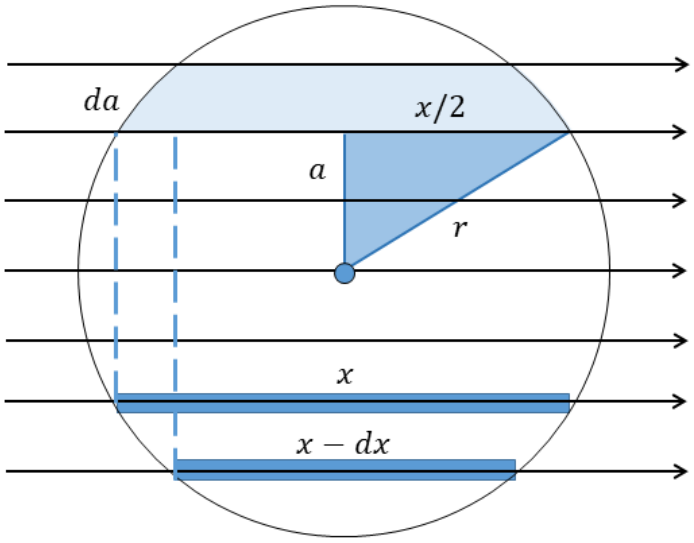

Figure 3.17: The simplified case of considering particles approaching from a single direction. Supporting labels are explained in the text.

Consider a sphere of radius r in an isotropic field of radiation. Assume that the radiation traverses space in straight lines and does not deviate from that path. Radial symmetry allows the two dimensional case to arrive at the same result as a sphere. Azimuthal symmetry allows for simplifying the case further and consider particles approaching from a single direction, as shown in **Figure 3.17**. The impact parameter, a, is the distance of the closest approach of a chord to the center of the circle. The probability that a chord will have an impact parameter between a and da is shaded in light blue in **Figure 3.9** [Rossi et. al., 1996]. This probability can be written as a function of impact parameter by,

$$P(a)da = \frac{2\pi\, a\, da}{\pi\, r^2}. \tag{3.4}$$

A right triangle can be made from the center of the circle with one side having length a and hypotenuse of length r. We call the chord length of a passing particle x, thus the other side of this triangle will have length $x/2$. This triangle is shaded in dark blue. The impact parameter can now be written as a function of chord length,

$$a(x) = \sqrt{r^2 - \left(\frac{x}{2}\right)^2}. \tag{3.5}$$

To find da, we differentiate equation (3.5) and find,

$$da = \frac{-x\, dx}{4\sqrt{r^2 - \left(\frac{x}{2}\right)^2}}. \tag{3.6}$$

By placing equation (3.5) and (3.6) into (3.4),

$$P(a) = \frac{-x\, dx}{2\, r^2}. \tag{3.7}$$

The probability that the particle will have a chord length between x and $x - dx$ will be the same as the probability of the particle having an impact parameter between a and $a + da$ [Rossi et. al., 1996]. Thus,

$$P(a)\, da = -P(x)\, dx. \tag{3.8}$$

This now gives us the probability of chord lengths as a function of x,

$$P(x) = \frac{x}{2\, r^2}. \tag{3.9}$$

This probability chord length distribution has a direct relationship to chord length and takes the shape of a triangle with a maximum when $x = r$. The most probable chord in a sphere is through its diameter.

Mean chord length of the volume is used for the calculation of absorbed dose and comes directly from the probability distribution of chords in a sphere. By substituting the diameter of the circle, d into (3.9) and integrating over all possible chord lengths

$$\bar{l} = \int_0^d P(x)\ x\ dx. \tag{3.10}$$

where $\bar{l}$ is the mean chord length. Solving (3.9) with (3.8) results in the mean chord length for a spherical volume,

$$\bar{l} = \frac{2d}{3}. \tag{3.11}$$

Equation (3.11) is the mean chord length for isotropic radiation for a spherical volume. Put simply, the mean chord length for a sphere is two-thirds its diameter. The mean chord length is a useful quantity precisely because we do not know the chord of each individual measured particle. The definition of lineal energy comes from the use of mean chord length, as each event regardless of its magnitude will be divided by $\bar{l}$. Mean chord length will relate the lineal energy and LET of measured particles, as discussed in the next section.

A spherical volume will always have the same chord length distribution, but a cylindrical volume will have a chord length distribution that changes depending on the direction of incident radiation. Cylindrical geometries have an advantage when the direction of incident radiation is unidirectional, as is illustrated in **Figure 3.18**, such as particle accelerators or with collimated radiation sources. The active volume can be oriented such that ionizing radiation will traverse only the height of the cylinder, thus making the chord length distribution uniform. This assumes that no straggling of particles happens across the gas volume, which is reasonable for the low density of the gas. The goal of this configuration is to directly measure LET instead of lineal energy. Also, uncertainties associated with dosimetric calculations will be less than for spherical geometries because of the uniform chord length distribution.

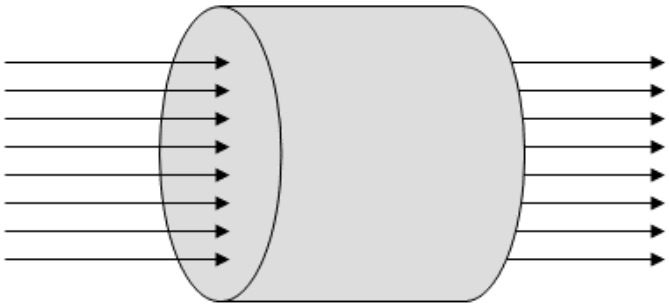

Figure 3.18: A right cylinder and incident ionizing radiation passing though the height of the cylinder. This kind of measurement will have a uniform chord length distribution.

A cylindrical geometry can also be used in an isotropic field. In order to simulate the benefits of having a spherical counter a right circular cylinder, whose length is equal to its diameter, is utilized. No geometric derivation exists for the mean chord length of this volume. Cauchy's theorem is used to calculate the mean chord length of this cylindrical geometry. This theorem states that the mean chord length of a given convex geometry is,

$$\bar{l} = \frac{4V}{S}, \tag{3.12}$$

where V is the volume and S is the surface area of the object [Cauchy, 1841]. The volume and surface area of a right circular cylinder is,

$$V = \pi r^2 h \tag{3.13}$$

and

$$S = 2\pi rh + 2\pi r^2. \tag{3.14}$$

By substituting (3.12) and (3.13) into (3.11) we arrive at,

$$\bar{l} = \frac{2hd}{d+2h}. \tag{3.15}$$

The cylindrical ATED volume has an active volume with a diameter equal to its height ($d = h$). Thus,

$$\bar{l} = \frac{2}{3} d. \tag{3.16}$$

The mean chord length of a right cylinder is also two-thirds its diameter. The reason to make the cylindrical active volume have equal height and diameter is so that it most closely relates to a spherical volume. Although the mean chord length for a cylindrical and spherical geometry is the same, the distribution of chord lengths differs drastically in an isotropic field. For example, a right cylinder will have chords longer than its diameter, which is impossible for a sphere

3.7 Lineal Energy Spectra

The measurements taken by ATED are in terms of lineal energy. Lineal energy is the measurement of energy deposited in a defined volume per unit length, as defined in Chapter 3.3. The magnitude of a measured lineal energy event is the result from the stopping power of the particle in the tissue equivalent gas and the chord length taken by ionizing radiation through the active volume. We can show lineal energy in terms of mass stopping power, S_{mass} (see Apendix 2), the density of the gas, ρ_g, and the mean chord length:

$$y = \frac{S_{mass}\, \rho_g\, x}{\frac{2}{3} d_t} = \frac{S_{mass} \rho_g x}{\bar{l}_t}. \tag{3.17}$$

Equation 3.17 shows the linear relationship between chord length and the stopping power of the measured particle.

This function and the corresponding ideal LET measurement is illustrated in **Figure 3.19**. The relationship between mass stopping power and LET is also linear. The main difference is lineal energy depends on a defined volume and LET is simply per unit length. Particles of a single LET will ideally take the shape seen in **Figure 3.19**. Equation 3.17 expresses how a measurement of single LET particles would ideally be distributed if measured by a spherical TEPC. The peak of

the triangle seen at y_{max} corresponds to particles crossing the full diameter of the sphere. Counts at the far left of the triangle are the result of particles crossing the smallest chords of the active volume. As the chord length increases, we see an equal increase in the lineal energy measured and frequency of counts. The most probable chord length for a sphere is its diameter.

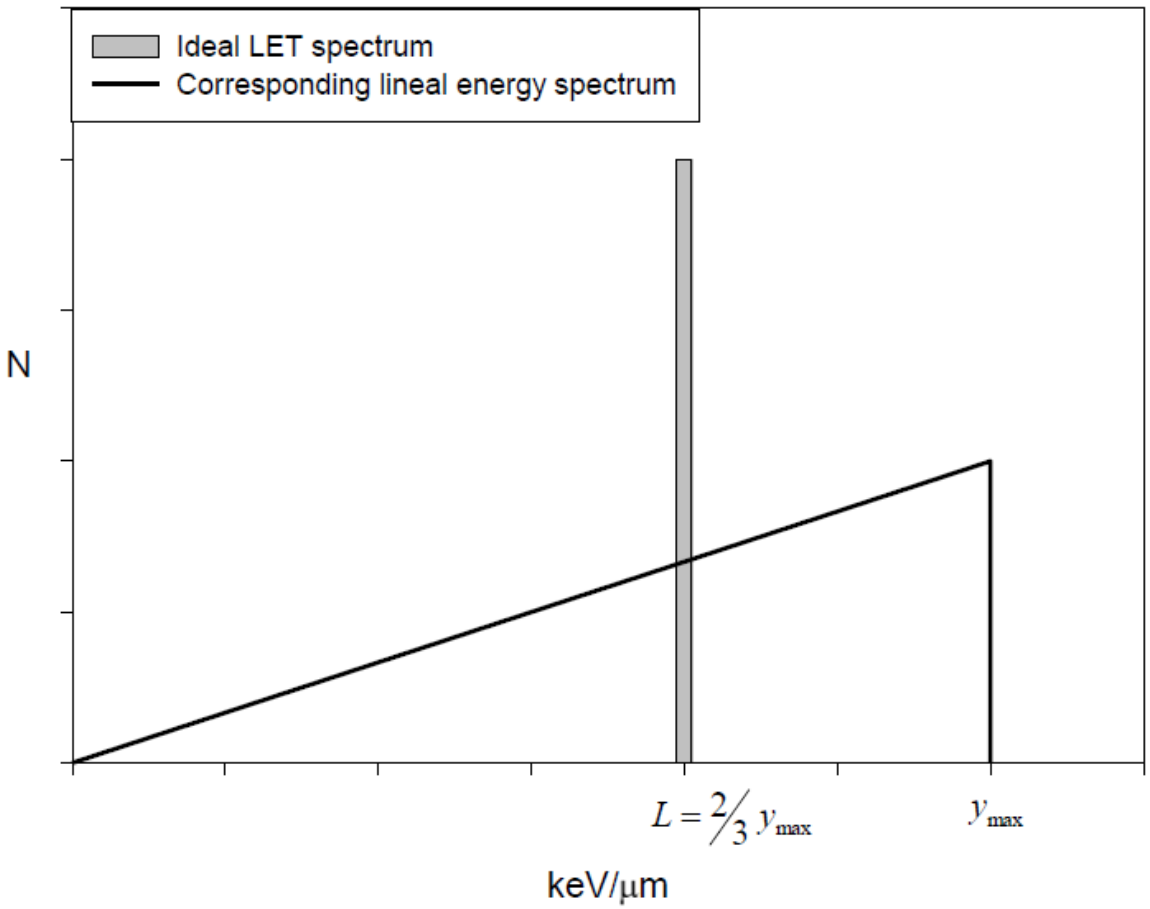

Figure 3.19: Number of counts (N, arbitrary) as a function of lineal energy bins, y. An ideal measurement of particles of a single LET and the corresponding lineal energy spectrum in a spherical TEPC [Rossi, 1996]

The ideal LET spectrum is located at the mean chord length of the sphere, and thus the following approximation can be made,

$$L = \frac{2}{3} y. \tag{3.18}$$

A more rigorous treatment of the relationship between lineal energy and LET is discussed in Chapter 5.

3.8 Tissue Equivalence and Simulated Volumes

Tissue equivalence is the property of tissue equivalent proportional counters that allows for the calculation of absorbed dose in biological tissue. TEPCs respond to ionizing radiation in a sufficiently similar way that tissue does [Rossi, et al., 1996]. This is achieved through the use of tissue equivalent gas inside a tissue equivalent plastic shell. The tissue equivalent gas has the following composition: 67.259% CH_4, 29.99% CO_2, and 2.751% N_2. The tissue equivalent plastic is acrylic with the following composition: $(C_5O_2H_8)_n$. Acrylic has been shown to be tissue equivalent [Collums, 2012].

TEPC active volumes simulate microscopic volumes of human tissue inside a macroscopic active volume [Brackenbush, 1990]. The gas inside the active volume is at a pressure such that the same number of gas molecules inside the plastic shell is equal to that of a single human cell. This will simulate micron-scale volumes of tissue inside the active volume. These simulated tissue volumes are called tissue phantoms. Site equivalence is defined as,

$$\bar{\epsilon}_g = \bar{\epsilon}_t \,, \tag{3.19}$$

where $\bar{\epsilon}_g$ is the mean energy deposited into the tissue equivalent gas and $\bar{\epsilon}_t$ is the mean energy deposited into a corresponding volume of tissue [Rossi et. al., 1996]. By the use of site equivalence, we can justify that the energy deposited in the tissue equivalent gas will be the same as in a microscopic cell [Rossi, et al., 1996]. The energy deposited in the tissue equivalent gas is,

$$\bar{\epsilon}_g = \frac{1}{\rho_{\mathrm{g}}}\left(\frac{dE}{dx}\right)_{el} \rho_{\mathrm{g}}\ \bar{l}_g \,, \tag{3.20}$$

where $\left(\frac{dE}{dx}\right)_{el}$ is the electronic stopping power, ρ_g is the density of the gas, and $\bar{l}_g$ is the mean chord length of the volume. All tissue equivalent materials have equal mass stopping power to that of tissue [ICRU, 1983]. Thus,

$$\frac{1}{\rho_g}\left(\frac{dE}{dx}\right)_{el} = \frac{1}{\rho_t}\left(\frac{dE}{dx}\right)_{el} \tag{3.21}$$

where the subscripts represent the tissue equivalent gas with g, or tissue with t. Using the right side of (3.19) into (3.20), and substituting into (3.18) yields the definition of tissue equivalence,

$$\rho_t\, \bar{l_t} = \rho_g\, \bar{l_g}\,, \tag{3.22}$$

[ICRU, 1983; Rossi et. al., 1996]. We approximate the density of tissue to be 1g/cm^3 and using the results of the mean chord length for a spherical volume in equation (3.11) for $\bar{l}_g$ and $\bar{l}_t$ we arrive at,

$$d_t = \rho_g\, d_g. \tag{3.23}$$

Equation (3.20) is the relationship between the diameter of the simulated volume of tissue and the diameter of the active volume. ATED usually simulates a 2 µm diameter spherical tissue phantom with its spherical volume. With the cylindrical volume, a 2 µm right circular cylindrical tissue phantom of equal height and diameter is simulated.

3.9 Measurement of Indirectly Ionizing Radiation

Energetic charged particles directly ionize the material they pass through via the Coulomb force. Neutrally charged particles can also be ionizing, but only through secondary reactions that produce energetic charged particles. Ionizing radiation with no charge is called indirectly ionizing

radiation. Examples of indirectly ionizing radiation are photons above 10 keV and neutrons of every energy [Cherry, 2012].

Figure 3.20 illustrates how a spherical ATED active volume measures the secondary products of indirectly ionizing radiation. The gas inside the ATED active volume is not dense enough to produce consistent interactions with photon and/or neutron radiation. The outer acrylic shell that surrounds the active volume is much denser, and therefore far more likely to interact with incident photon and neutron radiation. Neutrons and gammas interact with the atoms in the acrylic shell and produce secondary charged particles that can be ejected into the active volume and ionize the tissue equivalent gas. The amount of energy deposited will then be product of the LET of the ejected particle and the chord traveled in the active volume.

Neutrons are able to penetrate the nuclei of a material and can undergo various types of interactions because they have no charge. The type of interaction they undergo is heavily dependent on their kinetic energy [Rossi, et al., 1996]. Sometimes they initiate nuclear reactions with nuclei that produce charged secondary particles that can ionize the tissue equivalent gas. By far the most likely reaction for neutrons incident on the atoms in tissue is the recoil of protons from interactions with hydrogen atoms [ICRP, 1983]. A detailed description of neutron interactions with matter can be found here [Rinard, 1991].

High energy photons interact with the electrons of the atoms in the acrylic shell surrounding the active volume of ATED. This happens through three main processes: the photoelectric effect, Compton scattering, and pair production [Krane, 1988]. These processes produce energetic secondary electrons that, should they enter the active volume, ionize the tissue equivalent gas. How often these processes occur depends on the energy of the incident photon, and the atomic number (Z) of the material it penetrates [Podgorsak, 2016].

Charged particles with sufficient energy can also undergo nuclear interactions and produce secondary particles. This process is much rarer because these particles must overcome Coulomb repulsion with the nuclei in matter. More detail on secondary particles produced by charged particles is discussed in detail in Chapter 2.3.

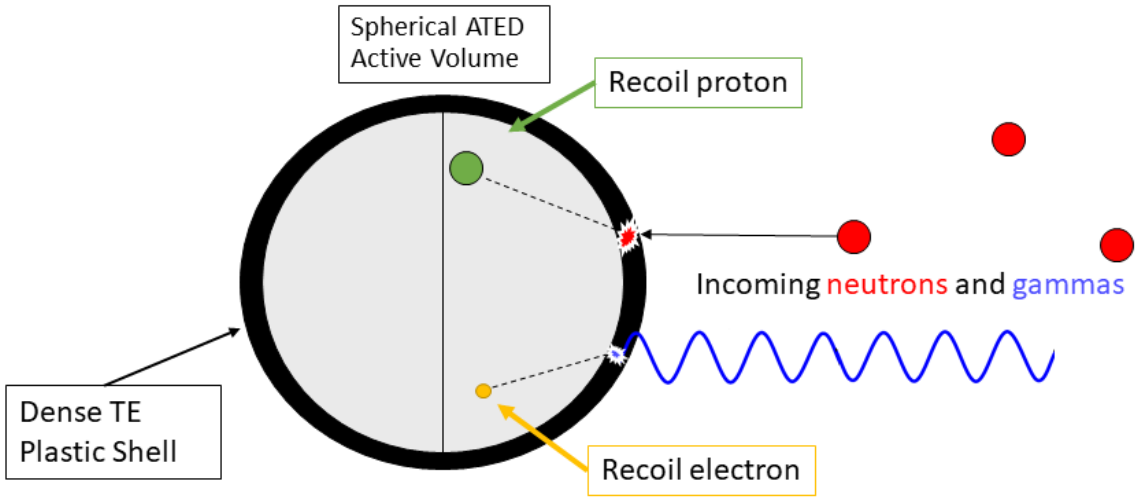

Figure 3.20: Indirectly ionizing radiation (gammas and neutrons) producing example secondary particles in the dense wall surrounding the active volume of a spherical ATED. TE stands for tissue equivalent. An identical process will happen for cylindrical geometries.

3.10 The Representation of Lineal Energy Spectra

The most basic representation of measured lineal energy spectra is counts as a function of bin number. A further step is to convert bin number into a known lineal energy using a calibration function. This results in the frequency of counts as a function of lineal energy, denoted by $f(y)$. This is the basic representation of calibrated TEPC data.

The quantity $f(y)$ is not useful for measurements that have more than one amplification channel, as discussed in Section 3.2. The resolution of the high gain channel and the entire range of lineal energies in the low gain channel tell the whole story of a measurement. These channels will then need to be put together into the same spectrum in order to take advantage of this setup. Each gain

channel will have different bin widths (in terms of lineal energy). The range of lineal energies for a specific bin are directly related to the amount of amplification signals receive. Larger bin widths will have more counts than a smaller bin width of the same mean lineal energy. More counts will be funneled into a large bin width. This will make the frequency of counts spectrum look discontinuous where the two gain channels are joined together.

To properly represent measurements taken by a system with two gain channels, the probability density normalized by bin width as a function of lineal energy, $p(y)$, is used. The $p(y)$ is calculated by,

$$p(y_i) = \frac{f(y_i)}{\sum_y f(y)} \frac{1}{y_i - y_{i-1}}, \tag{3.24}$$

where y_i is the lineal energy in the i^{th} bin. The right-hand term divides the bin-width of each channel, thus eliminating the discontinuity between gain channels. The units of $p(y)$ are typically (keV/μm)$^{-1}$. If we plot $p(y)$ against lineal energy, y, on a linear basis, almost no distinguishing features will arise. This is because measured counts typically span several orders of magnitude. ATED typically measures down to a lineal energy of 0.1-1 keV/μm.

Figure 3.21 shows the $p(y)$ for a 4 week exposure to a plutonium beryllium (PuBe) source as measured by a spherical ATED on a log-log scale. This ATED simulated a 2μm diameter spherical tissue phantom. Neutrons and gamma rays from the PuBe source will indirectly ionize the gas inside the active volume via recoils of nuclear interactions in the acrylic shell.

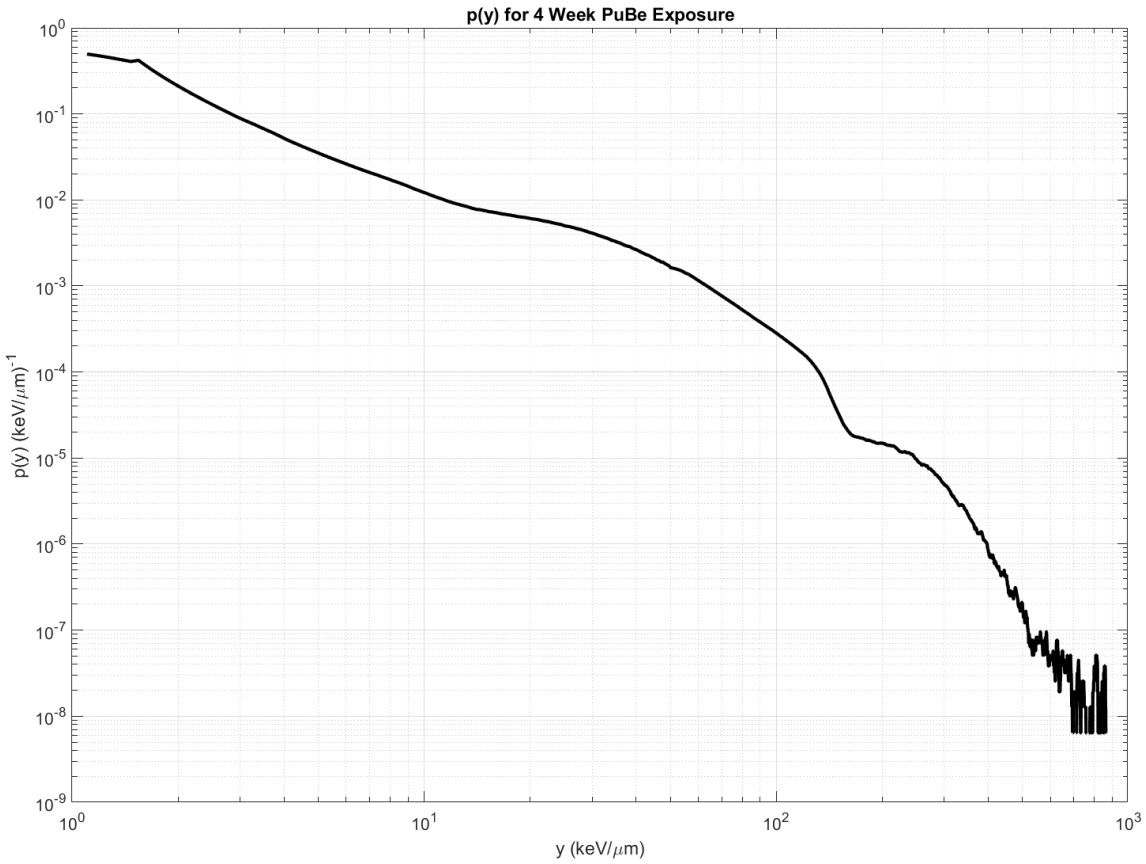

Figure 3.21: The probability density normalized by bin width, $p(y)$, as a function of lineal energy, y, of a four week measurement of a PuBe neutron source plotted on log-log axes. Because the number of counts measured spans several orders of magnitude p(y) is typically shown on a log-log fashion.

The most distinct feature seen in TEPC lineal energy spectrum measurements is the proton edge, seen around 150 keV/ µm. The proton edge is where protons have the highest LET, and thus energy deposition into the gas, as possible. The maximum LET of protons into tissue is 95 keV/µm (147 keV/µm in terms of lineal energy in a sphere) [Rossi, et al., 1996]. Protons in this range have kinetic energy where they are close to stopping, and thus their LET is at a maximum. Recoil protons that cross the full diameter of the active volume and then stop will deposit the maximum amount of energy possible by a proton into the ATED active volume. The proton edge is seen as a rapid decrease in counts in a small increase in lineal energy. It arises precisely because the contribution of counts by proton recoils suddenly stops at a lineal energy of 147 keV/µm. This feature is seen in proton dominated radiation fields, as well as in neutron measurements. The proton edge is commonly used as a calibration point.

At lineal energies above the proton edge, less frequent neutron-induced reactions are being measured. These secondary particles are possibly alpha particles, two protons from a single neutron interaction, or recoils of heavy nuclei like C, O, and N. In theory, every species of charged particle will have an edge due to its maximum lineal energy or LET in a particular medium (tissue equivalent gas in the case of ATED). With sufficient statistics, each particle edge looks like a drastic drop in $p(y)$ within a small increase in lineal energy. It is difficult to resolve these edges, even in the most controlled environments. A longer measurement time would eventually resolve these edges, but the above four-week measurement was not able to do so.

An ideal neutron lineal energy spectrum measurement with a spherical ATED will be monotonically decreasing for the entire range of lineal energies. Poor statistics lie at the largest values of lineal energy, around 1000 keV/µm, accounting for the non-monotonic behavior at these lineal energies. The peaks seen in $p(y)$ are the result of the rarest neutron induced events.

Another useful representation of microdosimetric data is the relative dose distribution, also known as $y{*}d(y)$. We define a distribution, $d(y)$, that is proportional to absorbed dose,

$$d(y) = y * p(y), \tag{3.25}$$

[Rossi et. al., 1996]. If $d(y)$ were plotted against y, the area under the distribution would not visually represent absorbed dose. We multiply by the abscissa by *y* again and obtain,

$$y * d(y) \; = \; p(y) \; * \; y^2. \tag{3.26}$$

When 3.25 is plotted in a semi-log form, the area under the curve delimited by any two values of *y* is proportional to the fraction of dose delivered by events with lineal energies in that interval [Rossi et. al., 1996]. With this representation of the data, we can visually interpret the intervals of lineal energy and determine the relative contribution of particles in that lineal energy interval to total absorbed dose.

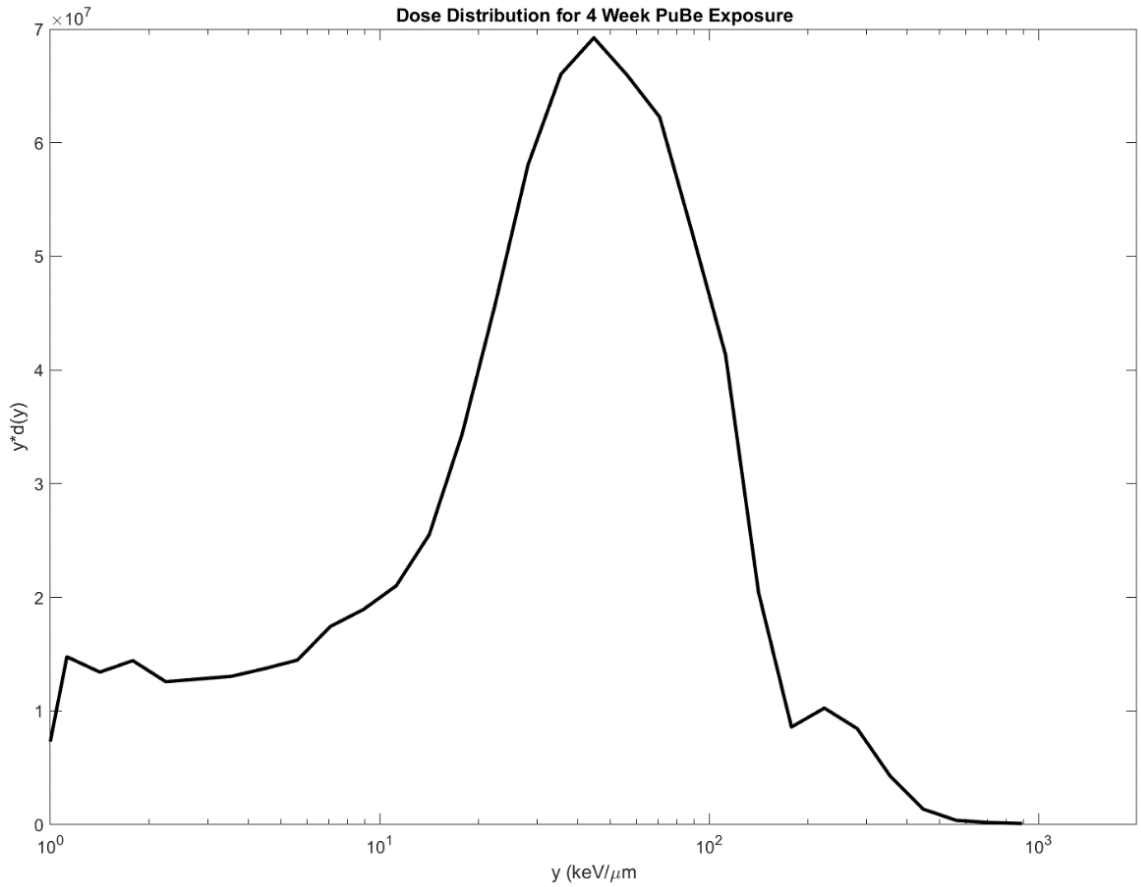

Figure 3.22: The relative dose distribution for the 4-week measurement with a spherical ATED measuring neutrons from a PuBe source. We can visually see that most of the dose came from a range of lineal energies between 10^1-10^2 keV/µm.

Figure 3.22 shows the relative dose distribution for the 4-week exposure to a PuBe neutron source shown previously. The maximum seen at 45 keV/µm is the result of the calculation of $y*d(y)$ and shows that most of the dose came from events of this lineal energy. Counts were much higher below 10 keV/µm than the rest of the spectrum, but the corresponding absorbed dose from these interactions is relatively small. This is because these events do not deposit much energy into the detector and their flux was not significant enough for them to be a large contributor to total absorbed dose.

The dose distribution at lineal energies above than the proton edge (147 keV/µm) are the result of the heavier, and rarer neutron-induced heavy recoils as stated previously. Very little absorbed dose came from lineal energies in this range because of how rare neutron-induced heavy particle

recoils are compared to proton recoils. Even though these events individually deposit a significant amount of energy per event, there is simply not enough of them to be a large contributor to total absorbed dose.

It should be noted that the data has been re-binned into bins with logarithmically increasing widths. This process retains the information of the y*d(y) curve, does not add information to the spectrum, and makes the area under the curve at high lineal energies easier to interpret [Gersey, 2018]. Otherwise, the poor statistics at high lineal energies will create numerous peaks that occlude the area under the curve. These peaks are difficult to interpret as the area under them is very small, but the sum of many of them may make a significant contribution to absorbed dose. More discussion on neutron measurements can be found in Chapter 10.

3.11 Calculation of Absorbed Dose and Dose Equivalent

Dosimetric calculations of ATED measurements will result in absorbed dose in tissue or dose equivalent in tissue. The distinction of absorbed dose in tissue as opposed to some other medium is important. Many times, instruments that report dosimetric quantities are not tissue equivalent. These reports are commonly the product of absorbed dose in silicon and some conversion factor into tissue [Pazmandi, et al., 2000]. These conversion coefficients are widely used, but there are significant, non-trivial differences in the response to ionizing radiation of different detecting materials [Banjac, et al., 2019]. This is mainly due to the fact that cross sections of tissue can be very different than the cross sections of other detecting materials.

To calculate absorbed dose in tissue from lineal energy measurements, the mass of gas inside the volume and the amount of energy absorbed are needed. The amount of energy absorbed will be

the product of the mean chord length of the volume and the lineal energy of each measured event. The resulting relationship between measured lineal energy spectra and absorbed dose is,

$$D(y) = y * f(y)\frac{\bar{l}}{m} * 1.602 * 10^{-16}\frac{J}{eV}, \tag{3.27}$$

where y is the lineal energy, $f(y)$ is the number of counts in the bin corresponding to lineal energy y, $\bar{l}$ is the mean chord length, and m is the mass of gas inside the active volume [Rossi, 1996]. The last term on the right is a conversion from electron volts to Joules, so that the units of $D(y)$ will be in Gray. The total absorbed dose is the sum over all lineal energies,

$$D = \sum_y y * f(y)\frac{\bar{l}}{m} * 1.602 * 10^{-16}\frac{J}{eV} \tag{3.28}$$

Dose equivalent is the biologically-weighted quantity calculated from tissue absorbed dose that quantifies biological damage [ICRU, 1983]. Dose equivalent is denoted by H and is calculated as the product of absorbed dose and a quality factor, $Q(L)$ [ICRP, 1991],

$$H = Q(L) * D \quad . \tag{3.29}$$

Quality factor is defined in terms of LET. We can estimate quality factor by using equation (3.11) that states $L = \frac{2}{3}y$. This results in quality factor to be approximated as a function of lineal energy:

$$Q(L) = Q\left(\frac{2}{3}y\right) = \begin{cases} 1 & y < 15\frac{keV}{\mu m} \\ 0.32(\frac{2}{3}y) - 2.210 & \leq y \leq 150\frac{keV}{\mu m}. \\ \frac{300}{\sqrt{\frac{2}{3}y}} & y > 150\frac{keV}{\mu m} \end{cases} \tag{3.30}$$

3.12 Utility of a Red Pitaya Field Programmable Gate Array as a MCA

The Red Pitaya is an open source hardware project designed to replace laboratory measurement and control instruments [Red Pitaya, 2017]. The Red Pitaya itself is a credit card sized, single-board computer that includes a Linux operating system, a field programmable gate array (FPGA), 14-bit ADCs and DACs, two radio frequency (RF) inputs and two RF outputs. The default software enables use of the Red Pitaya as an oscilloscope, spectrum analyzer, signal generator, and a LCR meter [Red Pitaya, 2017]. These features have been repurposed and programmed the Red Pitaya into a dual-input multi-channel analyzer (MCA) as the spectrometer module in the ATED instrument. The Red Pitaya replaces the two Amptek MCAs, which have a single input each, and effectively saves $8000 in the production of a single ATED instrument.

In addition to its many features, what makes the Red Pitaya attractive from an instrument development point of view is the FPGA which can be programmed to function as a lineal energy spectrometer. Code was written in C that used the built-in oscilloscope functions to repurpose the Red Pitaya to operate as a dual-input MCA. For TEPC measurements it is best practice to look signals at two different gains. This allows measurements to cover the entire range of lineal energy and ensure sufficient resolution at low lineal energies [ICRU, 1983].

Benefits of the Red Pitaya include: low cost, complete transparency in how signals are processed, two input channels, an online support community, and independent data storage. Disadvantages include: low processing power, minimal technical support, and unknown resilience to radiation damage. An online community has developed many projects addressing a large range of scientific and technical objectives.

Custom MCA software was written in the C language by utilizing the built-in oscilloscope functions and triggering on pulses above a set threshold. Accepted pulses are then organized by height into 1024 channels for both inputs (high and low gain channels). The frequency of

triggering is dependent on the frequency of pulse above a set threshold. Every time the program is triggered, it will read in ~3us worth of voltage values from both inputs, which covers the entire pulse from both CR-210 Gaussian shaping amplifiers. The height of the signal is found, which determines what channel will receive a count.

The high and low gain measurement of 400 MeV/n oxygen made by a Red Pitaya MCA is shown in **Figure 3.23**. The counts have been normalized by bin width and the bin number has been calibrated to lineal energy. What is immediately obvious is the difference in resolution between the two peaks. The low gain channel extends to much larger values of lineal energy compared to that of the high gain channel. The lower resolution of the low gain channel spreads the peak over a wider range of lineal energies, and when normalized by bin width has a smaller amplitude. Regardless, the number of counts in each curve of both peaks is the same without the normalization seen in **Figure 3.23**. This indicates that the only difference between the two gain channels is resolution. The high gain channel in red shows statistical fluctuations throughout the structure of the peak and includes the noise regime at low lineal energies. At the maximum values of lineal energy in the high gain channel there is pulse pile up due to the non-linearity of the Gaussian shaping amplifier at these voltages. The low gain channel in blue only shows the general shape of the peak, and does not include the noise portion of the spectrum.

The results shown in **Figure 3.23** are one example of a multitude of measurements made by the Red Pitaya MCA during testing and calibration. It has been shown to be an effective MCA for the ATED instrument and is now fully integrated into current ATED models.

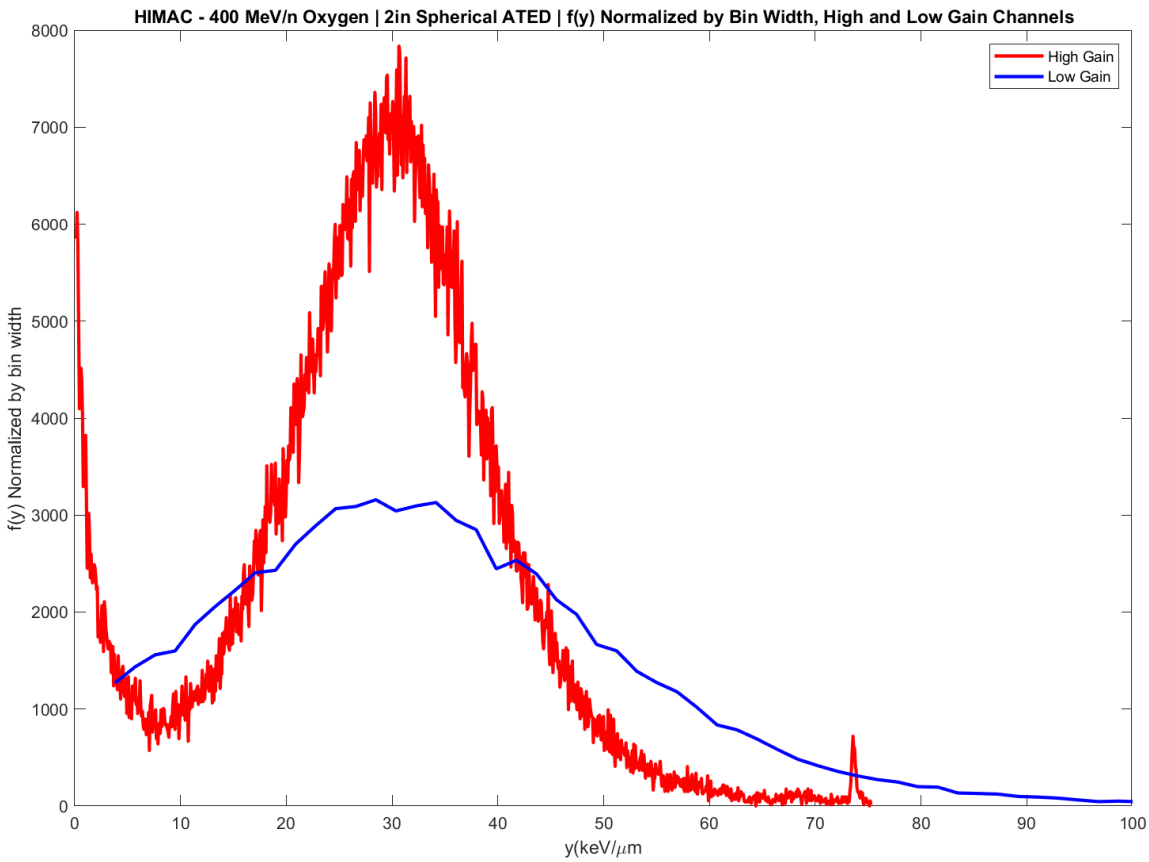

Figure 3.23: Measurement of counts as a function of channel number for 400 MeV/n Oxygen at HIMAC as measured by a Red Pitaya MCA. Red is the high gain amplification channel, and blue is the low gain amplification channel.

One disadvantage of the Red Pitaya is its low processing power. The Red Pitaya uses an ARM Cortex-A9 dual core 32-bit processer which cannot handle large amounts of computations quickly [Red Pitaya, 2017]. If the processing time of signals is too large, then signals may not be measured and thus information will be lost. The time that it takes for the formation of the pulse in the detector itself and the processing of the signal through its various components is called dead time [Tsoulfanidis, 1995]. If another particle is detected in this time, it will not be measured. The dead time of the Red Pitaya MCA by itself needs to be quantified to test its viability in different environments. The dead time of detector is bypassed by using a pulse generator that sends signals to the Red Pitaya MCA directly. Dead time is calculated by the MCA software by tracking the time it takes to process each pulse divided by the total acquisition time.

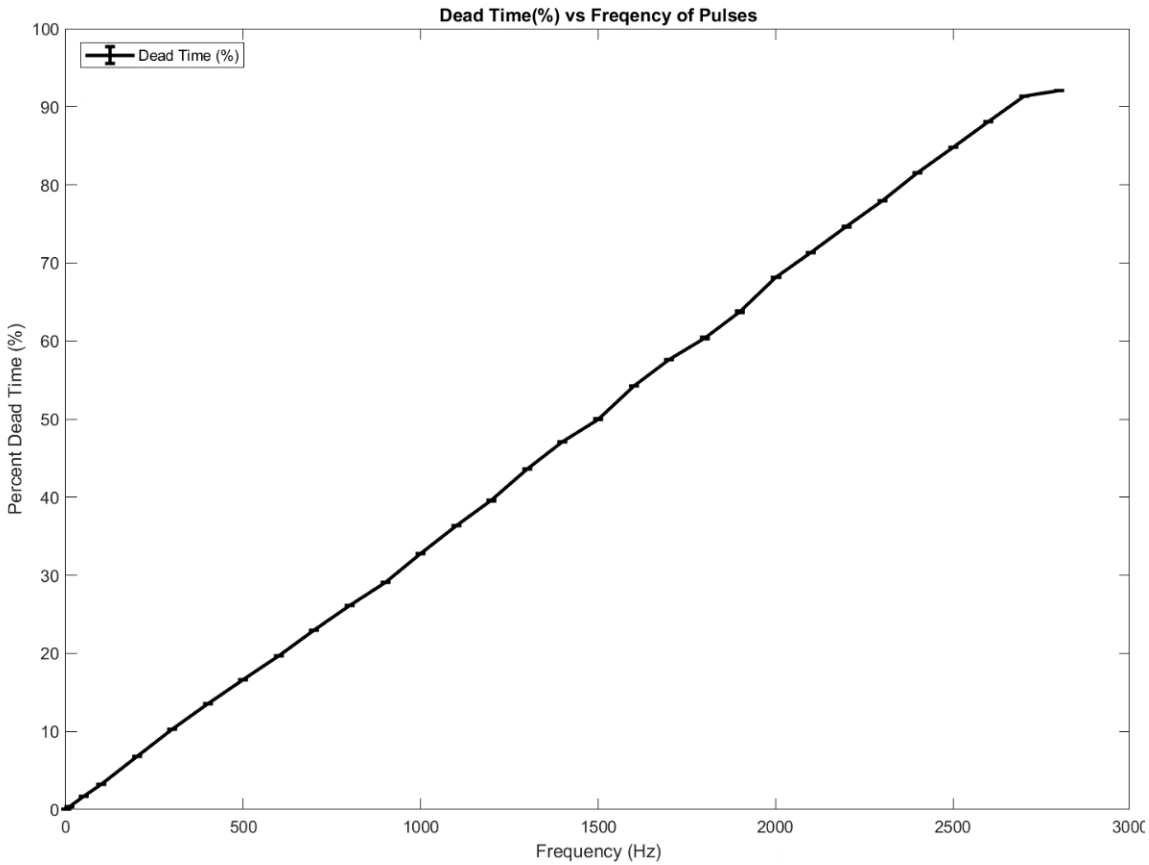

Figure 3.24: Percent dead time as a function of frequency for the Red Pitaya MCA. Dead time was calculated by the Red Pitaya MCA software by taking the time to digest pulses divided by the total acquisition time. Multiple measurements were made and uncertainty is quantified as the standard deviation.

Figure 3.24 shows the result of sending evenly spaced pulses at varying frequencies into the both inputs of the Red Pitaya MCA. The linear trend toward 2700 Hz is shown. Up to this frequency the Red Pitaya is measuring all incoming pulses. This is because dead time for evenly spaced pulses should be directly proportional to the input frequency. At 2800 Hz the data no longer follows this linear trend, and thus is not reading all pulses input to the system. This corresponds to a dead time of 357.10 ± 2.12 μs for each pulse. As stated previously, the width of each pulse is approximately 3 μs.

The consequences of this dead time in the MCA means that if a particle were to be detected less than 350 μs after a preceding particle, the Red Pitaya MCA would not record it. In reality, ionizing radiation will not be evenly spaced in time while being measured.

At the HIMAC, particles enter ATED 2-inch spherical detectors at a fluence of ~100 particles/cm^2 for each particle spill (~1s). This corresponds to a frequency of ~2020.8 Hz or a particle entering the sphere every 493 ± 17.1 μs. Uncertainty is quantified as the standard deviation a Poisson distribution around this point, as shown in **Figure 3.25**. Although this fits inside the confines of the Red Pitaya MCA dead time, the widely accepted maximum of dead time is typically 5%. At these frequencies the Red Pitaya MCA will experience dead time percentages up to ~70% during a single spill. The time between pulses will artificially lower the dead time calculated by the MCA software. We have thus concluded that for particle accelerator work, the Red Pitaya MCA is not suitable. A smaller fluence could conceivably be used, but time is limited at particle accelerators and a faster, more expensive MCA would be able to keep dead time at a minimum. As a result, we continue to use the Amptek 8000D MCA for particle accelerator experiments.

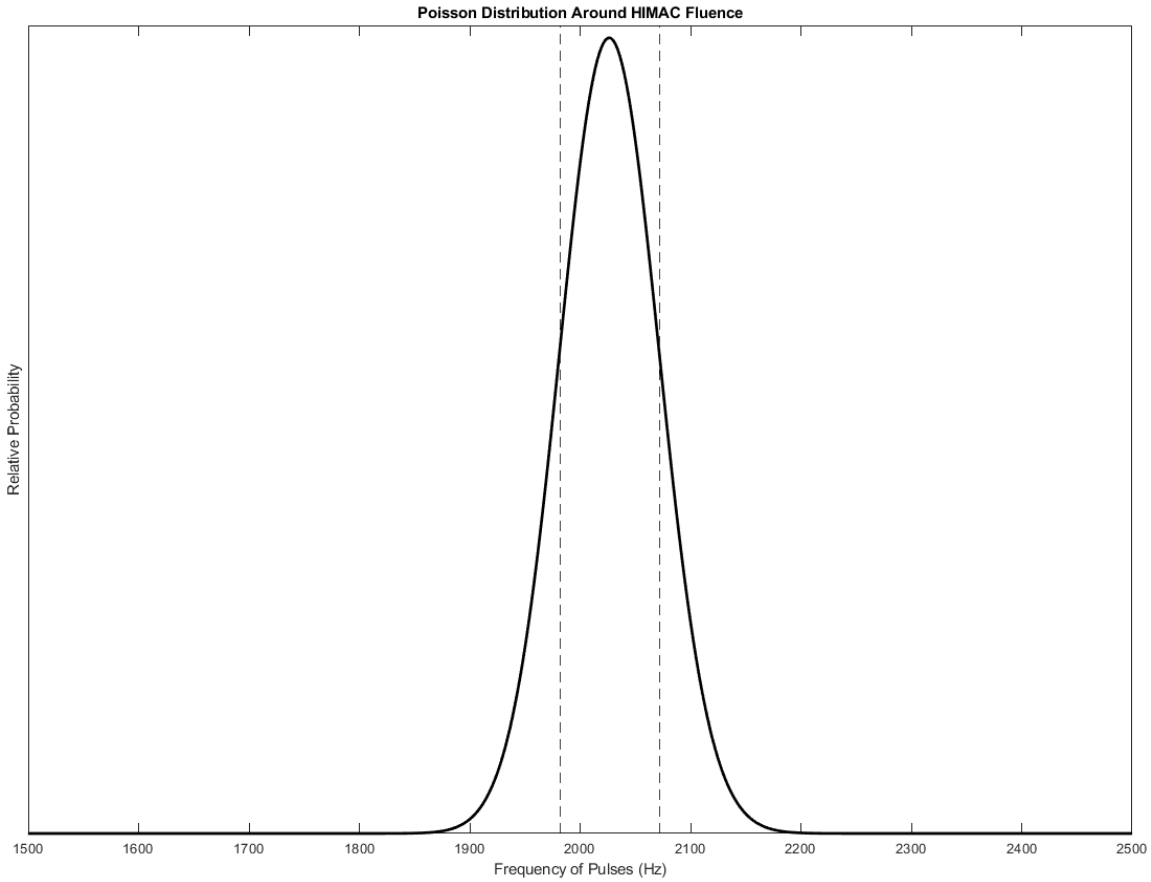

Figure 3.25: A Poisson Distribution around the frequency of particles measured at HIMAC (2026.8 Hz). The calculated standard deviation around this point yields the uncertainty in this value.

In space we do not expect the flux of particles to approach these intensities, except during a massive solar particle event [Benton, 2004]. Measurements of these events are important in the understanding of these phenomena. The Red Pitaya MCA could possibly underperform during a solar event in space. Absorbed dose values would then be less than what was actually received by astronauts. However, based on the length of dead time during a massive SPE, corrections could be made to the measurements.

Where the Red Pitaya FPGA boards are most useful are in ATED units designed for use in aviation. The flux of particles in the atmosphere is low enough that the Red Pitaya can easily stay under 5% dead time. During a solar event, the atmospheric reported flux of particles increases by 70% [Benton, 2004]. This increase in the particle flux in the atmosphere will not significantly

increase dead time. In addition, the low-cost of the Red Pitaya MCA is ideal to distribute many ATED instruments across several commercial, military, and private aircraft.

CHAPTER IV

CALIBRATION METHODS FOR THE ACTIVE TISSUE EQUIVALENT DOSIMETER

Calibration and characterization experiments on the various version of ATED described in this work were carried out at the HIMAC and with radioactive sources. The HIMAC provides high energy carbon nuclei for cancer therapy and other ions at high energies for experimental research [NIRS, 2006]. The energy of particles at HIMAC are similar to those found in the peak of the GCR energy spectrum (10^2-10^3 MeV/n). The mono-energetic beams from protons and heavy ion accelerators serve as the best means for calibration of ATED because the energy of the ion beams are known to a high degree of accuracy. Since the energy and species of the incident particles are known the LET, and lineal energy can be calculated and used for calibration of ATED.

Neutron and gamma ray measurements are an alternate method to calibrate ATED. This method is less expensive than calibrating to charged particle beams because it does not require traveling to them or the cost of operating them. Calibration of ATED using neutron, use of the electron edge as a calibration point, the method for combing spectra measured using two amplification gains, and the use of logarithmically increasing bin-widths in the relative dose distribution for neutron measurements are described in the following sections. The physics of neutron and gamma

measurements with ATED and the interpretation of their measurement is discussed in Chapter 3.9 and 3.10.

4.1 Calibration with Charged Particle Beams at HIMAC

To calibrate ATED over the range of lineal energy to which it is sensitive, ATED is exposed to a number of different mono-energetic heavy ion beams of different charge and energy, and hence of different LET and lineal energy. Each ion and energy will correspond to a different calibration point for ATED. These calibration points are used together to create a calibration function to change bin number into a corresponding lineal energy. Calibration functions from measurements at HIMAC consistently have R^2 values of nearly one. Measurements for calibration are done with no target between the accelerator beam port and the detector, a configuration known as the nominal, or bare, beam.

Figure 4.1 shows counts as a function of bin number for 400 MeV/n oxygen measured with a 2-inch spherical ATED, normalized to peak height. This ATED had two gain channels. The high gain channel is shown in red and low gain channel is shown in blue. To match a bin number to lineal energy, the nominal beam measurement data is subjected to an iterative Gaussian fit. The centroid of the resulting Gaussian fit is the bin number that corresponds to the LET of the beam itself. The LET of 400 MeV/n oxygen is 20.0 keV/μm, which corresponds to a lineal energy of 30 keV/μm for a sphere. Thus, the centroid of the fit will correspond to 30 keV/μm. This bin number and corresponding lineal energy becomes part of a calibration function. This beam was chosen for this example because it produces a peak in both gain channels. Other particle beams may produce a peak in only one gain channel or no peak at all. Multiple beams are used to ensure both gains are calibrated.

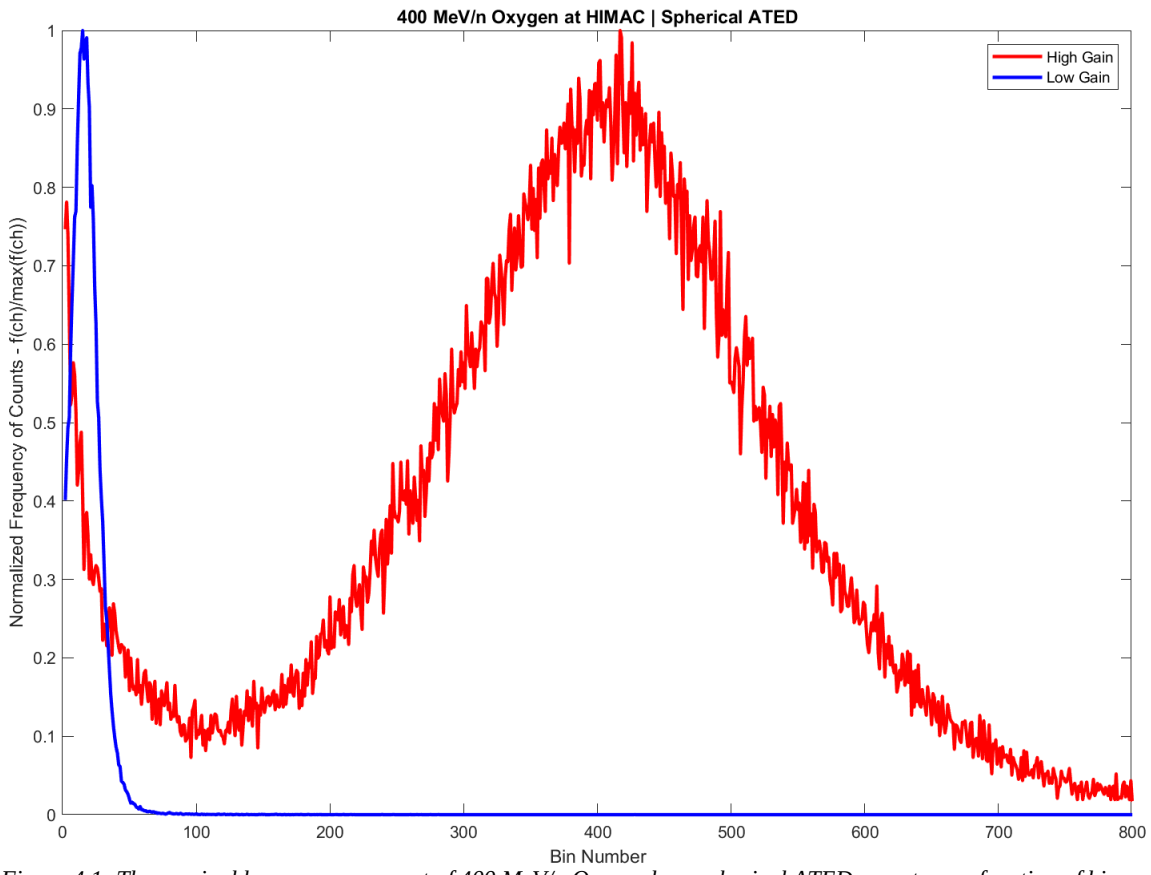

Figure 4.1: The nominal beam measurement of 400 MeV/n Oxygen by a spherical ATED, counts as a function of bin number normalized to peak height. The high gain channel is shown in red and the low gain channel shown in blue.

Figure 4.2 shows the lineal energy calibration points as a function of bin number from 500 MeV/n iron, 400 MeV/n oxygen, and 400 MeV/n carbon for both gains measured by a spherical 2" ATED. These beams have lineal energies of 303, 16.8, and 30.0 keV/µm, respectively. The 500 MeV/n iron could only be resolved in the low gain channel and the 400 MeV/n carbon could only be resolved in the high gain channel. A line is iteratively fit to the calibrations points and the resulting equation of the line is the calibration function. This calibration function converts bin number in each gain channel into lineal energy. Uncertainty in this fit would be the FWHM of the Gaussian fit, but is not included here.

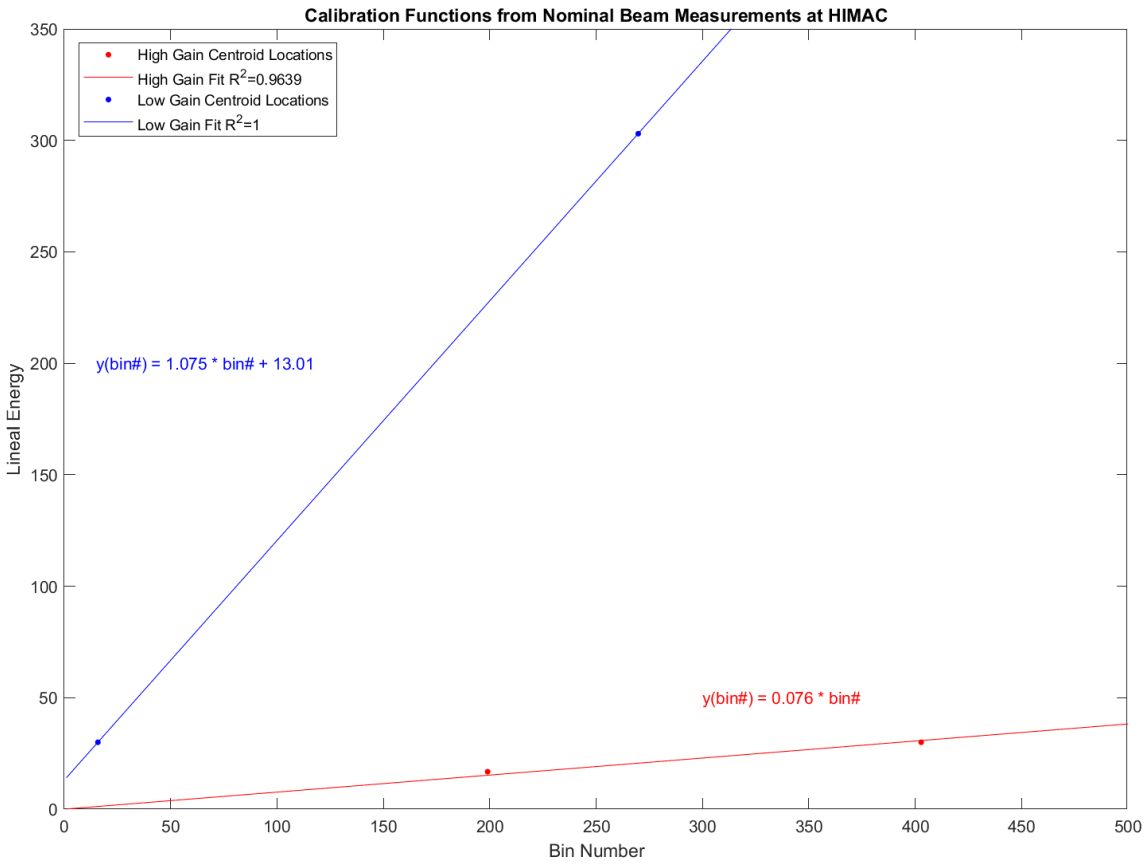

Figure 4.2: Calibration functions for the high and log gain channels from three separate measurements taken at HIMAC. The dots represent the centroids of Gaussian fits for nominal beam measurements by 500 MeV/n iron, 400 MeV/n oxygen, and 400 MeV/n carbon.

4.2 Calibration Using Neutrons

TEPCs are often calibrated with internal alpha-emitting radioisotopes that are built into the detector itself. These alpha particles are mono-energetic and provide precisely one data point for calibration. The ATED can use alpha-emitting radio isotopes for calibration, but having a radioactive isotope inside the detector head is a logistical problem when traveling across international borders or entering high security government facilities. Because of this, no such mechanism for an internal calibration source for the ATED was developed. An alpha particle source can be temporarily fixed inside the ATED for calibration but requires the detector head to

be disassembled. Some ATED detector heads are permanently sealed and cannot be disassembled without destroying the instrument.

Calibrations done at charged particle beams like HIMAC are preferred because they provide several calibration points across a wide range of lineal energy (see Chapter 8). However, using particle accelerators for calibration is not always possible. Using charged particle beams often requires travel and can they can only be accessed at very specific times.

Calibration using a neutron source has many advantages because it can be done in the lab and the detector head does not need to be disassembled. The Oklahoma State University Radiation Physics laboratory has access to a Plutonium-Beryllium (PuBe) neutron source. A measurement of PuBe neutrons by ATED gives a single calibration point. The disadvantage to using a PuBe source for calibration is a long measurement time, a minimum of 24 hours for a ~200 mCi source.

The ATED measures the secondary charged particles from neutron interactions with the dense plastic shell that surrounds the active volume (see Chapter 4.6). The most likely interaction for neutrons incident on the atoms of tissue are elastic recoils with hydrogen atoms [ICRP, 1983]. Elastic neutron collisions with hydrogen eject protons into the ATED active volume, where they are measured. Calibration with PuBe neutrons relies on finding the location of the proton edge. The proton edge is the value of lineal energy that coincides with the maximum LET of a proton in tissue (~100 keV/μm). As stated in Chapter 4.8, the proton edge in the lineal energy spectrum appears as a significant decrease in counts over a small interval of bins as lineal energy increases.

Figure 4.3 is the count spectrum as a function of bin number from a PuBe measurement. This data was taken by a 2-inch spherical ATED simulating a 2 μm diameter sphere of tissue. This ATED uses two amplification channels, each with 1024 bins. The first ten bins were omitted via a lower-level discriminator (LLD) set on the MCA software. The LLD is also responsible for the lower number of counts in the first bin, seen at the very left of the spectrum. Poor statistics at the

highest bin numbers result in spikes in the spectrum. Aside from these two features, the count spectrum has a monotonically decreasing trend expected for a neutron measurement.

The vertical line represents the bin where the proton edge is located. Statistical fluctuations spread the the proton edge slightly and thus it does not have a precise position. The bin that lies directly in the middle of the steep decrease, on a log-log scale, is the accepted calibration point for the proton edge [ICRU, 1983]. Uncertainty for this calibration has not been quantified. A calibration function can now be made by,

$$y(bin\ number) = \frac{proton\ edge\ lineal\ energy}{proton\ edge\ bin\ number} * bin\ number, \tag{4.1}$$

where y is the lineal energy. The proton edge lineal energy will change depending on the geometry of the active volume and where incident radiation is coming from. In the case of a sphere, the lineal energy of the proton edge is 147 keV/μm.

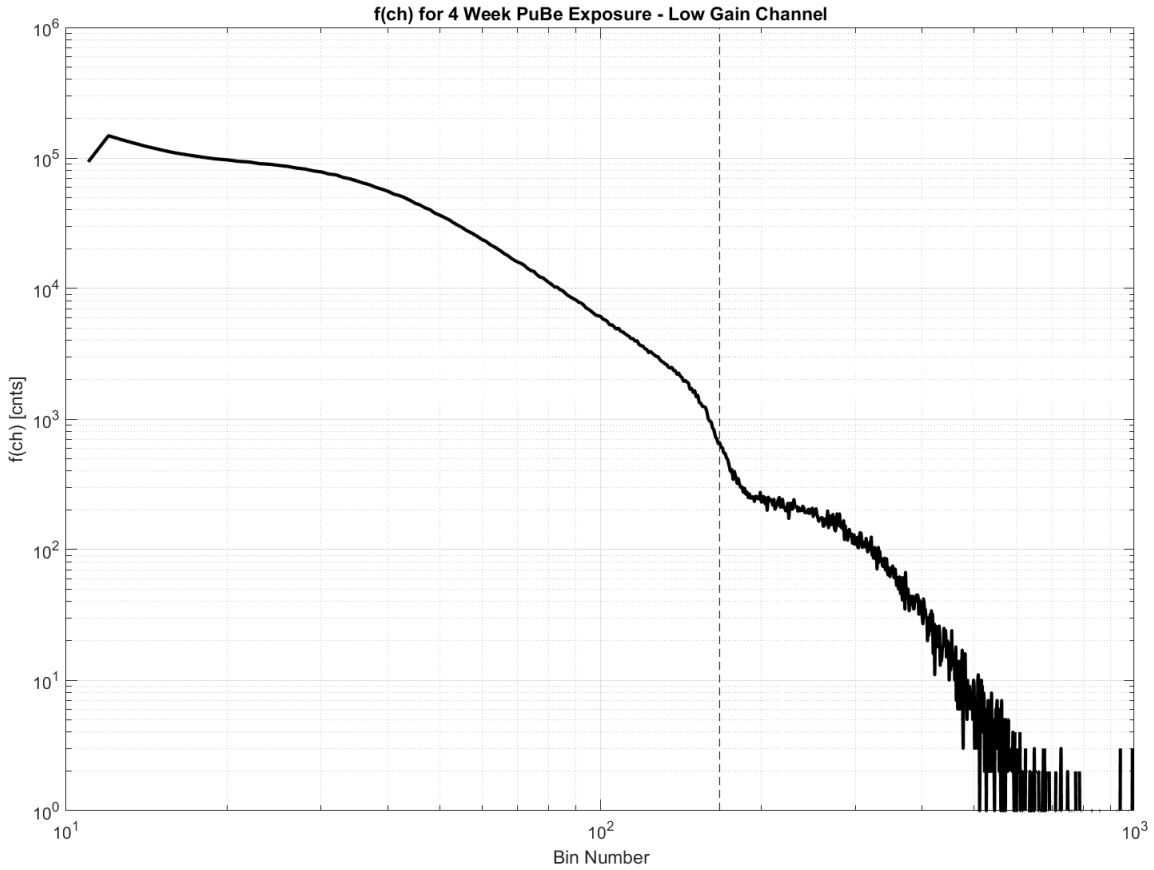

Figure 4.3: The low-gain channel of a measurement of neutrons from a PuBe source. The measurement was taken over four weeks to ensure the maximum amount of resolution of the proton edge. The vertical black dotted line is the bin value of the proton edge. This is then used for calibrating the low gain channel.

The location of the proton edge in **Figure 4.3** is bin number 167. Equation (4.1) can be used for the low gain channel,

$$y(i) = \frac{147\ keV/\mu m}{167} * \ i = 0.880 \frac{keV}{\mu m} * i \tag{4.2}$$

where i is the bin number. Equation 4.2 is multiplied through all bins to convert bin number into lineal energy.

When one amplification channel is used, the proton edge serves as a suitable calibration across all bins in the spectrum. In the case where two amplification channels are used, the low gain channel uses PuBe measurements for calibration while the high gain channel cannot. This is because signals are at an amplification such that the proton edge is beyond the range of measured lineal

energies in the high gain channel. Other means to calibrate the high gain channel are discussed in the next section.

4.3 Calibration Using Gamma Rays

Similar to the proton edge, the electron edge is the maximum value of lineal energy for an electron. It has a relatively low lineal energy (12 keV/μm for a sphere) and is used for high gain channel calibrations. Gamma rays are also emitted from a PuBe source. In fact, neutron radiation is invariably associated with gamma radiation [Rossi, et al., 1996].

In a mixed neutron-gamma radiation field, the electron edge placement is misleading, as depicted in the conceptual count spectrum of **Figure 4.4**. The superposition of electron, proton, alpha, and heavy ion ($Z > 2$) counts will superficially shift the electron edge to lower bin numbers. The true location of the electron edge is occluded because of the rapid decline in counts where the electron edge is located. Using the electron edge as a calibration point in a mixed neutron-gamma radiation measurement propagates error though calculations of absorbed dose.

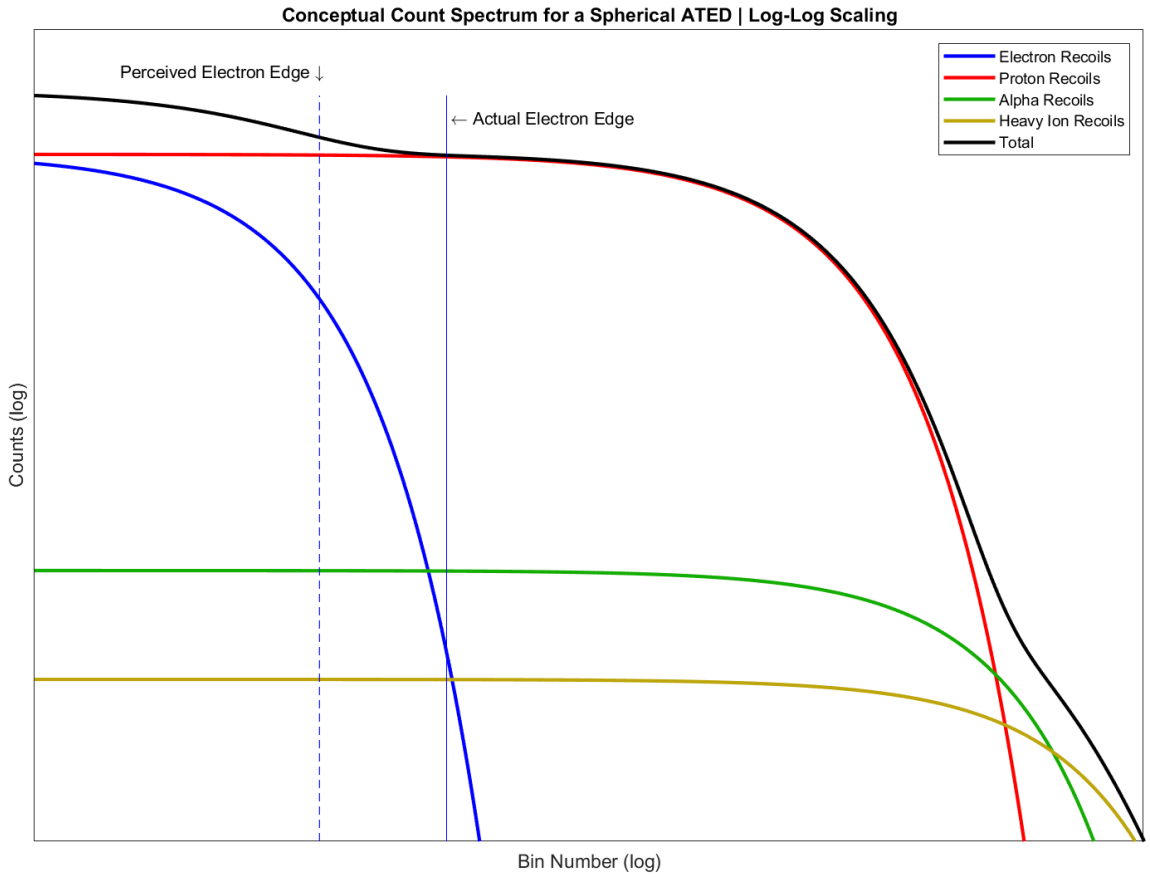

Figure 4.4: A conceptual count spectrum of the measurement of a mixed gamma-neutron radiation field by a TEPC. The vertical blue lines represent the perceived and actual electron edges.

To avoid this problem, measurements of pure gamma-emitting radioisotopes are made. This can done with common sources like Cobalt-60 and Caesium-137. Multiple isotopes can be used together as long as only their gamma componet is measured. In this way, only electron recoils from photon interactions with the tissue equivalent plastic are measured. Enough statistics to refine the electron edge are obtained in ~24 hours for ~10 µCi of gamma emitting radioisotopes. This method has the same advantages as using a PuBe source, as discussed above.

The high gain channel of a PuBe (red) and a gamma (black) measurement, on a log-log scale measured by the same spherical ATED are shown in **Figure 4.5**. The spectra have been normalized to their maximum height. Both measurments were taken with the same gain settings. Here, the first 15 channels have been omitted by an LLD for both measurments. The Gaussian-shaping amplifier becomes non-linear above bin ~900, which accounts for the peaks seen at the

highest channels in the PuBe measurement. This phenomenon is called pulse pile-up, and is where counts are no longer linearly organized [Datlowe, 1977]. These counts are ignored when both gain channels are combined (see next section). The gamma measurement drops off well before this non-linear region. The proton edge is not seen in the high-gain measurement of the PuBe source and thus we must rely on the electron edge for calibration.

The perceived electron edge from the PuBe lies at the red dotted line. The gamma measurment shows the location of the electron edge with the black dotted line. Similar to the proton edge, the electron edge is subject to statistical variation and thus does not have an precise location. The accepted value of the electron edge is the middle of the steep drop in counts, on a log-log scale, just as the proton edge was. Equation (4.1) is adapted for the electron edge for calibrating the high-gain channel.

The low-gain channel does not use the electron edge as a calibration point. The low resolution at these small lineal energies does not clearly show a location of the electron edge. In a system with only one amplification channel, and proper resolution, the electron edge serves as an additional calibration point that improves the quality of the calibration function.

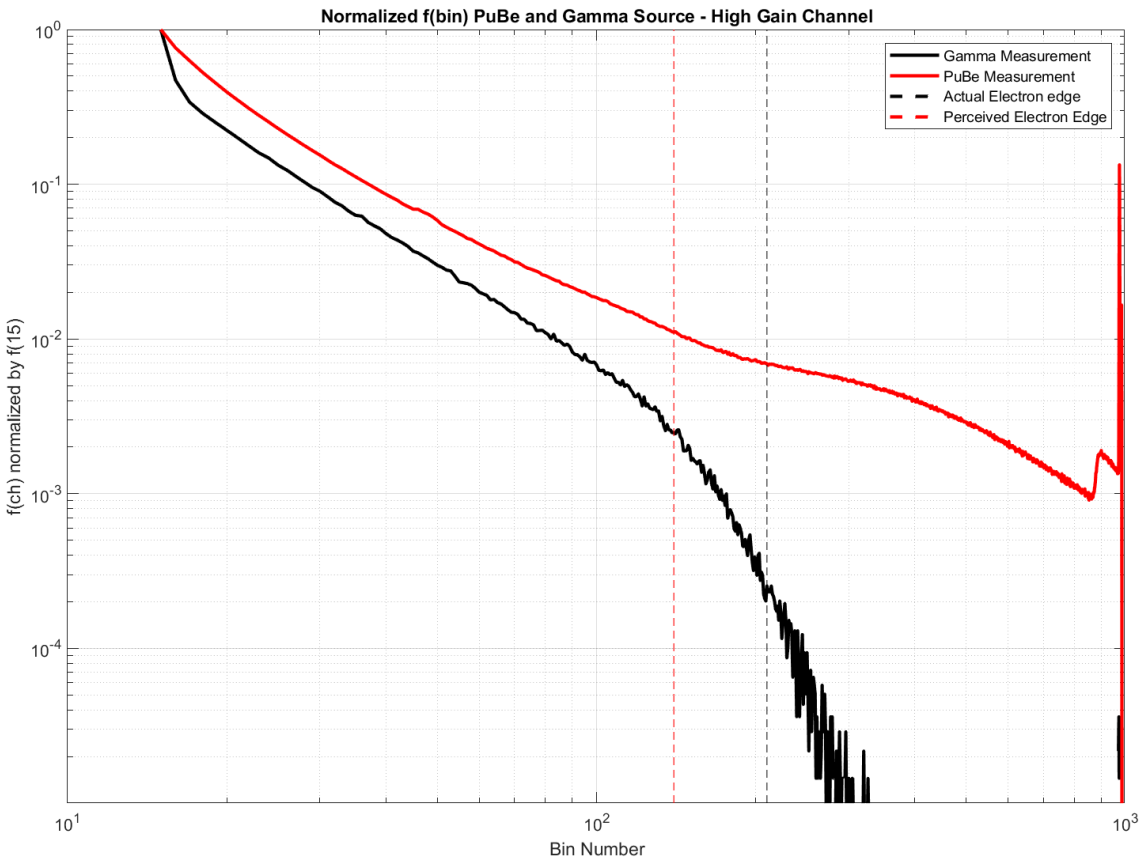

Figure 4.5: The high gain channel count spectra for a PuBe (red line) and gamma (black line) measurement. The dotted lines show the location of the electron edges for their associated measurement.

Table 4.1 shows the bin values where the electron edge locations were identified in **Figure 4.5**, the resulting calibration functions, and the percent difference between the two measurements. In this example, there is a 40% difference in the calibration between the two measurements. This shows that using the electron edge as a calibration point in a mixed neutron-gamma field will propagate significant error though calculations made by ATED.

	PuBe Measurement	Gamma Measurement	Percent Difference
Bin Number	140	210	40.0%
Lineal energy per bin	0.086 keV/µm/bin	0.057 keV/µm/bin	

*Table 4.1: The bin values of the electron edge location for the PuBe and Gamma measurement shown in **Figure 4.5** and the percent difference between the two.*

4.4 Combining Spectra Measured at Different Gain Settings

Current ATED models have adapted the use of two gain channels. The use of two gain channels allows for sufficient resolution of lineal energies below ~20 keV/µm while also covering the entire range of relevant lineal energies. To ensure proper representation of measurements with two gain channels each gain needs to be properly put together. One challenge combining spectra measured at different gain setting is the differing bin-widths of the two spectra. Low gain channels have more counts per bin for the range of lineal energies that overlap with high gain channels, since the bin-width of low gain channels are larger in terms of lineal energy than that of high gain channels. Typically, high gain channels have a resolution (bin-width) of about 0.1 keV/µm and low gain channels have a resolution of about 1 keV/µm. Dividing the counts in each gain channel by bin-width in terms of lineal energy makes the two gain spectra overlap and allows them to be combined.

Figure 4.6 shows the count spectrum as a function of lineal energy for both gain channels, normalized by their respective bin-widths, from a PuBe neutron measurement. In this graph there is a point, at 14.8 keV/µm where the two channels cross. The bin numbers that most closely match this lineal energy for both gains are the points where they are combined. Bins in the high

gain channel after this crossing, and bins in the low gain before it, are neglected in the calculation of absorbed dose.

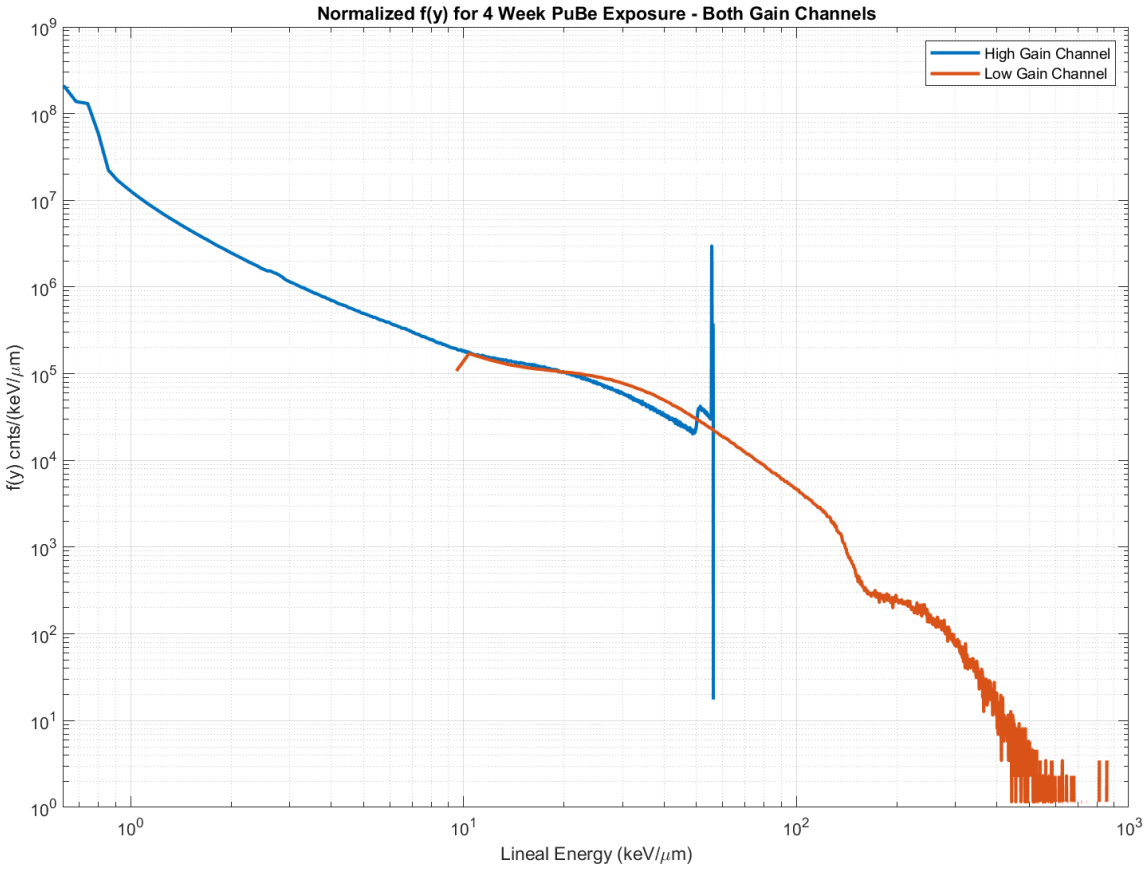

Figure 4.6: Both the high-gain and low-gain channel count spectra from the previous PuBe measurement, normalized by bin-width. The intersection of the two spectra is the point where they are combined.

It is possible that the two gain channels do not intersect. This happens when the gain settings between the two channels are too far apart, due to improper calibration of either gain channels, or when noise causes the spectra to diverge. Optimally, the two gains should be combined in the range of 15 to 50 keV/µm [Gersey, 2018]. The only way to ensure that the two gains are set properly is to empirically test them through calibration.

Figure 4.7 is the probability distribution normalized by bin width from a PuBe neutron measurement with both gains combined. When both gains are put together, the representation of the measurement is complete. A detailed description of this plot, and the associated relative dose distribution, are discussed in Chapter 4.10.

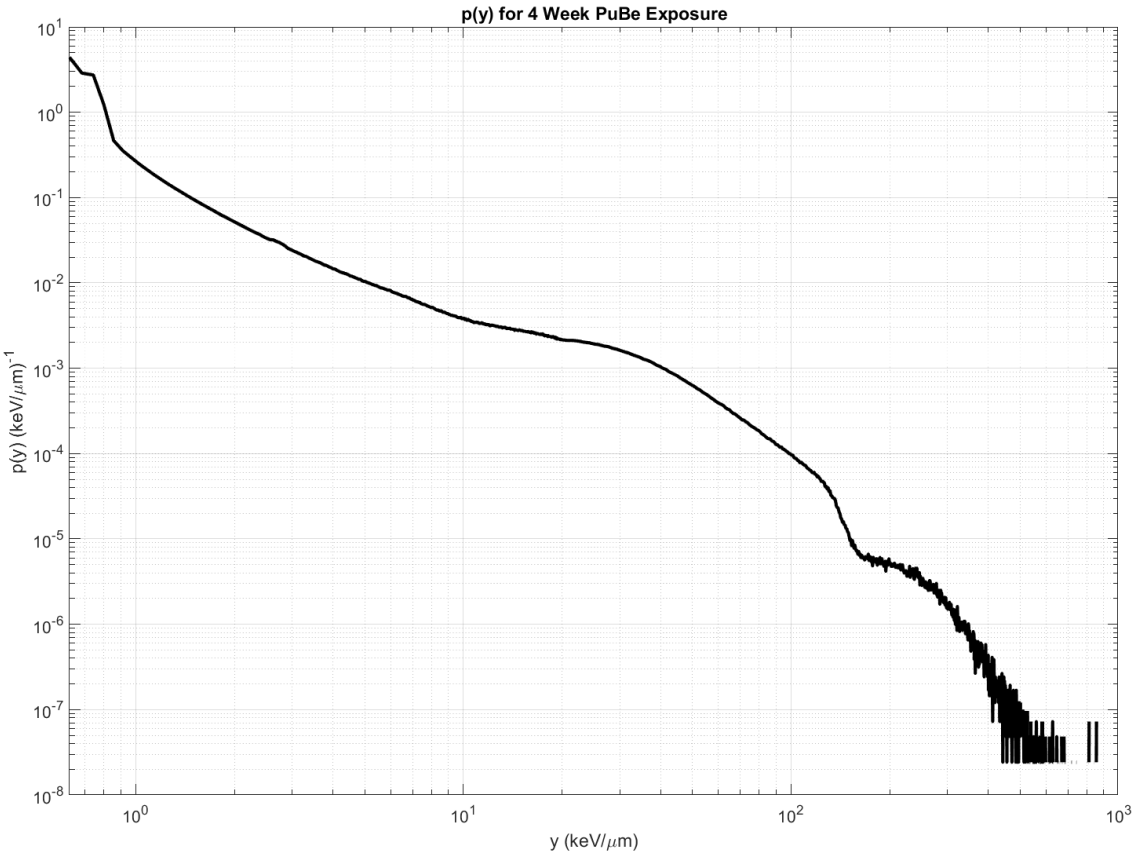

Figure 4.7: The probability distribution, normalized by bin-width, for a PuBe neutron measurement. Both amplification gains have been combined.

4.5 Logarithmically Spaced bins

Figure 4.8 shows the relative dose distribution from a measurement of neutrons at LANSCE, and discussed in more detail in Chapter 11. This plot illustrates the advantages of using logarithmically-spaced lineal energy bins. Neutron measurements almost always benefit from logarithmically spaced bins for the relative dose distribution because of significant statistical fluctuations in the data at high lineal energies. The original linearly-spaced data has many peaks at lineal energies from 30 up to 600 keV/μm. This is because the statistics in this range of lineal energy are poor and the calculation of relative dose distribution intensifies fluctuations in the data. The peaks in the relative dose distribution are difficult to interpret. The area under them is small, but their sum over a range of lineal energies may make a significant contribution to

absorbed dose. Also, the decreasing space between bins due to the log-scaled abscissa compounds this problem.

Measured counts are re-binned into a new set of bins that increase in their mean lineal energy logarithmically (red line). This process retains the information of the dose distribution curve, does not add misleading or additional information, and makes the area under the curve easier to interpret where there are poor statistics [Gersey, 2018]. Not every dose distribution benefits from the use of logarithmically spaced bins. Neutrons measurements often do so because of the poor statistics at the high lineal energies.

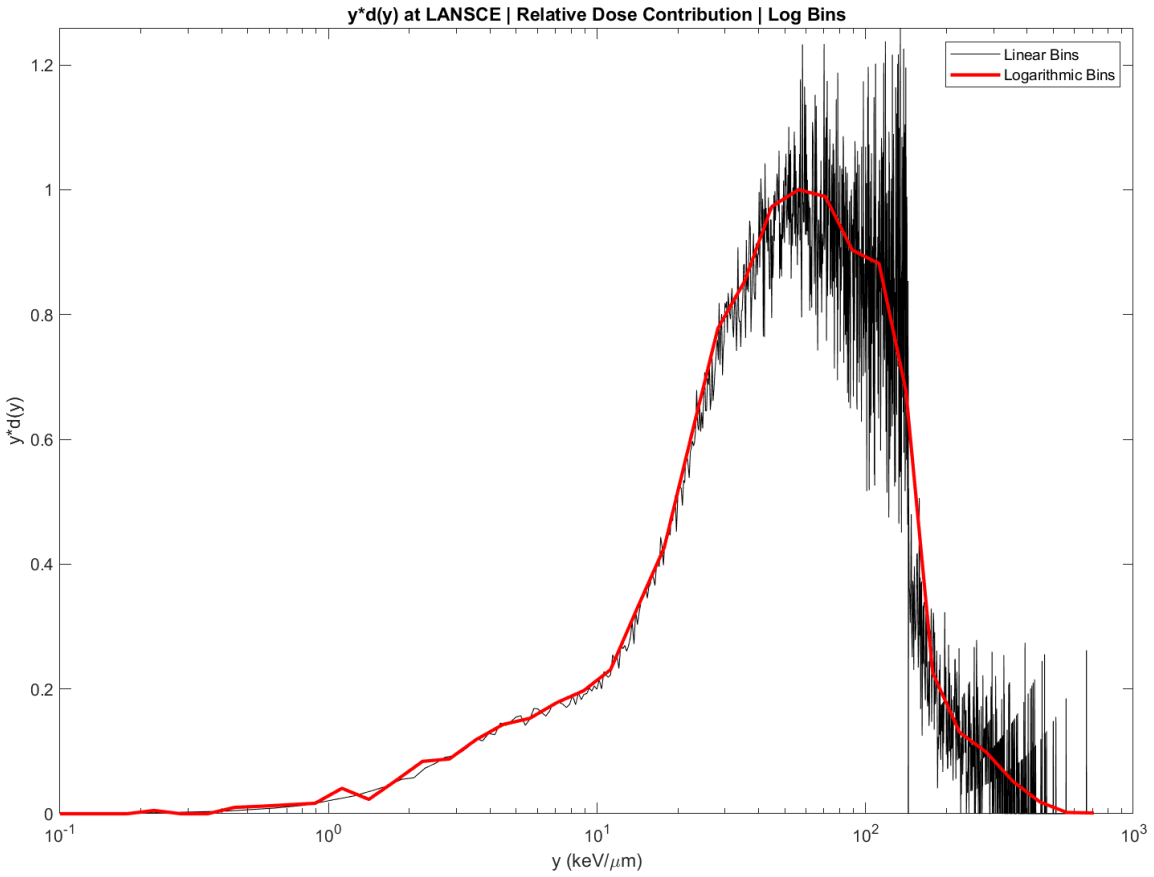

Figure 4.8: The relative dose distribution as measured at LANSCE. Linearly spaced bins (black) and logarithmically spaced bins (red) are shown.

CHAPTER V

CONVERSION OF LINEAL ENERGY MEASUREMENTS INTO LINEAR ENERGY TRANSFER

TEPC measurements take the form of a pulse-height distributions as a function of lineal energy and reflect energy deposition in the irradiated volume [Kellerer, 1972]. Lineal energy measurements are closely related to the energy deposited in living cells by ionizing radiation, but linear energy transfer (LET) is the standard quantity for dosimetric calculations [ICRP, 1991]. In this chapter, we show two different methods that convert lineal energy spectra into corresponding LET spectra. The purpose in exploring these methods is to convert measured lineal energy spectra in LEO into corresponding LET spectra. The results of the converted spectrum are reported in Chapter 12. This chapter serves as the derivation and discussion of the two methods used.

5.1 Motivation to Convert to LET Spectra

The spectral information from many radiation detectors come in the form of an LET spectrum. Few detectors measure lineal energy, and often their measurements cannot be directly compared

to other instruments. Computer programs can accurately calculate LET, but simulating lineal energy is much more difficult. Converting measured lineal energy measurements into corresponding LET spectra is desirable in that it allows for the direct comparison of TEPC measurements with detectors that directly measure LET (e.g. silicon spectrometers, CR-39 PNTD). It also permits the direct calculation of dose equivalent as defined by ICRP 60 [ICRP, 1990]. We will use the preceding LET conversions in Chapter 12 to test their validity in the space radiation environment.

Uncovering the LET information in TEPC measurements requires consideration of the geometry used. Spherical TEPCs have a relatively simple conversion to LET for an isotropic field of radiation. However, for cylindrical TEPCs no such conversion exists. The geometric conversion is a straight-forward derivation, but is limited to spherical geometries [Rossi et. al., 1996]. The Kellerer method is a mathematically intense approach that is not well understood by the author of this dissertation. Only the result of the Kellerer method is being tested for its viability to convert ATED lineal energy measurements into LET spectra. The advantage of the Kellerer method is that it is not limited to a single geometry [Kellerer, 1972].

NASA developed cylindrical TEPCs during the shuttle missions, but more recently have built a spherical TEPC that is currently operating aboard the ISS [Flores-McLaughlin, et al., 2012]. To date, there has not been an LET spectrum converted from lineal energy measurements from a spherical TEPC in LEO reported in the literature. This dissertation contains the first-time report of a converted LET spectrum from a spherical TEPC in LEO from the ATED Inernational Space Staion experiment.

5.2 Geometric Conversion to LET

A measured lineal energy spectrum from a spherical TEPC can be converted into a LET spectrum via a geometric process [Rossi et. al., 1996]. It is assumed that the straggling of heavy particles and finite track lengths inside the active volume can be neglected. It is also assumed that the LET of a particle traversing the active volume does not change. It is questionable whether or not these are reasonable assumptions. The energy deposited is then assumed to be the product of LET and mean chord length ($\bar{l}$).

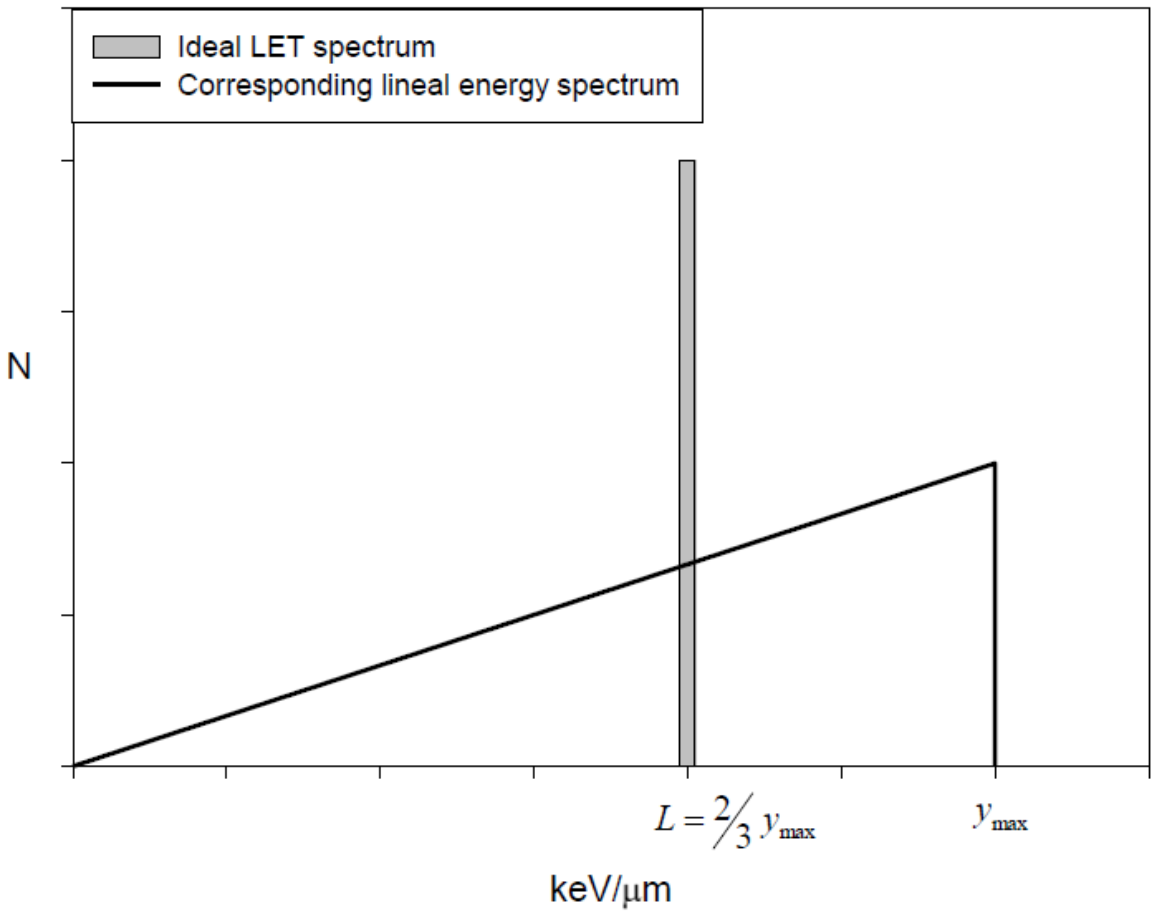

Figure 5.1: Number of counts (N, arbitrary) as a function of lineal energy, y. This is an ideal measurement of particles of a single LET and the corresponding lineal energy spectrum in a spherical TEPC [Rossi, 1996]

An ideal lineal energy distribution for a spherical cavity, measuring isotropic charged particles of a single LET will take the shape of a triangle as seen in **Figure 5.1**. The peak of this triangle at

y_{max} corresponds to particles crossing the full diameter of the sphere. The total number of particles measured in this lineal energy spectrum is the same number of events in the corresponding ideal LET spectrum. By integrating over all possible lineal energies, the total number of measured particles is found,

$$N_{total} = \int_0^{y_{max}} N_y(y)dy = N_L(L), \tag{5.1}$$

where $N_L(L)$ is the number of events in the corresponding LET spectrum at a single value of LET, L, and $N_y(y)$ is the number of measured events in the lineal energy spectrum over the entire range of measured lineal energies, y. Since the lineal energy distribution in **Figure 5.1** is a triangle, the integral can be replaced by the equation of the area for a triangle. Thus,

$$\int_0^{y_{max}} N_y(y)dy = \frac{1}{2} y_{max}\, N_y(y_{max}) = N_L(L). \tag{5.2}$$

This results in an LET distribution at a single value of L for the entire range of measured y. Again, this is a simplified, ideal case of a measurement of particles with a single LET by a TEPC.

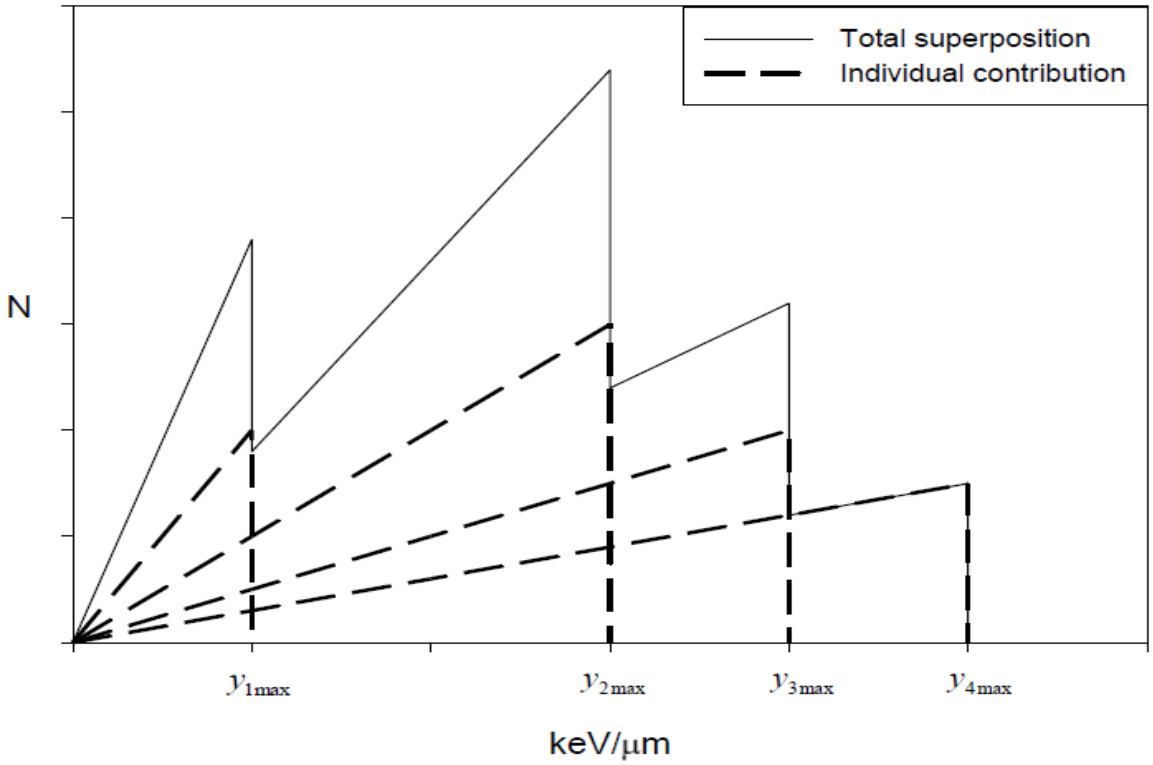

Figure 5.2: The superposition of four different triangles representing an ideal measurement of four different lineal energies [Adapted from Collums, 2012].

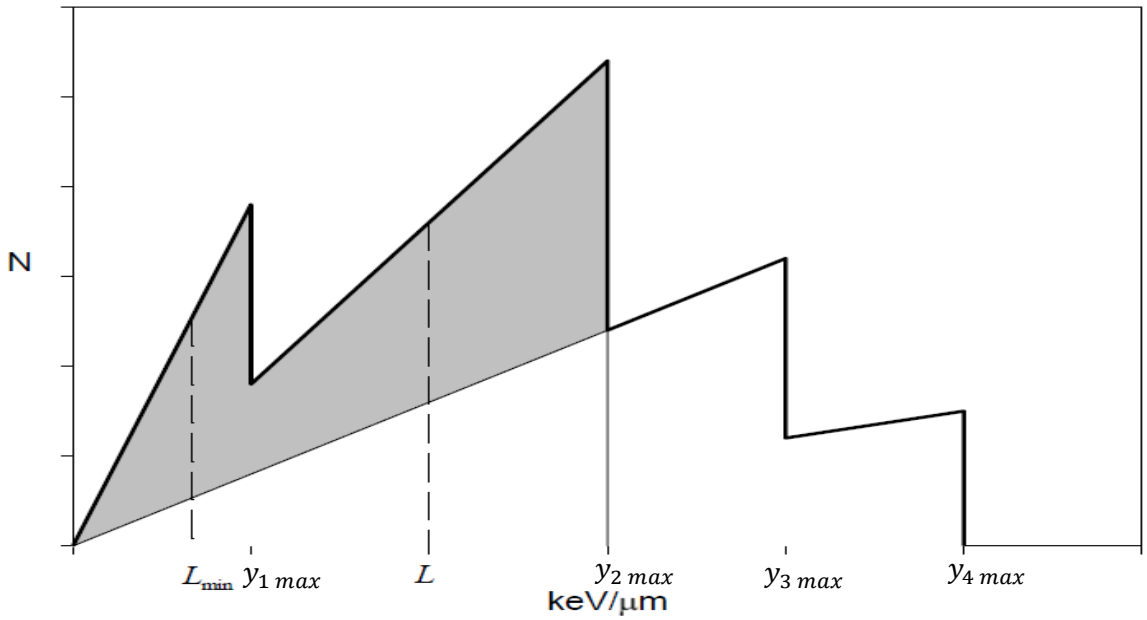

Figure 5.3: The shaded region represents the total number of particles contributing to the two smallest LET values [Adapted from Collums, 2012].

For a more realistic case, we consider a radiation field made of particles having a range of LET values. The lineal energy spectrum will then be a superposition of many triangles as seen in **Figure 5.2**. Each individual triangle corresponds to a different LET value. In this example, there are four discrete values of LET. The area of each triangle corresponds to the number of events by a single LET value.

To find the area of the triangles corresponding to $y_{1\,max}$ and $y_{2\,max}$ we must find the shaded areas in **Figure 5.3**.This shaded region is the combined area of the first two triangles and is also equal the total number of measured events with LET between the smallest measured LET L_{min} and the second LET value, L. For a realistic case where the measured LET spectrum is continuous,

$$\int_{L_{min}}^{L} N_L\, dy = \int_0^{y_0} N_y\, dy - \frac{1}{2} y_0 N_y(y_0), \tag{5.3}$$

where y_0 is equal to $3/2L$. The first term on the right is the entire area under the curve up to y_0. The second term subtracts the bottom triangular area from particles of higher LET. This is a general expression for the LET spectrum N_L in terms of N_y. Plugging in for y_0 in terms of L gives,

$$\int_{L_{min}}^{L} N_L\, dy = \int_0^{\frac{3}{2}L} N_y\, dy - \frac{3}{4} L\, N_y\left(\frac{3}{2}L\right). \tag{5.4}$$

We differentiate each side with respect to L,

$$\frac{d}{dL}\int_{L_{min}}^{L} N_L\, dy = \frac{d}{dL}\int_0^{\frac{3}{2}L} N_y\, dy - \frac{d}{dL}\left(\frac{3}{4} L\, N_y\left(\frac{3}{2}L\right)\right); \tag{5.5}$$

$$N_L(L) = \frac{3}{2} N_y\left(\frac{3}{2}L\right) - \frac{3}{4}\left(N_y\left(\frac{3}{2}L\right) + \frac{3}{2} L \frac{dN_y\left(\frac{3}{2}L\right)}{dL}\right). \tag{5.6}$$

Simplifying further gives us,

$$N_L(L) = \frac{3}{4}\left(N_y\left(\frac{3}{2}L\right) - \frac{3}{2}L\ \frac{dN_y\left(\frac{3}{2}L\right)}{dL}\right). \quad (5.7)$$

We now have an expression for the LET spectrum as a function of an ideal lineal energy spectrum. Equation (5.7) is limited to volumes of spherical geometry. No such derivation is possible for a cylindrical geometry.

The process of converting to LET from equation (5.7) involves taking the derivative of a measured y-spectrum. Taking the derivative of measurements that do not have a simple functional form or sufficient statistics can result in artifacts. This can potentially create negative $N_L(L)$ values, which are unphysical. It is necessary to smooth data by averaging the data over a fixed interval or by smoothing methods. However, smoothing measurements can eliminate important information contained in the measurement.

The assumption that lineal energy measurements take the shape of a triangle for a spherical active volume, like that seen in **Figure 5.1**, has not been observed in measurements of mono-energetic ions. This assumption and the assumptions of that the straggling of heavy particles and finite track lengths can be neglected are likely not valid. These processes shape the count distribution into a Gaussian-like distribution for particles of a single LET. Also, charged particles that travel along the periphery of the active volume create long range δ-rays (ionized secondary electrons) that can enter the active volume and be measured. This produces counts at low lineal energies, further reducing the resemblance of an ideal triangular distribution.

5.3 The Kellerer LET Conversion Method

An alternative method of LET-conversion has been provided by [Kellerer, 1972]. This is a mathematically abstract method to convert lineal energy measurements into LET spectra. We

make no claim that this methodology is valid given the fact that we do not fully understand the method ourselves. The proceeding section is a quick derivation of the Kellerer LET conversion method. For more a more detailed description, please see Kellerer's original 1972 paper.

In this method three variables are defined. The first is $g(l)$ which is the chord-length distribution of *any* defined geometry. For a sphere this is simply $g(l) = \frac{2l}{d^2}$ $[l \leq d]$ where l is the chord length and d is the diameter of the sphere. The second is $f(E)$, the pulse height distribution in terms of deposited energy. This is obtained approximately by multiplying the mean chord length by the $f(y)$ spectrum ($E(y) = y * \bar{l}$). The third is $t(L)$ the resulting LET distribution. The probability distributions of these three functions will be denoted by $F(E), G(l)$, and $T(L)$, respectively.

Taking the logarithm of the variables *E*, *L*, and l simplifies the math. New variables are designated by:

$$\epsilon = \ln(E), \quad \Lambda = \ln(L), \ and \quad \lambda = \ln(l). \tag{5.8}$$

Now the logarithm of the deposited energy is the sum of the logarithm of chord length and the logarithm of LET ($\epsilon = \Lambda + \lambda$). The probability distributions of these new variables are expressed in terms of their original variables and distributions,

$$\phi(\epsilon) = \frac{dF(E)}{dln(E)} = E\frac{dF(E)}{dE} = Ef(E). \tag{5.9}$$

And in the same way:

$$\tau(\Lambda) = \frac{dT(L)}{\ln(L)} = L * T(L), \tag{5.10}$$

and

$$\gamma(\lambda) = \frac{dG(l)}{dln(l)} = l * g(l). \tag{5.11}$$

Since ϵ is the sum of λ and Λ, its distribution is equated to the convolution integral of the distribution of λ and Λ:

$$\phi(\epsilon) = \int_{-\infty}^{\infty} \tau(\epsilon - \lambda)\gamma(\lambda)d\lambda \,. \tag{5.12}$$

The convolution theorem states that the Fourier transform of the distribution of ϵ is equal to the product of the Fourier transforms of the distributions of λ and Λ. This leads to the expression,

$$\phi^*(x) = \tau^*(x)\ \gamma^*(x), \tag{5.13}$$

and

$$\tau^*(x) = \frac{\phi^*(x)}{\gamma^*(x)}, \tag{5.14}$$

where $\phi^*(x), \tau^*(x)$, and $\gamma^*(x)$ are the Fourier transforms of $\phi(\epsilon), \tau(\Lambda)$ and $\gamma(\lambda)$, respectively. With an inverse Fourier transform, $\tau(\Lambda)$ and *t(L)* are obtained. Kellerer states that the final expression (5.14) effectively "folds" the count spectrum into all possible chords and results in the LET spectrum. With the use of modern computers, this method can be easily implemented using fast Fourier transform algorithms.

This method has only been demonstrated by Kellerer on a single neutron measurement by a spherical TEPC. The maximum significant LET in a neutron spectrum is the proton edge, at ~100 keV/µm. Past this point the contribution to the measured spectra is minimal. It is not known whether or not lineal energy measurements past 100 keV/µm are valid with this method. At LET, below about 5 keV/µm, the LET spectrum is artificially large due to the folding of counts into small chord lengths.

5.3 The Conversion of Measurements into LET

These methods are illustrated with the conversion of measurements of mono-energetic particle beams of known LET as measured by a 2-inch spherical ATED. **Figure 5.4** is the high-gain spectrum from a 400 MeV/n Oxygen beam at the HIMAC. The LET of these particles is known to be 20.0 keV/μm and thus the lineal energy measurement is centered over 30.0 keV/μm. The nominal beam measurement is shown in black and takes the form of a Gaussian-like distribution around 30.0 keV/μm. The Gaussian distribution comes about from the straggling of ions as they pass through the active volume. Low lineal energy bins are filled with counts from electronic noise, low LET projectile fragments, and δ-rays from periphery ions that do not enter the active volume themselves. Red is the result of the geometric LET conversion and blue is the Kellerer LET conversion.

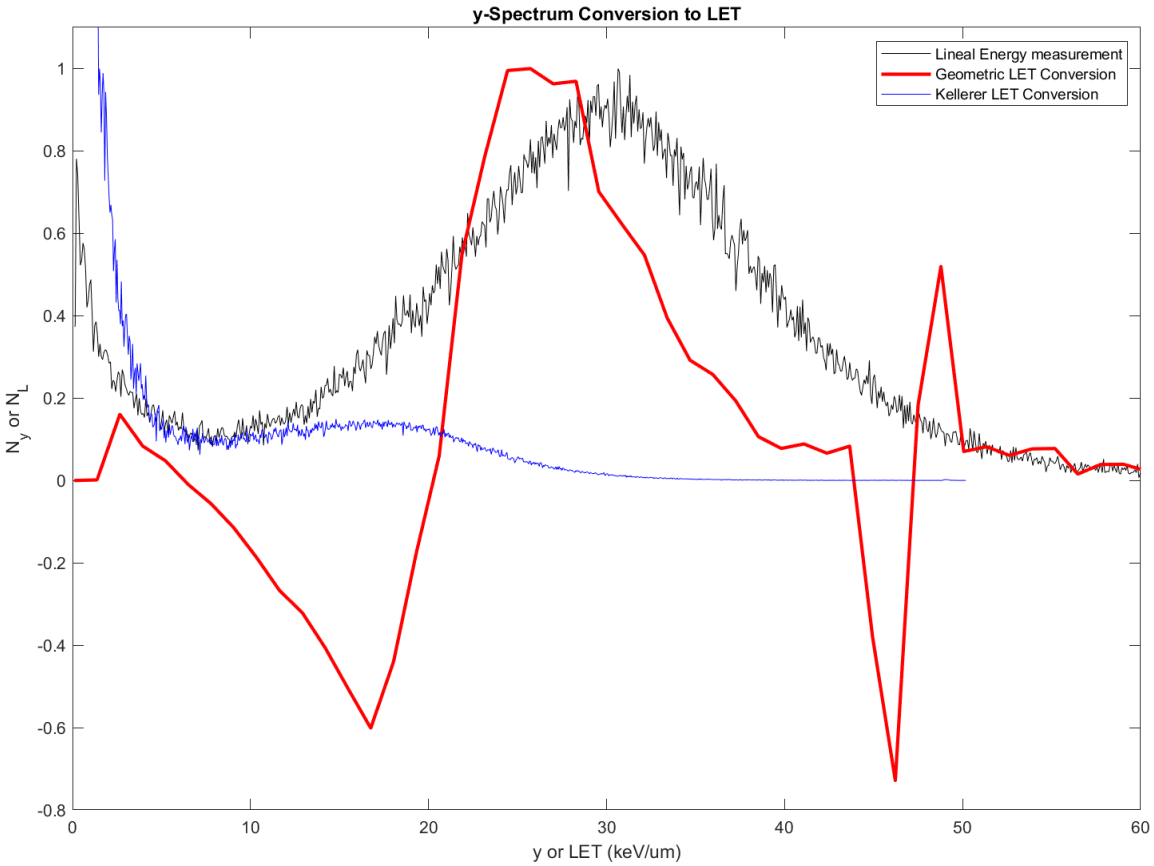

Figure 5.4: 400MeV/n Oxygen lineal energy measurement in black and its corresponding LET conversions in red and blue.

The Geometric conversion yields negative values from 7 to 20 keV/µm and 45 to 48 keV/µm. Non-positive counts are an erroneous by-product of this method and occur when the slope of the data is larger than the counts in the data itself (see equation 5.7). The remaining positive counts have a wide maximum around 25 keV/µm. Two more maxima are seen at 3 and 48 keV/µm, but do not reflect physical phenomena. Error from the geometric LET conversion is due to the assumption that measurements of single LET particles take the shape of a triangle. This is not realistic because charged particles straggle inside the active volume and δ-rays from outside the cavity populate the lower end of the lineal energy spectrum.

A peak in the Kellerer LET spectrum is centered at 18.81 keV/µm resulting in a 6.33% difference from the expected value of 20 keV/µm. The amplitude of the peak has been greatly reduced from the original measurement. The lower amplitude comes from the “folding” of the pulse height

spectrum into the chord-length distribution of a sphere. The Kellerer algorithm places many counts into small chord lengths which is why there are many counts at low LET. Any counts below 5 keV/μm should be ignored in the above Keller LET conversion because the unit length of the assumed chords artificially raise the count spectrum to unrealistic values.

The expected LET conversion of the 400 MeV/n oxygen lineal energy measurement by ATED would be a narrow peak at 20.0 keV/μm. The LET conversions did not give this expected result. The geometric conversion had made assumptions that are not accurate and thus produced an erroneous LET spectrum. The Kellerer conversion has a peak that is close to the expected value of LET, but there are many counts at small LET and as LET increases counts are reduced. Both methods make assumptions about TEPC measurements that are not valid for ATED. Other measurements by ATED have been converted into a corresponding LET spectrum, but have not shown any promising results. These methods are tested for their validity in the space radiation environment in Chapter 9.

CHAPTER VI

ANALYSIS OF THE CONTRIBUTIONS TO PULSE AMPLITUDE IN PROPORTIONAL COUNTERS

Previously, it was thought that the separated electrons from ionization events inside the ATED active volume were the only contribution to signal height [Causey, 2018]. However, theoretical predictions estimate that positive ions should be the largest contributor to signal amplitude in a proportional counter, not electrons [Wilkinson, 1950]. Because of this, the contribution to pulse amplitude by electrons are neglected in theoretical calculations [Segre, et al., 1953]. In this chapter, pulses from ATED's coupling capacitor are measured on an oscilloscope. An iterative fit was used on these recorded pulses to quantify the individual contributions to pulse amplitude by positive ions and electrons. To the best of our knowledge, this is the first time that the individual contributions to pulse amplitude in a proportional counter have been quantified

6.1 Motivation

When ionizing radiation passes through the active volume of ATED, it ionizes the gas inside. The

freed electrons inside the gas accelerate towards the collecting wire and undergo a Townsend avalanche, ionizing ~10^3 more gas molecules each. The electrons are collected quickly by the center wire However, the heavier positively charged molecules close to the center wire take a significantly longer time to be collected by the walls of the detector. Right after the electrons are collected, the positively charged ions induce a negative charge on the wire itself. This happens because the center wire is a conductor at a fixed potential in proximity to charge distribution [Jackson, 1999]. The positive ions slowly move away from the wire, relative to the electrons.

The process of how both positive ions and electrons produce a pulse inside the ATED active volume is illustrated in **Figure 6.1**. The induced charged on the collecting wire by the positive cloud of ionized gas slightly lowers the potential on the wire, which causes the electric field inside the coupling capacitor to decrease in magnitude. Electrons on the far side of the coupling capacitor are freed because of this drop in potential, producing a negative pulse. This pulse is then fed into the input of a charge sensitive preamplifier.

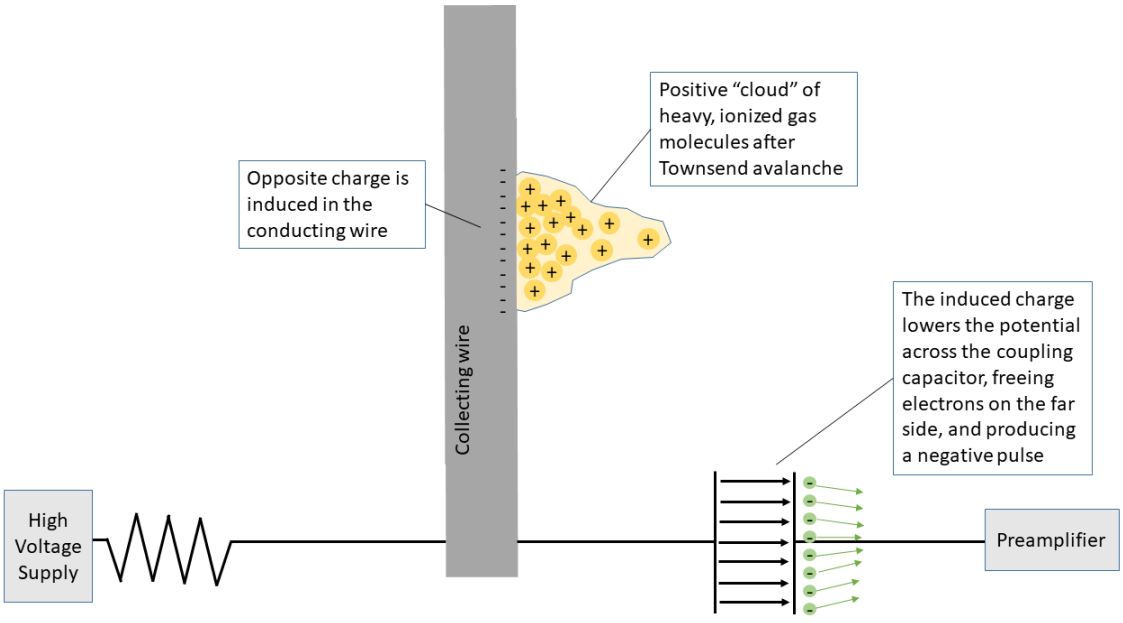

Figure 6.1: An illustration of how electrons and positive ions produce a pulse across the ATED coupling capacitor. For details, see accompanying text.

The positive ions are much more massive than electrons and thus can be considered stationary inside the gas volume as electrons are collected. The relatively long time spent by positive ions in proximity to the collecting wire makes positive ions the main contributor to pulse amplitude because more electrons are freed from the far side of the coupling capacitor. The collected electrons are collected so quickly that they do not have a significant impact on the number of freed electrons The positive ions eventually drift away from the wire and reach the wall of the detector where they become neutral. This entire process takes from 100 μs to 600 μs, whereas the collection of electrons happens in less than 1 μs [Segre, et al., 1953].

It is estimated that positive ions contribute ten times more to signal amplitude than electrons [Wilkinson, 1950]. It is assumed in theoretical calculations that the contribution to pulse amplitude by electrons can be neglected. This assumption has never been substantiated with experimental evidence. Modern electronics introduce the opposite assumption. Pulses in proportional counters are reduced in time down to ~1 μs. This shortening of pulse duration leads to the naïve assumption that only the collected electrons contribute to pulse amplitude, as they are much faster than the positive ions.

Based on a thorough review of the literation, it appears that the individual contributions by positive ions and electrons to pulse amplitude have never been measured, until now. Quantifying the individual contributions will substantiate or contradict previously made assumptions.

6.2 The Functional Form of Pulses Inside a Proportional Counter and Experimental Methods

The functional form of pulse amplitude, from only positive ions, as a function of time in a cylindrical proportional counter is given as,

$$P(t) = -\frac{e}{C}\frac{\log\left(\frac{2VKt}{a^2\,log\left(\frac{b}{a}\right)}+1\right)}{2\log\left(\frac{b}{a}\right)}, \tag{6.1}$$

where V is the voltage, C is the capacitance, K is the ion mobility of the gas, a is the radius of the center wire, and b is the radius of the cylindrical volume [Wilkinson, 1950]. Ion mobility (units: m^2/s/V) for single mixture gases can be found in tables [Rossi, et al., 1949]. The contribution by electrons are neglected in (6.1), but will have the same functional form as positive ions [Wilkinson 1950].

Close to the wire, the electric field inside a cylindrical and spherical proportional counter will be nearly identical. This allows the use of equation (6.1) to be used for both cylindrical and spherical ATED geometries.

To quantify the contributions to pulse amplitude from both electrons and positive ions, (6.1) is adapted to be a two term equation,

$$P(t) = \{A_E Log(\lambda_E t + 1) + A_P Log(\lambda_P t + 1)\}e^{-\frac{t}{\tau}} \tag{6.2}$$

where A_P is the signal amplitude contributed by positive ions, A_E is the signal amplitude contributed by electrons, λ_P is the signal rise time for positive ions, λ_E is the signal rise time of electrons, and τ is the RC time constant of the circuit. The RC decay of the system is added to more closely match measured pulses. The negative sign in (6.1) has been removed for simplicity.

Figure 6.2 shows the functional form of equation 6.2 and the individual contributions of each term. The ratio of λ_P to λ_E is chosen to be 1:100 and the ratio of A_P to A_E is chosen to be 10:1. The variables λ_P and λ_E determine the rise time of the pulse. The amplitudes of the positive ion contribution are determined by the variables A_P and A_E. The RC decay exponentially lowers the pulse back to zero.

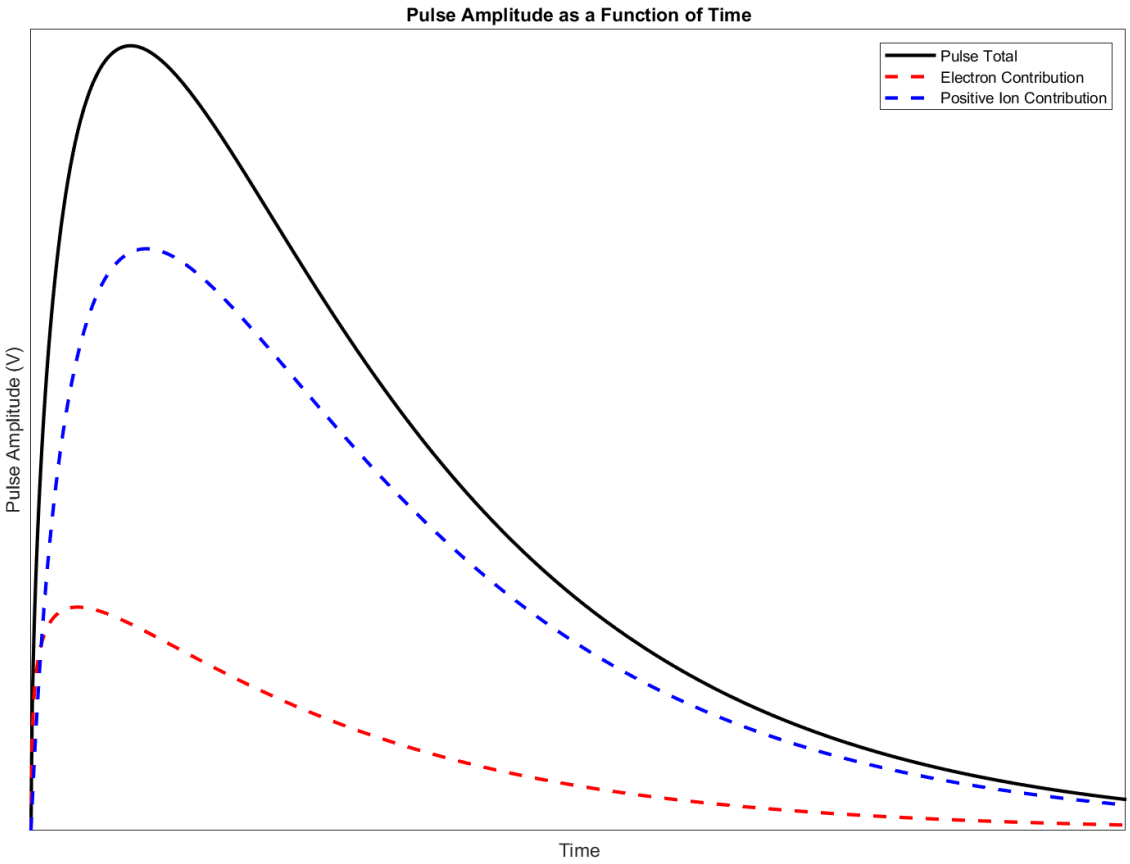

Figure 6.2: Pulse amplitude from an ionization event in a proportional counter as a function of time. This is the functional form of equation 6.2 and shows the contributions from electrons and positive ions. Relative values were chosen to illustrate the fast nature of electrons vs the slower positive ions.

Figure 6.3 shows an illustration of the experimental setup. This includes a re-sealable ATED can at a pressure that simulated a 2 µm diameter spherical tissue phantom and at the nominal operating voltage discussed in Chapter 6. The anode was directly coupled through a 1 nF coupling capacitor. Pulses were created by alpha particles, from an Americium-241 source, which traverse the active volume and ionize the tissue equivalent gas. These alpha particles traversed a single chord length ensuring that each pulse would be similar in amplitude. The pulses from the coupling capacitor were inverted, read into, and saved by a Tektronix Oscilloscope.

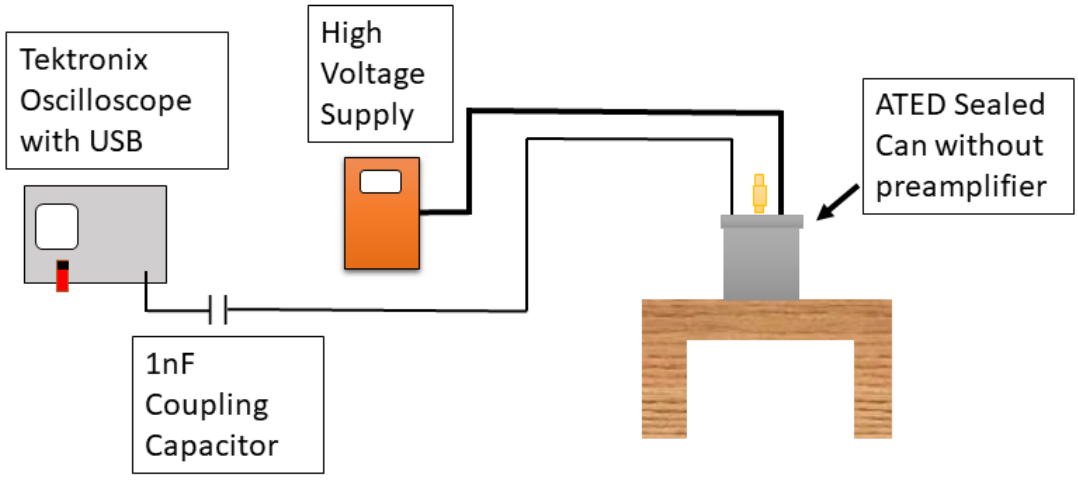

Figure 6.3: The experimental setup for the collection of pulses across a 1nF coupling capacitor. No preamplifier was used. The can was at the appropriate pressure and the active volume was biased at the appropriate voltage with a high voltage supply. Pulses were saved onto a USB drive.

The oscilloscope was set to trigger on pulses of 5 mV and above. When triggered, the oscilloscope saves 50 µs of voltage and time values on to a USB memory drive in a CSV format. Several pulses were saved to ensure for statistically significant values. Equation 6.2 was used in the MATLAB fitting toolbox, an iterative fitting program, on the recorded pulses. The iterative fitting process estimated the best values for A_P, A_N, λ_P, λ_N, and τ in order to match the data. These values are recorded for each fit of a recorded pulse.

6.3 Results

Figure 6.4 shows an example of saved pulse from a spherical ATED in black and the resulting fit in red. The equation of the fit is displayed on the graph. This fit has an R^2 coefficient of determination of 0.9918. The λ values in the fit equation let us identify which term is the electron and positive ion contribution. The larger value of λ will correspond the electrons, because of their fast rise time. The A terms indicate relatively how many electrons and positive ions are contributing to pulse amplitude. The left-most term in the equation in **Figure 6.4** is the

contribution of positive ions to the fitted pulse. From this equation, it is seen that positive ions contributed ~10x more to pulse amplitude than electrons.

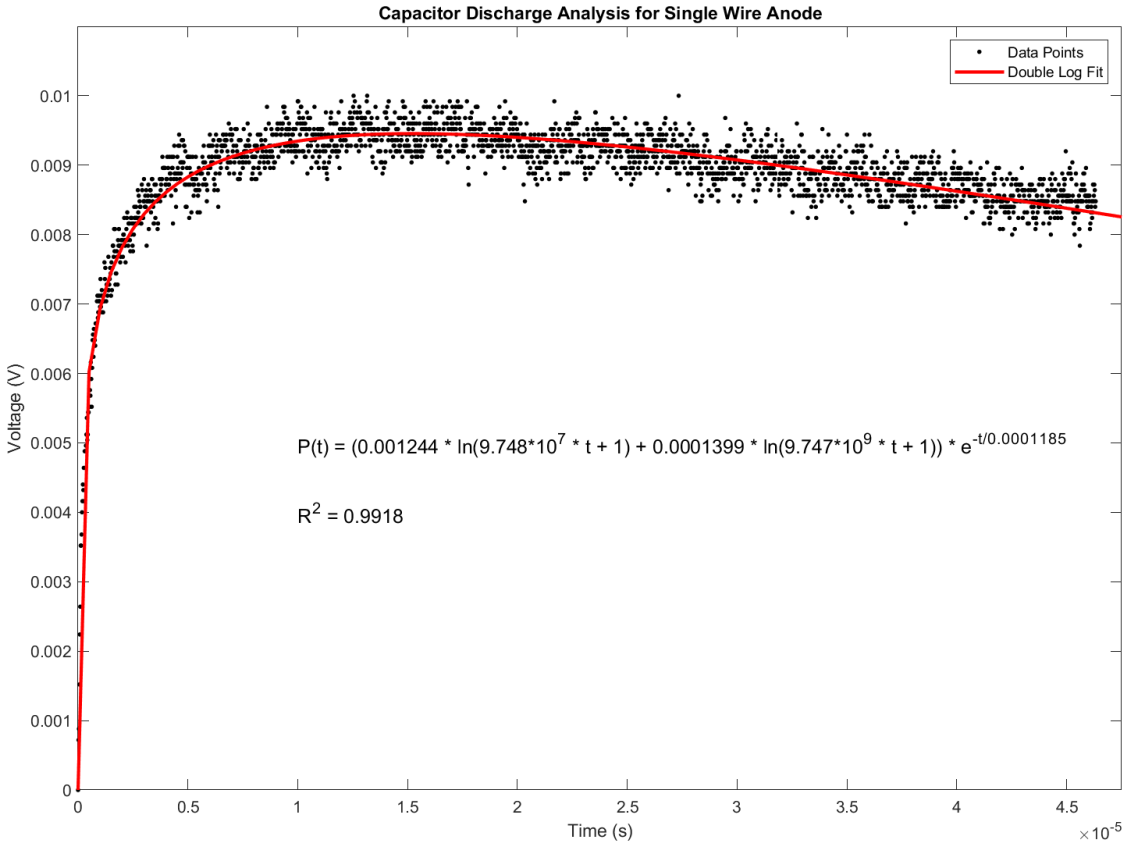

Figure 6.4: A saved pulse from an ATED capacitor discharge as a function of time, shown as black dots. The resulting fit is shown as a red line. The equation of the fit and the coefficient of determination are also displayed.

The individual contributions to pulse amplitude can be separated from this resulting fit. **Figure 6.5** shows the electron (magenta) and positive ion contributions (blue) to total pulse amplitude (red). The separation of each component illustrates the individual contributions to pulse amplitude by positive ions and electrons. Electrons contribute to the total amplitude only in the first few microseconds before RC decay dominates. Positive ions contribute to pulse amplitude for a longer amount of time and at a greater magnitude than electrons. The pulses from cylindrical and spherical geometries are identical, thus the same process happens with recorded pulses from a cylindrical ATED.

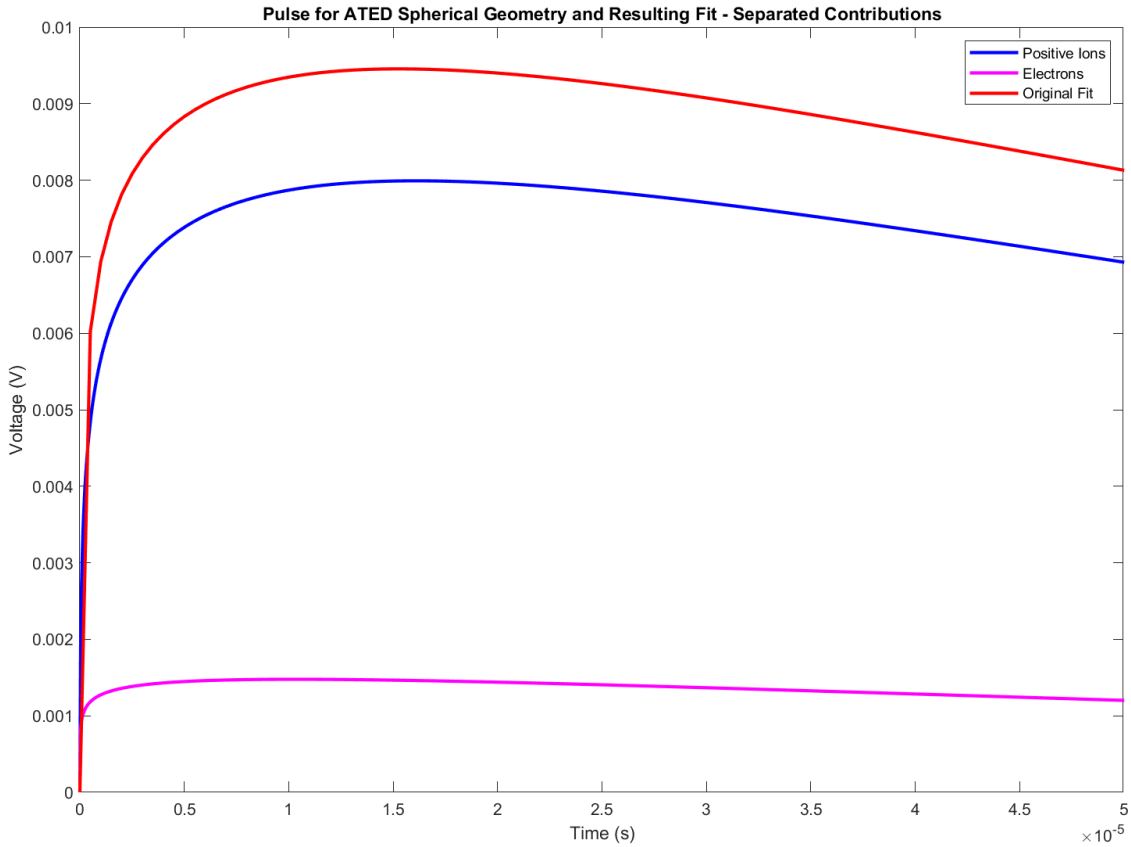

Figure 6.5: The fit of a pulse separated into its different parts. Fast electrons contribute to overall pulse height very briefly before RC decay dominates. Slower positive ions will contribute to pulse amplitude over a longer amount of time and thus contribute more to pulse amplitude.

Several pulses were saved and were subject to this fitting method for both the spherical and cylindrical ATED geometries. The average ratios of A_P to A_E and λ_P to λ_E from resulting fits and their standard deviation are recorded in **Table 6.1** for the spherical ATED and in **Table 6.2** for the cylindrical ATED. Positive ions consistently contribute 4-12 times more to pulse amplitude than electrons. The ratio of pulse amplitude between positive ions and elections is somewhat consistent with theoretical predictions, but the large standard deviation is inconsistent. The high variability in this ratio suggests that electrons may or may not be significant in their contribution to pulse amplitude on a case-by-case basis. It is not accurate to say that electrons can be neglected in the calculation of pulse amplitude. This is seen in both spherical and cylindrical geometries.

Positive ions have a consistently slower rise time than electrons, by a factor of ~100. This agrees well with theoretical predictions, and has a small value of standard deviation. The standard

deviation for the ratio between $\lambda_P : \lambda_E$ for the cylindrical geometry is significantly higher than the spherical geometry. This is likely due to a poor signal to noise ratio in the cylindrical detector that was not seen in the spherical detector.

	Mean	**Standard Deviation (%)**
$\boldsymbol{A_P : A_E}$	6.70 : 1	56.4
$\boldsymbol{\lambda_P : \lambda_E}$	1 : 101.40	4.64
$\mathbf{R^2}$	0.988	1.18

Table 6.1: The ratio of fitted values for the spherical ATED geometry

	Mean	**Standard Deviation (%)**
$\boldsymbol{A_P : A_E}$	6.95 : 1	45.36
$\boldsymbol{\lambda_P : \lambda_E}$	1 : 173.88	58.08
$\mathbf{R^2}$	0.945	3.20

Table 6.2: The ratio of fitted values for the cylindrical ATED geometry

CHAPTER VII

NEUTRON MEASURMENTS AT THE LOS ALAMOS NEUTRON SCIENCE CENTER

The Los Alamos Neutron Science Center (LANSCE) Irradiation of Chips Electronics (ICE) House provides a neutron energy spectrum that is similar in shape to the neutron energy spectrum present in the atmosphere, inside aircraft at aviation altitudes, and inside spacecraft in space [Hewitt, et al., 1978]. Neutrons are the main component of the radiation field found at aviation altitudes that cause biological damage [Benton, 2004]. A spherical, 2-inch diameter, ATED was tested at the LANSCE ICE House to calibrate its response to this neutron energy spectrum and study how absorbed dose changes behind various shielding materials. A comparison with a TEPC of the type formerly used aboard the NASA Space Shuttle is an independent source of a measured TEPC response to this neutron field. Finally, a comparison of the measured nominal beam by ATED and a simulation of the experiment in MCNP_6.2 helps to justify the measured response to these neutrons.

7.1 Description of the Beamline

The LANSCE facility houses an 800 MeV proton linear accelerator (LINAC). The proton beam is directed onto a tungsten target (Target 4) producing secondary neutrons in all directions via spallation [Lisowski, et al., 1990]. **Figure 7.1** shows the process of generating spallation neutrons and directing them to a targeted beamline. Charged particles are filtered by large sweep magnets before reaching the ICE House. Different beamlines exist at angles of ±15, ±30, 60, and 90 degrees of the incident proton beam. The ICE House uses the "30L" beamline, 30 degrees left of the target. A fission ionization chamber sits at the entrance of the ICE House beamline to monitor incident neutrons.

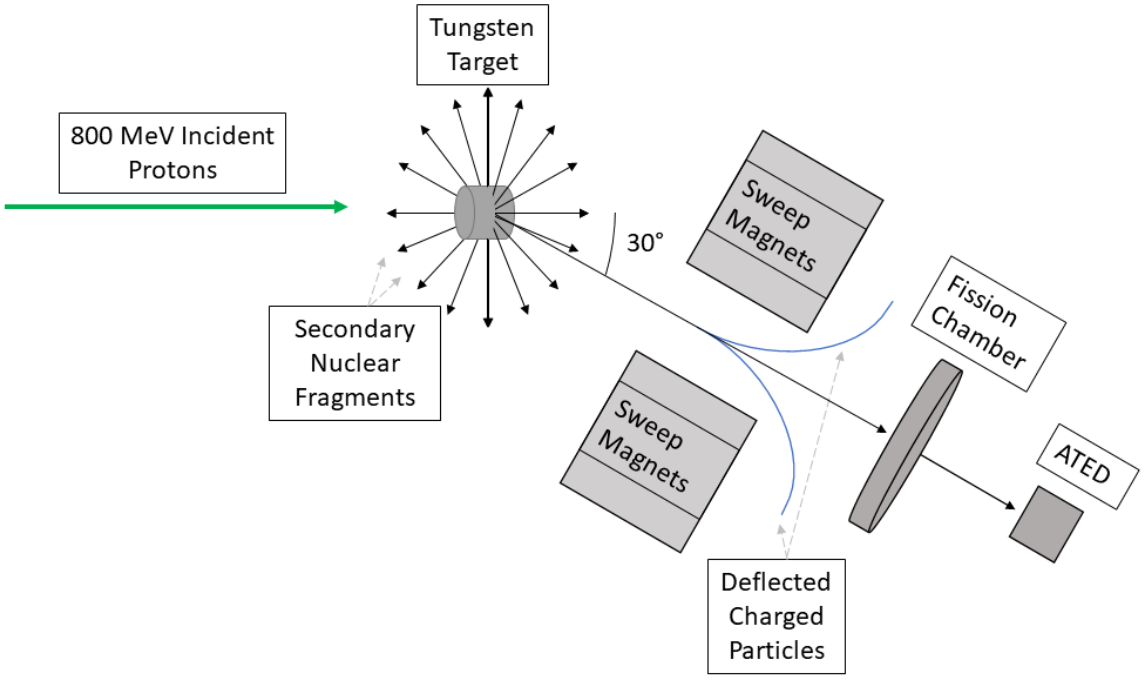

Figure 7.1: The process of how neutrons are created at LANSCE, Target 4. Pulsed protons are incident onto a tungsten target. Secondary particles are produced via spallation in all directions. Secondary particles leave at specific angles, where charged particles are deflected away from the beamline with sweeping magnets.

The ICE House neutron differential energy spectrum is shown in **Figure 7.2**. The neutron energy spectrum found at aviation altitudes spans energies from keV to in excess of a GeV in energy. At the ICE House, the neutron energy spectrum found in the atmosphere at 12 km altitude and the neutron energy spectrum in the beamline are of similar shape up to 800 MeV [Gersey, et al.,

2003]. This is the maximum proton energy from the LINAC. Absolute neutron energies at the ICE House are measured by the monitor fission chamber and a time of flight (TOF) system [Wender, et al., 1993]. The process of spallation also creates many gamma rays. These gamma rays are used as a trigger in the TOF system and contribute to the radiation field in the ICE House. The fission ionization chamber uses ^{238}U to measure neutron fluence and energy. It is sensitive to neutrons with kinetic energy of about 1 MeV and above. Neutron energies below 1.25 MeV are not reported by the TOF system.

The neutron energy spectrum generated at the ICE House has been well measured above 1.25 MeV and has a similar shape to that encountered at aircraft altitudes. Although the two energy spectra have good agreement, the flux at the ICE House is much larger than what is present in the atmosphere. The neutron energy spectrum in the atmosphere has been multiplied by $3x10^5$ in **Figure 7.2**. One hour in the ICE House beamline is equivalent to 10^4-10^6 hours at aviation altitudes, depending on the proton beam current [LANL, 2018]. This allows the simulation of long-term exposure to atmospheric neutrons in a relatively short amount of time.

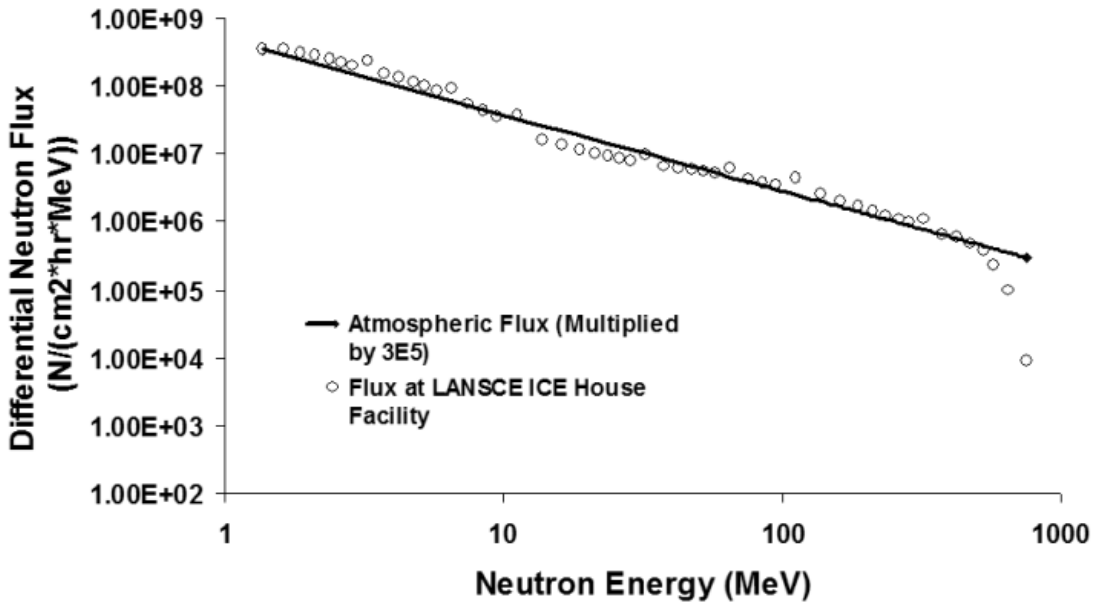

Figure 7.2: The Differential Neutron Flux as a function of energy at LANSCE ICE House facility and neutron flux found in the atmosphere at an altitude of 12km [Adapted from Gersey, et al., 2003].

Measuring the neutrons at the ICE House is a good test of the response of ATED to atmospheric neutrons. Using ATED in the ICE House beamline produces a probability distribution of counts and a relative dose distribution that is similar to a measurement in the atmosphere. Placing shielding materials in the beamline shows how absorbed dose and the relative dose distribution change as a function of these materials. These materials are similar to those found in commercial jetliners, business jets, and military cargo aircraft.

Figure 7.3 shows ATED at the ICE House beamline. The neutron beam is incident from the back wall, where the fission chamber is located. The fission chamber monitors the beam, and yields a scalar that is proportional to the number of incident neutrons above 1.25 MeV. This number is then used to normalize measurements. The ATED detector head was secured on top of foam blocks to reduce scatter of the beam. Supporting electronics for ATED are in the white box off of the beam line to reduce the risk of an electronic upset and interrupting data collection. This model of ATED simulated a spherical tissue phantom of 1.56 µm in diameter inside a 2-inch diameter spherical shell and measured a minimum lineal energy of 0.41 keV/µm.

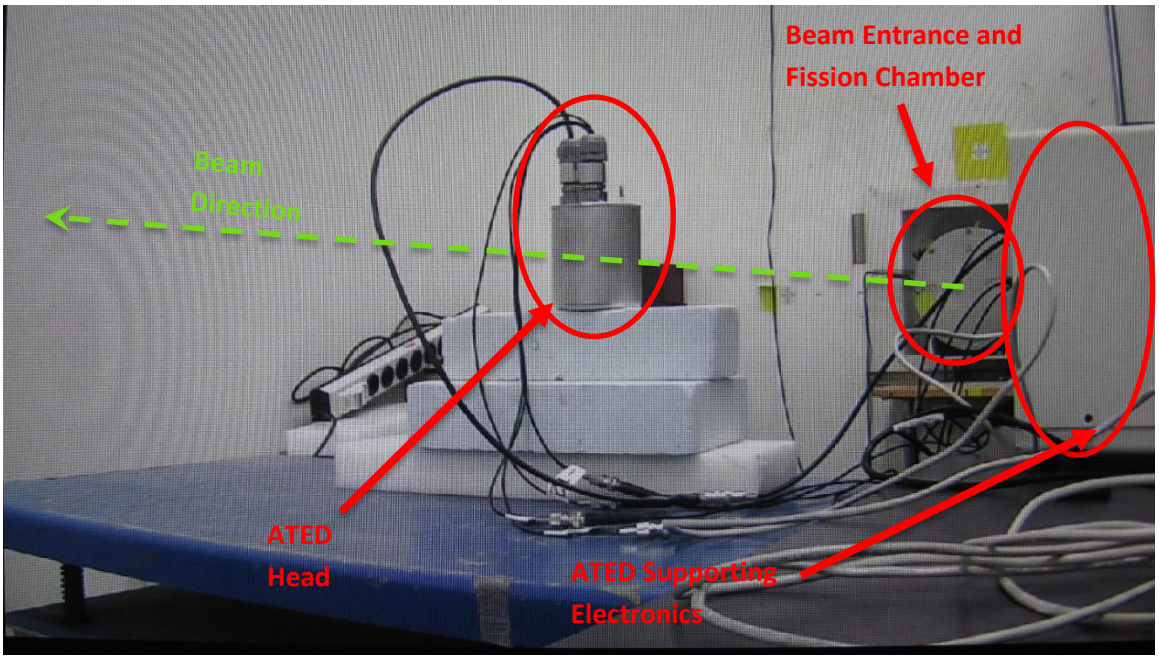

Figure 7.3: ATED on the ICE House Beamline. The neutron beam came from the far wall, through the fission chamber, and passed through ATED. The electronics were placed off-axis to the beamline.

7.2 Nominal Beam Measurement

Figure 7.4 shows the probability density of counts normalized by bin width as a function of lineal energy for the nominal beam measurement at the LANSCE ICE House. The first value at 0.4 keV/µm is lower than the second at 0.8 keV/µm because of a lower level discriminator. This first bin is neglected in the calculation of absorbed dose. Aside from this first point, the entire distribution of counts is monotonically decreasing, which is expected for the measurement of neutrons by a TEPC.

The proton edge is prominent at ~150 keV/µm. This is the lineal energy where protons deposit the maximum amount of energy possible into the ATED active volume (see Chapter 4.8). Neutrons will interact with the dense plastic wall that surrounds the ATED active volume and eject secondary particles, mostly protons, into the active volume. The high number of proton recoils from neutron interactions with the plastic wall is why the proton edge is an expected feature in any neutron measurement with a TEPC regardless of incident neutron energy. This edge was used for calibration.

Counts were recorded up to a maximum lineal energy of 700 keV/µm. The counts between the proton edge and 700 keV/µm are the measurement of less frequent heavy-ion recoils of He, C, and O from neutron interactions in the dense tissue equivalent plastic wall [Rossi, et al., 1996]. The actual composition of these rare heavy recoils is not accurately known, and makes a negligible contribution to absorbed dose. Poor statistics exist in this range of lineal energies due to the rare occurrence of these recoils. The neutron reactions in acrylic ($C_5O_2H_8$) that produce the largest signals are the recoils of carbon and oxygen nuclei due to their large atomic numbers. The maximum lineal energy measured around 700 keV/µm is reasonably close to the maximum lineal energies of carbon and oxygen at 677 and 752 keV/µm, respectively. These edges are not resolved because there are too few of these recoils.

ATED is not very sensitive to the photon component of the ICE House beam, but this component is still shown in the probability distribution. The decrease in *p(y)* immediately below 10 keV/µm is evidence of the electron edge, but it does not reside at the expected lineal energy of 12 keV/µm. This is because the superposition of proton and heavy ion recoil counts near 12 keV/µm shift the electron edge to lower lineal energies [Causey, 2018]. This is why the electron edge is not a suitable calibration point in a mixed neutron-photon field, as explained in detail in Chapter 4.

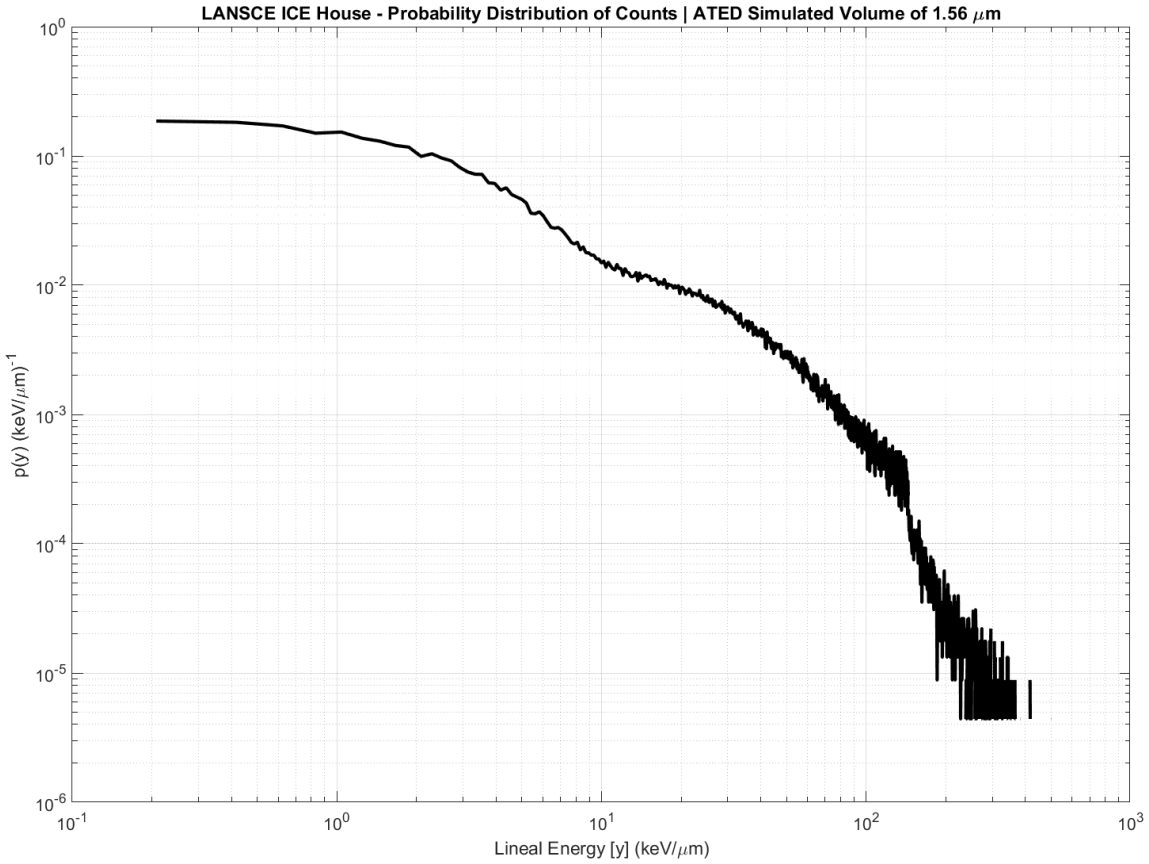

Figure 7.4: The probability distribution normalized by bin-width for the nominal beam at the LANSCE ICE House.

Figure 7.5 is the relative dose distribution from exposure to the nominal beam at the LANSCE ICE House as measured by ATED. The calculated spectrum has been re-binned into logarithmically-spaced bins. A peak in the relative dose distribution for the nominal beam resides at a lineal energy of 56 keV/µm. This lineal energy value made the single largest contribution to

absorbed dose. A single large peak before the proton edge is expected in the relative dose distribution of measured neutrons by a TEPC.

The proton edge is even more pronounced in the relative dose distribution than in the probability density of counts. The sharp decrease at 150 keV/µm also serves as an upper bound of lineal energies that are most significant to total absorbed dose. This indicates that proton recoils from neutron interactions with tissue are responsible for the largest portion of absorbed dose in tissue at aviation altitudes. The contribution to absorbed dose from events of lineal energy below 10 keV/µm is small compared to the rest of the spectrum. Even though the frequency of these events are largest in the probability distribution, they do not deposit enough energy per event into the active volume to be a major contributor to total absorbed dose. At lineal energies between 150 and 700 keV/µm, there is little contribution to absorbed dose. Even though these events individually deposit a large amount of energy, there are too few of them to be a large contributor to total absorbed dose.

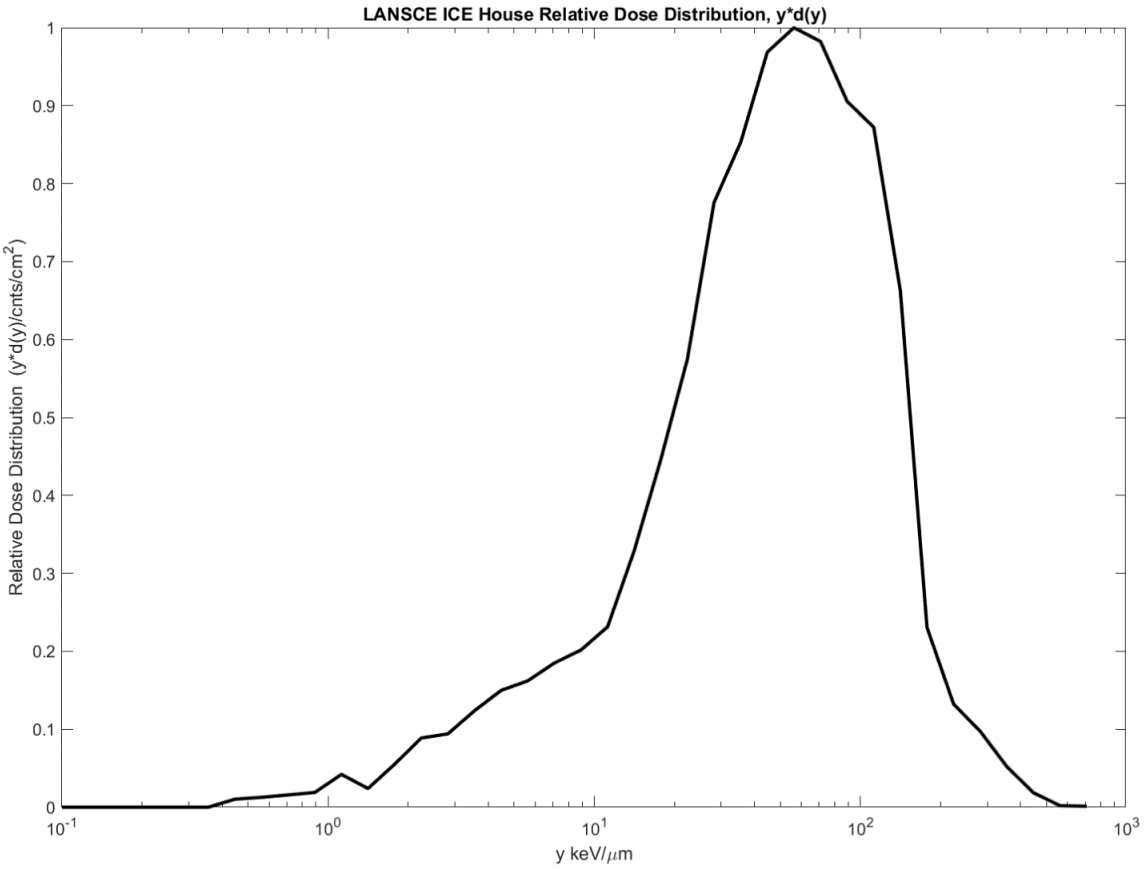

Figure 7.5: The relative dose distribution measured by ATED at the LASNCE ICE House (nominal beam).

7.3 Shielding Experiments

Different shielding materials were placed in the beamline to study changes in the relative dose distribution and absorbed dose per incident neutron. This also serves to show the effect that shielding of an aircraft has on neutrons encountered at aircraft altitudes. Three different materials were used: 5.34 g/cm² of aluminum, 5.38 g/cm² of high-density polyethylene (HDPE), and a simulated aircraft wall composed of 5.3 g/cm² of aluminum and 3.2 g/cm² of HDPE [Tobiska, et al., 2018]. The simulated aircraft wall has the aluminum layer facing the incident neutrons first, just as it would in an aircraft. Each material was placed 20 cm in front of ATED.

Neutrons enter shielding material and undergo interactions with nuclei. The frequency of these interactions is heavily dependent on the kinetic energy of individual neutrons and the atomic composition of the material, as reflected in the interaction cross section. Shielding reduces the amount of neutrons that reach ATED mainly through elastic scattering. In elastic scattering, neutrons that interact with nuclei are likely deflected away from their original trajectory. Other reactions are possible and are discussed in [Reilly, et al., 1991].

The relative dose distribution behind each material and for the nominal (unshielded) beam are shown in **Figure 7.6**. Each distribution is normalized to the number of incident neutrons as measured by the monitor fission ionization chamber. In each distribution, the proton edge remains at the appropriate lineal energy of ~150 keV/µm. At lineal energies between 200 and 700 keV/µm, each shielding material relative dose distribution agrees well with that of the nominal beam. This indicates that these shielding materials have little effect in the frequency of heavy ion recoils. In other words, the range of neutron energies responsible for heavy ion recoils has not been significantly attenuated by the shielding materials.

In each of the relative dose distributions measured behind shielding material, the peak is shifted to lower lineal energies compared to that of the nominal beam. This indicates an increase in the average kinetic energy of the neutron spectrum behind each shielding material. Higher energy neutrons produce recoils in the ATED active volume that also have a higher mean kinetic energy. More highly energetic recoils have correspondingly smaller LET and populate lower lineal energy bins, thereby shifting the peak in the relative dose distribution to a lower lineal energy. This indicates that lower energy neutrons are significantly reduced in number as a result of shielding as compared to higher energy neutrons.

The relative dose distribution behind 5.34 g/cm^2 of aluminum has the closest agreement with the nominal beam measurement. This is not surprising because neutron cross sections for aluminum

are small compared to most other elements [Cossairt, 2007]. The relative dose distribution measured behind 5.38 g/cm^2 of HDPE shows the largest disagreement with the relative dose distribution of the nominal beam. This is due to the relatively large neutron cross sections of hydrogen and carbon, the elements that make up HDPE. The relative dose distribution behind the simulated aircraft wall in **Figure 7.6** is likely similar to what would be measured inside an aircraft at aviation altitudes. Even though there is more material in the simulated aircraft wall compared to the HDPE, it did not reduce absorbed dose as much. This is because neutrons of all energies do not interact with aluminum with anywhere near the probability that they do with HDPE, as indicated by macroscopic cross sections.

The peak at 3.55 keV/μm in the HDPE relative dose distribution is of unknown origin. Defects in the measurement and instrument have been ruled out. It is possible that what is being measured are photons from radiative neutron capture in the polyethylene shielding. Radiative neutron capture is the absorption of a neutron by a nucleus and the emission of an energetic gamma: (n, γ). This interaction cross section increases dramatically for thermal and epithermal energy neutrons (10^{-8}-10^{-5} MeV). It is not clear at this time the amount of thermal and epithermal energy neutrons that exist in the ICE House beamline. The amount of gamma radiation required to significantly contribute to absorbed dose is substantial, considering that ATED is not very sensitive to photon radiation. This anomaly is surprising and more investigation is needed to justify this interpretation.

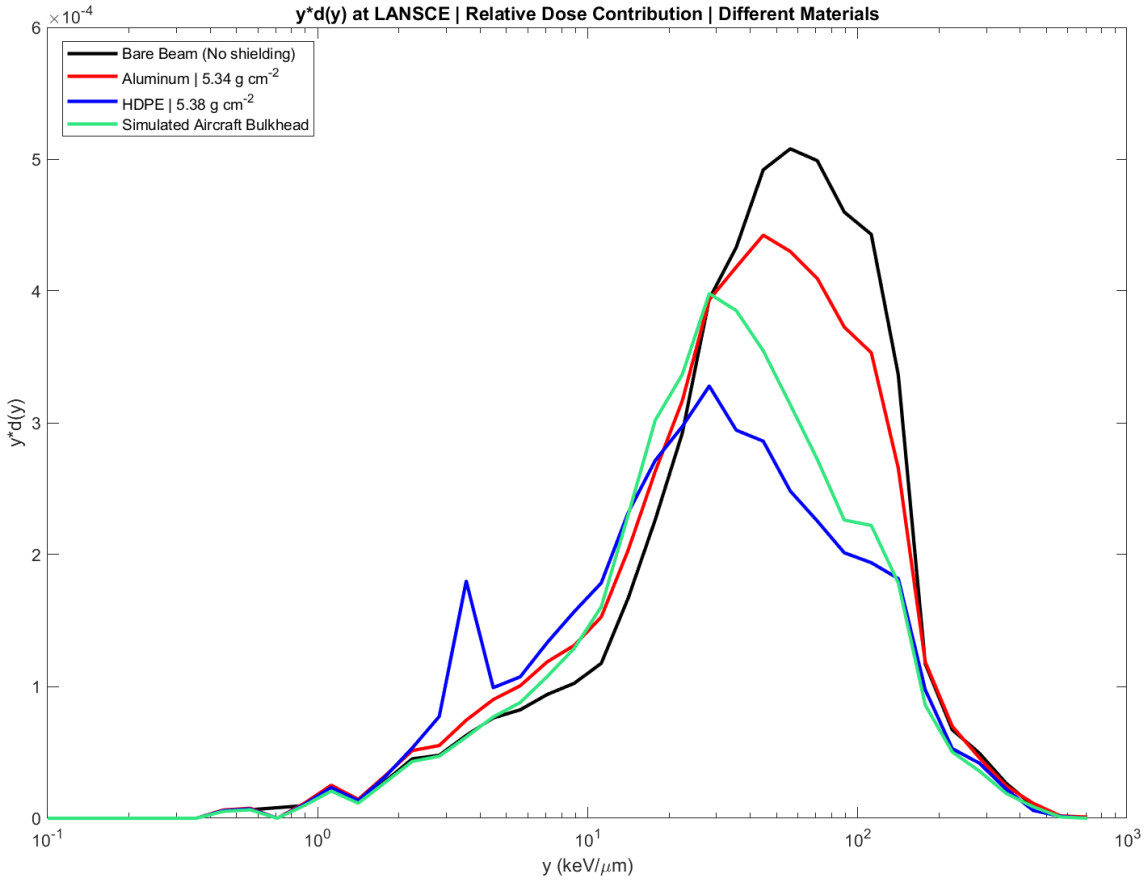

Figure 7.6: The Relative dose distribution of the nominal beam measurement and each shielding material. Each distribution has been normalized to the number of incident neutrons.

The absorbed dose per incident neutron and absorbed dose normalized to that of the nominal beam are shown in **Table 7.1**. Uncertainty is 6.37% for all absorbed dose measurements. The nominal beam measurement yielded the largest absorbed dose per incident neutron. Aluminum reduced absorbed dose the least of the shielding materials tested, about 23%, which is not surprising because of its low neutron cross section. The HDPE was most effective in reducing absorbed dose in tissue, by 47 ± 3% of that measured in the nominal beam. The simulated aircraft wall reduced absorbed dose 13.6 ± 9.0% more than the aluminum shield.

Material	Normalized Absorbed Dose in Tissue (Gy/n)	Absorbed Dose Normalized to Nominal Beam
Nominal Beam (no material)	$(2.08 \pm 0.13) \cdot 10^{-8}$	1
5.34 g/cm² aluminum	$(1.61 \pm 0.10) \cdot 10^{-8}$	0.772 ± 0.049
5.38 g/cm² HDPE	$(0.98 \pm 0.06) \cdot 10^{-8}$	0.470 ± 0.030
5.3 g/cm² aluminum + 3.2 g/cm² HDPE	$(1.33\pm 0.08) \cdot 10^{-8}$	0.636 ± 0.041

Table 7.1: Normalized absorbed dose for each material and the nominal beam at the ICE House

7.4 Comparison of Nominal Beam Measurement with Shuttle TEPC

The Shuttle TEPC was used on NASA Space Shuttle missions to measure the radiation exposure that astronauts received during space missions [Badhwar, et al., 1994]. It has a right cylindrical active volume with equal height and diameter surrounded by A-150 tissue equivalent plastic and simulates a right cylindrical tissue phantom of 2 μm in height and diameter. The Shuttle TEPC was exposed end-on to the nominal neutron beam at the LANSCE ICE House.

Figure 7.7 is the relative dose distribution, normalized to maximum peak height, for both ATED and Shuttle TEPC measurements taken at the LANSCE ICE House. Despite the differences between the two distributions, the overall shape and trends indicate good agreement [Gersey, 2020]. Differences between the two relative dose distributions are the result of different calibration methods and the different geometries of the active volumes.

The proton edge at ~ 150 keV/μm is readily seen in both relative dose distributions. They do not directly overlap, largely because the Shuttle TEPC was calibrated with an internal alpha source, while the ATED was calibrated with the proton edge itself. This places the proton edge for the Shuttle TEPC distribution at a slightly different lineal energy than if the proton edge were used for calibration itself.

The Shuttle TEPC relative dose distribution is slightly shifted to larger values of lineal energy compared to the relative dose distribution as measured by ATED. The cylindrical geometry of the Shuttle TEPC gives neutron recoils a longer mean chord length though its active volume than the spherical ATED volume. This is because neutron-induced secondary recoils will be forward-biased in their trajectory and will likely traverse the entire height of the Shuttle TEPC active volume. As a result of their longer chord lengths, recoil charged particles in the Shuttle TEPC deposit, on average, more energy than they would in ATED.

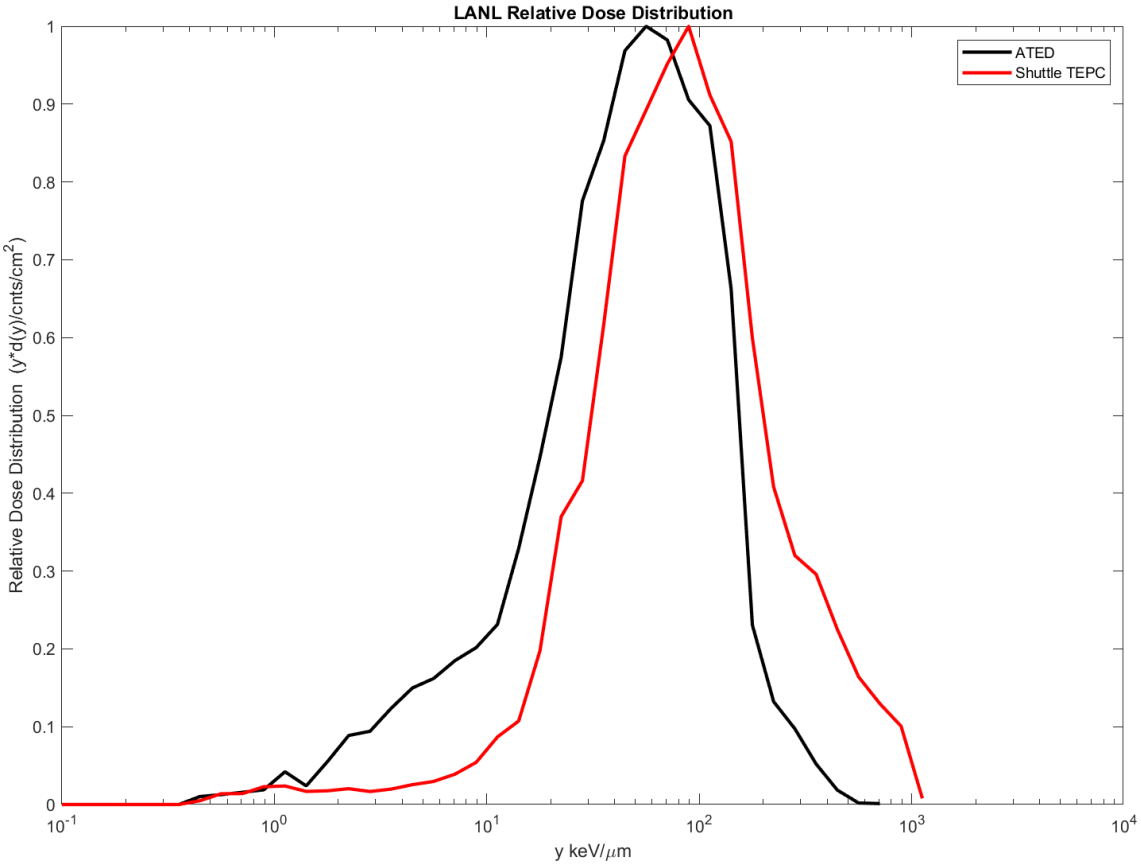

Figure 7.7: Relative dose distributions for the nominal beam at the LANSCE ICE House for the ATED and the Shuttle TEPC. Both distributions have been normalized by peak height in order to highlight differences between the two spectra.

Overall, both instruments have good agreement in their relative dose distributions. This agreement indicates that ATED had the proper response to the neutron energy spectrum that is found in the atmosphere. This argument is strengthened through this comparison because the two instruments are of completely independent designs.

7.5 Comparison with Simulation

To better understand the measurement of the nominal beam taken by ATED at the LANSCE ICE House, a simulation of the experiment was done with the MCNP_6.2 Monte Carlo radiation transport code. The simulation included the nominal ICE House neutron beam and a simplified ATED detector head. Lineal energy was calculated by MCNP_6.2 by dividing the energy deposited into the simulated tissue equivalent gas by the mean chord length of the sphere.

Figure 7.8 shows the relative dose distributions of the ATED measurement of the nominal beam at the LASNCE ICE House and the corresponding simulation in MCNP_6.2. The two relative dose distributions have been normalized by peak height. The small differences between the distributions are indicative of good agreement and is likely due to the limited fidelity of MCNP_6.2. The only significant disagreement between the relative dose distribution of the simulation and that of the ATED is from 1 to 20 keV/μm. The simulation has perfect efficiency at all lineal energies, whereas ATED has a reduced sensitivity to lower lineal energy events.

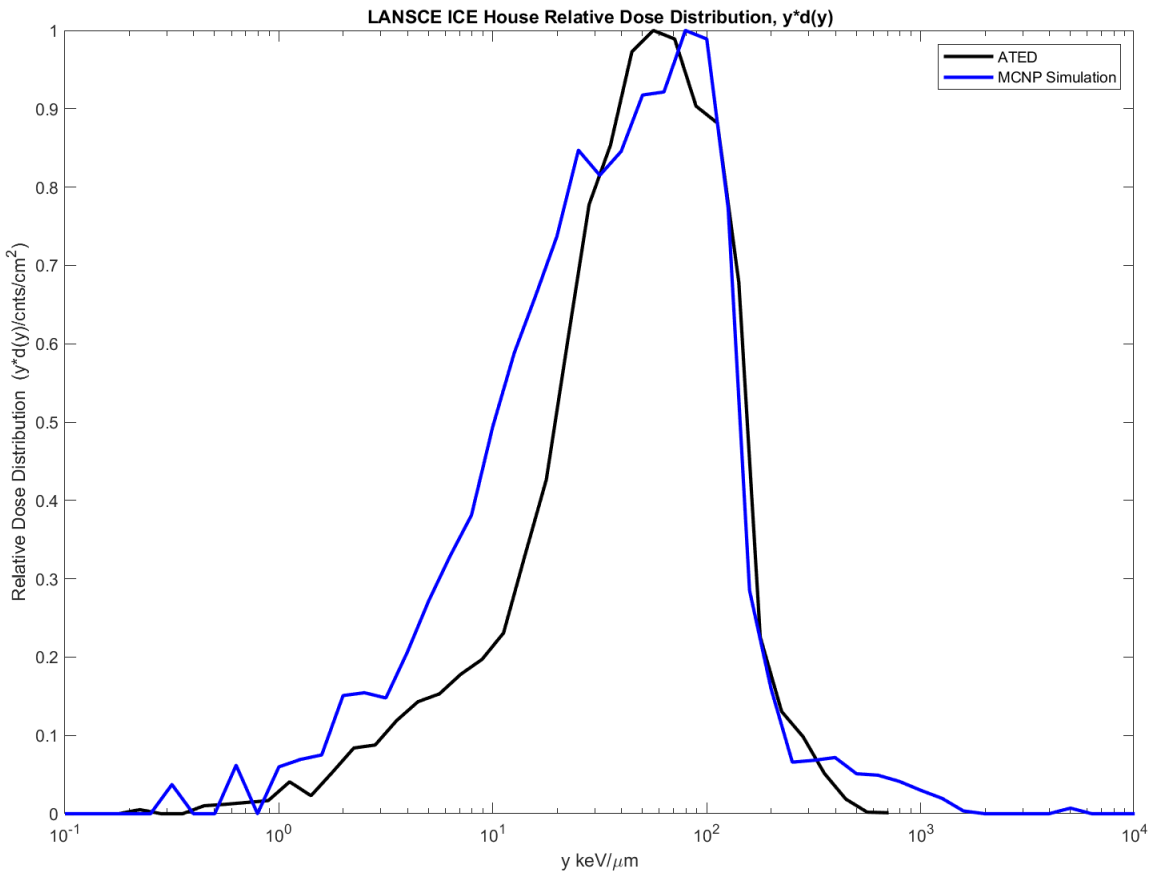

Figure 7.8: The relative dose distribution for ATED and a simulation of ATED at the LANSCE ICE House beamline. The simulation was performed in MCNP_6.2.

Given the limitations of the ATED instrument and the MCNP_6.2 simulation, better agreement is not expected than that seen in **Figure 7.8**. The agreement between the simulated relative dose distribution and that of the ATED at the LANSCE ICE House beamline is further evidence that ATED has the appropriate response to the neutron energy spectrum found at aviation altitudes.

CHAPTER VIII

OFF-AXIS MEASUREMENTS AT HIMAC

A new method for assessing the suitability of materials for use as radiation shielding in spacecraft, and specifically the propensity of materials to produce secondary neutrons due to charged particle interactions has been developed at HIMAC using ATED. Secondary neutrons produced in the hull of spacecraft by GCR are a significant contributor to absorbed dose to personnel inside. The composition and thickness of shielding materials in spacecraft will affect the amount of secondary neutrons produced.

8.1 Introduction and Motivation

Secondary neutrons are produced via nuclear interactions between incoming GCR and the nuclei of shielding materials in a spacecraft. Because neutrons have no charge, they are highly penetrating compared to charged particles. In general, as shielding material thickness is increased, the absorbed dose from secondary neutrons increases [Heilbronn, et al., 2004]. Neutrons are of particular concern because they have been found to be 4 to 5 times more damaging to human tissue than charged particles of similar energies [Cucinotta, 1998].

This method is designed to measure only secondary neutrons produced in different target materials. This is achieved through placing the ATED off-axis of the HIMAC beamline so that the vast majority secondary particles that will reach ATED will be photons and neutrons. ATED is not particularly sensitive to photons (due to the low lineal energy signal they produce), thus only the neutron component is measured. In this way, materials of different depths and atomic compositions can be tested for their propensity to produce secondary neutrons.

8.2 Description of the Experimental Setup

The off axis geometry of this experiment allows for the discrimination of secondary particles vs primary particles of the beam. The magnitude of calculated absorbed dose from measurements then is directly related to the propensity to create secondary particles.

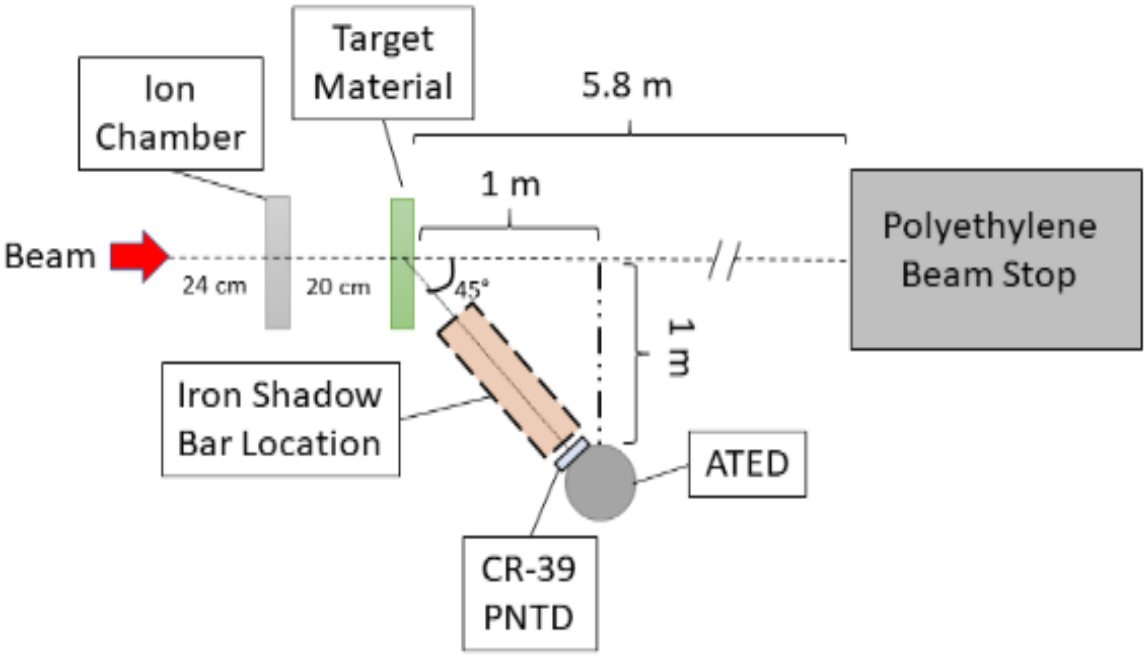

Figure 8.1: Geometry of the off-axis experimental setup. ATED and the CR-39 PNTD are located 45 degrees off the beamline from the target material.

Figure 8.1 shows the geometry of the off-axis experiment. A 2-inch spherical ATED was located 45 degrees off the beamline from the target material. This formed a right triangle with sides of 1m

x 1m. A polyethylene beam stop was located 5.8 m from the target material. For subtraction of background, a 60 cm long bar of iron (called a shadow bar) was placed between the detectors and the target material. An ionization chamber at the front of the beam was used monitoring the beam flux and allowing comparisons between beams of different energy and species.

Although many different secondary particles were created in this experiment, we can assume that only secondary neutrons were being detected by ATED for two reasons. First, any secondary charged particle at this angle will not likely have sufficient energy to reach the detector and can be considered negligible. Second, ATED is not very sensitive to energetic photons.

Measurements of lineal energy spectra by ATED and their relative dose distributions for different target materials were made on January 28-31, 2020. The target materials included: aluminum, high density polyethylene (HDPE), copper, and polypropylene doped with silicon carbide, 20% by weight (PPSiC20). The aluminum, HDPE and copper serve as baseline materials for radiation shielding of spacecraft [DeWitt, et al., 2020]. HDPE is the ideal radiation shielding material because of its high hydrogen percentage. Copper is a worst-case scenario for radiation shielding and serves as an upper limit. Aluminum is widely used in aerospace and is thus included. The beams used were 400 MeV/n carbon, 800 MeV/n silicon, and 650 MeV/n iron.

Comparisons between different targets and beams for the same depth of target material were made. Each target material had a depth of 5g/cm^2 for inter-comparison. Different depths of aluminum were used to demonstrate the function of absorbed dose with increasing thickness. PPSiC20 was compared to baseline materials of the same depth to quantify its usefulness as a space radiation shielding material.

8.3 Shadow Bar Subtraction

The beam stop, where the charged particle beam is stopped, is a large block of iron and cement that produces neutrons that can be measured by ATED. Also, many of the neutrons created in this experiment scatter around the room that the experiment took place in and can possibly contribute to the measurement. In order to ensure that the measured signals from the experiment come from only the target material, an iron shadow bar is used [Hopkins, et al., 1967]. This shadow bar effectively shields the detector from neutrons coming off of the target material so that the contribution of counts from the beam stop and the room can be subtracted. The subtraction of the shadow bar measurement eliminates ambiguity about secondary particles coming from any other source but the target material in the experimental setup.

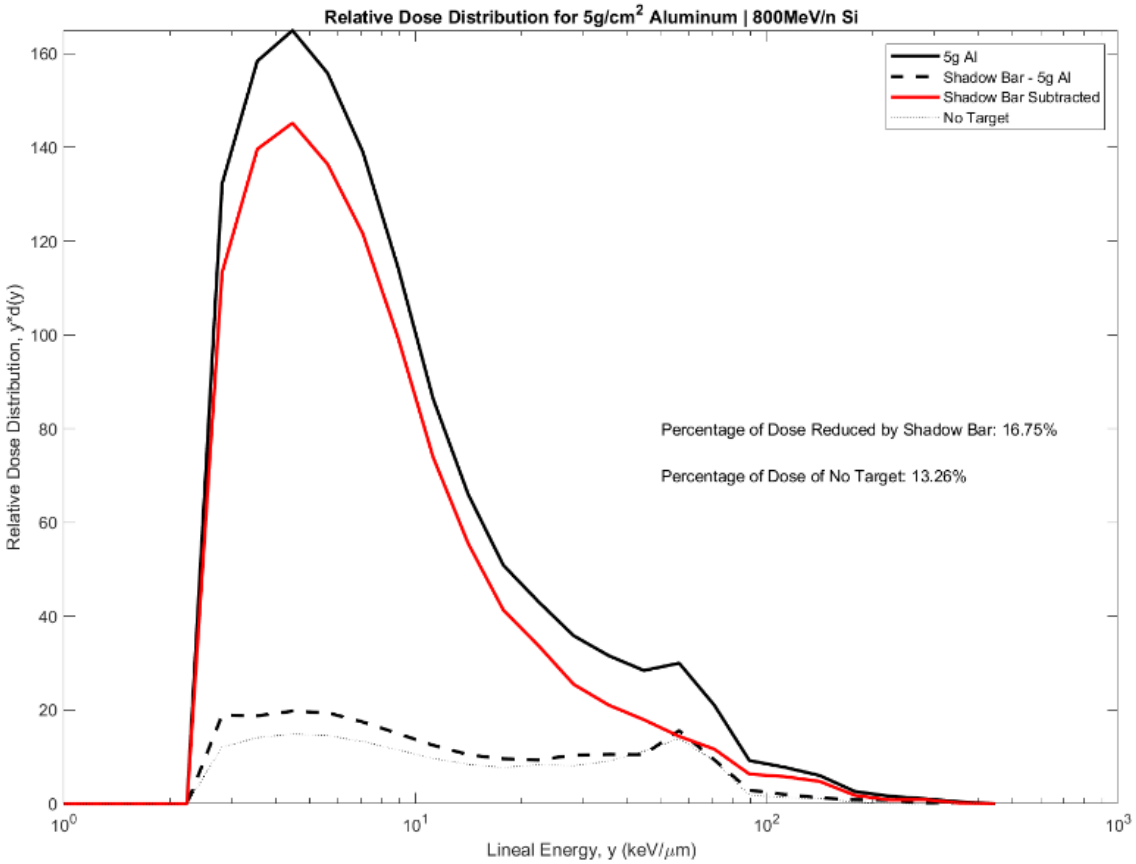

Figure 8.2: The relative dose distribution of 5g/cm^2 aluminum with and without a shadow bar for a 800 MeV/n Si beam.

Figure 8.2 shows the relative dose distribution of 5g/cm^2 aluminum target in an 800 MeV/n silicon beam. Also shown is the relative dose distribution for no target in the beamline. The shadow bar reduced the total absorbed dose by 84.25%. It was then subtracted from the normal measurement as shown in red. The exposure without target (no-target) illustrates that the beam will attenuate though the target material and produce a different scattered secondary neutron flux because the beam reaches the beam stop with more kinetic energy than if it had passed through a target. The no-target measurement will not be suitable for a background subtraction because it produces a different neutron flux than when the beam passes through a target material. Measurements with and without the shadow bar in place were repeated for each target material.

The percentage of reduction of total absorbed dose in each exposure by the shadow bar is shown in **Table 8.1.** In general, the use of the iron shadow bar reduced absorbed dose by about 10% to 20% from the nominal measurement. Each reported exposure has its corresponding shadow bar measurement subtracted.

Beam	**Target (depth of 5g/cm^2)**	**Reduction of Dose**
400 MeV/n C	Aluminum	9.49%
400 MeV/n C	HDPE	10.34%
400 MeV/n C	Copper	8.07%
800 MeV/n Si	Aluminum	16.75%
800 MeV/n Si	HDPE	20.34%
800 MeV/n Si	Copper	15.30%
800 MeV/n Si	PPSiC20	18.13%
800 MeV/n Si	No Target	13.26%
650 MeV/n Fe	Aluminum	8.96%
650 MeV/n Fe	HDPE	14.80%
650 MeV/n Fe	Copper	10.41%
650 MeV/n Fe	PPSiC20	8.64%
650 MeV/n Fe	No Target	8.68%

Table 8.1: Reduction of Dose due to use of the iron shadow bar

In **Figure 8.3** the compilation of all shadow bar and the no target measurements are shown for 800 MeV/n Si. Uncertainty is 6.37 % for measured absorbed dose. The no target measurement was lower for all lineal energies up to 50 keV/µm. After this point, all measurements converge within uncertainty due to low statistics. Once again, this is evidence that target materials effect the beam in a way that is unique to that material.

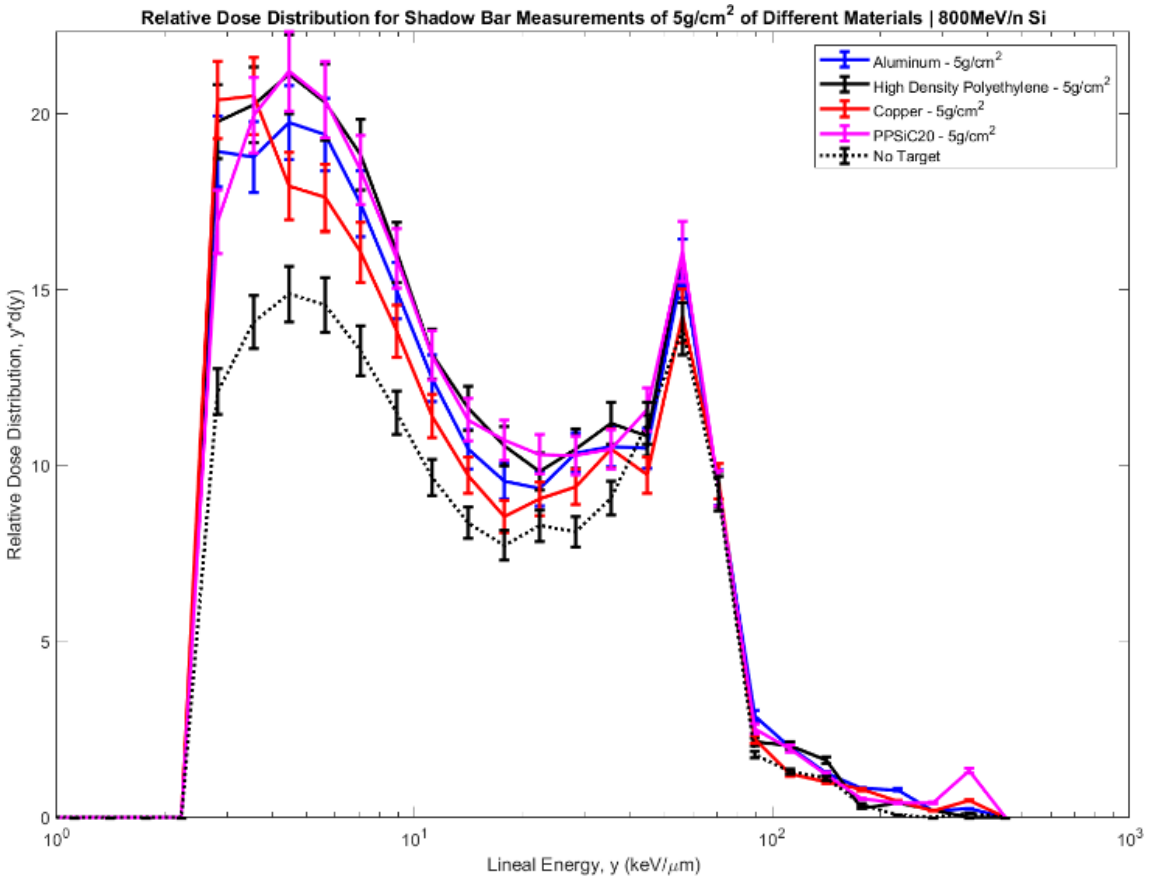

Figure 8.3: Relative dose distribution for all shadow bar and no target measurements.

8.4 Comparison of Different Materials

The relative dose distribution from 800 MeV/n Si incident on 5g/cm^2 of different materials is shown in **Figure 8.4.** Uncertainty is quantified as 6.37% for all points in the relative dose distributions. The HDPE relative dose distribution showed lowest distribution across all lineal

energies. This is because the Low-Z of HDPE reduces the amount of neutrons produced. Copper resulted in the highest absorbed dose across lineal energies greater than ~10 keV/µm. Aluminum fell between these two measurements. This shows a trend that with increasing atomic number (Z) the larger propensity of creating secondary neutrons. The PPSiC20 measurement falls between aluminum and HDPE for lineal energies greater than 10 keV/µm. All distributions agree past 70 keV/µm due to poor statistics.

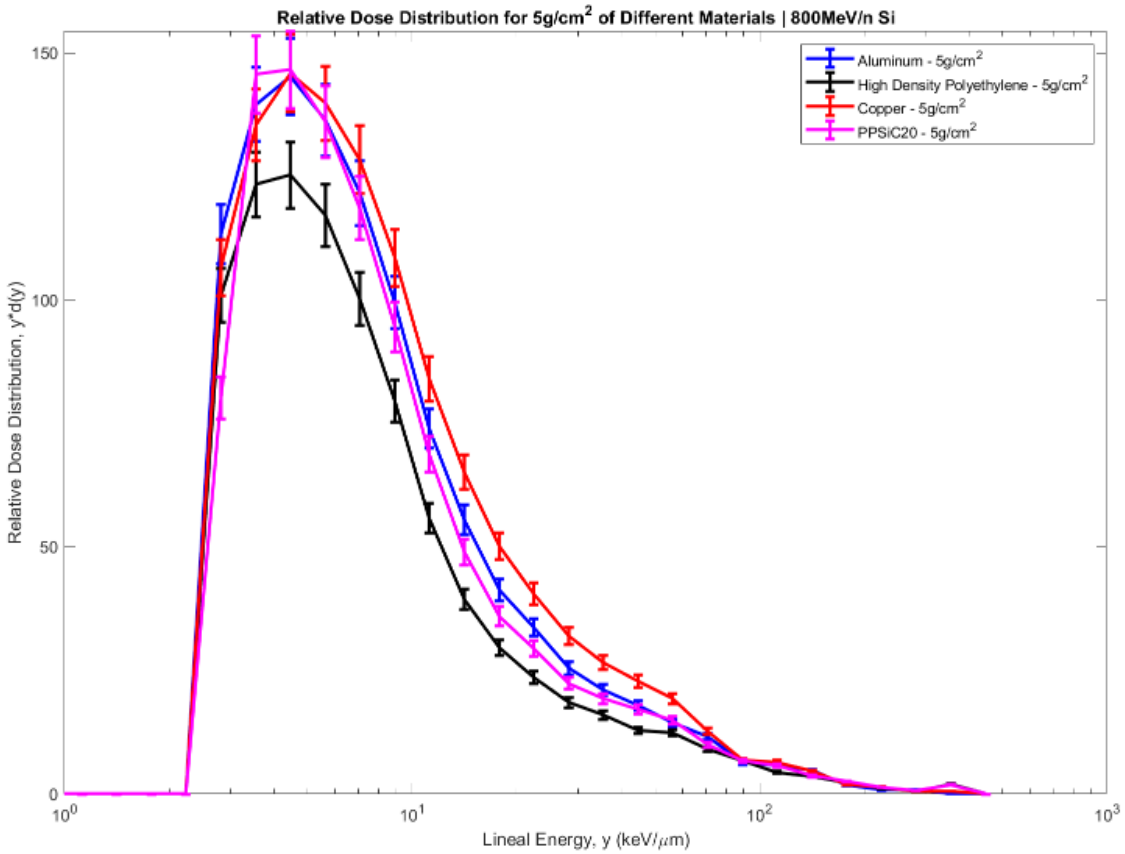

Figure 8.4: The relative dose distribution of 5g/cm^2 of different materials. Incident particles were 800 MeV/n Si.

Figure 8.5 Shows the relative dose distribution of 5 g/cm^2 of different materials for 650 MeV/n Fe. Once again, there is a trend towards larger absorbed dose with increasing Z. Below 8 keV/µm, only HDPE is outside of uncertainty of the other three materials. Above this, we see a similar trend that was seen in the 800 MeV/n Si measurements.

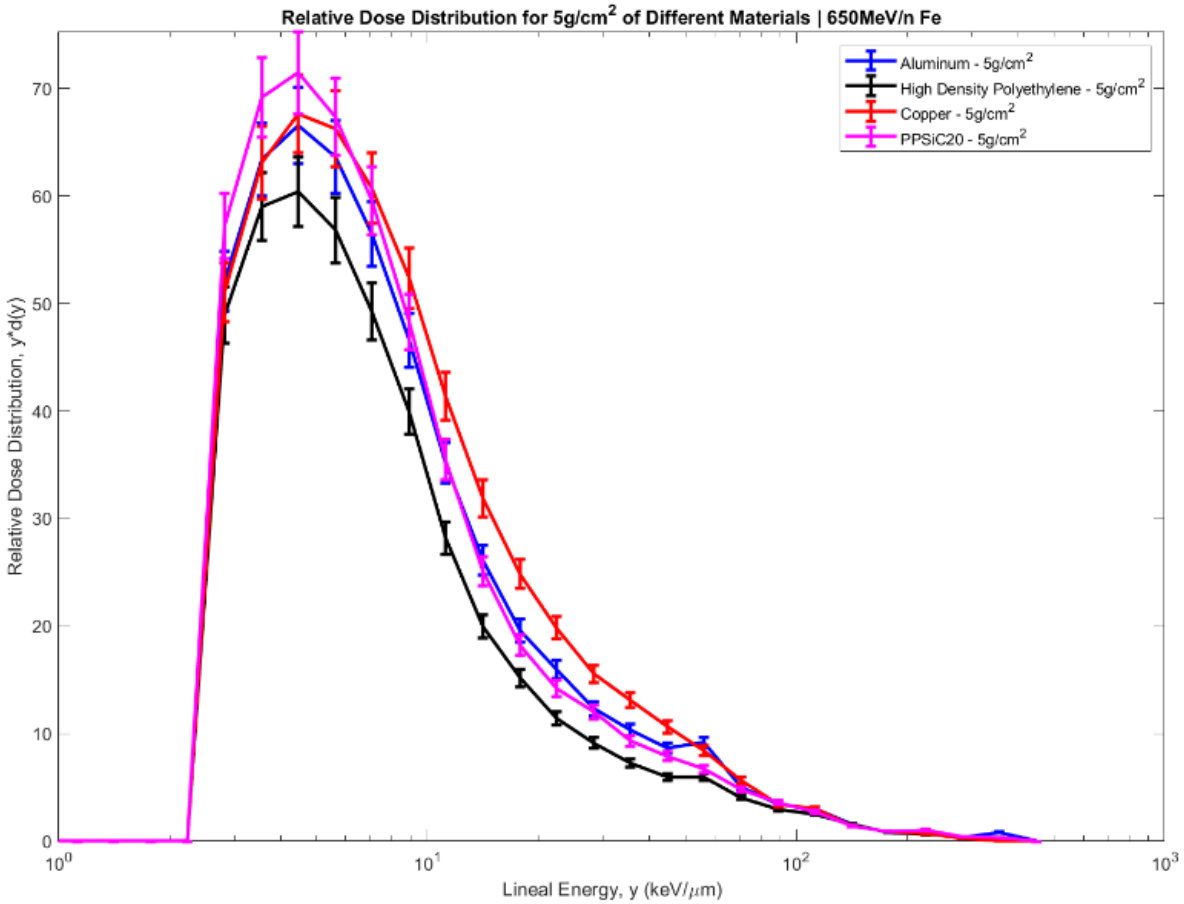

Figure 8.5: Relative dose distribution for 5g/cm^2 of different materials for 650 MeV/n Fe.

The expected behavior seen in the relative dose distributions shown in **Figure 8.5** demonstrate that materials with larger atomic numbers produce more secondary neutrons and indicates that the off-axis technique is a viable way to test potential space radiation shielding materials.

These relative dose distributions look very different than other neutron measurements shown in this dissertation. The reason why is because the neutrons being measured by ATED have a very high kinetic energy compared to the previous measurements in Chapters 9 and 10. The peak is shifted to lower lineal energies because higher energy neutrons produce recoils in the ATED that also have a higher mean kinetic energy. More energetic recoils have a correspondingly smaller LET, thereby shifting the peak in the relative dose distribution to a lower lineal energy than what has been shown before.

8.5 Comparison Between Beams

Ionization chamber counts were calibrated for each beam. This allows for proper normalization between the three beams. Comparisons were made for the same depth of the same target material to show how the propensity of producing secondary neutrons changes with incident particle charge and energy.

Figure 8.6 shows the relative dose distribution for 5 g/cm^2 of aluminum for each beam. The contribution to dose from 650 MeV/n Fe is drastically higher (10^2-10^3) than the carbon or silicon beams. The main difference between the carbon and silicon relative dose distributions lies below 10 keV/µm where silicon contributes more to total absorbed dose. Beyond this lineal energy, there is good agreement in measurements made to the carbon and silicon beams.

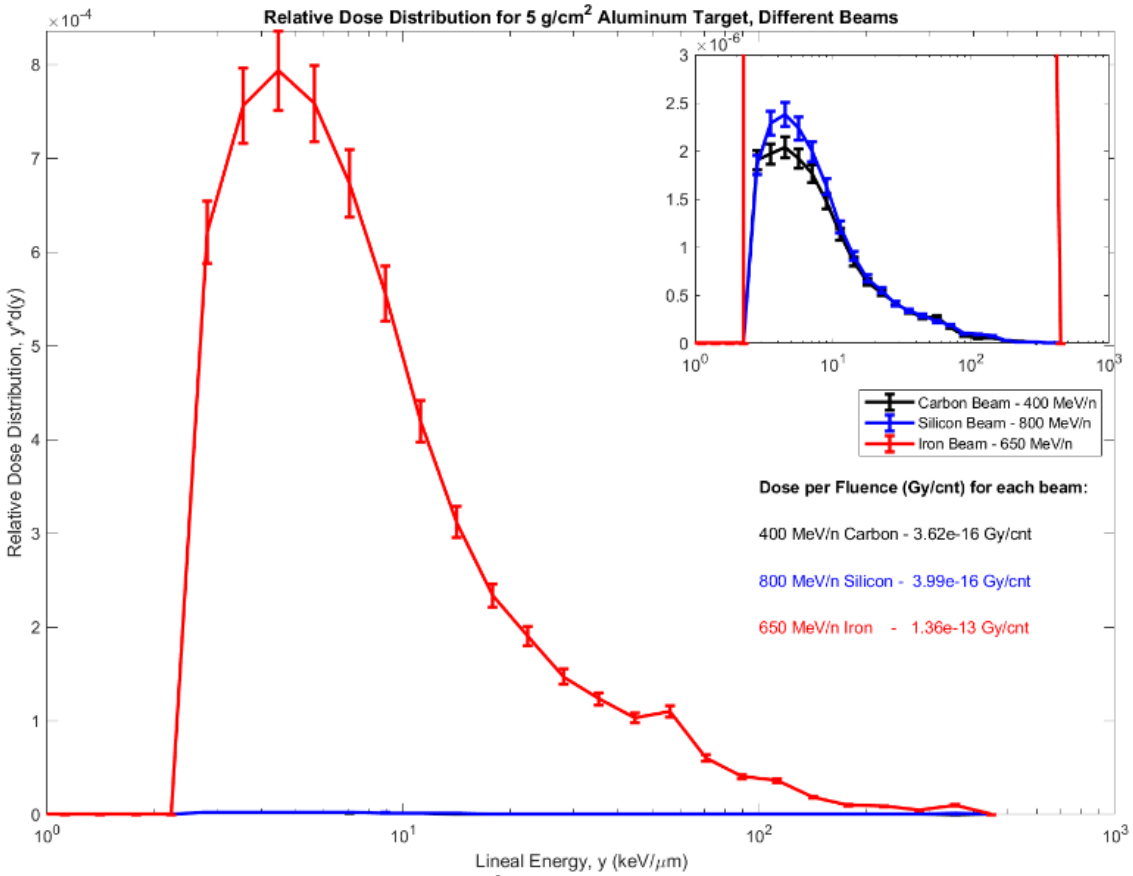

Figure 8.6: The relative dose distribution for 5g/cm^2 of aluminum across three different beams. Carbon and silicon beams are set on a different scale in the top-right. Also, the dose per fluence for each beam is shown.

Figure 8.7 shows the relative dose distribution for 5 g/cm^2 of HDPE. Once again, the contribution to absorbed dose from the iron beam is much higher than the silicon and carbon beams. There is almost no difference seen below 10 keV/µm between the carbon and silicon. This is possibly due to the lower propensity of HDPE to produce secondary neutrons than aluminum. This lower propensity could cause low statistics across relevant lineal energies thus accounting for the apparently good agreement seen.

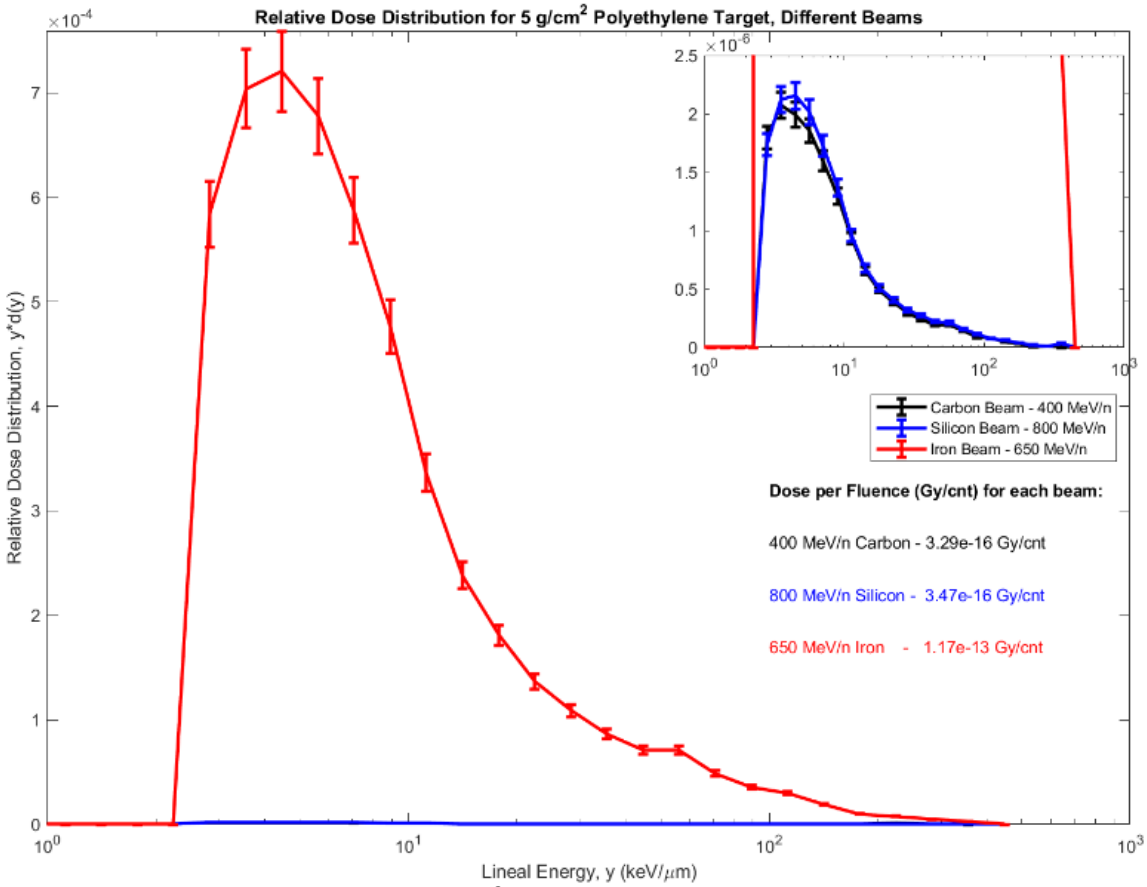

Figure 8.7: The relative dose distribution for 5g/cm^2 of HDPE for the three different beams. The dose per fluence for each beam is shown.

Figure 8.8 shows the relative dose distribution for 5 g/cm^2 of Copper. Similar trends are seen in this relative dose distribution. The difference between the silicon and carbon beams are more pronounced here than for HDPE or Al. For lineal energies up to 100 keV/µm neutrons from carbon contributes less to absorbed dose than do those from the silicon beam. Beyond this lineal energy, both the carbon and silicon relative dose distributions agree well.

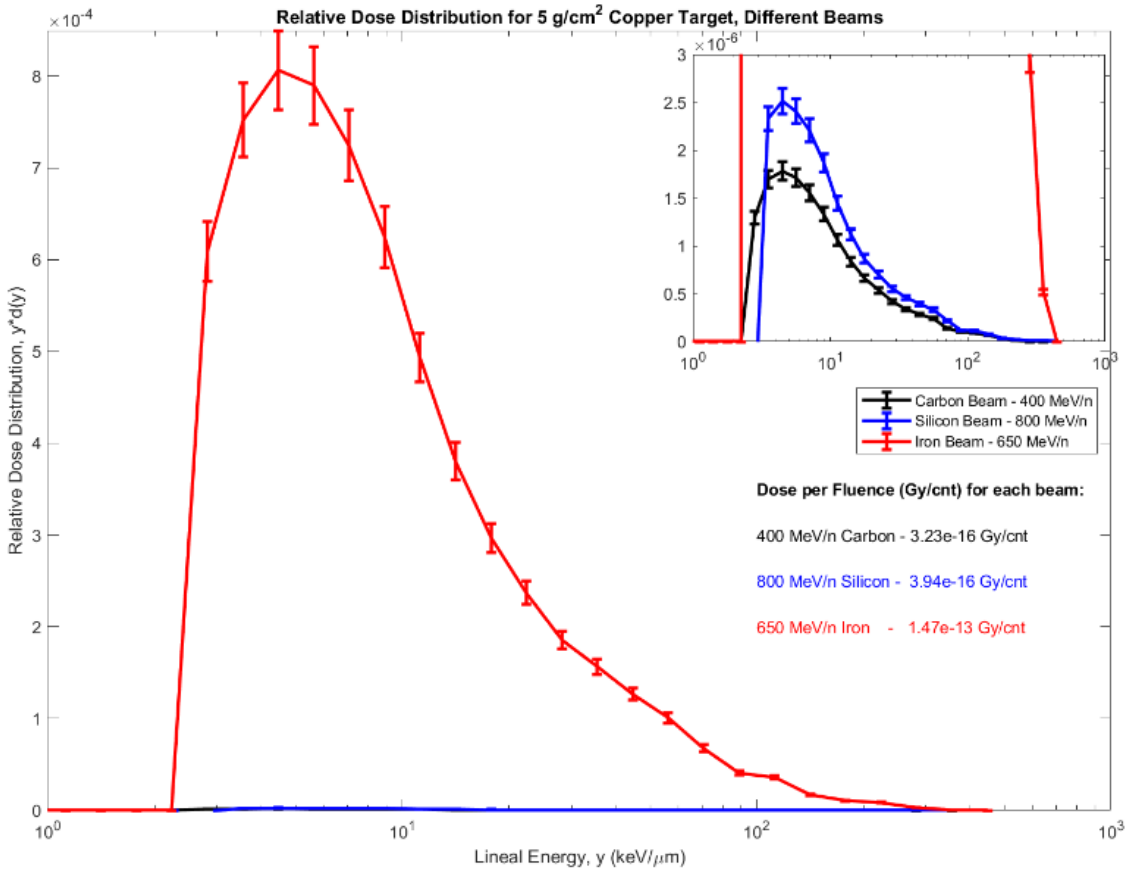

Figure 8.8: The relative dose distribution for 5g/cm^2 of copper. All three beams are shown along with their corresponding dose per fluence.

In each case, the absorbed dose from the 650 MeV/n iron beam showed ~100 times more absorbed dose than the other two beams. Carbon generally contributed less towards absorbed dose than silicon. This appears to demonstrate that increasing the atomic number of the beam increases the number of secondary neutrons produced.

8.5 Depths of Aluminum

Different depths of aluminum were tested to show how the propensity of producing secondary neutrons changes with varying depth of material. Aluminum was chosen for its wide use and large range of depths in spacecraft. Each measurement was normalized to fluence. Shadow bar

measurements were not made for each depth of aluminum. Thus each measurement has not been accounted for secondary neutrons scattered throughout the rest of the beam exposure room.

Figure 8.9 shows the absorbed dose per fluence (Gy/cnt) as a function of depth for various beams. Also included are the no-target runs for 0 g/cm^2. Measurements from the 650 MeV/n iron beam have been reduced by 100 for visualization purposes. A linear relationship is seen for both the silicon and iron beams for depths between 2.5 and 7.5 g/cm^2. For these depths an increase in the depth of aluminum results in an equal increase in absorbed dose per fluence within ATED confidence limits. The carbon beam has insufficient data to make the same claim.

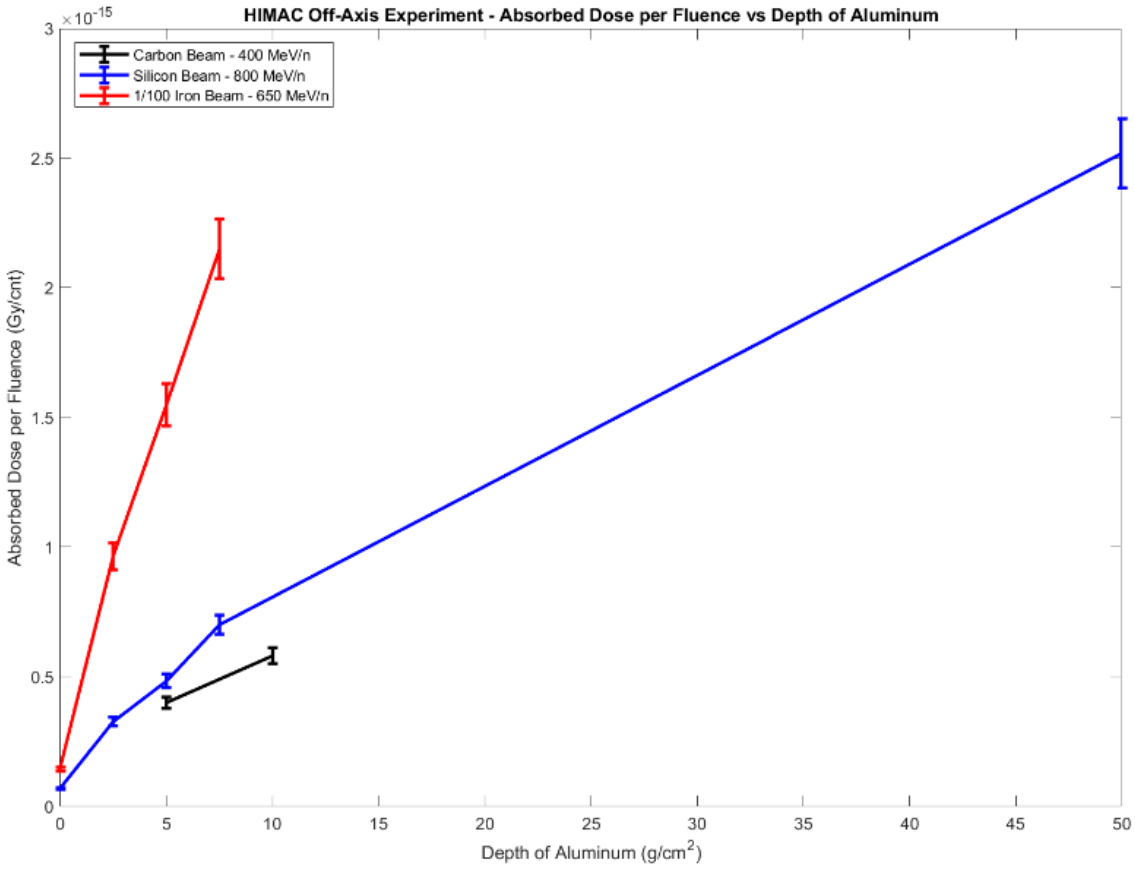

Figure 8.9: Absorbed dose per fluence as a function of depth of aluminum. As more material is placed in the beam, the more propensity of creating secondary neutrons.

This linear relationship is possibly due to the nuclear cross sections staying nearly the same as the primary particles traverse these depths of aluminum. In other words, the incident particles are not slowing down enough in the target material to drastically change these nuclear cross sections and

thus the propensity of creating secondary neutrons. The slope of these lines may also change with particle energy and species. The relative dose distributions for each of these measurements show the same trend. The main difference between them is their magnitude and thus only their absorbed dose per fluence are shown here.

With 50 g/cm^2 of aluminum in the 800 MeV/n silicon beam this relationship is no longer linear. The beam was stopped in this material and is a worst case scenario for producing secondary neutrons. Future experiments should explore the relationship of varying depths of HDPE and other relevant materials.

CHAPTER IX

MEASUREMENTS TAKEN ON THE INTERNATIONAL SPACE STATION WITH THE ACTIVE TISSUE EQUIVALENT DOSIMETER

The flight model of ATED was sent to the International Space Station on 21 May 2018. This experiment continuously measured the lineal energy spectrum and absorbed dose as functions of time with ~30 second resolution [Benton, et al., 2019]. The primary aim of this experiment was to demonstrate the operational capability of ATED as a space radiation dosimeter. Measured dosimetric data was correlated with time, the ISS orbital position, and altitude. With this information, ATED quantified the average absorbed dose rate from the entire ISS orbit, trapped protons in the SAA, trapped electrons at high latitudes, and the GCR region. The measured data was also separated by regions inside and outside of the SAA. Calculated absorbed dose values were compared to model predictions made with the On-Line Tool for the Assessment of Radiation In Space (OLTARIS) [Singleterry, et al., 2010]. The ATED lineal energy spectra were converted using two different methods into a corresponding LET spectra. These LET conversions were tested in the space radiation environment to possibly compare measurements with instruments that directly measure LET. Finally, an analysis of the operational performance of the

instrument provided information that will be useful in improving future ATED models and identifying lessons learned.

9.1 Description of the Experiment and Hardware

The ISS version of ATED utilized a 3-inch diameter acrylic spherical shell as the ionization cavity inside the detector head. This diameter shell was enlarged over other ATED models to maximize the cross-sectional area of interaction with rare high-energy heavy ions [Causey, 2018]. The active volume simulated a 2 μm diameter spherical tissue phantom. **Figure 9.1-3** shows the whole ATED instrument, the ATED active volume, and the various electrical components. The spectrometer used was an Amptek Pocket MCA-8000D that communicated with a Raspberry Pi single board computer for data acquisition. The experiment was originally planned to operate for six months with short interruptions to download data from the Raspberry Pi to ISS laptops for downlink. An 8K channel spectrum was saved every 30 seconds onto an external 32GB SDRAM Card. The ATED mass was 3.22 kg and had external dimensions of 25.5 cm x 15.8 cm x 9.0 cm. Voltage was supplied from the ISS 120 VAC inverter. ATED consumed a total of 7.6 W of power. Each electrical component was surrounded by a separate Faraday cage to minimize electrical noise. 3D printed plastic was used to insulate and secure each electrical component. The Oklahoma State University Physics and Chemistry Instrument Shop was responsible for the design and manufacture of much of the final ATED supporting structure.

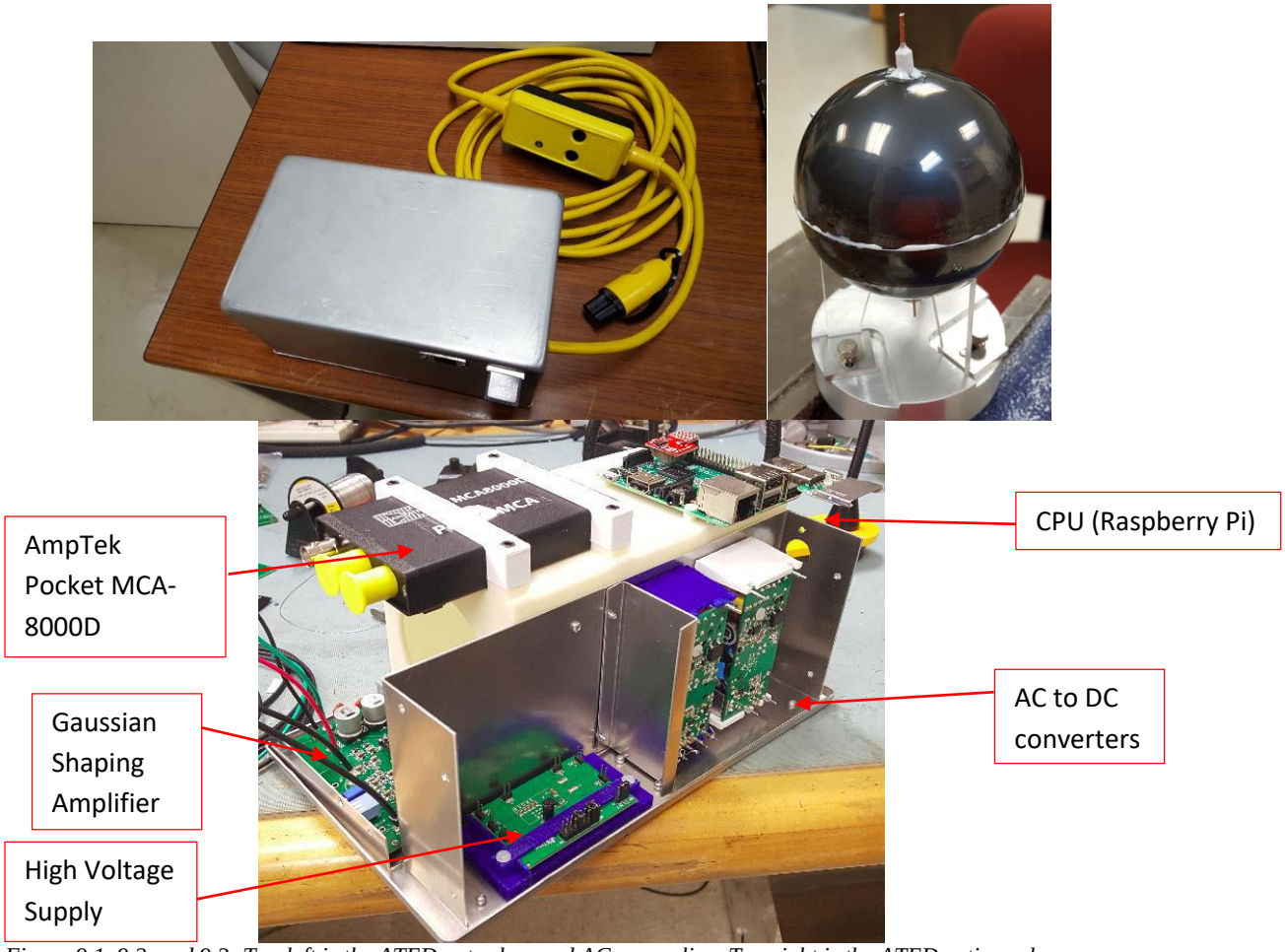

Figure 9.1, 9.2, and 9.3: Top left is the ATED outer box and AC power line. Top right is the ATED active volume showing the acrylic shell and the central wire holders. Bottom is the inside of the ATED box, showing the various faraday cages for each electrical component.

The operating system on the Raspberry Pi was an up-to-date Raspbian operating system from an online repository. Raspbian is a Linux (Debian-based) operating system that was found to be suitable for the ATED ISS experiment. All unnecessary software features were removed to limit power consumption. Every 30 seconds the Raspberry Pi communicated with the Amptek MCA-8000D via serial connection to receive the current measured spectrum and restart data acquisition. The data taken from the MCA was then time-stamped and stored onto the local hard drive and external SDRAM card.

ATED underwent extensive electromagnetic interference (EMI) testing by NASA at the Johnson Space Center in Houston, Texas. NASA mandates that EMI be below a given threshold in order

to not interfere with other mission-critical systems on the ISS. ATED successfully passed all EMI tests before being sent to the International Space Station.

ATED was calibrated before the flight using a combination of gamma and neutron sources. This allowed for the use of both the electron and proton edge as calibration points (See Chapter 4.7). This resulted in the calibration function: $y(ch) = 0.590 * ch - 0.11$ [Causey, 2018]. The original plan was to use mono-energetic beams of particles from HIMAC for calibration. Loss of the original flight instrument shortly before the flight required another means for calibration [Benton, et al., 2019]. Absorbed dose in tissue was calculated using the above calibration function.

The location that ATED took measurements on the ISS was on the Tranquility (known as Node-3) ISS module. **Figure 9.4** is a picture of ATED inside Node-3 after installation. Node-3 contains environmental controls, a toilet, life support systems, exercise equipment and observation windows [NASA, 2009]. This location was choosen to monitor absorbed dose on station where the astronauts spend a significant portion of their time. Additional velcro anchors were placed next to ATED for the Rad Detector and IV-TEPC for inter-comparison of absorbed dose values. Information on these instuments can be found here [Rios, 2015; Flores-McLaughlin, et al., 2012]. These instruments were not installed while ATED was active.

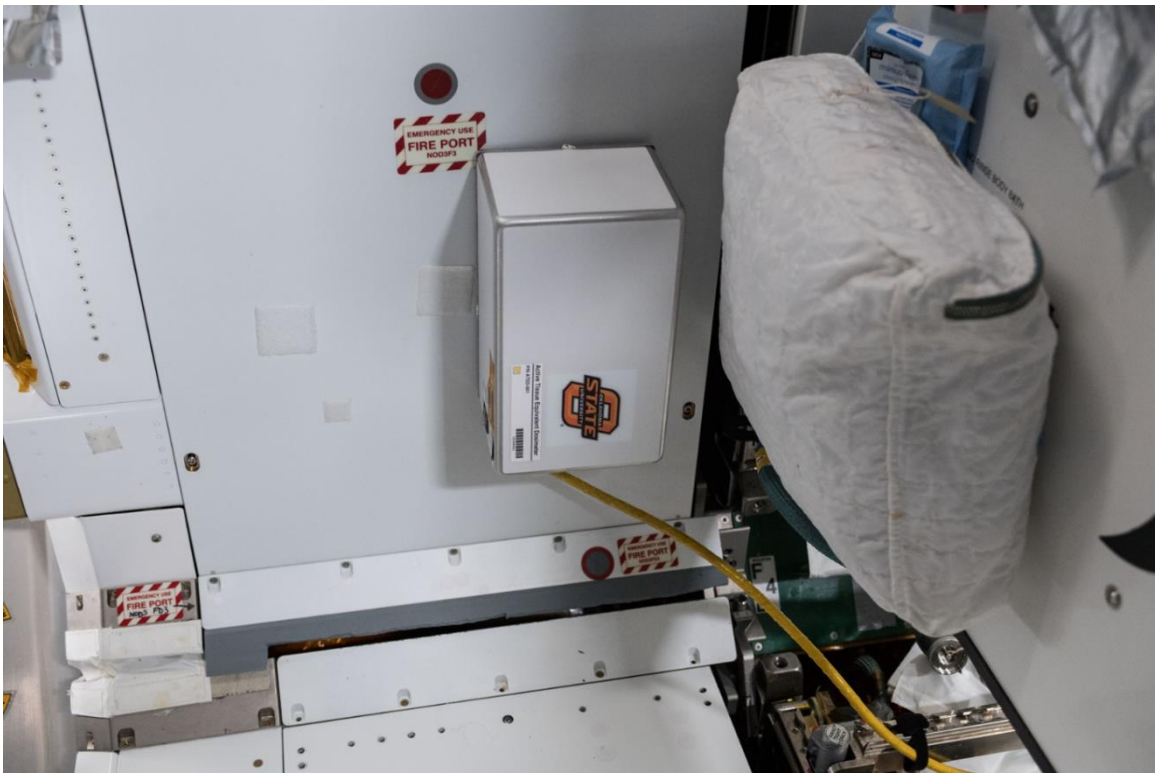

Figure 9.4: The ATED on ISS. ATED was located in Node-3. Additional instruments were to be placed next to ATED for comparison of measurements.

Figure 9.5 shows a more detailed view of the ATED location inside Node-3 as provided by Boeing. The shielding distribution around ATED at this location is not well known and can vary with time. The distribution of mass surrounding ATED was most likely eccentric and composed of several different materials. Radiation detectors are normally located in one of the lab modules, where shielding distributions have been modeled extensively [Norman, 2019]. Node-3 is somewhat unique in that it holds almost no scientific instuments. It can be assumed that the distribution of mass inside Node-3 is less than the lab modules because of the lack of various racks holding scientific equipment. Sheilding inside the lab modules can reach up to 50 g/cm^2 in depth [Badhwar, et al., 2001]. The adjacent module and wall are used for storage of supplies and waste [NASA, 2015]. As supplies and waste are moved to different locations, the distribution of mass around ATED would change. It is a non-trivial feat to model this problem and is outside the scope of this dissertation.

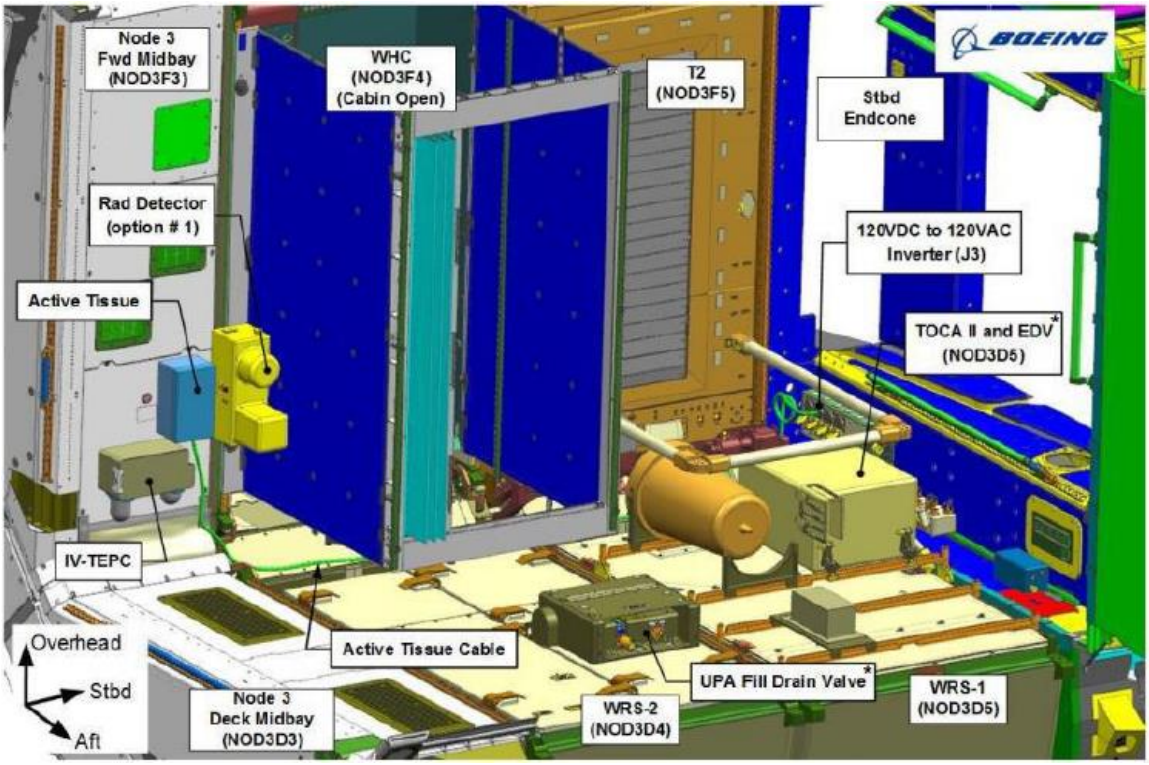

Figure 9.5 Detailed look inside Node-3 of the ISS. The location of ATED (labeled "Active Tissue" in this diagram) and the radiation instruments are next to the Waste Housing Compartment (WHC).

The location of Node-3 on the ISS is highlighted in **Figure 9.6**. The ISS as a whole will contribute to the mass distribution surrounding ATED. All that can be said is that the mass distribution in and around Node-3 is highly variable and complex. When comparing ATED measurements to the OLTARIS model, an assumption about the shielding surrounding ATED must be made. The most conservative estimate than can be made at this time is a uniform distribution of aluminum surrounding ATED. This assumption was used in comparisons between ATED measurements and OLTARIS model calculations in Section 9.3.

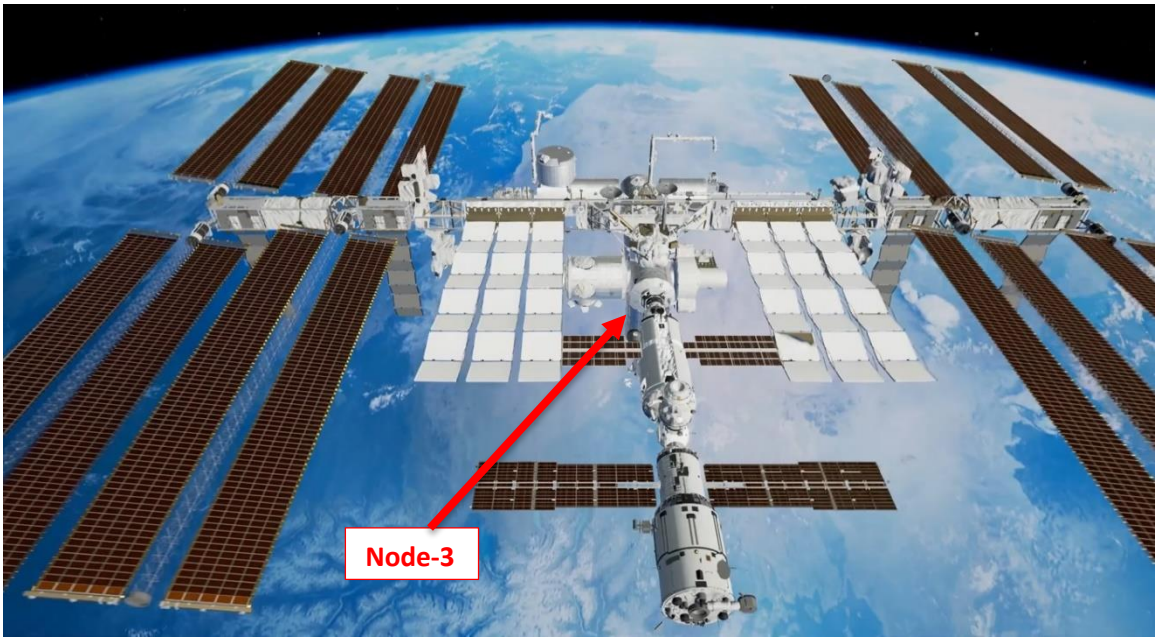

Figure 9.6: The location of Node-3 on the ISS. The shielding distribution around Node 3 is highly eccentric and not well known. Picture adapted from [ROADTOVR, 2017].

9.2 Results from ATED Measurements

ATED was installed and started taking data on the 14th of July, 2018 in Node-3 of the ISS [Keeter, 2018]. The data reported here is limited to the dates of 16 – 20 July 2018, a total duration of 4.5 days. Good quality data was lost after 12:10:17 on 20 July. ATED was turned off and inspected on September 24th, 2018, over concerns that no new data files were being transferred during downlink [Keeter, 2018]. The ATED external SD card reader was damaged and thus data could not be read off of the instrument. It is thought that this damage arose in large part of ATED's location in a crew translation pathway (high traffic area). The unit was sent back to Earth and all data files were recovered from the Raspberry Pi hard drive. Data quality assessment was done on 257,577 data files. Of these files, 13,064 were found to contain good quality data.

Many files were contaminated with possible microphonic or electrical noise. This produced lineal energy spectra dominated by apparent spurious counts or no counts at all. Attempts were made to compensate for the anomalous readings found in the remaining data files, but this effort was

unsuccessful. ATED was anchored to the Node-3 forward Midbay, directly next to the Waste Housing Compartment (WHC). The WHC uses a series of fans to push human waste into compartments. It has been reported by astronauts that the fans used in the WHC when turned on are very loud [Hadfield, 2013]. It is possible that the fans that operate the WHC were a source of microphonic noise in ATED measurements. Liquid waste is funneled into the Urine Processing Assembly (UPA), which is part of the Water Recovery System (WRS) that recycles urine into potable water. On July 20 (the day that good quality data was lost) the WHC underwent routine maintenance [Keeter, 2018]. This was probably the reason why data suddenly degraded in quality after 12:10:17 on 20 July. Data continued to be erratic until 23 July while maintenance on the WRS and WHC continued. From 23-July to 13-August data files were completely empty. Low quality data then returned for the remainder of the time ATED was operational. ATED was not operational upon return to lab.

Absorbed dose rate in tissue as a function of time was found for those dates in which good quality data exists. Data was smoothed by averaging over ± 5 minutes, as shown in **Figure 9.7**. There is a sinusoidal fluctuation in absorbed dose rate below 1 μGy/min. This fluctuation is due to the ISS traversing the magnetic equator and reaching its most southern or northern latitudes. The direction of the magnetic field lines over the equator is parallel to the surface of Earth and the ISS orbit. This means that incoming GCR will be deflected towards the poles with the greatest magnitude over the equator. At the magnetic poles, the field lines are perpendicular to the surface of Earth. Thus, deflection of GCR decreases as the distance from the magnetic equator increases. The minima in absorbed dose rate below 1μGy/min is because of the direction of the magnetic field is deflecting the most amount of incoming GCR. At higher latitudes, the direction of the magnetic field changes such that incoming GCR are deflected to a smaller degree. This accounts for the maxima seen below 1 μGy/min, when the ISS reaches its most Southern or Northern

approach to the poles. In addition, trapped electrons in the outer Van Allen belt will indirectly contribute to absorbed dose rate at higher latitudes via bremsstrahlung.

The large intermittent spikes in absorbed dose rate are due to the ISS passing through the SAA. This is where the inner radiation belt penetrates the ISS orbit due to the non-concentricity of the Earth's magnetic field. Protons in the SAA have kinetic energy up to 250 MeV [Benton, et al., 2001]. These protons will penetrate the ISS outer hull and directly contribute to absorbed dose as measured by ATED. SAA Protons can also produce secondary target fragments in the hull of the ISS that will also contribute to absorbed dose. Absorbed dose rate inside the SAA increased anywhere from 4 to 10 times than the rest of the ISS orbit. The ISS was observed to pass through the SAA 2 to 5 times each day. The variation in the magnitude of these spikes is due the non-uniformity of the SAA. The SAA has the approximate shape of an inverted cone whose point is closest to Earth [Benton, et al., 2001]. If the ISS would pass directly though the center of the SAA, we would see a much larger increase in dose rate than if it skimmed its outer limits.

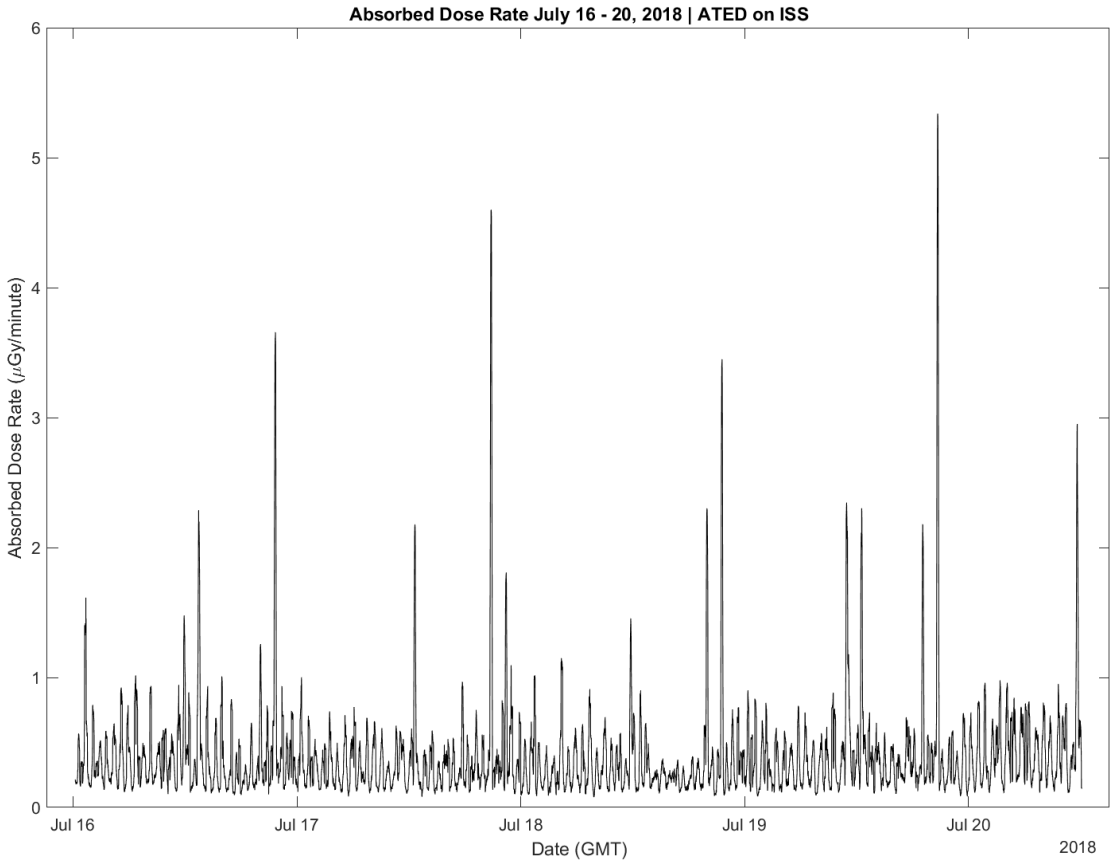

Figure 9.7 Absorbed Dose Rate as a function of time for ATED on the ISS. The fluctuation below 1 μGy/minute is due to the ISS traversing the equator and moving towards the poles. Intermittent large spikes are from the ISS passing through the SAA. Total absorbed dose was 3.1815 ± 0.2672 mGy for this period.

Calculated absorbed dose in tissue for each day (24 hours) of quality data is shown in **Table 9.1**. Total absorbed dose for July 16-20, 2018 was 3.18 ± 0.27 mGy. These results are consistent with what is seen by other radiation detectors exposed aboard ISS in the past [Flores-McLaughlin, et al., 2012; Rios, 2017]. Unfortunately, there is no available data from other tissue-equivalent detectors aboard the ISS for the period ATED was operational to compare absorbed dose values.

Date (GMT)	*ATED Calculated Absorbed Dose (mGy)*
07/16/18	0.76 ± 0.06
07/17/18	0.69 ± 0.06
07/18/18	0.53 ± 0.04
07/19/18	0.80 ± 0.07
*07/20/18**	0.40 ± 0.03
Total (4.51 days)	3.18 ± 0.27

Table 9.1: Absorbed dose for each day ATED was on ISS. (*) Data was lost after 12:10:17 on July 20th.

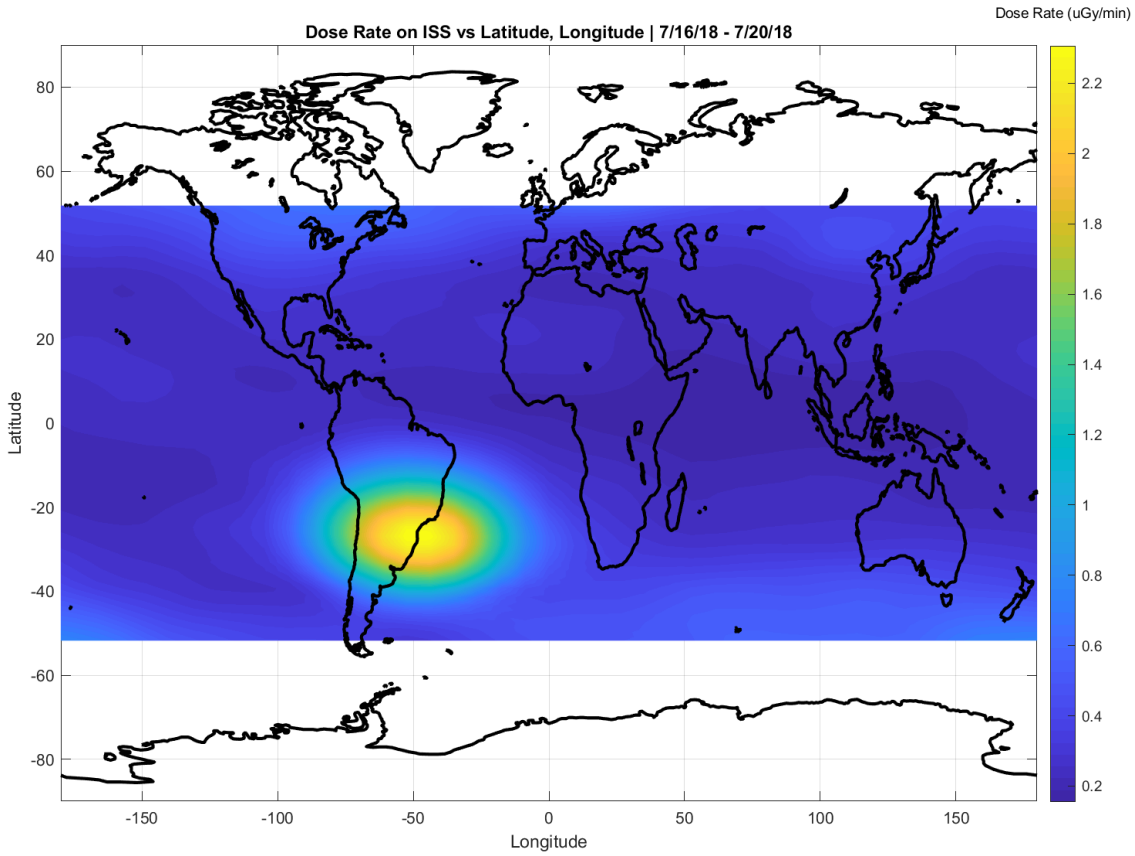

Figure 9.8: A linearly interpolated LOWESS fit of absorbed dose rate as a function of latitude and longitude. An exponential increase in absorbed dose rate is seen over the South Atlantic Ocean and South America. Also, elevated absorbed dose rates are seen close to the poles.

Orbital position data (latitude, longitude, and altitude) for the ISS during the time ATED was operational was provided by the NASA Space Radiation Analysis Group (SRAG) [Rios, 2019]. SRAG data was linearly interpolated to match ATED data to find orbital position, absolute magnetic field strength, and the McIlwain L-Shell parameter. A lowest regression fit of absorbed dose rate as a function of latitude and longitude is shown in **Figure 9.8.** The large increase in absorbed dose rate over the South Atlantic region is clearly seen. The offset of Earth's magnetic field causes trapped protons in the inner belt to penetrate into the ISS orbit, causing this significant increase in absorbed dose rate [McCormack, et al., 1987]. Absorbed dose rates at the center of the SAA are roughly 10 times larger than near the magnetic equator. The shape of the SAA in **Figure 9.8** was not expected to have a simple elliptical shape. The fixed time resolution of ATED measurements (30 s) smeared out the detail of the SAA outer bounds. Instruments in

LEO typically increase their measurement frequency when a large flux of particles is detected. This increase in time resolution allows for increased spatial resolution as well.

Absorbed dose rate in the Electron Cusp region over North America and the South Indian Ocean is roughly 2-3 times larger than over the geographic equator. Trapped electrons in the outer belt come closest to the surface of Earth in this region. Note that the maximum energy of these electron is about 6 MeV [Benton, et al., 2001]. These electrons are not able to fully penetrate the hull of spacecraft and directly contribute to absorbed dose. Instead, the rapid slowing of these electrons produces Bremstrulung that will then contribute to absorbed dose. The orientation of the Earth's magnetic field at these latitudes will also increase the GCR component.

The probability distribution of counts as a function of lineal energy (p(y)) on a log-log scale for the ISS ATED is shown in **Figure 9.9**. Uncertainty is quantified as the standard deviation of counts per unit time. Area under this curve is equal to unity. The probability distribution shows a mostly monotonic decrease in counts with increasing lineal energy. The first channel has lowered counts due to the lower level discriminator in the AmpTek 8000D MCA. The channels below this lineal energy were dominated by noise and were neglected in order to reduce dead time. The proton edge is seen at 150 keV/μm, where p(y) decreases significantly. This is the value of lineal energy where protons deposit the maximum amount of energy into the ATED active volume. Above this value, single proton events will not contribute to the ATED spectrum. This feature is expected to arise because of the large relative abundance of protons in the GCR spectrum and SAA. The large abundance of protons will contribute to counts in channels only below 150 keV/μm, which will resolve the steep drop-off of counts at 150 keV/μm. The significant decrease in counts at 150 keV/μm is strong evidence of a proton dominated radiation field like expected for the radiation environment in the ISS orbit. Also, secondary neutrons created in the ISS hull by high energy protons via nuclear target fragmentation can interact with the ATED active volume and produce recoil protons. This will further the definition of the proton edge. It is

not possible to discriminate with current ATED instruments whether primary or secondary protons are the result of a measured event.

From 150 keV/µm up to 1000 keV/µm we see the contribution of HZE particles from GCR. Poor statistics exist at high lineal energy due to the rarity of the particles that contribute to this part of the spectrum. Secondary neutrons can also contribute to dose in this region of lineal energies through recoil nuclei inside the ATED active volume. These event are also rare, and cannot be distinguished from a HZE GCR. No particle edges are seen in this range of lineal energies as they are exceedingly difficult to resolve even under highly controlled circumstances. No particles were measured with lineal energy exceeding 1000 keV/µm.

An unexpected peak is seen at 70 keV/µm and is of unknown origin. The entire p(y) spectrum is expected to be monotonic because the fluence of particles decreases rapidly with increasing LET. Minimum ionizing particles have peaks in LET, but the chord length distribution of ATED would smear these peaks across a large range of lineal energy and preserve the monotonic nature of the spectrum. Also, there are no peaks of minimum ionizing particles that would account for a peak in ATED measurements around 70 keV/µm. Elements like C, N, O, and Ne with kinetic energy in the broad peak of GCR fluence (~10^2 MeV/n) have LET values in this range. However, the relative abundance of these elements in the GCR spectra will not likely allow for a peak to manifest itself. Protons overwhelmingly contribute to ATED measured spectra and occlude any HZE GCR up to 150 keV/µm. The distribution of shielding around ATED in Node-3 could also have some influence on the peak seen at 70 keV/µm. If the distribution of mass around ATED was highly non-uniform, it is possible that lower energy particles could enter through a "window" of low shielding and be measured around 70 keV/µm.

The artifact seen at 70 keV/µm is most likely the result a problem with the instrument and not a phenomenon of the measured environment. It has been seen in lab that some ATED active

volumes produce spurious counts in a distribution around a point. The number of spurious counts, their location in the spectrum, and frequency is random. This is considered a feature of a damaged or low quality active volume. It is possible that damage incurred to the ATED active volume while on the way to or on the ISS. This damage possibly put spurious counts in a distribution around 70 keV/µm, resulting in the observed peak. The data used to calibrate ATED before flight also had unexpected peaks in the calibration neutron spectrum. No peak is seen at 70 keV/µm, but the spectrum did not have an expected monotonic trend as expected for neutron measurements. Unfortunately, the ATED detector head was not operational upon return to conduct further tests. More work and tests are needed to verify these interpretations.

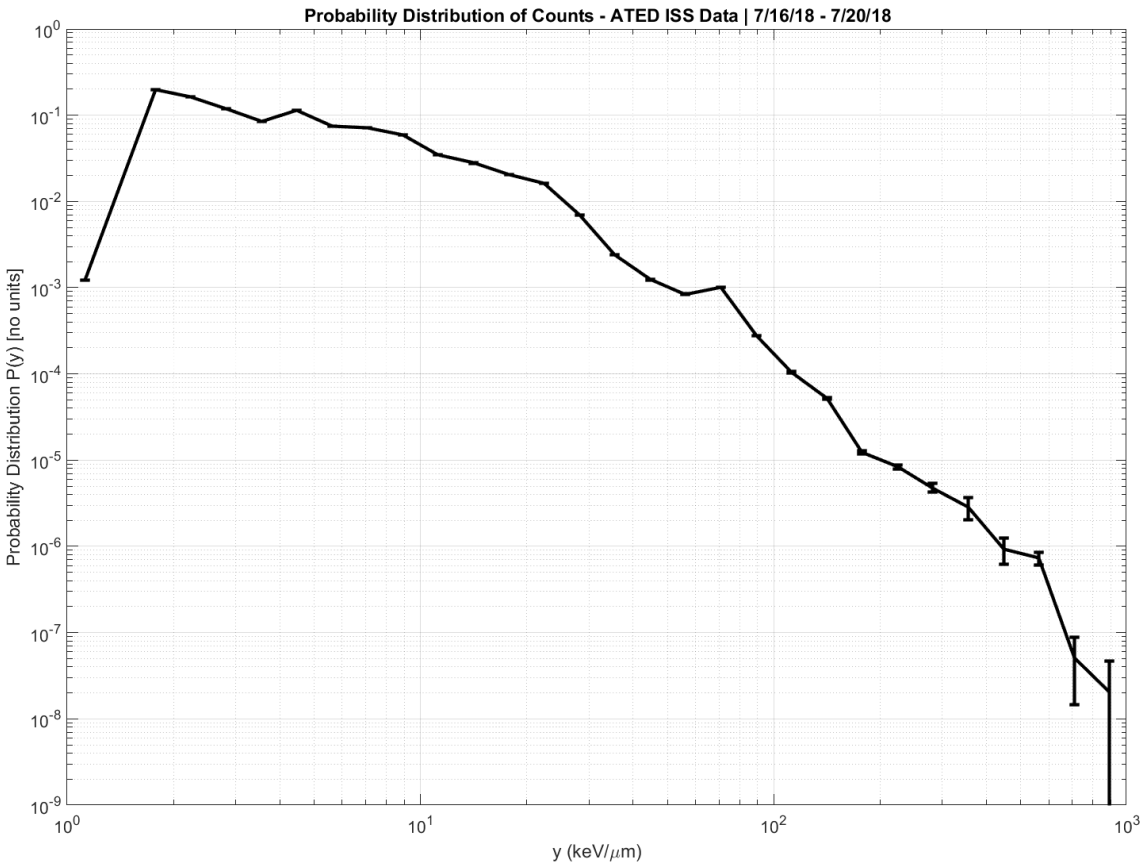

Figure 9.9: The probability distribution as a function of lineal energy (P(y)) for the ISS ATED for 16-20 July, 2018. The proton edge is seen around 150 keV/µm. HZE particles contribute to counts up to 1000 keV/µm. Uncertainty is quantified as the standard deviation of counts per unit time.

The relative dose distribution of good-quality ATED data from the ISS is shown in **Figure 9.10,** in a semi-log form. Uncertainty is quantified as the 8.40% uncertainty in ATED calculated absorbed dose. Most of the absorbed dose comes from a range of 4-150 keV/µm.

Even though many counts were seen below 4 keV/µm, these kinds of interactions do not contribute much to total absorbed dose because of the small amount of energy deposited into to the detector active volume. In the calculation of the relative dose distribution, events below 4 keV/µm are not a large contribution to absorbed dose.

Two peaks are seen at about 20 and 70 keV/µm. The maximum at 20 keV/µm is due to the calculation of y*d(y) and is not due to a physical phenomenon. The product of lineal energy and the number of counts resulted in the maximum seen. The interpretation of this maximum is that 20 keV/µm is the single value of lineal energy that contributed most to absorbed dose. The Peak at 70 keV/µm is the same peak seen in the probability distribution. It looks like a significant contribution to total absorbed dose due to the multiplying by the abscissa squared for the y*d(y) calculation. The valley between 20 and 70 keV/µm is not expected. Instead, we expect a monotonic decrease in the relative dose distribution after the maximum at 20 keV/µm. Again, this peak is most probably an artifact in the instrument and does not reflect an actual phenomenon in the environment. More work is needed to verify this interpretation.

Events past the proton edge, 150 keV/µm, contributed very little to total absorbed dose, even though these events deposit a significant amount of energy into the detector active volume. This is because the fluence of these particles is so low that they are not a large contributor to total absorbed dose. The large abundance of protons compared to these rare particles in the environment makes the range of 4-150 keV/µm the largest contributor. The events that contribute to lineal energies past 150 keV/µm can be rare HZE particles in the GCR spectrum, multiple particle events, or heavy-nuclei recoils from secondary neutron interactions.

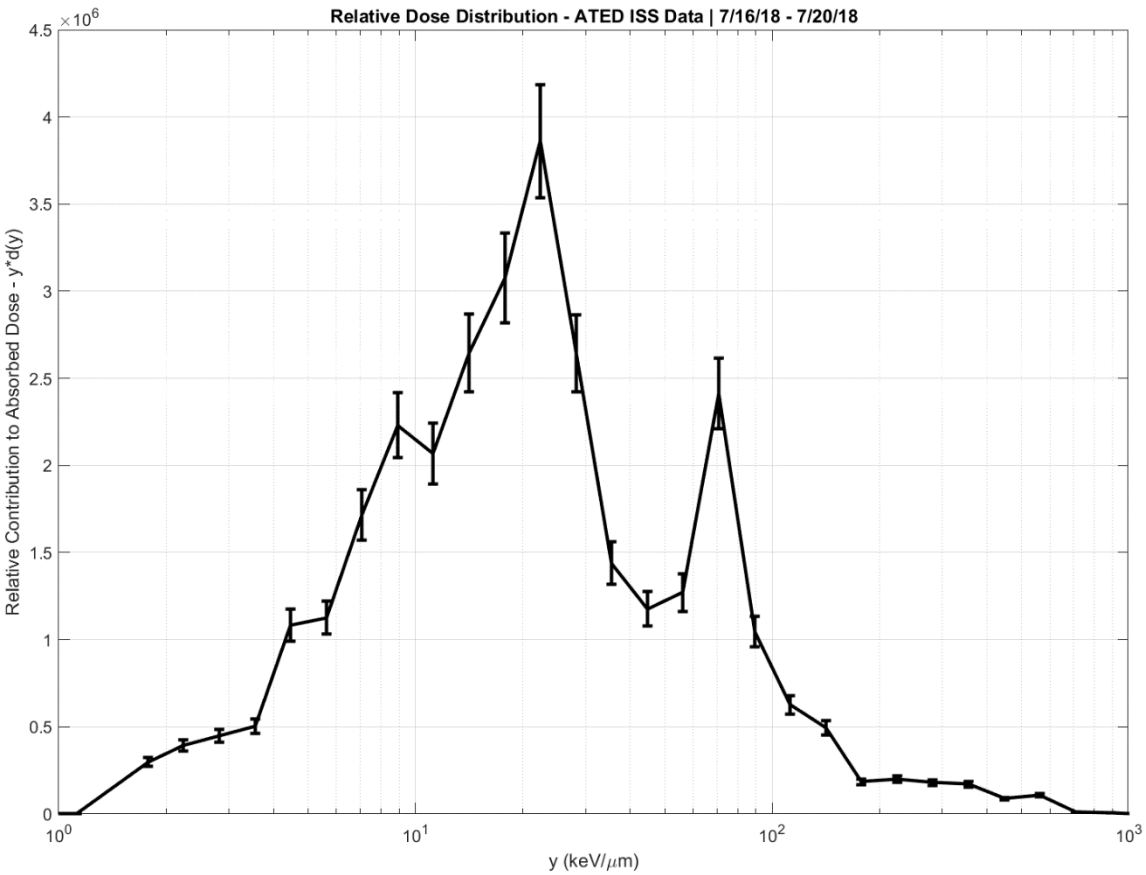

Figure 9.10: The relative dose distribution of the ISS ATED. The area under the curve is equal to the relative amount of contribution to absorbed dose in a range of lineal energies.

9.3 Comparison to Model Calculations

Daily absorbed dose for each day was compared to calculated absorbed dose from the OLTARIS computer model. OLTARIS is a web-based tool that aids scientists and engineers in studying the effects of space radiation on shielding materials, electronics, and biological systems [Singleterry, et al., 2010]. The basic code used in OLTARIS is High Z and Energy TRaNsport 2005 (HZETRN2005), which is a rigorously validated radiation transport code [Wilson, et al., 1991; Wilson, et al., 2005]. All heavy ion cross sections used in OLTARIS come from NUClear FRaGmentation Version 2 (NUCFRG2) [Singleterry, et al., 2010]. OLTARIS is designed so that non-experts in space ionizing radiation can run advanced simulations to assess radiation shielding

in spacecraft and their effects. In simulating the radiation environment in LEO, OLTARIS models trapped protons, GCR, and albedo neutrons in the calculation of absorbed dose.

When running the model, a user needs to specify the start/end date, altitude, inclination, etc. for their specific mission parameters. Trajectory files are also able to be read in. For comparison to ATED absorbed dose calculations, OLTARIS used an averaged trajectory of the ISS for the dates of good-quality data. The actual dates of the ATED flight are not available in the Badwhar-O'Neill 2014 Model that OLTARIS uses to calculate the incident GCR spectrum. It was suggested by the OLTARIS administrator to subtract 11 years from the actual dates in order to simulate a similar time in the solar cycle as to not significantly alter the incident GCR spectrum [Sandridge, 2019].

A thickness distribution of the vehicle in question needs to be specified. The user has the option to input CAD models, including human phantoms, into OLTARIS. Another option is to input slabs or spheres of chosen depths and materials directly on the web interface. In the case of a defined slab or sphere, particles are transported through the entire thickness of a slab or through the radius of a sphere [NASA, 2018]. These slabs/spheres can be made of many layers of different materials and are typically used as an approximate thickness for spacecraft. The resulting flux after transport across the defined material(s) is then used for dosimetric calculations.

The distribution and amount of shielding in Node-3 where ATED was located is not well known and changes with time. As stated previously in 9.1, the mass distribution around the location of ATED is highly non-uniform and of unknown depth. In order to make a reasonable assumption about the distribution of mass around ATED, we must decide on a material, distribution and depth of material that is realistic. The most conservative estimate of the distribution of shielding surrounding ATED is a uniform sphere of aluminum. It is a non-trivial problem to simulate the

actual mass distribution around ATED. At this time no efforts have been put forth to create and input a CAD model of Node-3 into OLTARIS. A sphere was used instead of a slab in order to simulate more accurate dosimetric quantities [NASA, 2018].

In order to make a best-guess of the average depth of aluminum in Node-3 surrounding ATED, different realistic depths of aluminum were simulated in OLTARIS. The depths of aluminum simulated were: 0, 5, 10, 15, and 50 g/cm^2. These depths of aluminum were chosen to be within the range of typical depths found on space craft [Adams, et al., 1991]. A resulting differential LET spectrum was calculated for each depth of aluminum. Comparison of the differential LET spectra to the differential lineal energy spectrum as measured by ATED allowed for a best guess of the amount of shielding in Node-3. In reality, the distribution of mass in Node-3 is certainly not uniform. The assumption of uniform depth serves only as a rough approximation of the shielding that surrounded ATED during its time on the ISS.

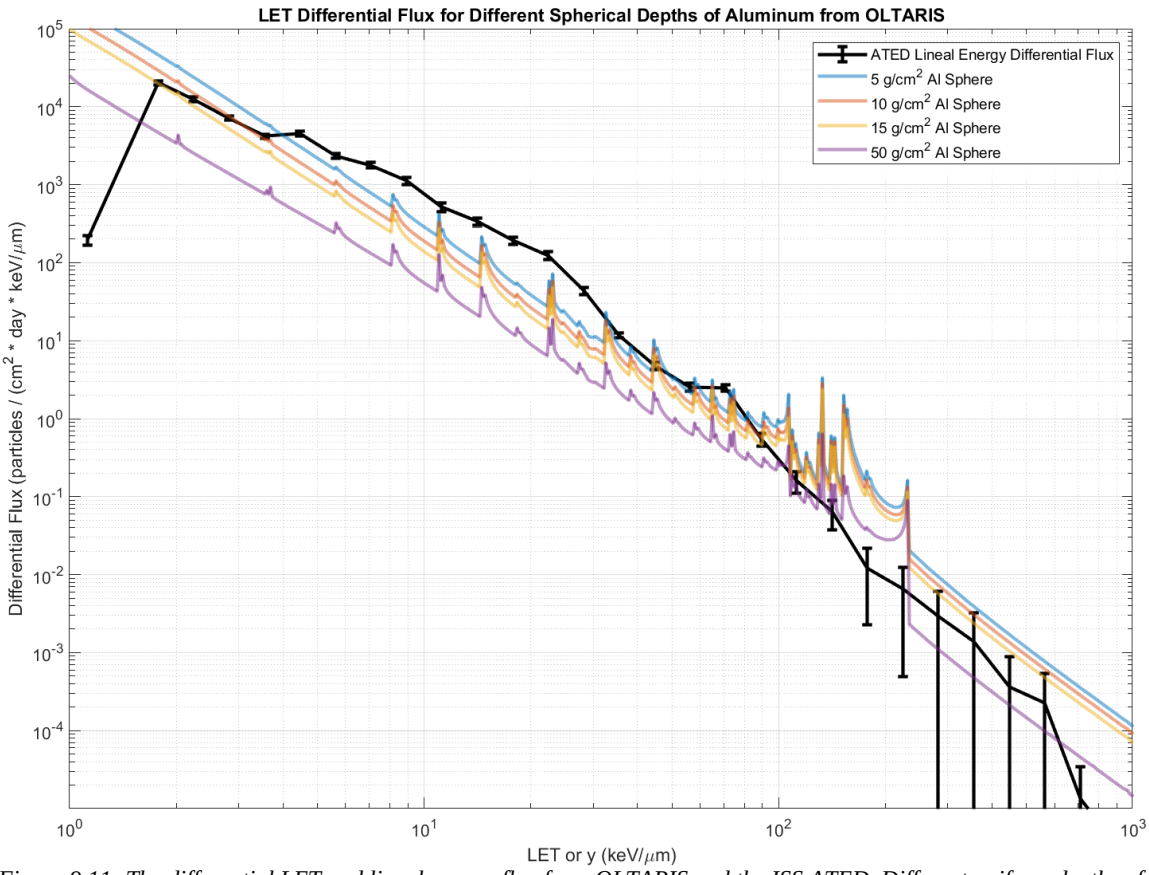

Figure 9.11: The differential LET and lineal energy flux from OLTARIS and the ISS ATED. Different uniform depths of aluminum were simulated in spherical distributions in the OLTARIS code to find the best agreement with ATED measurements. This will serve as an approximate depth of shielding for ATED simulation comparisons.

The differential flux as a function of LET for each simulated depth and ATED differential flux as a function of lineal energy are shown in **Figure 9.11**. The best agreement with OLTARIS calculated differential flux and ATED measurements is seen with 10 g/cm^2 of Al. Between 2-4 keV/µm ATED agrees well with a spherical distribution of 10 g/cm^2 of aluminum. From 5 up to 30 keV/µm, ATED measured a larger differential flux than all the OLTARIS simulations. This is likely due to the assumption of a uniform shielding distribution used in the OLTARIS simulations. From 100 keV/µm up to 1000 keV/µm, poor statistics in ATED measurements make an apparent agreement with 10, 15 and 50 g/cm^2. Thus, 10 g/cm^2 were used for daily absorbed dose calculations in OLTARIS and comparison to the differential LET flux of the environment.

Daily absorbed dose for each day is compared to OLTARIS calculated absorbed dose in tissue in **Table 9.2**. The uncertainty in ATED absorbed dose is 8.40% [Causey, 2018]. Currently,

OLTARIS does not provide uncertainty in their calculated values and thus disagreement seen in daily calculated dose values may appear larger than they should be. Disagreement may also be due to the assumptions made in the uniform distribution of aluminum used in the OLATRIS simulation. For the period of good ATED data, overall percent difference between ATED and OLTARIS calculated absorbed dose is 38.68 ± 4.75%.

Date (GMT)	*ATED Calculated Absorbed Dose (mGy)*	*OLTARIS Calculated Absorbed Dose (mGy)*	*Percent Difference (%)*
07/16/18	0.76 ± 0.06	0.37	51.19 ± 3.78
07/17/18	0.69 ± 0.06	0.50	27.16 ± 5.65
07/18/18	0.53 ± 0.04	0.37	29.38 ± 5.47
07/19/18	0.80 ± 0.07	0.47	41.54 ± 4.53
*07/20/18**	0.40 ± 0.03	0.24	41.16 ± 4.56
Total (4.51 days)	3.18 ± 0.27	1.95	38.68 ± 4.75

Table 9.2: Absorbed dose as calculated by ATED measurements and the OLTARIS computer code for each day ATED was on ISS. (*) Data was lost after 12:10:17 on July 20th.

OLTARIS calculated differential flux behind a spherical distribution of 10 g/cm^2 of aluminum as a function of LET is compared to ATED differential flux as a function of lineal energy in **Figure 9.9**. The spikes seen in the simulated LET differential flux spectrum from OLTARIS are the result of minimum ionizing particles of different species. Minimum ionizing protons create a spike at 0.198 keV/µm in differential flux and spikes that occur at higher LET will correspond to the elements: He, Li, B, C, etc. [Adams, et al., 2007]. These sharp spikes are not seen in ATED lineal energy spectrum due to chord length variations which will effectively spread them out over a wide range of lineal energies. Between 4 and 40 keV/µm, ATED measured an elevated differential flux compared to model predictions. This is likely due the non-uniform distribution of shielding inside Node-3 and the assumption of a uniform distribution of shielding in OLTARIS. There is good agreement between 40 and 100 keV/µm within ATED uncertainty. Counts of lineal energy past the proton edge have large uncertainties associated with them. With more data, these uncertainties would possibly decrease and better agreement would result. Regardless, some

agreement up to ~500 keV/µm within uncertainty exists. Again, OLTARIS does not provide uncertainties associated with its calculations. Thus any disagreement seen in LET differential flux may not reflect actual disagreement.

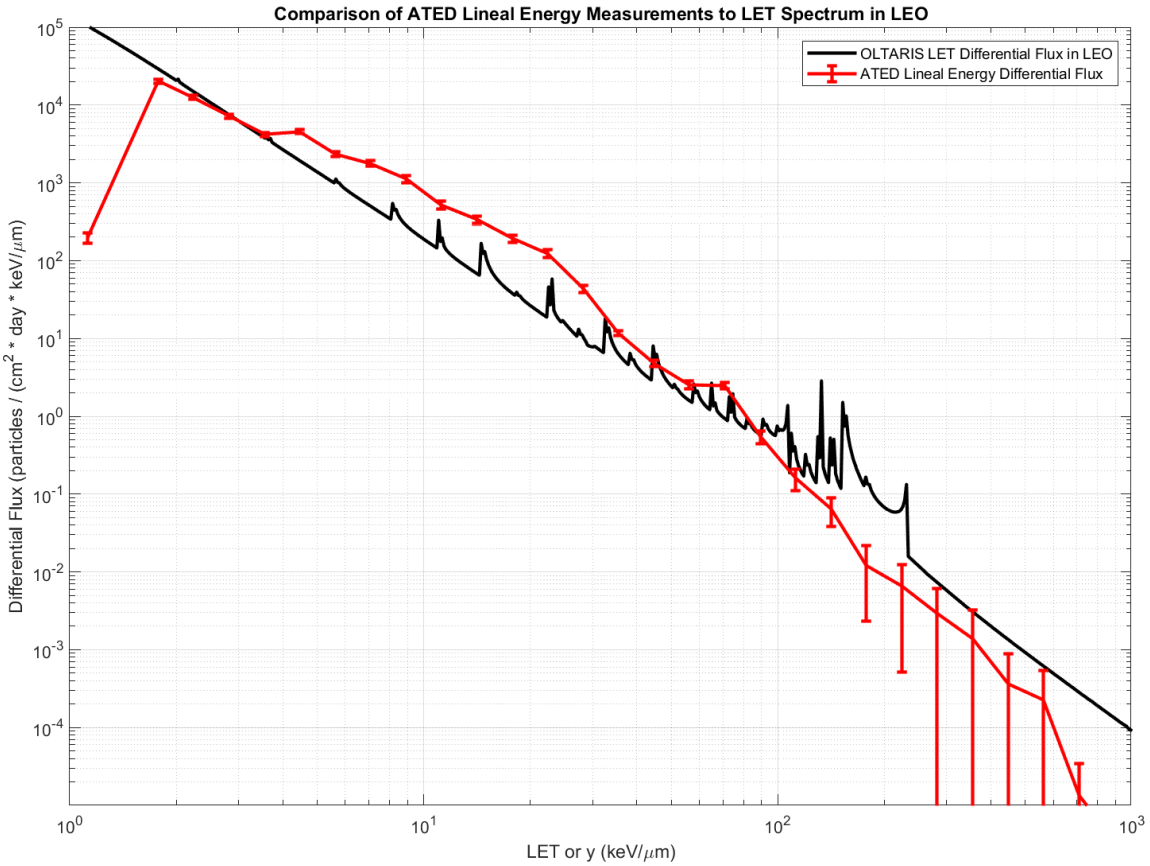

Figure 9.12: ATED differential flux as a function of lineal energy and the differential flux behind 10 g/cm2 of aluminum as a function of LET calculated by OLTARIS.

In the past, lineal energy and LET were used interchangeably for radiobiological calculations of TEPC measurements in LEO [Badhwar, et al., 1994]. The differences between the LET spectrum and y-spectrum for a radiation field with large numbers of particles in an isotropic field were assumed to be small. [Zhou, et al., 2007]. The definitions used by ICRP 60 for quality factor, and thus dose equivalent, use LET instead of lineal energy [ICRP, 1991]. Although the assumption that $L = y$ in LEO has been widely used for many years, there has not been rigorous testing to test this assumption. The agreement seen in **Figure 9.12** is strong evidence that this assumption is

valid for spherical TEPCs in LEO and can be used in the calculation of biological relevant quantities.

9.4 Separation into Orbital Regions

Data was sorted into the SAA, Electron Cusp, and GCR regions of the ISS orbit, as described in Chapter 2.2. The separation led to 1355 spectral measurements in the SAA region, 1738 in the Electron Cusp Region, and 9971 in the GCR region. **Figure 9.13** shows the location of each data point, and what region they belong to as a function of latitude and longitude.

The data points belonging to the SAA are over the South Atlantic Ocean and South America where the inner radiation belt dips to lower altitudes as a result of the offset of Earth magnetic field. The Electron Cusp is seen at only the most extreme of latitudes over the South Indian Ocean and North America where the outer radiation belt comes closest to the surface of Earth. The remaining data points in the GCR region do not have a significant contribution from trapped radiation and thus mainly GCR are measured.

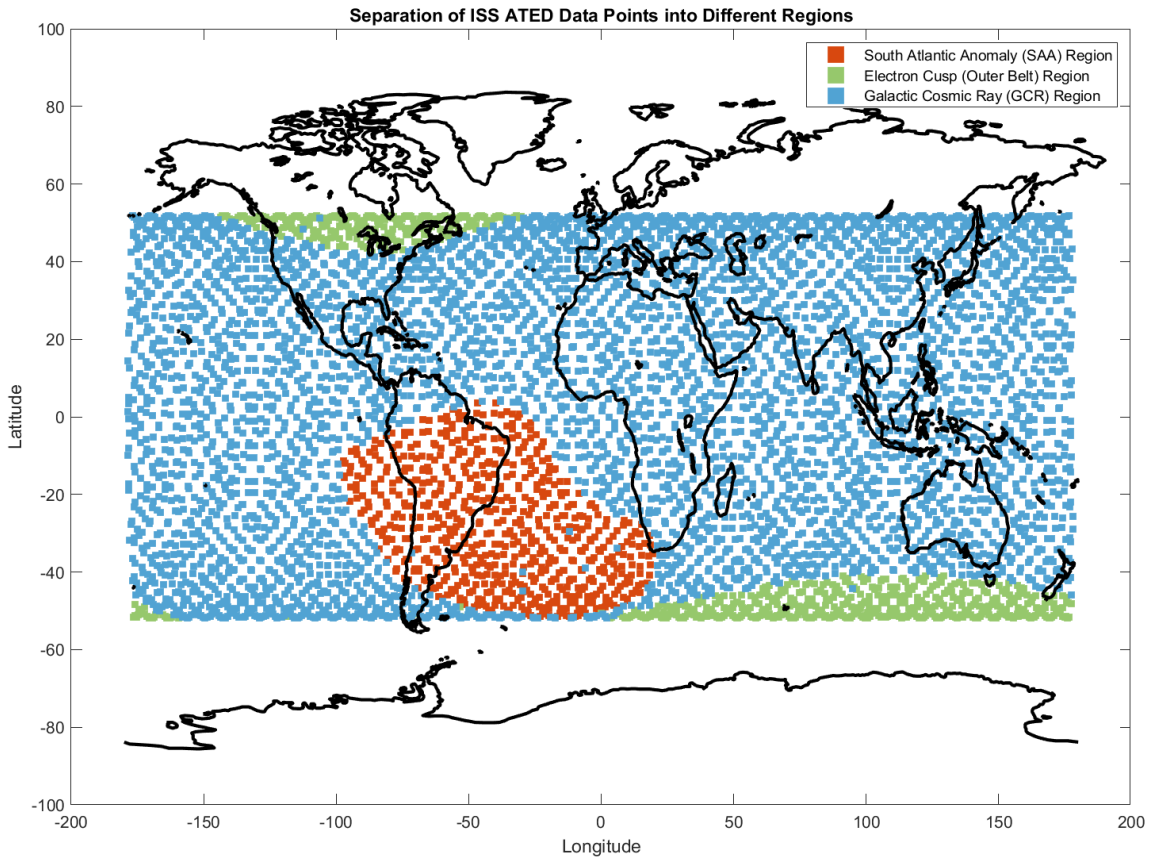

Figure 9.13: The location of each ATED data point used as a function of latitude and longitude. Each data point has been color-coded to show which region the data points belong to.

Flux as a function of lineal energy for the different regions are shown in **Figure 9.14**. As expected, the two trapped particle regions have significantly larger particle flux than in the GCR region at all lineal energies. This is especially true at low lineal energies, where the majority of the contribution to counts from trapped radiation is expected. The SAA contributed more flux than the electron cusp across most lineal energies. This is largely because ATED is more sensitive to the protons in the SAA than the bremsstrahlung radiation measured in the electron cusp. This sensitivity is due to the average higher lineal energy of protons and the gas medium of the detector. Also, dose rates are simply higher in the SAA than the electron cusp.

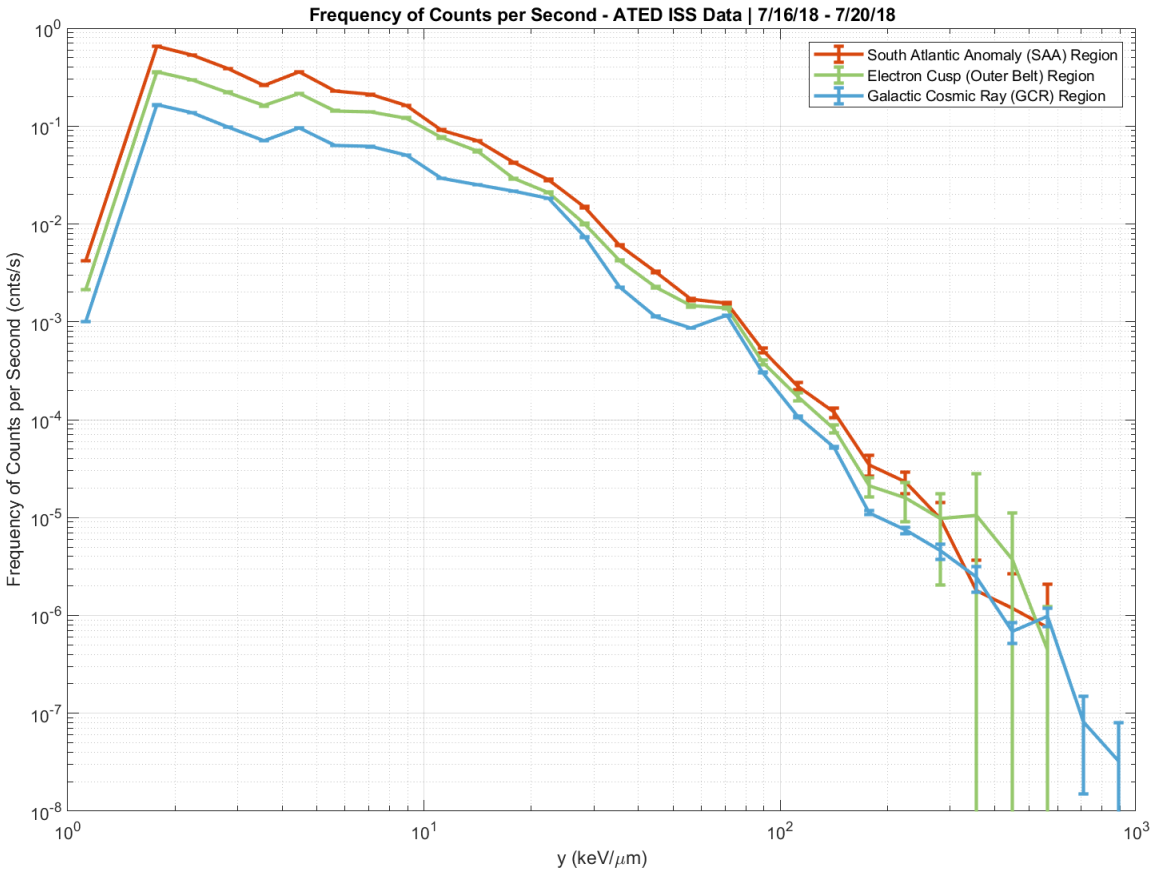

Figure 9.14: The frequency of counts per second as a function of lineal energy for the SAA, Electron Cusp, and GCR regions. Data is separated based on the regions described in the text.

Each spectrum has the same general trend, except for the small peak at 70 keV/µm in the GCR region. The trapped particle spectra measurements probably do not contain enough data to properly resolve this peak if it is the result of a phenomena of the environment. As stated before, this peak is most likely the result of damage to ATED. The lack of a peak at 70 keV/µm for the trapped particle spectra is likely due to their smaller data set size compared to the GCR region. The smaller data sets likely would not have enough time for spurious counts to resolve into a peak.

All three regions converge at 300 keV/µm where statistics are poor. Because the ISS spends less time in both the SAA and Electron Cusp regions, the statistics for these regions at the high lineal energies are larger for the GCR region. This is also why the GCR region extends to higher values of lineal energy than the other two regions.

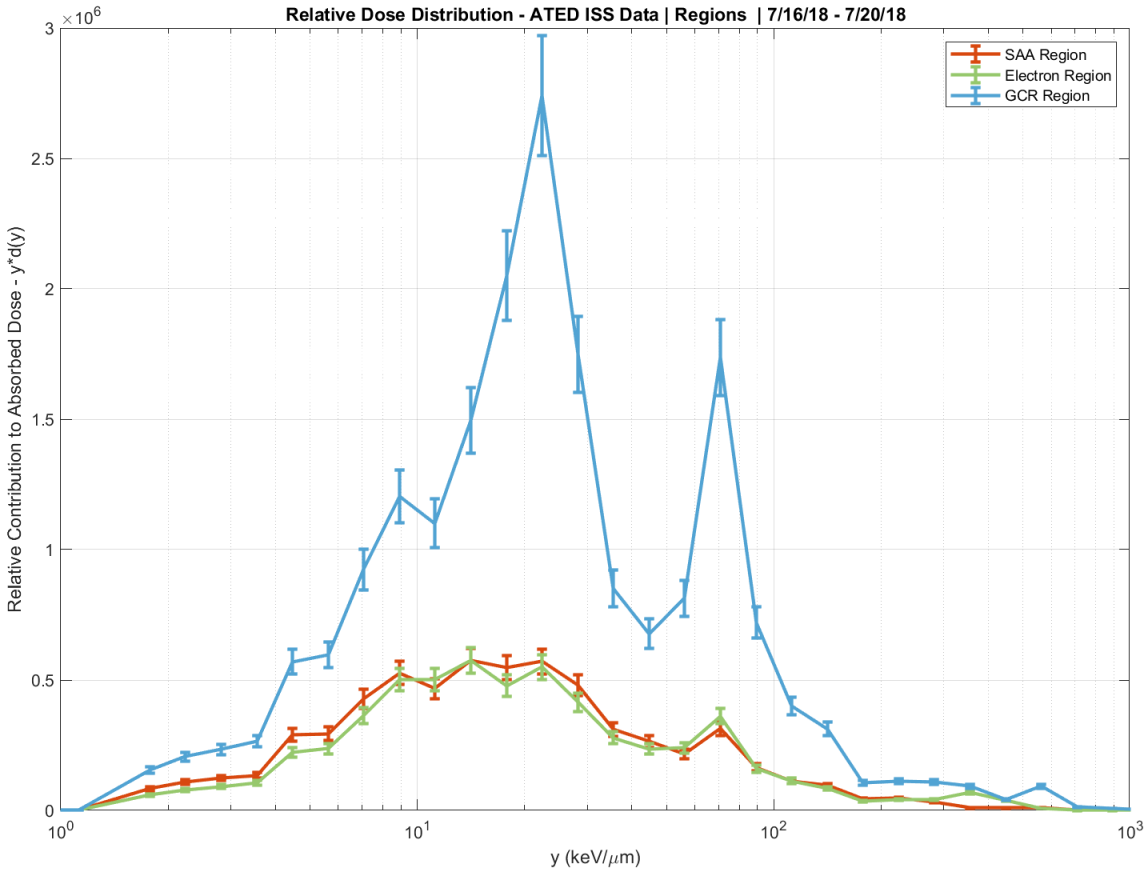

Figure 9.15: Dose Distribution of the ATED ISS data separated into different regions. the area under the curve corresponds to the amount of dose absorbed. Uncertainty is quantified as the 8.40% of ATED calculated absorbed dose values.

The relative dose distribution as a function of lineal energies for these regions is shown in **Figure 9.15.** Uncertainty is quantified as the 8.40% for calculated ATED absorbed dose values. In all three regions we see a maximum in the dose distribution around 20 keV/μm. These maxima are the result of the calculation of the dose distribution, indicating that this central value of lineal energy that is contributing most to absorbed dose. The GCR spectrum contributes more to absorbed dose across all lineal energies than do either the SAA or Electron Cusp. This is largely due to the fact that the majority of the ISS orbit lies within the GCR region.

The peak at 70 keV/μm is much more pronounced in the GCR than the other two regions. Again, the trapped particle regions probably do not have enough data to fully resolve this peak. The ratio of peak heights at 70 keV/μm for all three regions is roughly the same as the ratio of data points

in each region. The ratio of peak height at 20 keV/μm does not follow this trend. This is evidence that spurious counts came in at a pseudo-constant rate and the trapped particle regions did not have enough time to resolve this peak.

GCR is more likely to contribute toward dose at higher lineal energies. The high energy particles that make up GCR can be directly measured by ATED, but these particles are also able to produce secondary particles through nuclear target fragmentation in the hull of the ISS. These secondary particles can contribute to the high lineal energy region directly, or through heavy nuclei recoils from neutron interactions inside ATED.

Trapped protons dominate in the SAA region, and thus the effects from GCR are minimal but still present. These trapped protons will directly contribute to dose, but, just like high energy GCR, they can also undergo nuclear target fragmentation in the hull and produce counts at high lineal energies. The primary protons have kinetic energy such that lower lineal energy channels are elevated in the contribution to dose. This results in a broader peak at 20 keV/μm. A similar phenomenon is happening in the electron cusp, but because of bremsstrahlung from trapped electrons. Also, in the electron cusp a lower cutoff rigidity will allow GCR to contribute more to dose at higher lineal energies than the SAA region, which is indicated by the elevated counts at higher lineal energies.

The percentage of total absorbed dose and percentage of the ISS orbit inside each region is shown in **Table 9.3**. The ratio of these two percentages show the large increase in dose rate inside the SAA. It has been previously reported that the SAA accounts for roughly 50% of the absorbed dose in the ISS orbit [Badhwar, 2002]. ATED calculated the percentage of total absorbed dose from the SAA to be 19.37 ± 1.66%. This results in a factor of about 2.5 in disagreement. This disagreement is possibly due to differences in the solar cycle, detector sensitivity, or differences in the definition of the SAA boundary. The Electron Cusp resulted in a similar percentage of total

absorbed dose to the SAA region. The GCR region was by far the largest contributor to absorbed dose since the ISS orbit lies predominantly within this region.

Region	*Percentage of Total Absorbed Dose (%)*	*Percentage of ISS Orbit inside Region*
SAA	19.82 ± 1.66	10.37
Electron Cusp	18.67 ± 1.57	9.30
GCR	61.51 ± 5.17	76.32

Table 9.3: Percentage of absorbed dose for each region and percentage of ISS orbit each region occupies as calculated by ATED measurements.

OLTARIS provides the differential flux of trapped protons as a function of LET. In **Figure 9.16** the separated ATED measurements inside the SAA are compared to the differential flux of trapped protons behind a spherical distribution of 10 g/cm^2 of aluminum as calculated by OLTARIS. Uncertainty in ATED differential lineal energy spectrum is quantified as the standard deviation of the flux measurements inside the SAA. There is good agreement from 7 to 200 keV/µm. Large uncertainties exist in ATED measurements past 80 keV/µm due to the relatively small number of measurements in the SAA. It should be pointed out that ATED measured both trapped protons and GCR which explains why ATED measurements extend to higher values of LET than the modeled trapped protons. Also, trapped protons could possibly contribute to high lineal energies through nuclear target fragmentation. The resulting fragments would contain neutrons and other high lineal energy products. OLTARIS does not include target fragments in the trapped proton LET spectrum, but does include them in the calculation of absorbed dose. ATED is not sensitive to particles of lower LET, and thus falls below the differential flux calculated by OLTARIS below 7 keV/µm.

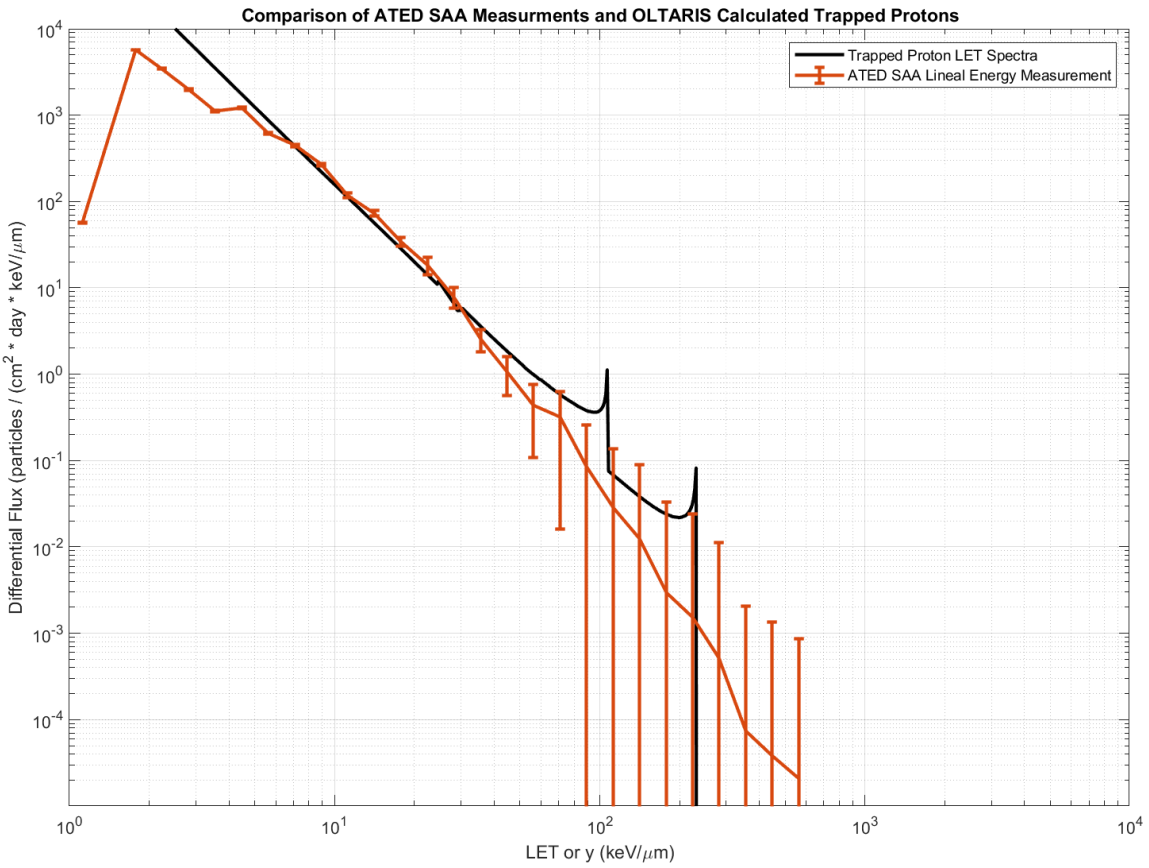

Figure 9.16: The Comparison of ATED measurements taken inside the SAA and the calculated differential flux of trapped protons as calculated by OLTARIS. Uncertainty is quantified as the standard deviation of SAA files.

Figure 9.17 shows absorbed dose rate as a function of the absolute magnetic field flux density for region-separated ATED measurements. The majority of absorbed dose rate values fall between 0.4 and 1 μGy/min for all three regions. Dose rates above 1 μGy/min are possibly due to rare, high-energy GCR. Evidence for this comes in the fact that these elevations in dose rate come at all values of magnetic flux density. High-energy GCR have a high enough rigidity such that their trajectories would not be altered much by the magnetic field.

The SAA region ($|B| < 23\mu$T) shows a clear increase in absorbed dose rate with decreasing magnetic flux density. The trapped particles in the SAA come closest to the surface of Earth where the magnetic flux density is smallest. It is clear that dose rate levels are highest at the center of the SAA where the magnetic field is the most offset from the center of Earth. There is a less drastic increase with increasing magnetic flux density. At higher latitudes there will be an

increase in magnetic flux density as magnetic field lines converge. At the same time, the orientation of the magnetic field will decrease cutoff rigidity, allowing more low-energy GCR to penetrate the ISS orbit. This accounts for the slight increase in dose rate as magnetic flux density increases. The measurements taken at high magnetic flux density are at the highest latitudes on the ISS. This is also where the majority of measurements will reside inside the Electron Cusp. A better parameter for showing a decrease in cutoff rigidity is the L-Shell factor.

Figure 9.17: Absorbed dose rate as a function of magnetic flux density for region-separated ATED measurements aboard the ISS. Each region is color-coded to its corresponding region.

In **Figure 9.18**, absorbed dose rate is shown as a function of L-Shell parameter in Earth Radii. The L-Shell parameter was discussed in Chapter 2.1. For the ISS, L-Shell parameter (L) corresponds to the magnetic field lines that pass through its orbit and the equatorial plane at a certain Earth radius. The majority of points for the GCR and election cusp regions lie under 1 μGy/min. The SAA has a definite maximum in absorbed dose rate at an L-Shell of about 1.25.

This is the L-Shell value where the offset of the Earth's magnetic field is largest, the center of the SAA.

For the lower bound of dose rates, a linear trend arises with increasing L-Shell. Two black dashed lines are used to show the upper and lower trends for dose rate. These lines are the upper and lower bounds of dose rate inside two standard deviations of the mean for the GCR and electron cusp regions. The lower bound increases linearly with increasing L-Shell. The increase in absorbed dose rate at higher L-Shell values is expected because cutoff rigidity is inversely proportional with L-Shell. This means that more GCR are able to penetrate the ISS orbit and contribute to dose. Although the SAA region was ignored in the calculation of the lower bound, its data follows the lower boundary. Fewer points are also seen at high L-Shell values because the ISS does not spend as much time at these higher latitudes. With more data, this lower trend would be more defined. Data points that are above the upper dashed line may be the result of rare high-energy GCR.

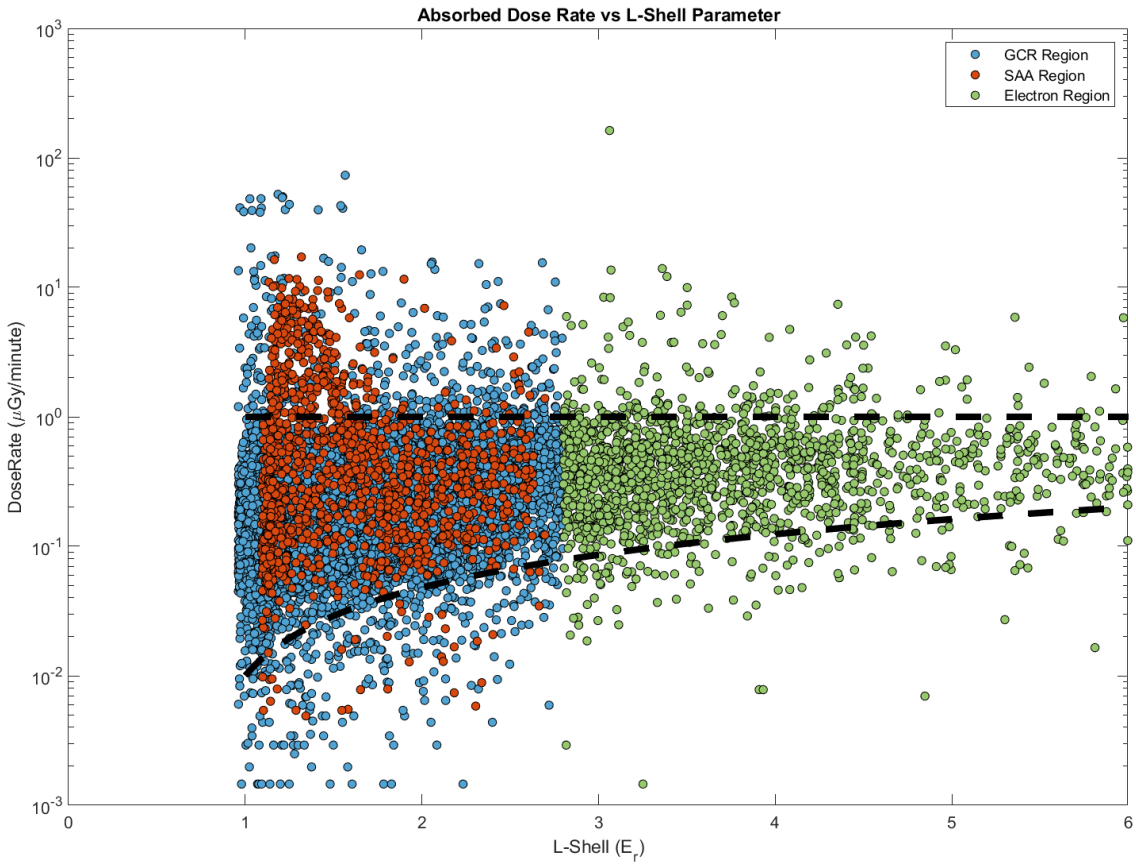

Figure 9.18: Absorbed dose rate as a function of L-Shell parameter in Earth radii. The dashed lines represent the general trend for the upper and lower bounds of data and encompass 95% of all data in the GCR and electron cusp regions. The lower bound is a linear trend with increasing L-Shell.

9.4 Conversion of ATED Measurements into LET

We investigate the use of two methods to convert lineal energy measurements to LET. Conversion of lineal energy spectra to LET spectra permits comparison with measurements from other instruments that directly measure LET spectra (e.g. silicon spectrometers, CR-39 plastic nuclear track detectors) as well as permitting a direct calculation of dose equivalent as defined by ICRP 60, since this definition is in terms of LET and not lineal energy [ICRP, 1990]. One method to convert measured y-spectra from a TEPC of any geometric configuration into a corresponding LET spectra has been provided by [Kellerer, 1972]. A second method is based on a geometric conversion for spherical TEPC lineal energy spectra into corresponding LET spectra has been

provided by [Rossi et. al., 1996]. These methods are discussed in detail in Chapter 5. This effort is by in large to test the viability of these methods in the space radiation environment, compare with measurements from instruments that directly measure LET, and to explore the possibility of using these techniques for past and future experiments. To date, no direct comparison of LET converted lineal energy spectra from a spherical TEPC in LEO and model-calculated LET values has been made.

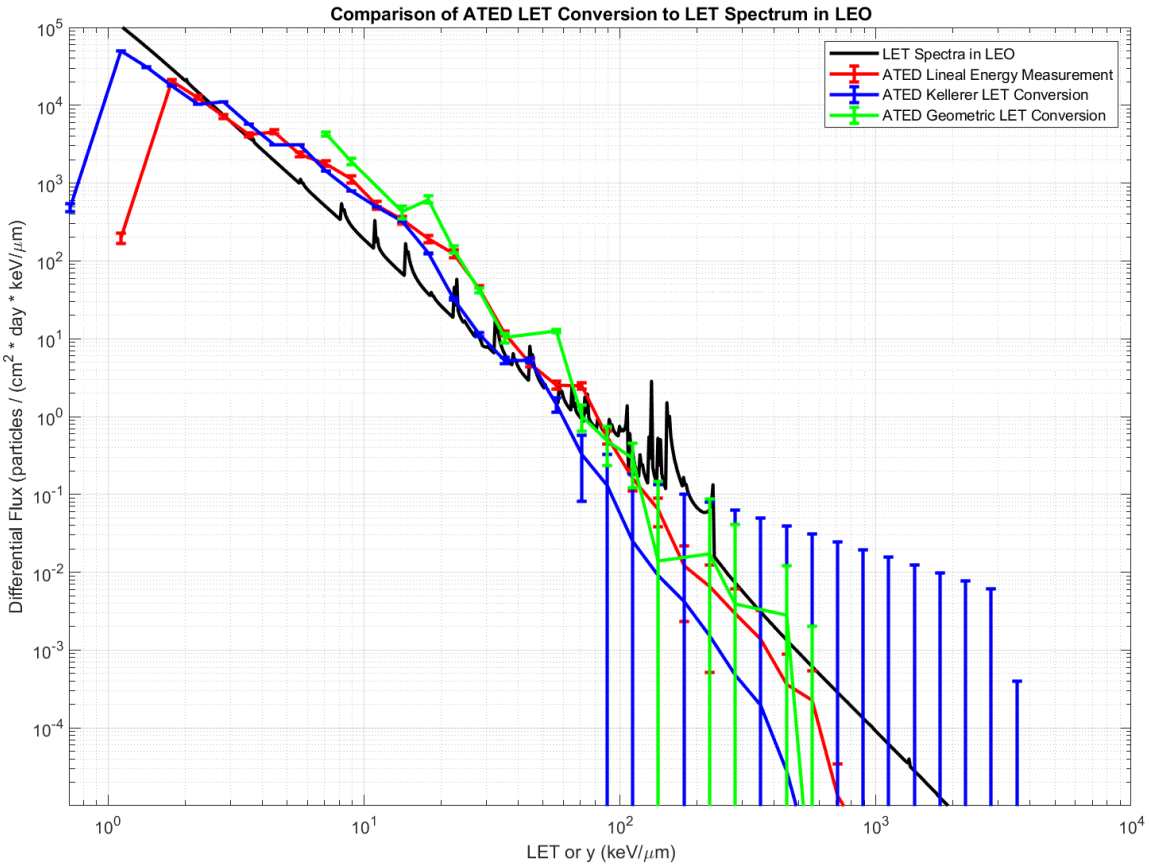

Figure 9.19: Differential Flux of the LET found in Low Earth Orbit, the measured lineal energy spectrum measured by ATED, and the two LET conversions of ATED measurement.

In **Figure 9.19** the LET differential flux as modeled by OLTARIS (black), the differential flux of lineal energy measurements from ATED (red), the differential flux of the Kellerer LET conversion (blue), and the differential flux of the Geometric LET conversion (green) is shown as a function of LET or y. Differential flux of the radiation environment was provided by OLTARIS and assumed a sphere of 10 g/cm2 of aluminum as previously discussed in 9.3.

The Kellerer LET conversion from the lineal energy measurements generally agrees with the original ATED lineal energy spectrum from 2 to 70 keV/μm. However, both spectra lie above the OLTARIS calculated LET spectra over this range. This is possibly due to the model assuming uniform shielding where in reality the distribution of shielding around ATED was eccentric. The Kellerer LET conversion extends down to 0.7 keV/μm, reporting lower differential flux up to 2 keV/μm. This may be due to the loss of sensitivity of ATED measurements in these lower LET values. This method does not reliably provide useful information below ~5 keV/μm due to the folding of many counts into the smallest chord lengths of the detector active volume [Kellerer, 1972]. The peak seen at 70 keV/μm in ATED measurements has been shifted to 45 keV/μm in the Kellerer spectrum due to the conversion of lineal energy into LET. From 70 keV/μm up to 3500 keV/μm the uncertainty in Kellerer converted differential flux is large. The Kellerer method was originally developed using neutron data, where LET values above the proton edge (~150 keV/μm) are usually negligible. Thus the Kellerer method is probably not suited for the wide range of LET like that found in the space radiation environment. The conversion of lineal energy measurements into a corresponding LET spectrum with the Kellerer algorithm does not add any novel information about the environment. The assumptions of this method seem to limit it to specific applications that do not include use in space radiation environments.

The geometric LET conversion of Rossi et. al. produced negative values of differential flux for some LET channels. These negative values have been omitted. Because of this, no information from the geometric LET conversion was obtained below 10 keV/μm. The geometric conversion depends heavily on finding the slope of the measured spectrum, and thus it is susceptible to produce erroneous values due to random fluctuations in the data. Also, the geometric LET conversion assumes that particles of the same LET will have triangular distributions for a spherical counter. The radiation environment on the ISS is highly mixed and thus no triangular features exist in the measured data. For the remaining positive geometric LET converted values,

there is general agreement to the measured lineal energy spectrum from 7 to 100 keV/μm. Two significant disagreements within this range are at 30 and 90 keV/μm. These disagreements are artifacts of this conversion method from, again, the sensitivity of calculating the slope of data. For lineal energies higher than the proton edge, the uncertainty in the geometric LET converted values becomes large. The poor statistics in this range are extended further after the geometric conversion process. No useful information has come from converting measured lineal energy measurements to LET with the geometric method. The radiation environment is possibly too highly mixed with various particles of various LET or the method itself relies too heavily on ideally measured TEPC spectra.

CHAPTER VI

CONCLUSIONS

The work described in this dissertation has advanced the ATED development program to the point where it is nearly completed. This work has demonstrated the validity of key assumptions about how ATED operates, has significantly reduced cost of production, and demonstrated that ATED can effectively measure absorbed dose in tissue both in the atmosphere and in space. The Oklahoma State University Radiation Physics Laboratory is now in a position of having an ATED instrument for use in routine commercial flights, and easily adaptable for space and baloon payloads. Already the ATED has been demonstrated its usefulness at accelerators, in neutron radiation fields, in the atmosphere, and in space to give insights to the human health impact by ionizing radiation. Areas of improvement have been identified, and will be part of the final development of the ATED instrument.

10.1 Accomplishments

Assumptions that ATED collected 100% of the separated have been confirmed. The collected charge per unit time as a function of applied bias demonstrated that ATED collects all of the separated charge inside its active volume. This experiment also outlined a method to find the optimal voltage for any new ATED active volume.

The individual contributions to pulse amplitude by positive ions and electrons have been measured for the first time. A method has been developed that uses saved pulses from the ATED coupling capacitor and an iterative fitting process to quantify the contribution of electrons and positive ions to pulse amplitude. It was seen than positive ions contributed four to twelve times more to pulse amplitude than electrons. The large standard deviation in this value suggests that electrons are not negligible to pulse amplitude. It was also found that positive ions consistently had a rise time 100 times longer than electrons, which agrees with theoretical predictions.

A Red Pitaya FPGA board was programmed to work as a dual-input spectrometer for ATED instruments. By using the Red Pitaya FPGA board as an MCA, the cost of building a single ATED instrument has been reduced by ~$8000, allowing more ATED instruments to be built. One disadvantage of the Red Pitaya MCA is that it has low processing power. This has led to the belief that the Red Pitaya MCA is best suited for measurements in the atmosphere. The low-cost of the Red Pitaya is ideal for the distribution many ATED instruments across several commercial, military, and business aircraft.

The experiments conducted at the LANSCE ICE House facility demonstrated that ATED had the appropriate response to a similar neutron energy spectrum as that encountered in the atmosphere. This was indicated by expected trends in the lineal energy spectrum, good agreement with the same measurement by a NASA Space Shuttle TEPC, and good agreement with an MCNP_6.2 simulation of the nominal beam experiment. The small differences in the relative dose

distributions of the NASA TEPC and ATED are explained by differences in geometry of the two instruments. The differences in the relative dose distributions produced by the MCNP simulation and the measurement by ATED are likely due to the limited fidelity of the MCNP simulation and geometry model. The efficacy of various materials to shield radiation were studied and changes in the relative dose distribution and absorbed dose per incident neutron as a function of material and thickness were measured. The materials tested were 5.34 g/cm² of aluminum, 5.38 g/cm² of HDPE, and a simulated aircraft wall composed of 5.3 g/cm² of aluminum and 3.2 g/cm² of HDPE. It was found that HDPE reduced absorbed dose by 50%, the aluminum by 23%, and the simulated aircraft wall by 36%. These results were not surprising as they directly follow the trends of neutron cross section for each material.

A method of testing the propensity of materials to produce secondary neutrons has been developed at the HIMAC, using ATED off-axis to the beamline. The charged particle beams were 400 MeV/n carbon, 800 MeV/n silicon, and 650 MeV/n iron. It was found necessary to repeat measurements with an iron shadow bar between the detector and target material to subtract counts contributing from the beam stop. A no target run showed a different relative dose distribution than the shadow bar due to the properties of the beam changing through the target material before reaching the beam stop. Comparisons between the contributions to dose for aluminum, HDPE, copper and PPSiC20 were made. In general, the higher the Z component of the target material the larger contribution to absorbed dose, which directly relates to the propensity of target materials to produce secondary neutrons. The main differences in the relative dose distributions for each measurement were found to be below 100 keV/µm. Above 100 keV/µm each beam/material combination were in good agreement, likely due to poor statistics. Comparisons between beams also showed a Z dependence of the beam. The iron beam contributed 100-1000 times more towards absorbed dose than the silicon and carbon beams.

The ATED operated aboard to the ISS successfully measured absorbed dose as functions of time, orbital position, and lineal energy and demonstrated its capability to be used as a dosimeter in LEO. Analysis of ATED measurements on the ISS resulted in 4.51 days of useful data, from 16 - 20 July, 2018. Absorbed dose rate as a function of time showed expected fluctuations, minima as the ISS traversed the geomagnetic equator, small maxima when the ISS approached the poles, and large intermittent spikes when crossing through the SAA. Orbital position data correlated with absorbed dose rate showed the SAA in the expected location, where absorbed dose rate was ~10 times higher than the rest of the orbit. There was also a slight elevation in absorbed dose rate over North America and the South Indian Ocean due to the Electron Cusp of the outer radiation belt. The lineal energy spectrum had expected features like the proton edge and a monotonically decreasing trend. A small peak at 70 keV/μm was seen and is likely an artifact of the instrument and not a real phenomenon of the measured environment. Comparisons with OLTARIS showed good agreement, with less than 40% difference in absorbed dose values. The percentage of total absorbed dose was calculated to be 19.82 ± 1.66%, 18.67 ± 1.57%, and 61.51 ± 5.17% for the SAA, Electron Cusp, and GCR regions, respectively. This disagrees with previous reports that 50% of absorbed dose on the ISS comes from the SAA. Last, the lineal energy spectrum from the ISS fight was converted into corresponding LET spectra. Both methods to convert LET did not provide realistic spectra because of their assumptions, making these conversions unsuitable for the space radiation environment.

10.2 Future Work

Although the ATED development project is near completion, there are still questions to be answered and improvements that can be made to the design. Currently, a limitation in the ATED design is the thickness and non-uniformity of the spherical tissue equivalent plastic shell out of

which the ionization cavity is made. The hemispherical shells are currently of thickness that just achieves charged particle equilibrium, which is necessary to ensure proper calculation of absorbed dose. Thicker plastic walls are desirable to ensure charged particle equilibrium. The non-uniformity of the shells introduces uncertainty into measurements of absorbed dose, as discussed in Appendix 1. The hemispherical shells used currently are low-cost, commercially available hemispheres and there is no control in the thickness or uniformity of the plastic. New fabrication methods or source of sphere cavities are needed to improve the ATED instrument.

Many practical lessons were taken from the ATED ISS experiment. While onboard the ISS, the SD RAM card slot had been damaged, meaning no more data could be taken off of the instrument. In the future, a more structurally sound data storage solution is needed and a better location on the ISS to be chosen. Also, the use of a single channel did not sufficiently yield the resolution needed at low lineal energies. Future models of ATED have dual-input spectrometers to ensure proper resolution of low lineal energies in a high gain channel and sufficiently large range in the low gain channel. The possible contamination of the measured signal by microphonic noise led to an investigation of a more rigid anode design. The fixed time resolution of the ISS ATED measurements could be dynamic depending on the amount of radiation that is being measured. This would give more information about radiation levels during SPE and inside the SAA.

Iron beams have been shown to saturate the ATED active volume. At a flux of 100 particles/cm^2/spill at HIMAC, the measured lineal energy spectrum has consistently been at a lower bin value than expected and produced anomalous spectra. It is thought that as the iron beam turns on, counts are initially put into bins surrounding the expected lineal energy. As more of these highly-ionizing iron particles deposit energy into the cavity, the tissue equivalent gas does not have time to fully return to a neutral state before another particle begins to ionize the gas. This has the effect of lowering the strength of the electric field inside the active volume which in

turn lowers the gas gain and total amplification that signals receive. This is why a peak is measured at a lower lineal energy than expected. This phenomenon has led to erroneous calibrations to iron beam data. A study should be performed that varies the flux of iron particles to characterize this effect.

A new cylindrical active volume design that includes the use of field tubes is currently in production. The field tubes will shield the center wire from end effects, as discussed in Chapter 4.8. A more rigorous study of using a cylindrical ATED at particle beams needs to be done. This will answer the question of whether or not a cylindrical ATED can directly measure LET. If true, dose equivalent could be easily calculated and make ATED a powerful instrument for experiments at charged particle beams.

Plans are currently in place to fly ATED on a month long, 24 km altitude balloon flight. The balloon unit will timestamp and save a lineal energy spectrum every 30 seconds along with latitude, longitude, and altitude information. The unit that will be flown on the balloon is in production, along with a commercial flight ATED unit. The commercial flight ATED uses a standard AC power cable to plug into AC power supplies readily available on most flights. This unit will timestamp and save a lineal energy spectrum every 30. These timestamps can then be correlated into websites like FlightAware that give accurate latitude, longitude, and altitude information for commercial flights around the world.

10.3 Final Words

The ATED meets the need for a low-cost, tissue equivalent, easy to use dosimeter to measure the radiation exposure received by humans in the aviation and space radiation environments. Now that the development of ATED is close to being finished, its measurements on various flights,

high altitude balloons, and spacecraft will provide important and reliable insights to the human health impact on these vehicles. The Oklahoma State University Radiation Physics Laboratory is actively seeking opportunities to fly ATED on aircraft and in space.

REFERENCES

Adams D. A., Howell L. W. and Adams J. H. On the use of Lineal Energy Measurements to Estimate Lmear Energy Transfer Spectra [Journal]. - NASA Marshall Space Flight Center, Huntsville, Alabama : [s.n.], 2007.

Adams J.H. [et al.] The Absolute Spectra of Galactic Cosmic Rays at Solar Minimum and Their Implications for Manned Spaceflight [Conference] // Proceedings of the 22nd International Cosmic Ray Conference. - Dublin : [s.n.], 1991.

AMS Integrating Space Weather Observations & Forecasts into Aviation Operations [Report]. - [s.l.] : American Meteorological Society Policy Program, 2007.

Arimoto M. Harita, S. [et al.] Development of a 32-channel ASIC for an X-ray APD detector onboard the ISS [Journal] // Nuclear Instruments and Methods in Physics Research, Section A: Accelerators, Spectrometers, Detectors and Associated Equipment. - Feb 21, 2018. - Vol. 882. - pp. 138-147.

Attix F.H., Roesch W.C. and Tochilin E Radiation Dosimetry [Book]. - New York : Academic Press Inc., 1966. - 2nd : Vol. II.

Badavi F.F., Nealy J.E. and Wilson J.W. The Low Earth Orbit validation of a dynamic and anisotropic trapped radiation model through ISS measurements [Journal] // Advances in Space Research. - October 2011. - 8 : Vol. 48. - pp. 1441-1458.

Badhwar G.D. [et al.] Measurements on the Shuttle of the LET Spectra of Galactic Cosmic Radiation andComparison with the Radiation Transport Model [Journal]. - [s.l.] : Radiation Research Society, Sep. 1994. - 3 : Vol. 139. - pp. 344-351.

Badhwar G.D. [et al.] Validation of the galactic cosmic ray and geomagnetic transmission models [Journal] // Radiation Measurements. - [s.l.] : PubMed, July 2001. - 3 : Vol. 33. - pp. 361-367.

Badhwar G.D. The radiation environment in low-Earth orbit. [Journal] // Radiation Research. - [s.l.] : Radiation Research Society, Nov 1997. - Supplement: Space Radiation Damage and Biodosimetry : Vol. 148. - pp. S3-S10.

Badhwar G. D. Shuttle Radiation Dose Measurements in the International Space Station Orbits [Journal]. - [s.l.] : Radiation Research, 2002. - 1 : Vol. 157. - pp. 69-75.

Banjac S. [et al.] Galactic Cosmic Ray induced absorbed dose rate in deep space – Accounting for detector size, shape, material, as well as for the solar modulation [Journal] // Journal of Space Weather and Space Climate. - May 08, 2019. - Vol. 9.

Benjamin P. W., Kemshall C. D. and Redfearn J. A HIGH RESOLUTION SPHERICAL PROPORTIONAL COUNTER [Journal] // Nuclear Instuments and Methods. - Aldermaston, Berkshire, England : North-Holland Publishing Co., 1968. - Vol. 59. - pp. 77-58.

Benton E. R. [et al.] OSU Dosimetric Experiments aboard the ISS [Conference] // The Workshop on Radiation Monitoring for the International Space Station (WRMISS). - Athens, Greece : [s.n.], 2019.

Benton E.R. and Benton E.V. Space radiation dosimetry in low-Earth orbit and beyond [Journal] // Nuclear Instruments and Methods in Physics Research Section B Beam Interactions with Materials and Atoms. - Oct 2001. - Vol. 182. - pp. 255-294.

Benton Eric R. Radiation Dosimetry At Aviation Altitudes And In Low-Earth Orbit [Report]. - 2004.

Berger T. [et al.] DOSIS & DOSIS 3D: radiation measurements with the DOSTEL instruments onboard the Columbus Laboratory of the ISS in the years 2009–2016 [Journal] // JSWSC. - 2017. - J. Space Weather Space Climate : Vol. 7.

Booz J. [et al.] Report 36 [Journal] // Journal of the International Commission on Radiation Units and Measurements. - 1983. - 1 : Vol. 19. - p. NP.

Brackenbush L.W. USING TISSUE EQUIVALENT PROPORTIONAL COUNTERS TO DETERMINE DOSE EQUIVALENT" [Journal]. - 1990.

Bustamante Mauricio [et al.] Neutrino and cosmic-ray emission from multiple internal shocks in gamma-ray bursts [Journal] // Nature. - [s.l.] : Nature Communications, 2015. - Vol. 6. - Article Number: 6783.

Cauchy A Exercices d'analyse et de physique mathematique [Journal]. - Paris : Bachelor, Dec 31, 1841. - Vol. 2. - p. 428. - French.

Causey O.c. Active Tissue Equivalent Dosimeter: Development of a Dosimeter for the International Space Station [Report]. - Stillwater : Oklahoma State University, 2018.

Cherry R. N. Encylopaedia of Occupational Health and Safety 4th Ed [Book]. - 2012.

Cockroft A. L. and Curran S. C. The Elimination of the End Effects in Counters [Journal]. - Glasgow : The Review of Scientific Instuments, 1951. - 1 : Vol. 22.

Collums T COMPARISON OF PLASTICS USED IN TISSUE EQUIVALENT PROPORTIONAL COUNTERS (TEPC) AND DEVELOPMENT OF A BALLOON BORNE TEPC [Report]. - Stillwater : Oklahoma State University, 2012.

Cossairt D. J. Radiation physics for Personnel and Environmental Protection [Report] : TM-1834. - [s.l.] : FermiLab, 2007.

Cronin J.W. Cosmic Rays at the Energy Frontier [Journal]. - [s.l.] : Scientific American, 1997. - Vol. 6.

Cucinotta F. A., Kim M. Y. and Chappell L. J. Evaluating Shielding Approaches to Reduce Space Radiation Cancer Risks [Report]. - Houston, Texas : NASA, 2012.

Cucinotta F.A. Relative contribution of Neutrons, Protons, and HZEs to Radiation Risk on ISS [Conference] // Predictions and Measurements of Secondary Neutrons in Space. - Houston, TX : [s.n.], 1998.

Dachev Tsvetan [et al.] Overview of the ISS radiation environment observed during the ESA EXPOSE-R2 mission in 2014-2016: ISS radiation environment [Journal] // Space Weather / ed. Wiley. - [s.l.] : AGU, 2017. - 11 : Vol. 15.

Datlowe D. W. Pulse pile-up in nuclear particle detection systems with rapidly varying counting rates [Journal]. - [s.l.] : Nuclear Instruments and Methods, 1977. - 2 : Vol. 1.

DeWitt J. M. Radiation Shielding for Future Space Exploration Missions [Report] : PhD Thesis / Physics ; Oklahoma State University. - Stillwater, OK : [s.n.], 2011. - p. 330.

DeWitt J.M. and Benton E.R. Shielding effectiveness: A weighted figure of merit for space radiation shielding [Journal]. - [s.l.] : Applied Radiation and Isotopes, July 2020. - Vol. 161.

Dwyer J Estimation of the fluence of high-energy electron bursts produced by thunderclouds and the resulting radiation doses received in aircraft [Journal]. - [s.l.] : Journal of Geophysical Research, 2010. - Vol. 115.

Flores-McLaughlin J. [et al.] On-Orbit Status of the ISS Intravehicular Tissue Equivalent Proportional Counter (IV-TEPC). - Austin : [s.n.], 2012.

Friedlander Michael W. Cosmic Ray. - 2011.

Fry R.J.M. Risk Assesment and Late Effects of Radiation in Low-Earth Orbits [Conference] // Symposium on radiation hazards in space and biological consequences. - 1989.

FWT Detector Data Sheets [Online] // www.fwt.com. - Far West Technology, Inc, 2003. - 06 29, 2020. - https://www.fwt.com/detector/prod_det.htm.

Galiautdinov Andrei and Finkelstein David High-Energy cosmic ray production by a neutron star falling into a black hole [Journal]. - [s.l.] : Cornell, 2018.

Gersey B Disscusion of the ATED at LANSCE [Interview]. - 2020.

Gersey B. [et al.] Correlation of Neutron Dosimetry Using a Silicon Equivalent Proportional Counter Microdosimeter and SRAM SEU Cross Sections for Eight Neutron Energy Spectra [Journal]. - [s.l.] : IEEE Transactions of Nuclear Science, 2003. - Vol. 50.

Gersey B. Dosimetry Array Vincula Instument for Neutrons and Charged-particle Ions [Interview]. - 2019.

Gersey B. Personal Interview [Interview]. - Nov 2, 2018.

Gjestelant T. Effects of dead time losses on terrestrial gamma ray flash measurements with the Burst and Transient Source Experiment [Journal]. - [s.l.] : Journal of Geophysical Research , 2010. - Vol. 115.

Grefenstette B. W. [et al.] Time evolution of terrestrial gamma ray flashes [Journal] // Geophysical Research Letters. - [s.l.] : AGU, 2008. - 6 : Vol. 35.

Guetersloh S. [et al.] Polyethylene as a Radiation Shielding Standard in Simulated Cosmic-Ray Environments [Journal]. - [s.l.] : Lawrence Berkeley National Laboratory, 2006.

Hadfield Col. C. Toilet Starting on Station [Sound Recording] : Electronic // Space Sound. - [s.l.] : Sound Cloud, 2013.

Heilbronn L. [et al.] Overview of secondary neutron production relevant to shielding in space [Journal]. - Madeira Island : LBNL Publications, 12 03, 2004.

Heilbronn L., Miller J. and Zeitlin C. Fragmentation Physics and Spacecraft Shielding Studies [Journal] // Radioisotop,es. - 2019. - 6 : Vol. 68.

Hewitt J. E. [et al.] Ames collaborative study of cosmic ray neutrons: Mid-latitude flights [Journal]. - [s.l.] : Health Physics, 1978. - Vol. 34.

Hopkins J.C., Martin J.T. and Seagrave J.D. Shadow-bar design for fast-neutron scattering experiments [Journal] // Nuclear Instruments and Methods. - Los Alamos : North-Holland Publishing Co, 1967. - Vol. 56.

Hurst G. S. and S. A. B. M. An Absolute Tissue Dosemeter for Fast Neutrons [Journal]. - Oak Ridge National Laboratory, Oak Ridge, Tennessee : The British Institute of Radiology, 1954.

ICRP ICRP Publication 60 1990 Recommendations of the International Commission on Radiological Protection [Report]. - [s.l.] : ICRP, 1990.

ICRU Basic Aspects of High Energy Particle Interactions and Radiation Dosimetry [Report]. - Bethesda, MD : ICRU Publications, 1978.

ICRU Microdosimetry. ICRU report 36 [Journal]. - 12 31, 1983.

International Commission of Radiological Protection Publication 103 // 2007 Recommendations of the International Commission of Radiological Protection. - 2007. - Vol. 1.

J. E. McFee A. A. Faust, H. R. Andrews, V. Kovaltchouk, E. T. Clifford and H. Ing A Comparison of Fast Inorganic Scintillators for Thermal Neutron Analysis Landmine Detection [Journal]. - [s.l.] : IEEE Transactions on Nuclear Science, 2009. - 3 : Vol. 56.

Jackson J.D. Classical electrodynamics [Book]. - New York : Wiley, 1999. - Vol. III.

Kampert K. and Watson A. A. Extensive air showers and ultra high-energy cosmic rays: a historical review [Journal] // The European Physical Journal H. - [s.l.] : Springer Link, 2012. - Vol. 37. - pp. 359-412.

Keeter B. ISS Daily Summary Report - 7/13/2018 [Report]. - 2018.

Keeter B. ISS Daily Summary Report - 7/20/2018 [Report]. - 2018.

Keeter B. ISS Daily Summary Report - 9/24/2018 [Report]. - 2018.

Kline S. J. The Purposes of Uncertainty Analysis [Journal]. - Stanford, CA : ASME, 1985. - Vol. 107.

Knoll Radiation detection and measurement [Book]. - New York : Wiley, 1999. - Vol. 3rd.

Kosterev V.V, Tsov'yanov A.G and Sivenkov A.G. Natural and Industrial Background Irradiation Doses for the General Public [Journal] // Atomic Energy. - 2016. - pp. 419-423.

Krane K.S. Introductory Nuclear Physics [Book]. - [s.l.] : Wiley, 1988.

Kroupa M. [et al.] A semiconductor radiation imaging pixel detector for space radiation dosimetry [Journal] // Life Sciences and Space Research. - July 2016.

LANSCE 2018 Run Cycle Report [Report]. - Los Alamos : LANL, 2018.

Lisowski P. A. [et al.] The Los Alamos National Laboratory spallation neutron sources [Journal]. - [s.l.] : Nucl. Sci. Engrg, 1990. - Vol. 106.

Little P.F. Secondary Effects - Electron-emission-Gas Discharches I [Book Section] // Encyclopedia of Physics. - New York City : Springer-Verlag, 1956. - Vol. XXI.

Los Alamos National Lab Los Alamos Neutron Science Center [Online] // lancse.lanl.gov. - 2018. - https://lansce.lanl.gov/.

Lugaz N. [et al.] Earth’s magnetosphere and outer radiation belt under sub-Alfvénic solar wind [Journal] // Nature Communications. - [s.l.] : Nature, 2016. - Vol. 7.

McCormack P. D., Swenberg C E. and Bucker H. Terrestrial Space Radiation and Its Biological Effects [Book]. - NASA Headquarters, Washington, D.C. : Plenum Press, 1987. - Vol. A154.

Meier Matthias M. [et al.] First Steps Toward the Verification of Models for the Assessment [Journal] // Space Weather. - [s.l.] : AGU, 2018.

Mertens Christopher J. Overview of the Radiation Dosimetry Experiment (RaD-X) Flight Mission [Journal] // Space Weather / ed. Wiley. - [s.l.] : AGU, 2016. - pp. 921-1016.

NASA Flashes in the Sky: Earth's Gamma-Ray Bursts Triggered by Lightning. - 2005.

NASA Module Relocated Prepping Station for Commercial Crew. - 2015.

NASA NASA Receives Tranquility [Webpage]. - John F Kennedy Space Center : [s.n.], 2009.

NASA OLTARIS User Guide. - 2018.

NCRP Guidance on Radition Received in Space Activities [Report]. - Bethesda, MD : National Council on Radiation Protection and Measurements, 1989.

NIRS HIMAC Facility [Online]. - 2006. - https://www.nirs.qst.go.jp/ENG/rd/1ban/himac_inf.html.

Norman R. OLTARIS - designing for next-generation exploration [Conference] // ASEC2019. - [s.l.] : ASEC, 2019.

NWRA Geomagnetic Latitude. - [s.l.] : NorthWest Reseearch Associates, 2000.

OSU RPL Studies in Cosmic Ray Muons.

P. Krehbiel [et al.] How Terrestrial Gamma-Ray Flashes are Produced [Conference] // International Union of Geodesy and Geophysics. - Montreal, Canada : IUGG, 2019.

Pazmandi T. [et al.] A new system for measurement of the space radiation [Journal]. - Pozsony : International Youth Nuclear Congress, December 2000.

Pinsky Lawerence S. [et al.] Medipix in space on-board the ISS [Journal] // Journal of Radiation Research. - Mar 2014. - Vol. (Suppl 1). - pp. i62-i63.

Podgorsak E. B. Interactions of Photons with Matter [Book Section] // Radiation Physics for Medical Physicists. - [s.l.] : Springer Link, 2016. - Vol. 1.

Reames Donald V. Solar Energetic Particles [Book]. - Heidelberg : Springer, 2017. - Vol. 932.

RedPitaya Red Pitaya documentation [Online] // redpitaya.readthedocs.io/en/latest/. - Red Pitaya d.d., 2017. - https://redpitaya.readthedocs.io/en/latest/.

Reedy R. Constraints on solar particle events from comparisons of recent events and million-year averages [Conference] // Proceedings of the National Solar Observatory/Sacramento Peak 16th International Workshop on Solar Drivers of Interplanetary and Terrestrial Disturbances. - 1996.

Reilly D., Ensslin N. and Smith H. Passive Nondestructive Assay of Nuclear Materials [Book]. - Washington DC : Office of Nuclear Regulatory Research, 1991. - Vol. I.

Richardson David B. [et al.] Risk of cancer from occupational exposure to ionising radiation: retrospective cohort study of workers in France, the United Kingdom, and the United States (INWORKS) [Journal]. - [s.l.] : BMJ, 2015. - 351:h5359.

Rinard P Neutron interactions with matter [Book Section] // Passive non-destructive assay of nuclear materials / book auth. Reilly D., Ensslin N. and Smith H.. - Washington D.C. : Office of Nuclear Regulatory Research, 1991.

Rios R. Calibration and Readiness of the ISS-RAD Charged Particle Detector [Report]. - Houston : NASA Technical Reports Server, 2015.

Rios Ryan Personal Communication. - Feb 11, 2019.

ROADTOVR NASA's 'Mission: ISS' is an Impressively Detailed View of Life in Zero Gravity. - 2017.

Rossi B.B. and Staub H.H. Ionization Chambers and Counters [Book]. - [s.l.] : McGraw Hill, 1949. - 1.

Rossi H.H. and Zaider M. Microdosimetry and Its Applications [Journal]. - [s.l.] : Springer, 1996.

Sandridge C. A. [Interview] = Personal Communication. - 2019.

Schwadron N.A. [et al.] Particle Radiation Sources, Propagation and Interactions in Deep Space, at Earth, the Moon, Mars, and Beyond: Examples of Radiation Interactions and Effects [Journal] // Space Science Reviews 212(10). - July 2017.

Segre E. [et al.] Experimental Nuclear Physics [Book]. - New York : Wiley, 1953. - Vol. 1.

Shcherbakov A. A. [et al.] Calculation of meridional neutral winds in the middle latitudes from the Irkutsk incoherent scatter radar [Journal]. - [s.l.] : AGU Space Physics, 2015. - Vol. 120.

Singleterry R. C. [et al.] OLTARIS: On-Line Tool for the [Report]. - NASA Langley Research Center, Hamption, Virgina : NASA, 2010.

Smart D.F. and Shea M.A. Fifty years of progress in geomagnetic cutoff rigidity determinations [Journal] // Advances in Space Research . - Nov 2009. - 10 : Vol. 44. - pp. 1107-1123.

Smith M.B. [et al.] Bubble-detector measurements of neutron radiation in the international space station: ISS-34 to ISS-37. [Journal] // PubMed. - 2016.

Spurney F and Dachev Ts. Long-term monitoring of the onboard aircraft exposure level with a Si-diode based spectrometer. [Journal]. - [s.l.] : Advanced Space Research, 2003. - 1 : Vol. 32. - pp. 53-58.

SRAG "Solar particle events from a risk management perspective." = Transactions on Plasma Science,. - 2016.

Stassinopoulos E. G. The Earth's Trapped and Transient Space Radiation Environment [Journal] // Terrestrial Space Radiation and Its Biological Effects. - NASA-Goddard Spece Flight Center, Greenbelt, MD 20771 : Springer, Boston, MA, 1988. - 1 : Vol. 154.

Stassinopoulos E.G., Xapsos M.A. and Stauffer C.A. Forty-Year "Drift" and Change of the SAA [Journal]. - Greenbelt, Maryland : National Aeronautics and Space Administration, December 2015. - p. 78. - NASA Technical Publication .

Thomas G.A. and Symonds P. Thomas GA, Symonds P. Radiation Exposure and Health Effects - is it Time to Reassess the Real Consequences?. Clin Oncol (R Coll Radiol). 2016;28(4):231–236. doi:10.1016/j.clon.2016.01.007 [Journal]. - [s.l.] : Clinical Oncology, Feb 12, 2016. - pp. 231-236.

Tobiska K.W. [et al.] Analytical Representations for Characterizing the Global Aviation Radiation Environment Based on Model and Measurement Databases [Journal] // Space Weather. - [s.l.] : AGU, Sept 2018.

Tsoulfanidis N. Measurement and Detection of Radiation [Book]. - Washington D.C. : Taylor and Francis, 1995. - 2.

Van Allen J.A. Radiation Belts around the Earth [Journal]. - [s.l.] : Scientific American 200:3, 1959.

Wender S. A. [et al.] A fission ionization detector for neutron flux measurements at a spallation source [Journal]. - [s.l.] : Nuclear Instumentation Methons, 1993. - Res. A : Vol. 336.

Wilkinson D.H. Ionization Chambers & Counters [Book]. - London : The Cambridge University Press, 1950.

Wilson J.W. [et al.] Transport Methods and Interactions for Space Radiations [Reference Publication 1257]. - [s.l.] : NASA, 1991.

Wilson J.W. [et al.] Verification and Validation: High Charge and Energy (HZE) Transport Codes and Future Development [NASA Technical Paper 213784]. - 2005.

Xilinx FPGA Leadership across Multiple Process Nodes [Online] // xilinx. - xilinx, 2019. - https://www.xilinx.com/products/silicon-devices/fpga.html.

Zaconte V. [et al.] High energy radiation fluences in the ISS-USLab: Ion discrimination and particle abundances [Journal] // Radiation Measurements. - February 2010.

Zhou D. [et al.] Radiation measured with TEPC and CR-39 PNTDs in low earth orbit [Journal]. - [s.l.] : Advances in Space Research, 2007. - 40. - pp. 1571-1574.

APPENDICES

Appendix 1: Uncertainties in ATED Measurements

The significant sources of uncertainty for measured absorbed dose by ATED are uncertainty in the mass of tissue equivalent gas inside the active volume, and the mean chord length of the simulated tissue phantom [Causey, 2018]. These uncertainties come from the non-uniformity of the physical dimensions of the tissue equivalent plastic that surround and define the borders of the active volume. The uncertainties associated with ATED calculated absorbed dose values, and how these values are arrived at, are discussed in this appendix. We proceed to describe these sources of uncertainty, quantify the uncertainty of all three ATED active volumes, and show methods that further reduce these uncertainties.

A.1.1 Negligible Sources of Error in ATED Absorbed Dose Calculations

The instruments used to measure pressure, volume, and temperature of the tissue equivalent gas as the ATED active volume is filled are negligible sources of uncertainty. Pressure is measured by a Far West Technology GFS-1 Gas Filling System that is accurate to 0.12 Torr [FWT, 2003].

Ambient room temperature is measured by a PDT650 Pocket Thermometer, accurate up to 0.1° C. The dimensions of the active volume were measured with a digital caliper, accurate up to 0.01mm. These instruments do not significantly contribute to uncertainty in the amount of gas inside the ATED active volume. The composition of the tissue equivalent gas used is 2.751% N_2, 29.99% CO_2, and 67.259% CH_4. Respective molar masses of each of molecule are 28.01, 44.01, and 16.04 g/mol. Molar mass of the tissue equivalent gas is 24.7576 g/mol. These values are known with high precision and thus are not involved in the propagation of uncertainty.

A 1.2 Description of Uncertainty Associated with the Mass of Tissue Equivalent Gas

The mass of the tissue equivalent gas inside the active volume is used in calculating absorbed dose in tissue from ATED measurements [ICRU, 1985]. It is the largest contributor to uncertainty when calculating dosimetric quantities from ATED measurements. The uncertainty in mass is from the uncertainty in dimensions of the tissue equivalent plastic that surround and define the border of the active volume. The dimensions of the active volume are used to find the pressure needed to simulate the desired tissue phantom size. The pressure of tissue equivalent gas inside the ATED active volume is subject to the ideal gas law,

$$P = \frac{nRT}{V}, \tag{A.1.1}$$

where, P is the pressure of gas inside the detector head, n is the number of moles, R is the universal gas constant, T is the temperature, and V is the volume. The ideal gas law is used to calculate the pressure needed to achieve the same number of moles of gas as a microscopic volume of tissue (see chapter 3),

$$n = \frac{PV}{RT}. \tag{A.1.2}$$

The variables that contribute to uncertainty in the number of moles are: the pressure, the volume, and the temperature of the gas inside the ATED active volume. The spherical and cylindrical tissue equivalent plastic shells are not uniform in thickness, height, or diameter. The internal diameters of the 2-inch and 3-inch spheres, the height of the right circular cylinder, and their associated absolute uncertainties are shown in **Table A.1.1**. The height of the cylinder is only considered because it is used in experiments were particles will only traverse its height. Absolute uncertainty was calculated by finding the standard deviation of a large population of measurements.

Active Volume	**Internal Diameter or Height (mm)**	**Absolute Uncertainty (±mm)**
2 Inch Spherical Shell	45.44	0.47
3 Inch Spherical Shell	70.53	0.36
2 Inch Right Circular Cylindrical Shell (height)	51.43	0.10

Table A.1.1: Internal diameters of the ATED spherical active volumes and the height of the cylindrical ATED volume with their associated uncertainties

The mass needed to simulate 2μm diameter sphere or right circular cylinder of tissue of 2 μm height are found using the definition of tissue equivalence in Chapter 3. The molar mass of the gas is used to find the number of moles needed to simulate the microscopic volumes of tissue. The desired pressure can then be solved as a function of temperature by using equation 9.1. This relationship is used when filling the detector head with tissue equivalent gas. It specifies the required pressure at the measured ambient room temperature. **Table A.1.2** lists the different functions of pressure for each volume and their associated absolute uncertainties.

Active Volume	Pressure as a function of temperature (Torr/K)	Uncertainty (±Torr/K)
2 Inch Spherical Shell	0.110870	0.005917
3 Inch Spherical Shell	0.0726535	0.002119
2 Inch Right Circular Cylindrical Shell (height)	0.098333624	0.001565

Table A.1.2: The functions of pressure as a function of temperature as a function of temperature for each ATED active volume.

The relative uncertainties of the mass inside each active volume are shown in **Table A.1.3**. Relative uncertainty is calculated by the quotient of the absolute uncertainty and the best estimate [Kline, 1985]. Previously, the ambient room temperature was not measured and resulted in a relative uncertainty of ~5% for the mass of gas in the active volume for the 3-inch sphere [Causey, 2018]. By measuring the ambient room temperature, a 3.08% gain in certainty is achieved for the mass inside the 3-inch spherical shell.

Active Volume	Relative Uncertainty in Mass (%)
2 Inch Spherical Shell	5.34%
3 Inch Spherical Shell	2.92%
2 Inch Right Circular Cylindrical Shell (height)	1.59%

Table A.1.3: The relative uncertainty in mass for ATED active volumes

A.1.2 Description of Uncertainty in Chord Length of the Simulated Volume

Uncertainty is also propagated by the mean chord length of the simulated volume used in the calculation of absorbed dose. The uncertainty in the dimensions of the active volume will be directly related to the uncertainty of the simulated volume dimensions. The internal diameter of the spheres and height of the cylinder will follow the relationship

$$d_g \pm \delta d_g = d_t \pm \delta d_t \tag{A.1.3}$$

where d_g is the diameter of the gas-filled volume, d_t is the diameter of the simulated volume (2 μm) and δd_x are the absolute uncertainties for the volume x. The diameter of a sphere can be changed into mean chord length via the relationship: $\bar{l} = 2/3d$, where $\bar{l}$ is the mean chord length. For the 2-inch spherical shell, the simulated volume has a diameter of:

$$d_t \pm \delta d_t = 2.0 \ \pm 0.0205 \mu m. \tag{A.1.4}$$

This correlates to a mean chord length of:

$$\bar{l} \ \pm \delta d_{\bar{l}} = 1.33 \ \pm 0.0137 \ \mu m, \tag{A.1.5}$$

where $\delta d_{\bar{l}}$ is the absolute uncertainty of the mean chord length. The relative uncertainty of mean chord length for each active volume is shown in **Table A.1.4**.

Active Volume	**Relative Uncertainty in Mean Chord Length (%)**
2 Inch Spherical Shell	1.03%
3 Inch Spherical Shell	0.72%
2 Inch Right Circular Cylindrical Shell (height)	0.20%

*Table A.1.**Error! No text of specified style in document.**4: Relative uncertainty in mean chord length for ATED simulated volumes*

A.1.3 Uncertainty in Absorbed Dose

Both the chord length and mass of gas inside the active volume will contribute to uncertainty in absorbed dose. The uncertainties found are placed into the calculation of absorbed dose for ATED measurements (equation 4.26). This results in the expression,

$$D(y) = y * f(y) \frac{\bar{l} \pm \delta \bar{l}}{m \pm \delta m} * 1.602 * 10^{-16} \frac{J}{eV}, \tag{A.1.6}$$

where $\delta\bar{l}$ is the absolute uncertainty in the mean chord length and δm is the absolute uncertainty in the mass of gas used. The uncertainty in the measured $f(y)$ spectrum and y are negligible and thus not considered. The quotient of two uncertainties results in their summation [Kline, 1985]. The relative uncertainties in absorbed dose for each volume are shown in **Table A.1.5**.

Active Volume	**Relative Uncertainty in Absorbed Dose (%)**
2 Inch Spherical Shell	6.37%
3 Inch Spherical Shell	3.64%
2 Inch Right Circular Cylindrical Shell (height)	1.79%

*Table **Error! No text of specified style in document.**A.1.5: The relative uncertainty in absorbed dose measurements for different ATED active volumes.*

The ATED flown on the ISS had a relative uncertainty in absorbed dose of 5.80% [Causey, 2018]. The ambient temperature when the active volume was filled with tissue equivalent gas was not measured and resulted in a larger uncertainty than above.

Appendix 2: Dosimetric Quantities in Microdosimetry

The units and definitions of dosimetric and microdosimetric quantities used in this dissertation and the field of dosimetry in general are outlined in this appendix. This serves to eliminate confusion with the terminology used in this dissertation for those who may be unfamiliar with them. For those who are familiar with the terms used in dosimetry, this appendix serves as a brief summary and can be skipped. The proceeding definitions come from the International Commission of Radiation Units and Measurements (ICRU) and the International Commission of Radiological Protection (ICRP).

A.2.1 Particle Fluence and Flux

The definition of the number of particles crossing a cross-sectional area is called particle fluence, Φ, and is defined as:

$$\Phi = \frac{\partial N}{\partial A} \tag{A.2.1}$$

where ∂N is the number of particles incident on a cross sectional area, ∂A. Particle Fluence has the SI units of m^{-2}.

Particle flux, similar to particle fluence, is the number of particles crossing a cross-sectional area per unit time. This leads to the definition for particle flux:

$$\dot{\Phi} = \frac{\partial \Phi}{\partial t} = \frac{\partial^2 N}{\partial A\, \partial t} \tag{A.2.2}$$

where ∂t is a unit change of time. The SI units of particle flux are $m^{-2}s^{-1}$.

A.2.2 Stopping Power and Linear Energy Transfer

The mechanism that slows down charged particles as they traverse matter is called stopping power. Stopping power is equivalent to the loss of energy of a charged particle per unit path length:

$$S = \frac{dE}{dx} \tag{A.2.3}$$

where dE is the loss of energy by the particle and dx is the unit path length. The units for stopping power are commonly given as MeV cm^{-1}. Similar to stopping power, mass stopping power is characteristic to a material and is obtained by dividing the stopping power by the density of the material:

$$S = \frac{s}{\rho} = \frac{1}{\rho}\frac{dE}{dx} \tag{A.2.4}$$

where ρ is the mass density. The typical units for mass stopping power are given in MeV cm^2 g^{-1}. Mass stopping power is commonly used because it expresses the loss of energy of a charged particle normalized to density.

To clarify the physical processes involved in the loss in energy per unit length, we can further separate mass stopping power into its constituent parts:

$$S = \frac{1}{\rho}\left\{\left(\frac{dE}{dx}\right)_{el} + \left(\frac{dE}{dx}\right)_{rad} + \left(\frac{dE}{dx}\right)_{nuc}\right\} \tag{A.2.5}$$

where $\left(\frac{dE}{dx}\right)_{el}$ is the loss of energy from interactions with electrons, $\left(\frac{dE}{dx}\right)_{rad}$ is the loss of energy from radiative interactions (Bremsstrahlung x-ray emission), and $\left(\frac{dE}{dx}\right)_{nuc}$ is the loss of energy due to coulomb interactions with nuclei. As ionizing radiation traverses a medium, the main way energy will be lost is through ionization, where electrons will be ejected from their nuclei.

Linear energy transfer (LET) is quantified by the average loss of energy for a particle per unit distance it has traveled due to interactions with electrons. LET is very closely related to stopping power, but LET only includes the electronic component. Many radiation detectors directly measure LET. Only unrestricted LET is discussed for the purposes of this dissertation. Unrestricted LET is equivalent to electronic stopping power:

$$L_\infty = \left(\frac{dE}{dx}\right)_{el} = L. \tag{A.2.7}$$

Unrestricted LET is represented by L and has the units of keV/μm. The LET of a particle is dependent on two factors: the charge of the particle and its kinetic energy. This is made apparent in the Bethe-Bloch formula,

$$-\left\langle\frac{dE}{dx}\right\rangle = \frac{4\pi}{m_e c^2}\cdot\frac{nZ^2}{\beta^2}\cdot\left(\frac{e^2}{4\pi\epsilon_0}\right)^2\cdot\left[\ln\left(\frac{2m_e c^2\beta^2}{I\cdot(1-\beta^2)}\right)-\beta^2\right], \quad \text{(A.2.6)}$$

where c is the speed of light, ϵ_0 is the vacuum permittivity, β is the Lorentz factor, e is the charge of an electron, m_e is the mass of the electron, Z is the atomic number, n is the electron number density, and I is the mean excitation potential [Segre, et al., 1953].

A.2.3 Lineal Energy

Gas-filled detectors cannot directly measure LET. What is instead measured is the current induced in electrodes (ionization chambers) or voltage pulses (proportional counters). All gas-filled detectors have a volume that holds gas and where radiation is detected. This is called the active volume of the detector. The path taken through the active volume by ionizing radiation is called a chord. If the chord inside active volume is known, then the pulse height may be converted to LET [Collums, 2012]. In the case of a spherical volume in an isotropic field of ionizing radiation, individual chords are not known. In cases like this, lineal energy is measured instead of LET. Lineal energy is the quotient of the energy imparted by a single event and the mean chord length of the volume,

$$y = \frac{\epsilon}{\bar{l}} \quad , \quad \text{(A.2.7)}$$

where $\bar{l}$ is the mean chord length of the volume and ϵ is the energy imparted by a single event [Rossi et. al., 1996]. For certain volumes the mean chord length can be found analytically. For a spherical active volume, the mean chord length is given by the relation $\bar{l} = 2d/3$ where d is the diameter of the sphere.

A.2.4 Absorbed Dose and Dose Equivalent

An important quantity to measure in terms of radiation protection is absorbed dose. Absorbed dose is the mean amount of energy deposited by ionizing radiation divided by the mass into which the energy was deposited,

$$D = \frac{d\bar{\epsilon}}{dm} \tag{A.2.8}$$

where $d\bar{\epsilon}$ is the mean energy absorbed in a unit mass, dm. The SI units for absorbed dose are J/kg. The ICRU defines this as the unit for absorbed dose, the Gray, where 1Gy = 1 J/kg. It is usually specified what material energy was deposited in, i.e. absorbed dose in silicon, tissue, etc. Absorbed dose rate is simply the temporal derivative of absorbed dose,

$$\dot{D} = \frac{dD}{dt} = \frac{d^2\bar{\epsilon}}{dm\,dt}. \tag{A.2.9}$$

Absorbed dose rate takes on many units, depending on the suitable time frame. Thus the units reported will reflect the nature of the experiment.

Dose equivalent (H) is the biologically relevant correspondent of absorbed dose. Dose equivalent is a more accurate metric on the biological damage of ionizing radiation than absorbed dose. The ICRP has defined dose equivalent as the product of absorbed dose and a quality factor Q,

$$H = D \cdot Q. \tag{A.2.10}$$

Dose equivalent has units of Sieverts (Sv). The quality factor is defined as a function of LET [ICRP, 1991]:

$$Q(L) = \begin{cases} 1 & L < 10\frac{keV}{\mu m} \\ 0.32L - 2.210 & \leq L \leq 100\frac{keV}{\mu m} \\ \frac{300}{\sqrt{L}} & L > 100\frac{keV}{\mu m} \end{cases} . \tag{A.2.11}$$

Assumptions in the chord lengths in gas-filled detectors can be used to convert $Q(L)$ into a function of lineal energy (y). **Figure A.2.1** shows the quality factor as a function of LET as defined in ICRP 60 [ICRP 1991].

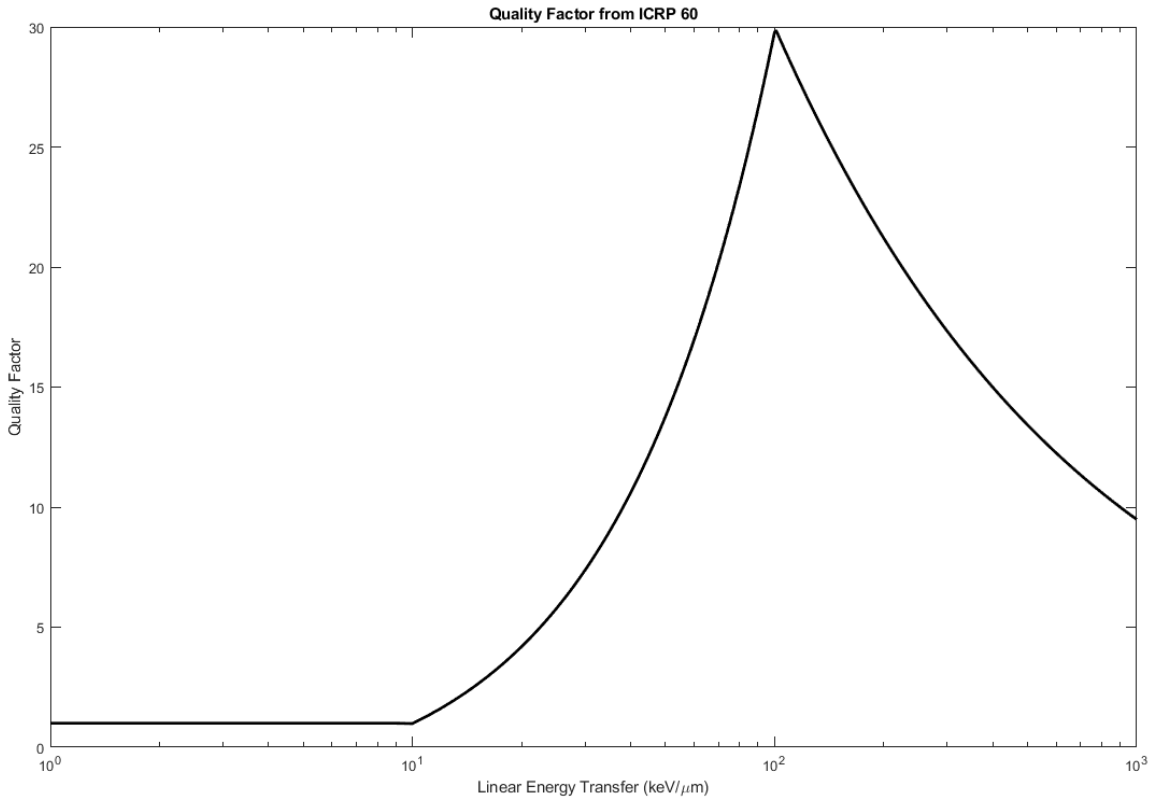

Figure A.2.1: Quality factor as a function of LET. These values are derived from the definition in ICRP 60.

The ICRP defines the recommended annual dose limits for planned exposure situations [ICRP, 2007]. They define two groups: occupational and public. Recommended Occupational annual exposure is 20 mSv per year, averaged over 5-year periods and should not exceed 50 mSv in any single year. Recommended public annual exposure is 1 mSv. In some circumstances, a higher value could be allowed for the public as long as the average exposure over 5 years does not exceed 1 mSv. In aviation, aircrew members are considered part of the occupational group. Exceptional cases for annual dose limits are made, like in space travel, and are dealt with separately.

Appendix 3: Preliminary Cylindrical ATED Measurements at HIMAC

The various beams at HIMAC simulate very narrow bands of energy and ions in the GCR spectrum. In the search for better spacecraft materials, candidate materials are placed in the beam and tested for their shielding ability for this radiation. ATED is used to measure the absorbed dose behind different materials to quantify their effectiveness to shield space radiation. A cylindrical ATED is in development specifically for these experiments to improve measurements compared to spherical ATED instruments.

A.3.1 Dose-Depth Experiment with Cylindrical ATED

The approximate effect that different materials have on shielding space radiation can be quantified using mono-energetic heavy ion beams at HIMAC of energy and charge similar those found in the peak of the GCR energy spectrum (10^3-10^4 MeV/n; see Chapter 2.1). The effectiveness of a particular material to shield radiation is quantified through dose-depth experiments, where absorbed dose is measured behind various depths of particular material. Depth is defined as the product of the density of a material and its thickness (units of g/cm^2). ATED is used to measure the absorbed dose in tissue.

The dose-depth trend of a particular material is compared to aluminum and polyethylene. Aluminum is widely used in spacecraft and polyethylene is the standard for radiation shielding experiments [Guetersloh, et al., 2006]. Aluminum is a strong and lightweight material, but is not a good radiation shield since the relatively high Z of the aluminum can produce a lot of secondary neutrons during nuclear interactions with incident GCR. Polyethylene is not used as spacecraft shielding because it has poor structural strength despite its good radiation shielding properties. Multi-functional materials are desired for future designs of spacecraft as they can have both good

structural properties and similar radiation shielding to that of polyethylene [Cucinotta, et al., 2012]. Polypropylene doped with silicon carbide, 20% by weight (PPSiC20), is a multi-functional material that was tested for its radiation shielding effectiveness at HIMAC. A comprehensive study on the physics of space radiation shielding is discussed in [DeWitt, et al., 2020].

In the past, CR-39 plastic nuclear track detector (PNTD) was used for measuring absorbed dose behind shielding materials. One goal of the ATED development project is to replace CR-39 PNTD with an active instrument for use in particle beam shielding experiments. Data processing is much less labor intensive with ATED as compared to CR-39 PNTD.

Figure A.3.1 shows the absorbed dose per fluence as a function of depth and thickness for 230 MeV protons measured by a spherical ATED. The materials are aluminum, polyethylene and PPSiC20. Uncertainty is quantified as 6.37% for absorbed dose measurements by a 2-inch spherical ATED. Each measurement has been normalized to fluence measured by a 1 cm x 1 cm plastic scintillator. The uncertainty of each measurement is large compared to the fluctuations in measured absorbed dose. The absorbed dose per fluence between 0 and 17 g cm^{-2} of depth for PPSiC20 and polyethylene are the same within uncertainty. These results show that PPSiC20 is comparable to polyethylene in terms of reducing absorbed dose.

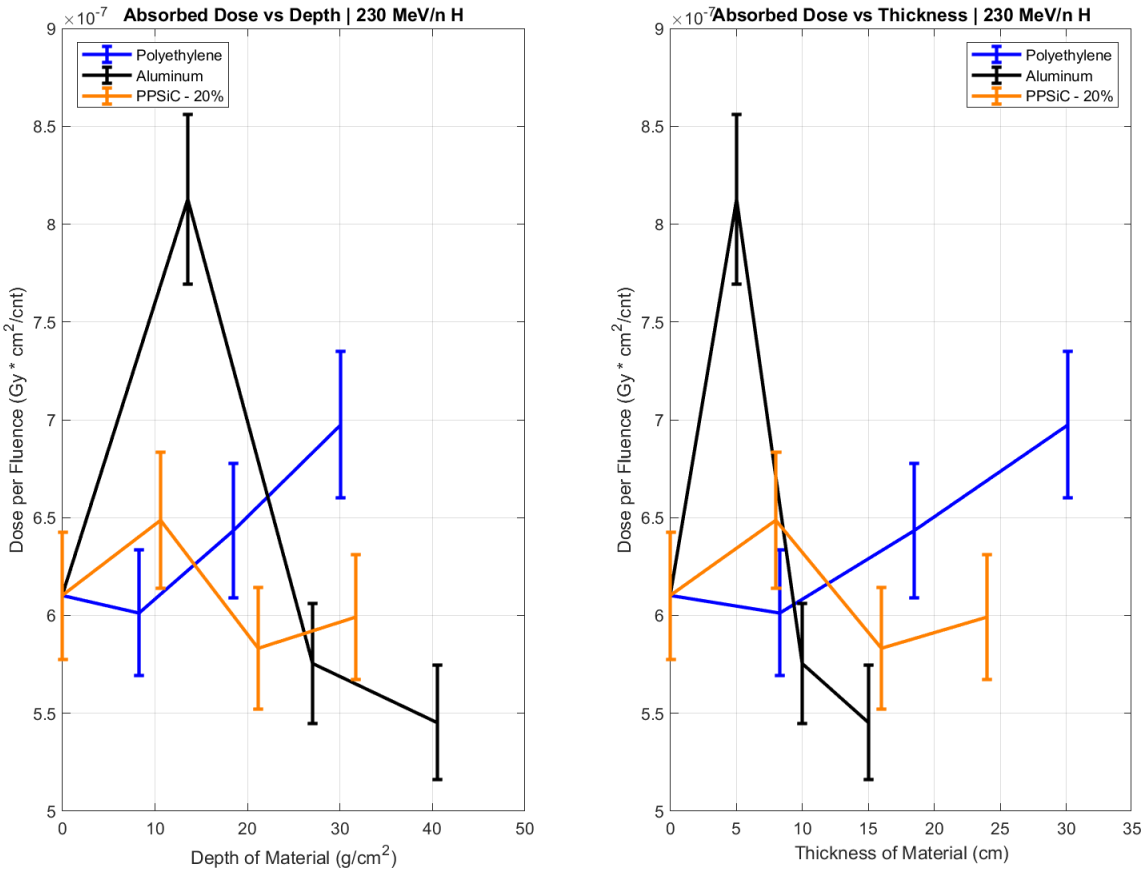

Figure A.3.1: Absorbed dose normalized by fluence as a function of depth (left) and thickness (right) for aluminum, polyethylene and PPSiC20 as measured by a spherical ATED.

A cylindrical ATED has been developed for use in shielding experiments to replace spherical ATED instruments used in space and aviation dosimetry. When irradiated end on, a cylindrical ATED has the advantage of having a uniform chord length when particles are unidirectional, like at HIMAC. Also, cylindrical ATED volumes have a smaller associated uncertainty in the measurement of absorbed dose compared to spherical volumes (see Appendix. 1). This makes cylindrical ATED instruments more desirable to characterize space radiation shielding at particle accelerators.

Figure A.3.2 shows the absorbed dose vs depth and absorbed dose vs thickness from a 500 MeV/n iron beam as measured by a cylindrical ATED. The tested materials were aluminum, polyethylene and PPSiC20. Uncertainty was quantified as 2.16% for the absorbed dose measurements. Each measurement has been normalized to fluence measured by a 1 cm x 1 cm

plastic scintillator. The uncertainty in each absorbed dose measurement is much smaller compared to the spherical ATED measurement in **Figure A.3.1**. At a depth of ~5.5 g/cm2 the uncertainty of absorbed dose for each material is small enough that they do not overlap. If this measurement was done with a spherical ATED, the uncertainty between all three materials would overlap.

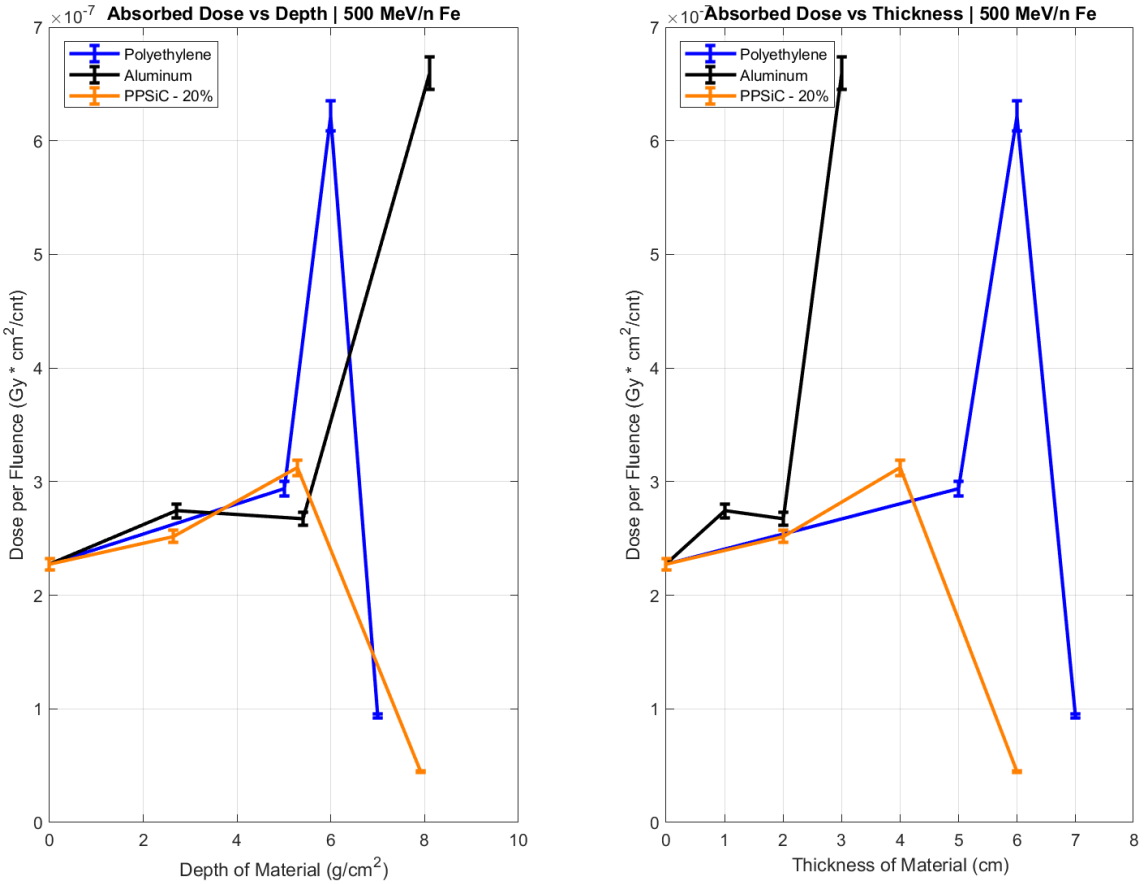

Figure A.3.2: Absorbed dose from 500 MeV/n Fe, normalized by fluence, as a function of depth (left) and thickness (right) as measured by a spherical 2-inch ATED. The materials are aluminum, polyethylene and PPSiC20.

The reduction in uncertainty from 6.37% for spherical ATED absorbed dose measurements to 2.16% for cylindrical ATED absorbed dose measurements is a significant improvement. Note that this is only true for mono-directional charged particles such as those produced by particle accelerators. For neutrons or in isotopic radiation fields, the uncertainty in absorbed dose for a cylindrical ATED will be comparable to a spherical ATED. Future direct beam shielding experiments will be conducted with cylindrical ATED instruments. By orienting the cylindrical

ATED active volume such that charged particles cross the height of the volume, it is possible that LET can be directly measured by ATED. More tests are needed to confirm this possibility.

VITA

Bryan Michael Hayes

Candidate for the Degree of

Doctor of Philosophy

Thesis: ANALYSIS OF MEASUREMENTS AND IMPROVEMENTS UPON THE ACTIVE TISSUE EQUIVALENT DOSIMETER

Major Field: Physics

Biographical:

Education:

Completed the requirements for the Doctor of Philosophy in Physics at Oklahoma State University, Stillwater, Oklahoma in July, 2020.

Completed the requirements for the Bachelor of Science in Physics at University of La Verne, La Verne, California in 2016.